國立臺灣大學理學院化學系

博士論文

Department of Chemistry
College of Science
National Taiwan University
Doctoral Dissertation

應用於染料敏化太陽能電池及有機太陽能電池之小分子及高分子材料的設計與合成

Design, Synthesis, and Exploitation of Small-Molecule and Polymeric Materials for Dye-Sensitized Solar Cells and Organic Solar Cells

林立彥

Li-Yen Lin

指導教授：汪根欉 博士

Advisor: Ken-Tsung Wong, Ph.D.

中華民國102年6月

June 2013

國立臺灣大學博士學位論文
口試委員會審定書

（論文中文題目）應用於染料敏化太陽能電池及有機太陽能電池之小分子及高分子材料的設計與合成

（論文英文題目）Design, Synthesis, and Exploitation of Small-Molecule and Polymeric Materials for Dye-Sensitized Solar Cells and Organic Solar Cells

本論文係 林立彥 君（學號 F97223103 ）在國立臺灣大學化學系完成之博士學位論文，於民國 102 年 6 月 5 日承下列考試委員審查通過及口試及格，特此證明。

口試委員：

汪根欉 （簽名）

（指導教授）

周必泰　　吳忠幟

蔡吉良　　林皓武

洪文誼　　鄭彥如

系主任、所長 張煥宗 （簽章）

謝誌

很高興即將迎接人生下一階段的挑戰，漫長的學生生涯終於結束了！能夠順利地取得博士學位，首先要特別感謝指導教授汪根欉老師從大三專題時代至今共七年的指導，讓學生能夠在染料敏化太陽能電池以及有機太陽能電池這兩個領域中稱得上是半個專家，汪老師除了在學術研究上給予學生全方位的訓練以及自由揮灑的空間外，更大方地提供學生出國從事訪問研究的機會和給予學生各項獎學金申請上的全力支持，而汪老師在待人處事上的風格與智慧，更為學生樹立了良好的典範。感謝吳忠幟老師、蔡志宏老師和林皓武老師及其團隊的合作，讓我們在分子設計上的構想得以在元件端得到印證，你們高超的元件製作技術，更使得我們開發的材料有著超乎預期的表現，很開心在畢業前就能夠共同將這些成果發表於優秀國際期刊上。感謝芝加哥大學 Luping Yu 老師在美國訪問研究期間的指導，Yu 老師在研究態度上的堅持，著實啟發學生對學術研究有著不同的思考。感謝周必泰老師、洪文誼老師和鄭彥如老師在口試時的指教與建議，除了使得本論文更加完整，亦讓學生獲益良多。感謝 KTW 實驗室裡所有伙伴在實驗上的協助，使得我的研究能夠順利地進行，你們的陪伴也讓我的研究生活不致於枯燥乏味。最後特別感謝家人的栽培和生活上的照顧，你們無私的付出和包容，讓我得以專心地完成學業。

中文摘要

在過去的一二十年間，日益增加的能源需求以及對於全球暖化的關注正促使不污染環境的再生能源的發展，利用光伏打科技將太陽能轉換為電力提供一個永續的方法來解決上述議題。相較於目前市場上為主的矽基太陽能電池，染料敏化太陽能電池和有機太陽能電池都被視為其高度有希望以及經濟合算的替代物。

此論文敘述我在設計與合成應用於染料敏化太陽能電池及有機太陽能電池之小分子及高分子材料上的研究工作，主要著重於探討化學結構和物理性質之間的關係，以及此關係和元件表現之間的關聯。其整體架構如下，第一章簡略地綜述共軛芳香系統能隙的操縱；第二章論及三系列應用於染料敏化太陽能電池的有機染料分子的設計、合成及鑑定；第三章敘述八個應用於蒸鍍型有機太陽能電池的小分子予體材料，其合成、物理性質以及光伏打性能會被詳述；第四章敘述兩個p-型共軛高分子的合成、光電鑑定及其作為濕式製程高分子塊材異質接面太陽能電池中的予體材料的表現。此外，在第二、第三和第四章的開頭部分會各自地介紹目前最先進的應用於染料敏化太陽能電池的光敏分子以及應用於有機太陽能電池的小分子和高分子予體材料。

Abstract

Increasing energy demands and concerns about global warming have been driving a great need to develop environmentally friendly renewable energy resources in the past few decades. Conversion of solar energy into electricity via photovoltaic technologies provides a sustainable approach to addressing these issues. Both dye-sensitized solar cells (DSSCs) and organic solar cells (OSCs) have been regarded as highly promising and cost-effective alternatives to the market dominant silicon-based counterparts.

This dissertation describes my research efforts in the design, synthesis, and characterization of small-molecule and polymeric materials for DSSCs and OSCs, with the focus on the exploration of structure–property relationships and their correlations to device performance. It is organized as follows. Chapter 1 gives a brief overview of bandgap engineering of π-conjugated aromatic systems. Chapter 2 deals with the design principles, synthesis, and characterization of three series of organic sensitizers as well as their application in DSSCs. Chapter 3 describes eight small-molecule donor materials for use in vacuum-deposited OSCs. Their synthesis, physical properties, and photovoltaic performance are discussed. Chapter 4 describes the synthesis and optoelectronic characterization of two p-type conjugated polymers as well as their use as donors in solution-processed polymer bulk heterojunction solar cells. Furthermore, a short summary of state-of-the-art photosensitizers for DSSCs as well as molecular donors and polymeric donors for OSCs is respectively presented in the beginning of Chapter 2, 3, and 4.

Contents

List of Figures

List of Schemes

List of Tables

Chemical Structure Index

Target Compounds

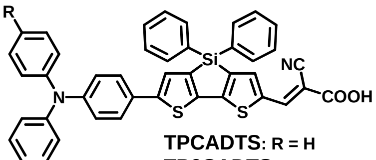

TPCADTS: R = H
TP6CADTS: R = OC_6H_{13}

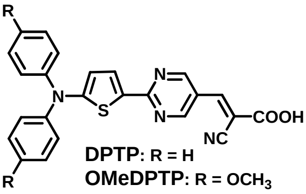

DPTP: R = H
OMeDPTP: R = OCH_3
OHexDPTP: R = OC_6H_{13}

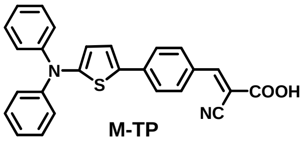

M-TP

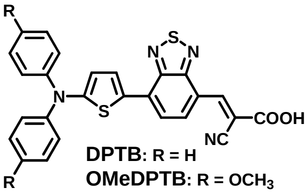

DPTB: R = H
OMeDPTB: R = OCH_3
OHexDPTB: R = OC_6H_{13}

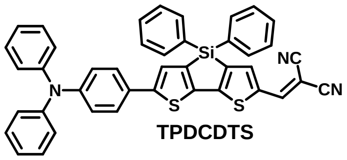

TPDCDTS

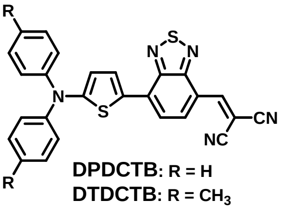

DPDCTB: R = H
DTDCTB: R = CH_3

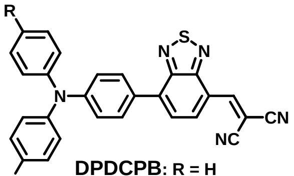

DPDCPB: R = H
DTDCPB: R = CH_3

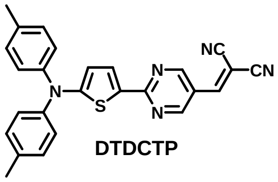

DTDCTP

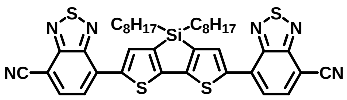

BCNDTS

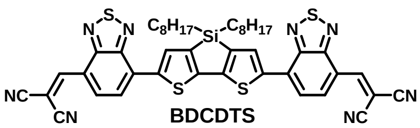

BDCDTS

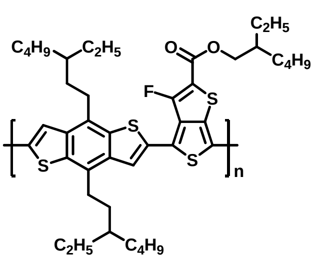

PTB10

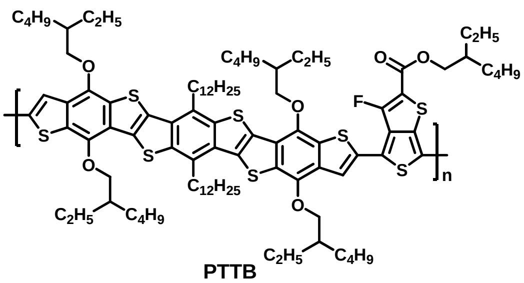

PTTB

Intermediates

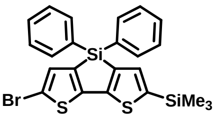
2-1

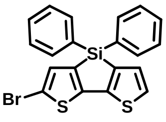
2-2

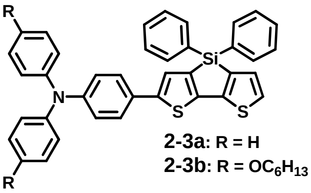
2-3a: R = H
2-3b: R = OC_6H_{13}

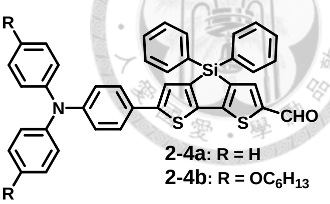
2-4a: R = H
2-4b: R = OC_6H_{13}

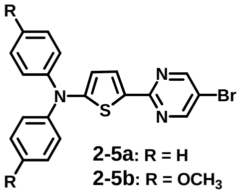
2-5a: R = H
2-5b: R = OCH_3
2-5c: R = OC_6H_{13}

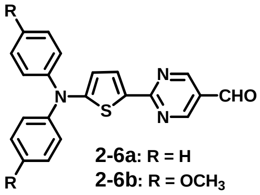
2-6a: R = H
2-6b: R = OCH_3
2-6c: R = OC_6H_{13}

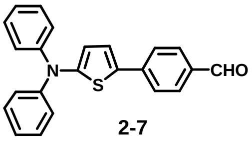
2-7

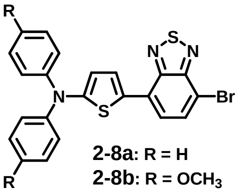
2-8a: R = H
2-8b: R = OCH_3
2-8c: R = OC_6H_{13}

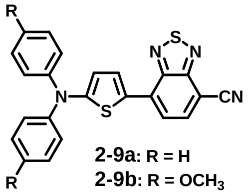
2-9a: R = H
2-9b: R = OCH_3
2-9c: R = OC_6H_{13}

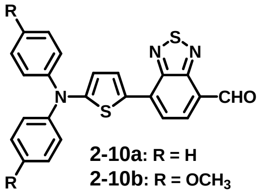
2-10a: R = H
2-10b: R = OCH_3
2-10c: R = OC_6H_{13}

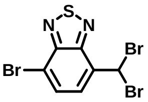
3-1

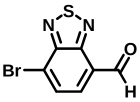
3-2

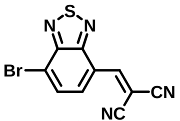
3-3

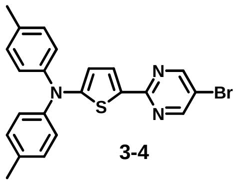
3-4

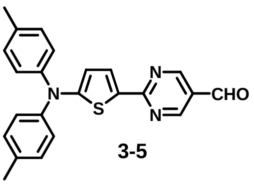
3-5

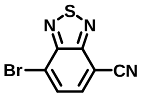
3-6

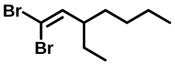
4-1

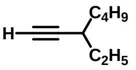
4-2

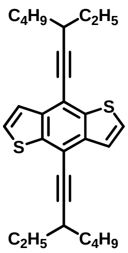
4-3

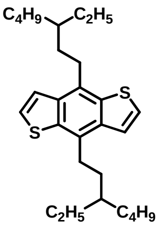
4-4

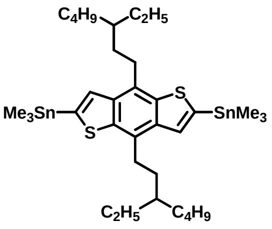
4-5

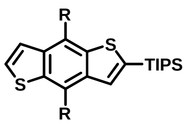
4-6a: R = 2-ethylhexyloxy
4-6b: R = 3-ethylheptyl

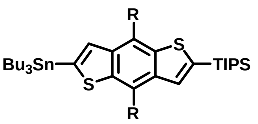
4-7a: R = 2-ethylhexyloxy
4-7b: R = 3-ethylheptyl

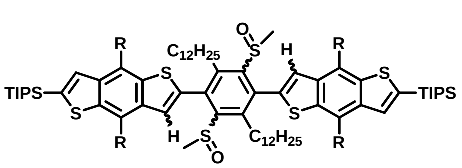
4-8a: R = 2-ethylhexyloxy
4-8b: R = 3-ethylheptyl

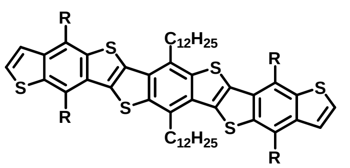
4-9a: R = 2-ethylhexyloxy
4-9b: R = 3-ethylheptyl

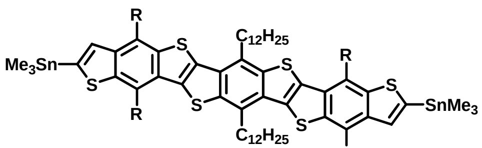
R = 2-ethylhexyloxy
4-10

Chapter 1. Bandgap Engineering of π-Conjugated Aromatic Systems

The control of bandgaps is of prime importance in the design of photoactive materials for use in organic photovoltaics (OPVs). The solar spectrum is distributed over a wavelength range from 280 nm to 4000 nm and has maximum photon flux densities between 600 nm and 800 nm (Figure 1-1). Thus, in order to effectively harvest solar photons, it is necessary to develop solar-active materials with suitable bandgaps so that their absorption profile can cover the visible and the near-infrared (NIR) regions to overlap well with the major part of the solar spectrum while also retaining high absorption coefficients at relevant wavelengths.

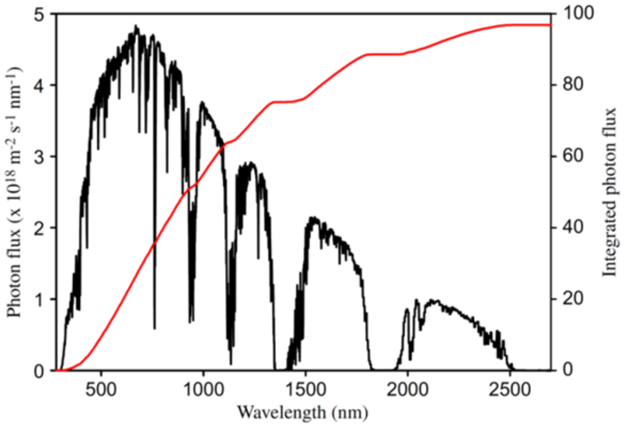

Figure 1-1. AM1.5 photon flux from the sun at the earth's surface as a function of wavelength.[1] The black trace indicates the photon flux, and the red trace represents the percentage of solar photons below the given wavelength as obtained by integrating the photon flux.

The ground state of a π-conjugated aromatic system is composed of two energetically nondegenerate resonance structures: the so-called aromatic form and quinoid form (Figure 1-2). In the aromatic form, the π-electrons are confined within the aromatic rings to maintain their aromaticity. In the quinoid form, however, the π-electrons are delocalized over the whole structure and hence the π-framework becomes fully conjugated. Due to the destruction of aromaticity and the consequent loss of aromatic stabilization resonance energy, the quinoid form is higher in energy than the aromatic form and thus has a smaller bandgap.[2] The relative contribution of the two limiting mesomeric forms to the ground-state structure of a molecule is related to a geometrical parameter, bond length alternation (BLA), which is defined as the average difference in length between adjacent single and double bonds in the molecule. In general, if π-electrons are more delocalized over the whole conjugated backbone, the contribution of the quinoid form to the ground state increases, which in turn leads to a decrease in BLA and reduction of the bandgap. Therefore, any structural factors that are able to facilitate π-electron delocalization over the molecular backbone would result in an increase in quinoidal contribution to the ground-state geometry and thus afford the resulting molecule with a smaller bandgap. Several strategies have been developed to control these bandgap controlling factors,[3] and they would be briefly illustrated with a few examples below.

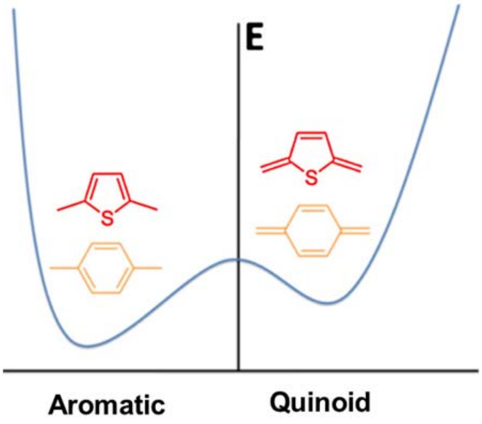

Figure 1-2. Schematic presentation of the non-degenerate aromatic and quinoid resonance forms.[4]

Conjugation Length

Generally, the bandgaps of organic semiconductors decrease as the conjugation length increases through raising the energy level of highest occupied molecular orbital (HOMO) and simultaneously lowering the energy level of lowest unoccupied molecular orbital (LUMO). The decrease in bandgaps is also accompanied by an increase in molar extinction coefficients. As can be clearly seen in Scheme 1-1, the absorption maxima of the terminally dicyanovinylene-substituted oligothiophenes (**1-1**~**1-3**) [5] and thiophene end-capped oligothieno[3,4-*b*]pyrazines (**1-4**~**1-6**) [6] are bathochromically shifted with increasing number of thiophene and thieno[3,4-*b*]pyrazine units, respectively. However, the existence of single bonds between the aromatic/heteroaromatic rings results in interannular rotations and thus a decline in the extent of π orbital overlap. This in turn leads to a reduction of effective conjugation. Therefore, unlimited extension of the conjugation length would only yield a limited reduction of bandgaps due to the saturation of effective conjugation.

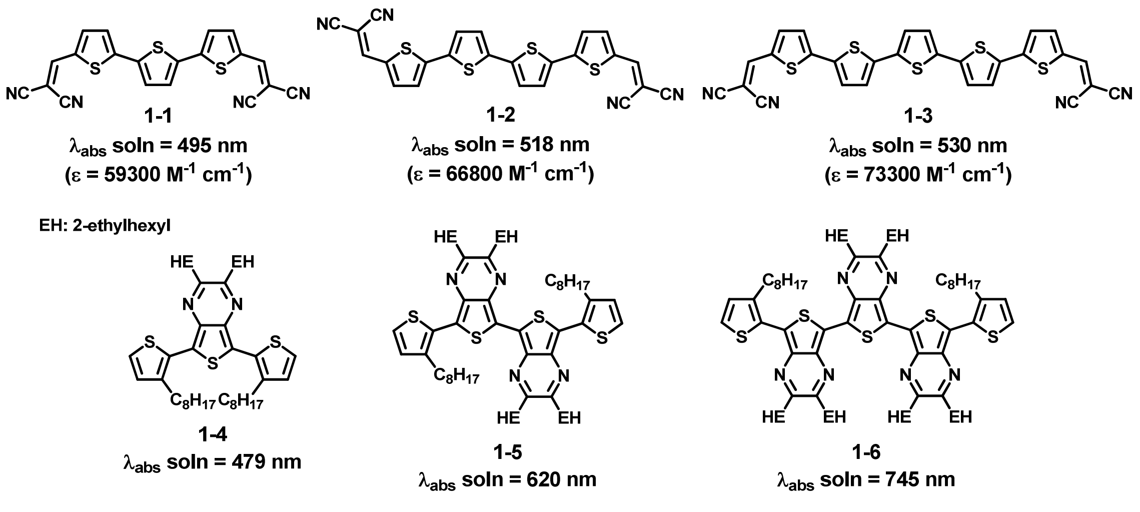

Scheme 1-1. Examples that illustrate the effect of conjugation length on bandgaps.

Aromatic Stabilization Resonance Energy

Aromatic stabilization resonance energy is a crucial factor that affects the bandgaps of π-conjugated aromatic systems. In general, the larger the resonance energy of aromatic cycles is, the larger the bandgap is. This is because a high degree of aromaticity tends to confine π-electrons within the aromatic rings and thus prevent their delocalization along the whole conjugated backbone, leading to a decrease in quinoidal contribution to the ground-state structure. For example, because benzene has a higher aromatic resonance energy than thiophene (1.56 vs 1.26 eV), the *p*-terphenyl **1-7** shows a larger bandgap and a blue-shifted absorption maximum as compared to the terthiophene **1-9** (Scheme 1-2).[7] Of course, the larger bandgap of the *p*-terphenyl **1-7** is also contributed by the torsion angle resulting from *ortho–ortho* steric interactions between adjacent phenyl rings. Comparison of their energy levels reveals that the *p*-terphenyl **1-7** has a lower-lying HOMO level and higher-lying LUMO level than the terthiophene **1-9**. Likewise, substitution of the inner phenyl ring of the triphenylamine donor moiety by thiophene leads to a reduction of the bandgap between **1-10** and **1-11**.[8]

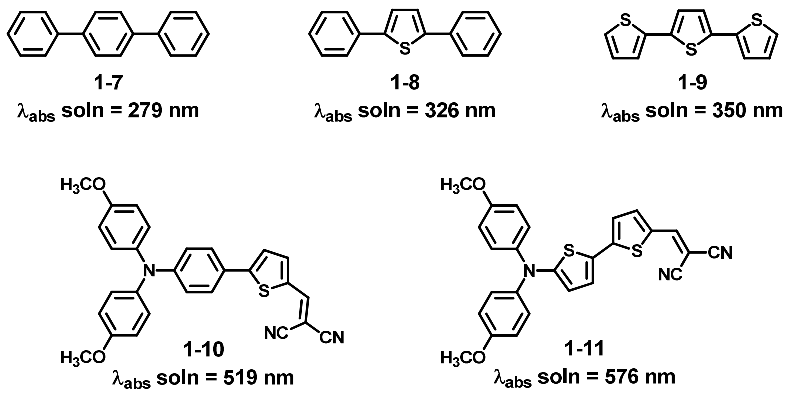

Scheme 1-2. The effect of aromatic stabilization resonance energy on bandgaps: phenylene vs thiophene.

Insertion of a double bond between two aromatic rings can cause a decrease in the overall aromaticity of the system and thus a reduction of the bandgap. With an equal number of double bonds, the vinylene-containing **1-13** shows a lower bandgap in comparison to the α-heptathiophene **1-12** (Scheme 1-3).[3b,9]

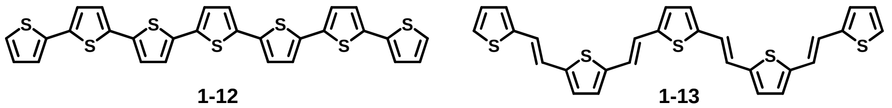

1-12
λ_{abs} soln = 440 nm

1-13
λ_{abs} soln = 490 nm

Scheme 1-3. The effect of aromatic stabilization resonance energy on bandgaps: insertion of a double bond between two aromatic rings.

The number of π-electrons of aromatic units in a conjugated system also influences the magnitude of the bandgap. For instance, the alternating polymer **P1**[10] of benzo[2,1-*b*:3,4-*b'*]dithiophene and cyclopentadithiophene has a larger bandgap than the cyclopentadithiophene-based homopolymer **P2**[11] (Scheme 1-4). This can be rationalized by the fact that the high degree of aromaticity of the 14-π-electron benzo[2,1-*b*:3,4-*b'*]dithiophene suppresses electron delocalization over the polymer backbone and thus reduces the quinoid character of the ground state, leading to a larger bandgap.

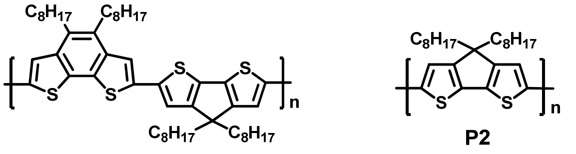

P1
bandgap = 2.00 eV

P2
bandgap = 1.7-1.8 eV

Scheme 1-4. The effect of aromatic stabilization resonance energy on bandgaps: the number of π-electrons of aromatic units.

Introduction of a multicyclic prequinoid building block, which is fused in a particular geometry so that the aromatic ring not directly linked to the conjugated backbone is able to gain in aromaticity in the quinoid resonance structure, into a conjugated system constitutes one effective approach to narrowing the bandgap. In this regard, the 1,3-dithienylbenzo[*c*]thiophene **1-14** and 1,3-dithienylnaphtho[*c*]thiophene **1-15** both possess a smaller bandgap than their parent counterpart **1-9** (Scheme 1-5).[12] This is due to the fact that the stabilization of the quinoid resonance structure achieved by the aromatization of the benzene/naphthalene ring leads to an increased quinoidal contribution to the ground-state structure.

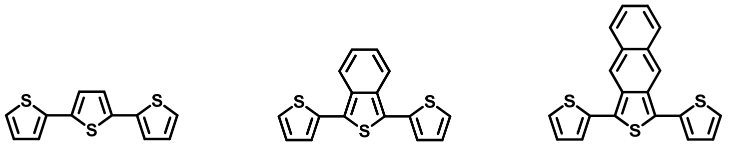

1-9 λ_{abs} **soln = 350 nm**

1-14 λ_{abs} **soln = 433 nm**

1-15 λ_{abs} **soln = 570 nm**

Scheme 1-5. The effect of aromatic stabilization resonance energy on bandgaps: quinoid resonance structure stabilization by using benzo[*c*]thiophene and naphtho[*c*]thiophene.

Also, the incorporation of thieno[3,4-*b*]thiophene into the conjugated backbone is capable of increasing the quinoid character of the ground state through stabilization of the quinoid resonance structure and thus endowing the resulting system with a small bandgap. As can be seen in Scheme 1-6, the bandgaps of the thieno[3,4-*b*]thiophene-based polymers **P3** gradually decrease as its content (*m*/*n* value) increases through a rise of the HOMO level and a concomitant lowering of the LUMO level.[13]

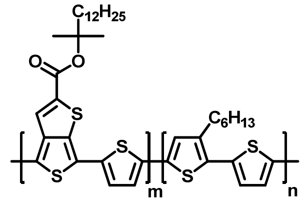

P3a	**m/n = 1/0**	**bandgap = 1.22 eV**
P3b	**m/n = 1/1**	**bandgap = 1.27 eV**
P3c	**m/n = 1/1.9**	**bandgap = 1.31 eV**
P3d	**m/n = 1/3.7**	**bandgap = 1.45 eV**
P3e	**m/n = 1/6.3**	**bandgap = 1.78 eV**

Scheme 1-6. The effect of aromatic stabilization resonance energy on bandgaps: quinoid resonance structure stabilization by adopting thieno[3,4-*b*]thiophene.

Using the same strategy, the two alternating polymers **P5**[14] and **P6**[15] containing thieno[3,4-*b*]thiophene and benzo[*c*]thiophene, respectively, both show a narrower bandgap than the benzo[1,2-*b*:4,5-*b'*]dithiophene-based homopolymer **P4**[16] (Scheme 1-7).

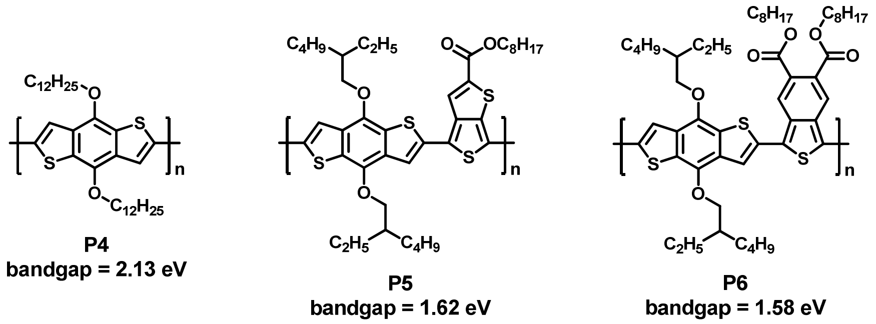

Scheme 1-7. Chemical structures and bandgaps of the homopolymer **P4** and the alternating polymers **P5** and **P6**.

Donor-Acceptor Effect

Concomitant implementation of electron-rich donor (D) and electron-deficient acceptor (A) units into a conjugated system represents another powerful strategy for reducing the bandgap, through which the degree of π-electron delocalization along the conjugated backbone and the corresponding contribution of the quinoid mesomeric structure to the ground state ($D–A \leftrightarrow D^+=A^-$) are increased via intramolecular charge transfer (ICT) from the donor side to the acceptor side. One unique feature of this approach is that the HOMO and LUMO are largely localized on the donor moiety and the acceptor moiety, respectively. Accordingly, a judicious combination of donor and acceptor units of various strengths allows for proper tuning of the frontier energy levels and thus the bandgap.

In this respect, the class of so-called donor–acceptor (D–A) polymers[17] consisting of alternating donor and acceptor repeat units along the conjugated main chain is the most dominant in the category of conjugated polymers with narrow bandgaps. As shown in Scheme 1-8, the incorporation of the proquinoid acceptor 2,1,3-benzothiadiazole leads to large decreases in bandgaps between the homopolymers (**P2**[11] and **P4**[16]) and the D–A polymers (**P7**[18] and **P8**[16]). Note that the reduction of bandgaps in fact stems from a synergistic combination of the D–A effect and quinoid resonance structure stabilization.

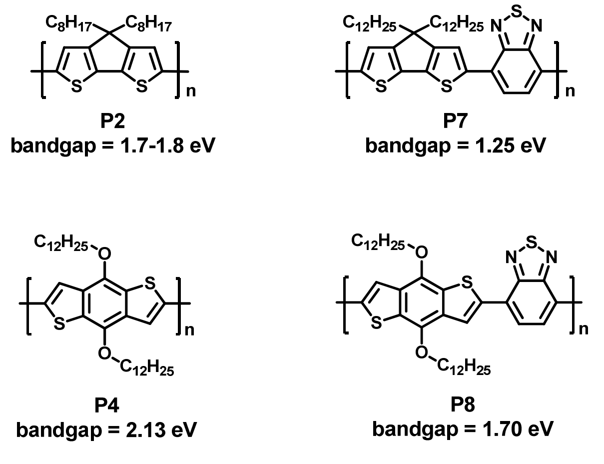

Scheme 1-8. Chemical structures and bandgaps of the homopolymers (**P2** and **P4**) and the D–A polymers (**P7** and **P8**).

Regarding the structural design of small molecules based on this approach, different molecular configurations have been developed to meet the requirements for respective purposes. The symmetrical quadrupolar acceptor−donor−acceptor (A−D−A, e.g., **1-1~1-3**[5]) and donor−acceptor−donor (D−A−D, e.g., **1-4~1-6**[6]) systems represent the most ubiquitous molecular scaffolds in the design of molecular donors for use in OPVs, whereas the asymmetric dipolar push−pull systems dominate the design of organic sensitizers for dye-sensitized solar cells (DSSCs). Note that the design principle of the compounds **1-4~1-6** represents another example of a synergistic combination of the D–A effect and quinoid resonance structure stabilization.

In addition to utilization of the archetypical donor and acceptor units, introduction of electron-withdrawing or electron-donating substituents directly onto/in these units allows for further fine-tuning of the frontier energy levels of these aforementioned systems through either inductive or mesomeric effects. In general, introduction of electron-withdrawing groups lowers both HOMO and LUMO energy levels, yet the degree of the shift in the LUMO level is larger than that in the HOMO level, thus leading to a decreased bandgap (Scheme 1-9).

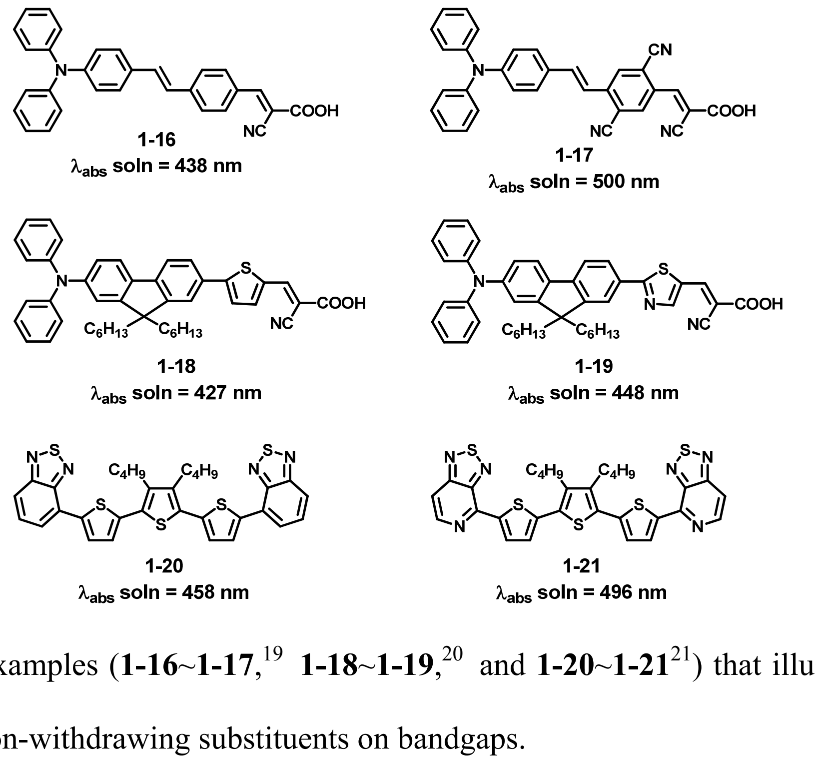

1-16
λ_{abs} soln = 438 nm

1-17
λ_{abs} soln = 500 nm

1-18
λ_{abs} soln = 427 nm

1-19
λ_{abs} soln = 448 nm

1-20
λ_{abs} soln = 458 nm

1-21
λ_{abs} soln = 496 nm

Scheme 1-9. Examples (**1-16~1-17**,[19] **1-18~1-19**,[20] and **1-20~1-21**[21]) that illustrate the effect of electron-withdrawing substituents on bandgaps.

Conversely, incorporation of electron-donating groups results in a reduction of the bandgap through a different degree of positive shift in the frontier energy levels (Scheme 1-10).

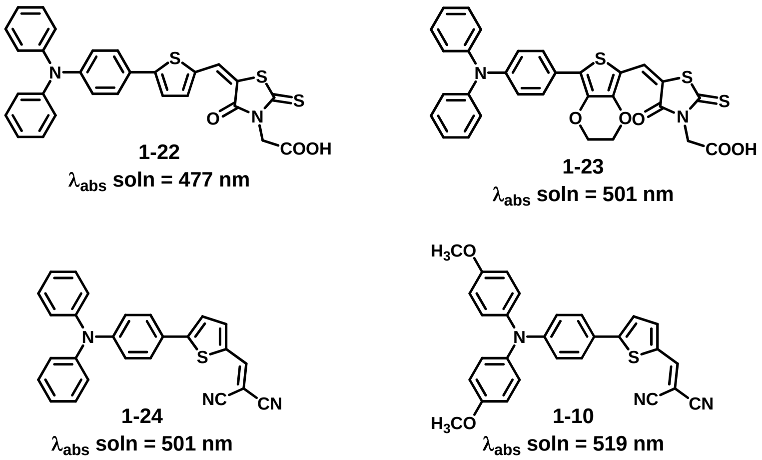

Scheme 1-10. Examples (**1-22**~**1-23**[22] as well as **1-24**[23] and **1-10**[8]) illustrating the effect of electron-donating substituents on bandgaps.

Planarization/Rigidification Effect

Planarity and rigidity of a π-conjugated system also play important roles in bandgap control. As such, rigidification of a conjugated system by covalent bridging of elemental units constitutes another effective strategy for the reduction of the bandgap. This is because a rigid and coplanar conformation can suppress rotational disorder around interannular single bonds and thus can allow for maximum π orbital overlap between adjacent aromatic/heteroaromatic rings, which in turn extends the effective conjugation length to facilitate π-electron delocalization.

As shown in Scheme 1-11, the rigidified compounds **1-25** and **1-26** both show a red-shifted absorption maximum and a smaller bandgap as compared to their non-rigid counterparts **1-8** and **1-9** through a rise in the HOMO level and a concomitant decrease in the LUMO level.[24] In another example, the covalent bridging of the dicyanovinylene group with the adjacent thiophene by a phenyl ring leads to a considerable reduction of the bandgap between **1-24** and **1-27** due to a large decrease in the LUMO level.[23] Interestingly, the covalent rigidification by an ethylene bridge conversely causes a rise of the LUMO level and thus an increase in the bandgap owing to the inductive electron-donating nature of the ethylene group (**1-10** vs **1-28** and **1-11** vs **1-29**).[8]

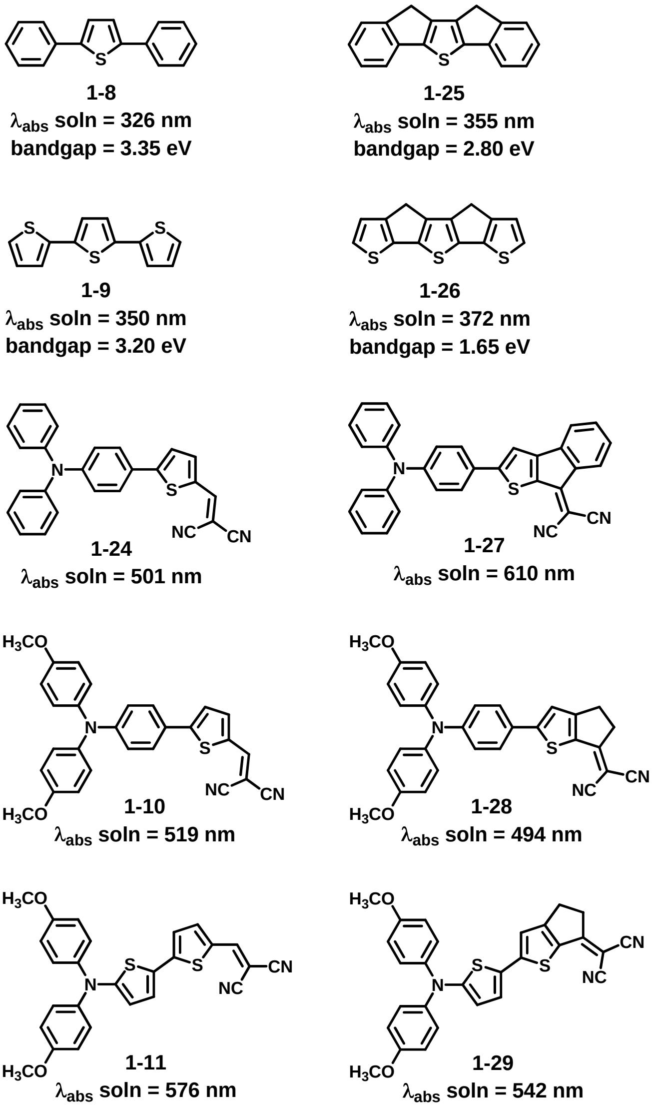

Scheme 1-11. Examples illustrating the planarization/rigidification effect on the bandgap of small molecules.

Likewise, the two D–A polymers (**P10** and **P12**) based on alternating fluorene-dicyclopentathiophene or carbazole-dicyclopentathiophene and 2,1,3-benzothiadiazole units both have a smaller band gap than their non-fused analogues (**P9** and **P11**) mainly through a rise in the HOMO level (Scheme 1-12).[25] This demonstrates the adoption of these seven-ringed ladder-type heteroacenes with forced planarity as the monomer unit enhances the electron coupling between the donor and the acceptor units along the polymer backbone.

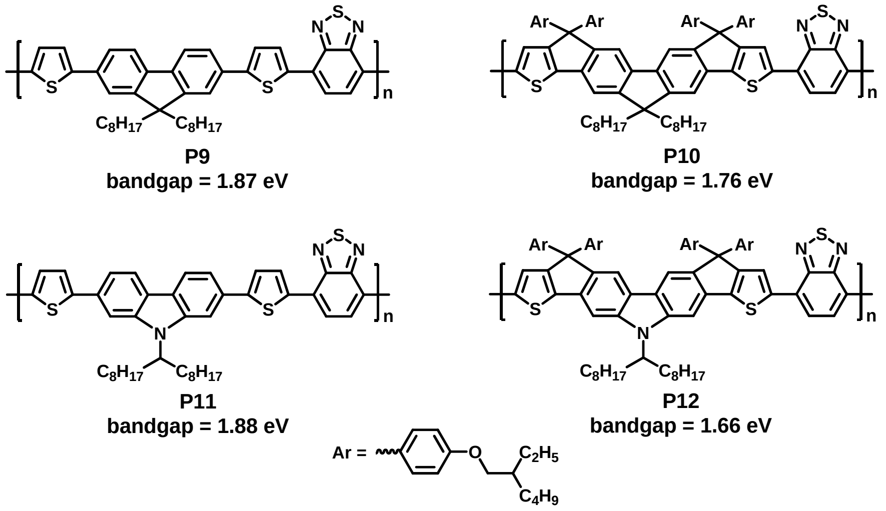

Scheme 1-12. Examples illustrating the planarization/rigidification effect on the bandgap of D–A polymers.

To sum up, the bandgap of a π-conjugated system is dependent on several structural parameters including conjugation length, aromatic stabilization resonance energy, donor-acceptor effect, and planarization/rigidification effect. In the design of photoactive materials with small bandgaps and suitable frontier energy levels, all of these factors need to be simultaneously taken into account. Moreover, intermolecular interactions between individual molecules or polymer chains should also be tailored for optimizing bulk properties.

References

---

[1] Smestad, G. P.; Krebs, F. C.; Lampert, C. M.; Granqvist, C. G.; Chopra, K. L.; Mathew, X.; Takakura, H. *Sol. Energy Mater. Sol. Cells* **2008,** *92,* 371.

[2] Brédas, J. L. *J. Chem. Phys.* **1985,** *82,* 3808.

[3] (a) Roncali, J. *Chem. Rev.* **1997,** *97,* 173. (b) Roncali, J. *Macromol. Rapid Commun.* **2007,** *28,* 1761.

[4] Chochos, C. L.; Choulis, S. A. *Prog. Polym. Sci.* **2011,** *36,* 1326.

[5] Fitzner, R.; Reinold, E.; Mishra, A.; Mena-Osteritz, E.; Ziehlke, H.; Körner, C.; Leo, K.; Riede, M.; Weil, M.; Tsaryova, O.; Weiß, A.; Uhrich, C.; Pfeiffer, M.; Bäuerle, P. *Adv. Funct. Mater.* **2011,** *21,* 897.

[6] Karsten, B. P.; Janssen, R. A. J. *Org. Lett.* **2008,** *10,* 3513.

[7] Raimundo, J.-M.; Blanchard, P.; Brisset, H.; Akoudad, S.; Roncali, J. *Chem. Commun.* **2000,** 939

[8] Demeter, D.; Jeux, V.; Leriche, P.; Blanchard, P.; Olivier, Y.; Cornil, J.; Po, R.; Roncali, J. *Adv. Funct. Mater.* **2013,** DOI: 10.1002/adfm.201300427.

[9] Frère, P.; Raimundo, J.-M.; Blanchard, P.; Delaunay, J.; Richomme, P.; Sauvajol, J.-L.; Orduna, J.; Garin, J.; Roncali, J. *J. Org. Chem.* **2003,** *68,* 7254.

[10] Xiao, S.; Zhou, H.; You, W. *Macromolecules* **2008,** *41,* 5688.

[11] Coppo, P.; Cupertino, D. C.; Yeates, S. G.; Turner, M. L. *Macromolecules* **2003,** *36,* 2705

[12] Clement, J. A.; Mohanakrishnan, A. K. *Tetrahedron* **2010,** *66,* 2340.

[13] Liang, Y.; Xiao, S.; Feng, D.; Yu, L. *J. Phys. Chem. C* **2008,** *112,* 7866.

[14] Liang, Y.; Feng, D.; Wu, Y.; Tsai, S.-T.; Li, G.; Ray, C.; Yu, L. *J. Am. Chem. Soc.* **2009,** *131,* 7792.

---

[15] Long, G.; Wan, X.; Zhou, J.; Liu, Y.; Li, Z.; He, G.; Zhang, M.; Hou, Y.; Chen, Y. *Macromol. Chem. Phys.* **2012,** *213,* 1596.

[16] Hou, J.; Park, M.-H.; Zhang, S.; Yao, Y.; Chen, L.-M.; Li, J.-H.; Yang, Y. *Macromolecules* **2008,** *41,* 6012.

[17] Havinga, E. E.; ten Hoeve, W.; Wynberg, H. *Polym. Bull.* **1992,** *29,* 119.

[18] Coffin, R. C.; Peet, J.; Rogers, J.; Bazan, G. C. *Nat. Chem.* **2009,** *1,* 657.

[19] Tian, H.; Yang, X.; Chen, R.; Zhang, R.; Hagfeldt, A.; Sun, L. *J. Phys. Chem. C* **2008,** *112,* 11023.

[20] Chen, C.-H.; Hsu, Y.-C.; Chou, H.-H.; Thomas, K. R. J.; Lin, J. T.; Hsu, C.-P. *Chem. Eur. J.* **2010,** *16,* 3184.

[21] Steinberger, S.; Mishra, A.; Reinold, E.; Levichkov, J.; Uhrich, C.; Pfeiffer, M.; Baüerle, P. *Chem. Commun.* **2011,** *47,* 1982.

[22] Liu, W.-H.; Wu, I-C.; Lai, C.-H.; Lai, C.-H.; Chou, P.-T.; Li, Y.-T.; Chen, C.-L.; Hsub, Y.-Y.; Chi, Y. *Chem. Commun.* **2008,** 5152.

[23] Leliège, A.; Régent, C.-H. L.; Allain, M.; Blanchard, P.; Roncali, J. *Chem. Commun.* **2012,** *48,* 8907.

[24] Roncali, J.; Thobie-Gautier, C. *Adv. Mater.* **1994,** *6,* 846.

[25] Wu, J.-S.; Cheng, Y.-J.; Dubosc, M.; Hsieh, C.-H.; Chang, C.-Y.; Hsu, C.-S. *Chem. Commun.* **2010,** *46,* 3259.

Chapter 2. Development of Organic Sensitizers for Dye-Sensitized Solar Cells

2-1 Introduction

Dye-sensitized solar cells (DSSCs) have attracted a great deal of attention since the breakthrough made by Grätzel and co-workers in 1991[1] in view of their ease of production, potential to allow for low-cost manufacturing, and ability to be fabricated onto light-weight flexible substrates. During the last two decades, combined developments of new photosensitizers[2] and electrolytes[3] have contributed to significant improvements both in power conversion efficiencies (PCEs) and long-term stability.[4] At present, ruthenium sensitizers, such as **N3**,[5] **N719**,[6] **black dye**,[7] and **C106**,[8] have exhibited PCEs of over 11% in liquid electrolyte-based DSSCs (Scheme 2-1). However, the rarity and high cost of the ruthenium metal may impede their further development for large-scale applications. Accordingly, organic sensitizers have also been the subject of intense research interest in the field of DSSCs due to their several predominant advantages over the ruthenium ones, including larger molar extinction coefficients, great flexibility in structural modification, facile synthesis, and relatively lower cost. In general, most of organic sensitizers are modeled on the donor–π-bridge–acceptor (D–π–A) system due to its effective photoinduced intramolecular charge transfer (ICT) characteristics. Among them, electron-rich arylamine-based derivatives are employed as the electron donor moiety, whereas an electron-withdrawing carboxylic acid, cyanoacrylic acid, or rhodanine-3-acetic acid is utilized as the electron acceptor moiety as well as the anchoring group to the TiO_2 surface. A variety of chromophores are selectively incorporated as the π-bridge between the donor moiety and acceptor moiety for tuning the structural and optoelectronic characteristics required for efficient sensitizers.

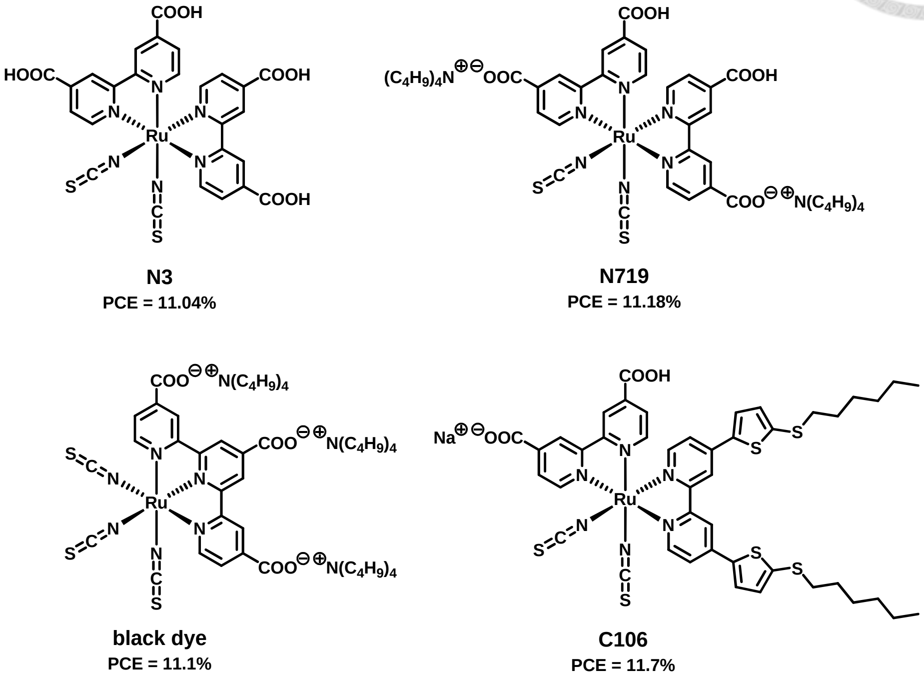

N3
PCE = 11.04%

N719
PCE = 11.18%

black dye
PCE = 11.1%

C106
PCE = 11.7%

Scheme 2-1. Highly efficient ruthenium sensitizers for DSSCs.

The amphiphilic push–pull organic sensitizer **C219** featuring a dihexyl-substituted dithienosilole and 3,4-ethylenedioxythiophene as a binary π-conjugated spacer between a lipophilic alkoxy-substituted triphenylamine and a hydrophilic cyanoacrylic acid is the first displaying PCEs of over 10% (the highest of 10.3%) in DSSCs with an iodide/triiodide (I^-/I_3^-) electrolyte (Scheme 2-2).[9] Recently, a remarkably high PCE of 11.9% was realized for a DSSC employing a D–π–A zinc porphyrin dye **YD2-*o*-C8** in conjunction with a $Co^{(II/III)}$tris(bipyridyl)-based redox electrolyte.[10] The efficiency was further improved to a record value of 12.3% [certified by the Photovoltaic Laboratory at the Institute of Micro Technique (IMT)] when the device was co-sensitized with another organic dye **Y123**.[11] On the other hand, the current record PCE for solid-state DSSCs is

6.08% [certified by National Renewable Energy Laboratory (NREL)] and was achieved with an organic dye **C220** in combination with 2,2',7,7'-tetrakis(*N*,*N*-dimethoxyphenylamine)-9,9'-spirobifluorene (spiro-MeOTAD) as the organic hole-transporting material.[12] Although the performance of organic sensitizers has lagged behind that of ruthenium sensitizers over a long period of time, these results unambiguously demonstrate a bright future for organic dye-based DSSCs.

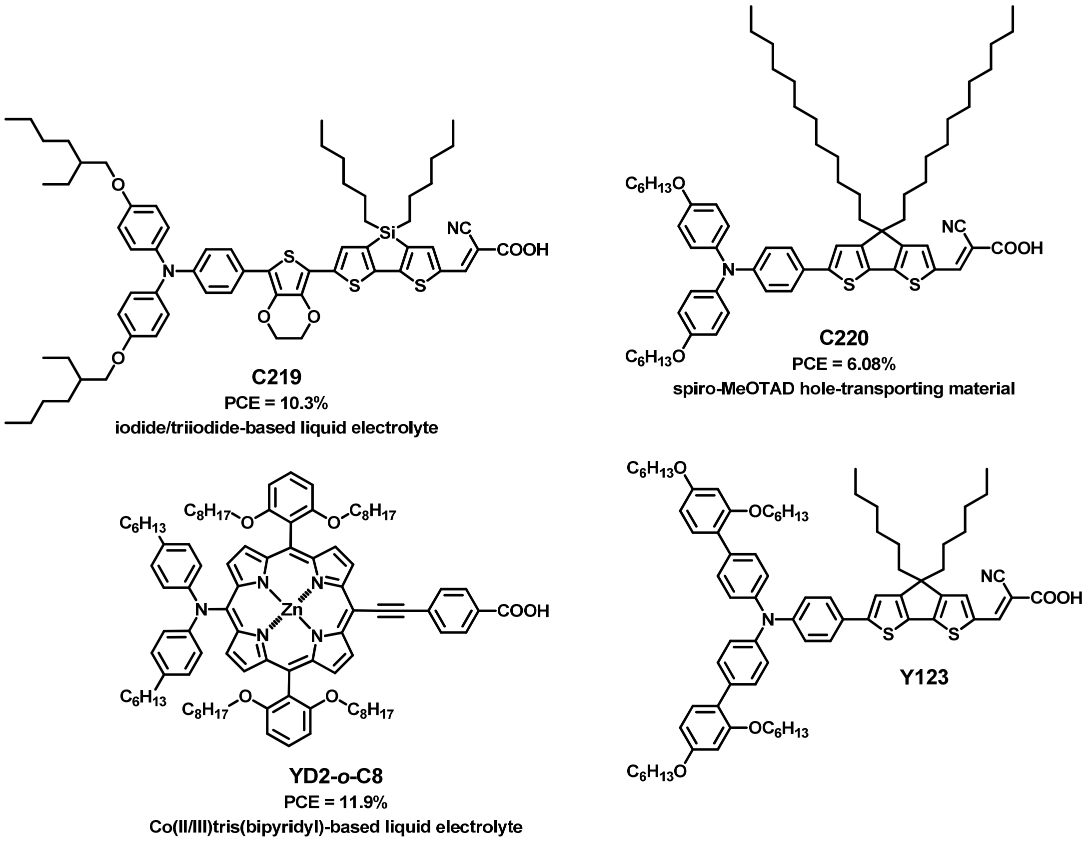

Scheme 2-2. Champion organic sensitizers for DSSCs.

In this chapter, three series of metal-free organic sensitizers would be discussed. Their corresponding solar cell devices were fabricated and tested by Dr. Chih-Hung Tsai in the Prof. Chung-Chih Wu research group at the Graduate Institute of Photonics and Optoelectronics, National Taiwan University.

2-2 Organic Donor–π-Bridge–Acceptor Dyes Containing a Coplanar Diphenyl-Substituted Dithienosilole as the π-Bridge

In this work, we developed two organic D–π–A dyes (**TPCADTS** and **TP6CADTS**, Scheme 2-3) that contain a simple triphenylamine or dihexyloxy-substituted triphenylamine as the electron donor moiety, a coplanar diphenyl-substituted dithienosilole (DTS) as the π-bridge, and cyanoacrylic acid as the electron acceptor moiety as well as the anchoring group. The triphenylamine unit has been widely utilized as a building block to construct optoelectronic materials owing to its good electron-donating nature and high hole-transporting capability.[13] In addition, tailoring the molecular structure through the addition of the electron-donating alkoxy substituents on triphenylamine allows us to fine-tune the energy levels and the absorption properties of the resulting dyes. These two long aliphatic hexyloxy chains can also potentially suppress undesirable dye aggregation and charge recombination between the electrolyte and the TiO_2 electrode (*vide infra*), both of which are detrimental to device performance.[14] On the other hand, the introduction of the diphenyl-substituted DTS as the central linkage for the organic sensitizers possesses several key advantages: (i) the existence of the silicon bridge forces the 2,2'-bithiophene unit to retain a syn configuration with high planarity and thus affords effective π orbital overlap in the rigidified system.[15] Accordingly, the adoption of this coplanar DTS as the π-bridge can facilitate the electronic coupling between the donor and acceptor blocks, hence leading to a small bandgap for the resulting sensitizers; (ii) the HOMO–LUMO gap of DTS is smaller than those of 2,2'-bithiophene and cyclopentadithiophene due to the lower-lying LUMO level,[16] which originates from the interaction of the silicon σ*-orbital and bithiophene π*-orbital, namely, σ*–π* conjugation.[17] Therefore, the smaller bandgap of DTS might offer the resulting sensitizers a better light-harvesting ability; (iii) the tetrahedral silicon center of the diphenyl-substituted DTS does not distort the coplanarity of the π-conjugated system. Instead, the diphenyl substitution on silicon atom may reduce the π–π stacking interactions of dye molecules. It was reported that the formation of dye aggregates on the semiconductor surface leads to fast back electron transfer[18] and inefficient electron injection,[19] both of which have an adverse effect on the device efficiency.

2-2-1 Synthesis

The synthetic pathways to the dyes **TPCADTS** and **TP6CADTS** are illustrated in Scheme 2-3. Unlike the previously reported DTS-containing dyes,[9,20] we adopted 5,5’-bis(trimethylsilyl)-3,3’-diphenylsilylene-2,2’-bithiophene as the starting material, which underwent selective monobromination to give the key intermediate **2-1** in 66% yield. Compound **2-1** was then desilylated with trifluoroacetic acid to produce **2-2** in 98% yield. Suzuki cross-coupling of **2-2** and 4-(*N*,*N*-diphenylamino)phenylboronic acid afforded **2-3a** in 83% yield, whereas **2-3b** was synthesized in 61% yield via Stille coupling of **2-2** with tributyl[4-(*N*,*N*-bis(4-hexyloxyphenyl)amino)phenyl]stannane. The free α-position of the DTS core in **2-3a** and **2-3b** was subsequently converted to its corresponding carbaldehyde by performing Vilsmeier–Haack reaction, affording **2-4a** and **2-4b** in 64% and 78% yield, respectively. Finally, the aldehydes **2-4** were condensed with cyanoacetic acid to give the target compounds **TPCADTS** and **TP6CADTS** in 85% and 86% yield, respectively, via Knöevenagel reaction in the presence of ammonium acetate.

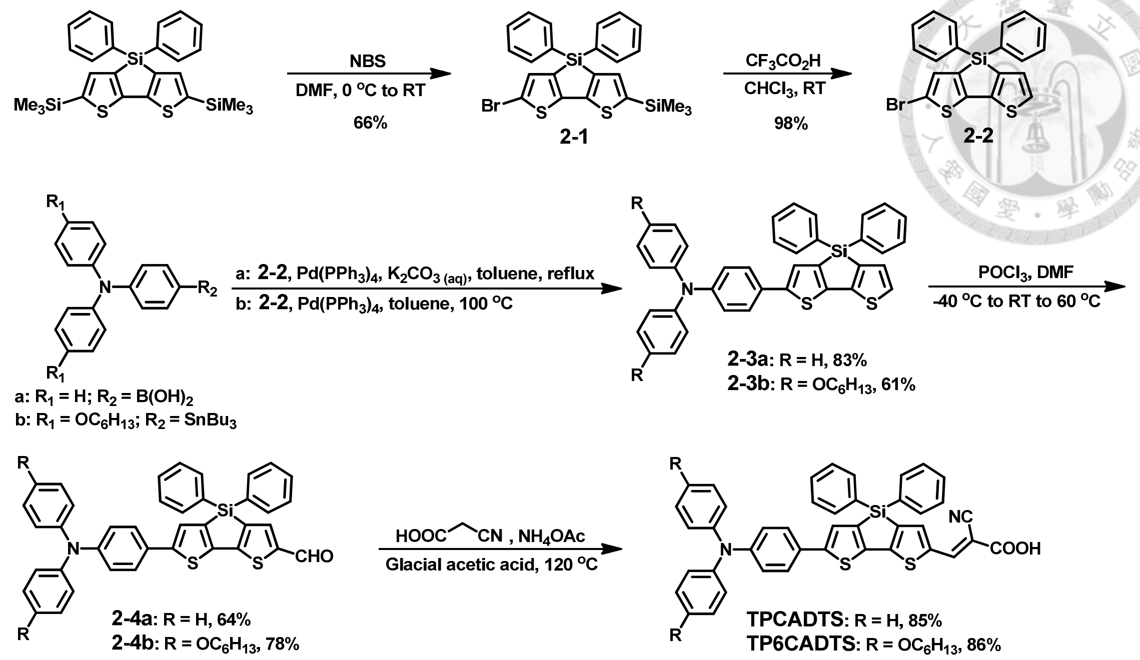

Scheme 2-3. Synthesis of **TPCADTS** and **TP6CADTS**.

2-2-2 Optical Properties

The UV–vis absorption and normalized emission spectra of **TPCADTS** and **TP6CADTS** in *tert*-butanol–acetonitrile [1:1, by volume (v/v)] solutions (10^{-5} M) are depicted in Figure 2-1(a), and the corresponding data are summarized in Table 2-1. The absorption spectrum of **TPCADTS** showed an intense band at λ_{abs} = 495 nm with a molar extinction coefficients (ε) of 44500 M^{-1} cm^{-1}, which is assigned to the ICT transition. Compared to **TPCADTS**, **TP6CADTS** exhibited a red-shifted λ_{abs} value of 511 nm (ε = 36900 M^{-1} cm^{-1}) due to the stronger electron-donating nature of the hexyloxy substituents. **TPCADTS** and **TP6CADTS** displayed emission bands centered at 579 and 605 nm, respectively, as excited on their absorption maxima. Upon anchoring on the 7 μm porous TiO_2 nanoparticle films, the absorption maxima of these two dyes were blue-shifted [Figure 2-1(b)] in comparison with those in *tert*-butanol–acetonitrile (1:1, v/v) solutions. The blue shift is attributed to the deprotonation of carboxylic acid upon adsorption onto the TiO_2 surface, and the resulting carboxylate–TiO_2 unit is a weaker electron acceptor than the carboxylic acid.[21]

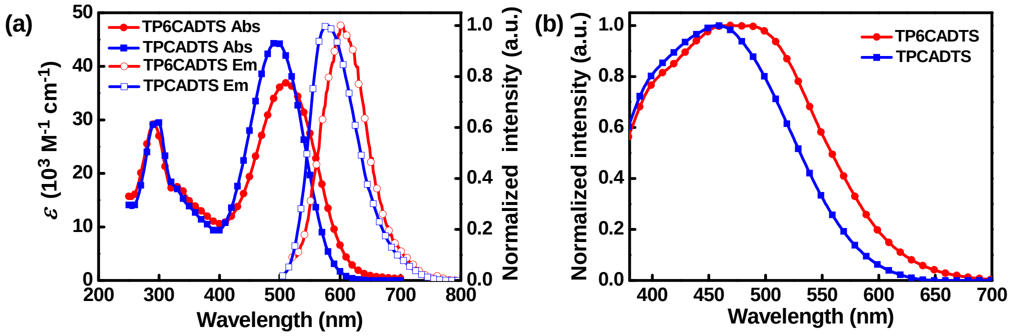

Figure 2-1. (a) Absorption and emission spectra of **TPCADTS** and **TP6CADTS** measured in *tert*-butanol–acetonitrile (1:1, v/v) solutions. (b) Absorption spectra of the dyes anchoring on the 7 μm porous TiO_2 nanoparticle films.

Table 2-1. Photophysical and electrochemical parameters of the dyes **TPCADTS** and **TP6CADTS**.

dye	λ_{abs} (nm)[a]	ε (M^{-1} cm^{-1})[a]	λ_{em} (nm)[a]	λ_{abs} on TiO_2 (nm)[b]	E_{0-0} (eV)[c]	E_{ox} (V)[d]	E_{red} (V)[e]	E_{ox}^{*} (V)[f]
TPCADTS	495	44500	579	458	1.95	1.07	−0.96	−0.88
TP6CADTS	511	36900	605	470	1.87	0.88	−0.99	−0.99

[a]Measured in *tert*-butanol–acetonitrile (1:1, v/v) solutions (10^{-5} M). [b]Otained through measuring the dyes adsorbed on 7 μm TiO_2 nanoparticle films in *tert*-butanol–acetonitrile (1:1, v/v) solutions. [c]Estimated from the onset point of the absorption spectra in *tert*-butanol–acetonitrile (1:1, v/v) solutions. [d]Measured in DMF solutions with 0.1 M tetrabutylammonium hexafluorophosphate ($TBAPF_6$) as a supporting electrolyte. [e]Measured in THF solutions with 0.1 M tetrabutylammonium perchlorate (TBAP) as a supporting electrolyte. [d,e]Calibrated with the ferrocene/ferrocenium (Fc/Fc^+) redox couple as an external reference and converted to NHE by addition of 630 mV.[22] [f]$E_{ox}^{*} = E_{ox} - E_{0-0}$.

2-2-3 Theoretical Calculations

To gain more insight into the electronic structures of **TPCADTS** and **TP6CADTS**, density function theory (DFT) calculations were performed at the B3LYP/6-31G(d) level for geometry optimization. As shown in Figure 2-2, the HOMOs of both sensitizers are mainly populated over the triphenylamine and DTS blocks with considerable contribution from the former, whereas LUMOs are delocalized through the DTS and cyanoacrylic acid fragments with sizable contribution from the latter. Examination of the frontier molecular orbitals of both sensitizers suggests that the HOMO–LUMO excitation shifts the electron density distribution from the triphenylamine unit to the cyanoacrylic acid moiety, facilitating efficient photoinduced/interfacial electron injection from excited dyes into the TiO_2 electrode.

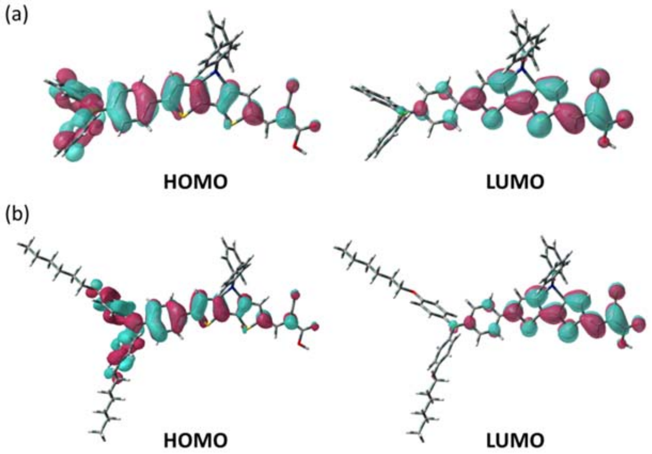

Figure 2-2. Frontier molecular orbitals of (a) **TPCADTS** and (b) **TP6CADTS** calculated with DFT.

2-2-4 Electrochemical Properties

Cyclic voltammetry (CV) measurements were conducted to investigate the electrochemical properties of the dyes **TPCADTS** and **TP6CADTS**. As shown in Figure 2-3, both dyes exhibited one quasi-reversible oxidation wave corresponding to the oxidation of the triphenylamine donor moieties and one quasi-reversible reduction wave assigned to the reduction of the cyanoacrylic acid block. Both oxidation (E_{ox}) and reduction (E_{red}) potentials of **TP6CADTS** were more negative than those of **TPCADTS**, yet the difference in oxidation potentials of the two dyes was larger than that in reduction potentials (Table 2-1). It suggests that the introduction of the hexyloxy substituents on the triphenylamine donor moiety has a significant influence on the oxidation potential but a more limited effect on the reduction potential of **TP6CADTS**. The different influences on the oxidation and reduction potential by incorporating the hexyloxy substituents lead to a narrower energy gap of **TP6CADTS**. The zero–zero excitation energy (E_{0-0}) estimated from the onset point of the absorption spectrum in a *tert*-butanol–acetonitrile (1:1, v/v) solution and the oxidation potential were used to calculate the excited-state oxidation potential (E_{ox}^{*}). The deduced E_{ox}^{*} values of these two dyes were more negative than the conduction band edge of the TiO_2 [−0.5 V vs normal hydrogen electrode (NHE)],[23] indicating that the electron injection process shall be energetically favorable. On the other hand, the oxidation potentials of these two dyes were more positive than the redox potential of the I^-/I_3^- couple (0.4 V vs NHE). It suggests that the oxidized dyes shall be able to accept electrons from I^- thermodynamically for effective dye regeneration.

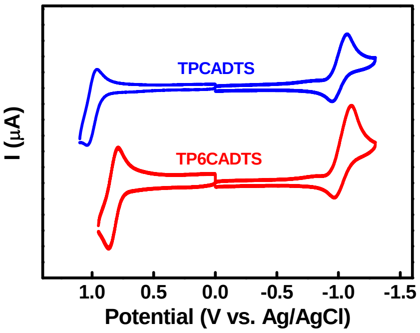

Figure 2-3. Cyclic voltammograms of **TPCADTS** and **TP6CADTS** recorded in solutions.

2-2-5 Photovoltaic and Electrochemical Impedance Characteristics

The photovoltaic characteristics of **TPCADTS** and **TP6CADTS** as the sensitizers for DSSCs were evaluated with a sandwich cell comprising 0.6 M 1-butyl-3-methylimidazolium iodide, 0.05 M LiI, 0.03 M I_2, 0.5 M 4-*tert*-butylpyridine (4-TBP), and 0.1 M guanidinium thiocyanate in a mixture of acetonitrile–valeronitrile (85:15, v/v) as the redox electrolyte. It was reported that the incorporation of 4-TBP can shift the conduction band edge of TiO_2 to a more negative potential and decrease the dark current, and thus improve the open-circuit voltage (V_{oc}) and fill factor (FF) of the corresponding cell,[24] while the addition of guanidinium thiocyanate can enhance both the short-circuit current density (J_{sc}) and V_{oc} through the positive shift of the conduction band edge of TiO_2 and the suppression of surface recombination, respectively.[25] In addition, deoxycholic acid was used as a co-adsorbent here. The coadsorption of deoxycholic acid with organic dyes has proven to be effective to dissociate dye aggregates and lead to suppressed charge recombination, which is respectively favorable for the increase in J_{sc} and V_{oc}.[21,24a] The incident monochromatic photon-to-current conversion efficiency (IPCE) spectra of the DSSCs are shown in Figure 2-4(a). The IPCE spectrum of the **TP6CADTS**-based cell was broader than that of the **TPCADTS**-based cell, which is coincident with their absorption spectra. Moreover, the **TP6CADTS**-based cell showed higher IPCEs than the **TPCADTS**-based cell over the whole spectral range, even though the maximal molar extinction coefficient of **TP6CADTS** is smaller than that of **TPCADTS**. This is likely due to the reduced charge recombination at the TiO_2/dye/electrolyte interface and the inhibition of dye aggregation by tailoring two long aliphatic hexyloxy chains on the triphenylamine donor moiety (*vide infra*).[14] Altogether, the **TP6CADTS**-based cell showed high IPCEs in excess of 70% from 350 to 560 nm, with a maximum of 84% at 450 nm. Figure 2-4(b) shows the current density–voltage (*J*–*V*) curves of the DSSCs under standard global AM 1.5G solar irradiation. The **TP6CADTS**-based cell delivered a J_{sc} of 13.39 mA/cm^2, V_{oc} of 0.81 V, and FF of 0.70, yielding an overall PCE of 7.60%. Under the same conditions, the device based on **TPCADTS** gave a relatively lower J_{sc} and V_{oc}, thus leading to an inferior PCE of 6.65% (Table 2-2). For a fair comparison, the **N719**-sensitized DSSC was also fabricated under the same conditions. The efficiency of the **TP6CADTS**-based cell reached ~96% of the **N719**-sensitized cell efficiency (7.93%). The higher J_{sc} value of the **TP6CADTS**-based cell relative to the **TPCADTS**-based cell is in accordance with the observation on their IPCE spectra.

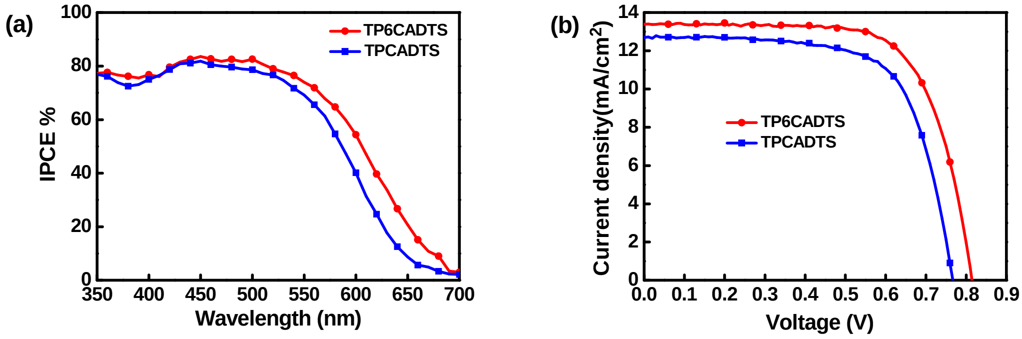

Figure 2-4. (a) IPCE spectra and (b) *J*-*V* curves of DSSCs based on **TPCADTS** and **TP6CADTS**.

Table 2-2. Performance parameters of DSSCs sensitized with the dyes **TPCADTS**, **TP6CADTS**, and **N719**.[a]

dye	J_{sc} (mA/cm^2)	V_{oc} (V)	FF	PCE (%)
TPCADTS	12.70	0.76	0.69	6.65
TP6CADTS	13.39	0.81	0.70	7.60
N719	14.65	0.77	0.70	7.93

[a] The concentration of the dyes was maintained at 0.5 mM in a *tert*-butanol–acetonitrile (1:1, v/v) solution, with 0.5 mM deoxycholic acid as a co-adsorbent. Performance of DSSCs was measured with a working area of 0.125 cm^2.

On the other hand, through the introduction of two long aliphatic hexyloxy chains on the triphenylamine donor moiety, one also notes that the **TP6CADTS**-based cell gives a 50 mV increase in V_{oc} in comparison with the **TPCADTS**-based cell. The effects of the presence of the two long hexyloxy chains on photovoltaic characteristics were further elucidated by electrochemical impedance spectroscopy (EIS). The EIS is a useful tool for characterizing important interfacial charge-transfer processes in DSSCs, such as the charge recombination at the TiO_2/dye/electrolyte interface, electron transport in the TiO_2 electrode, electron transfer at the counter electrode, and I_3^- transport in the electrolyte, etc..[26] In this study, the EIS was carried out by subjecting the cell to the constant AM 1.5G 100 mW/cm^2 illumination and to the bias at the V_{oc} of the cell (namely, under the conditions of no dc electric current), for better manifestation of the process at the TiO_2/electrolyte interface of a cell under operation. Figure 2-5(a) shows the EIS Nyquist plots (i.e., the minus imaginary part of the impedance －Z” vs the real part of the impedance Z’ when sweeping the frequency) for DSSCs based on **TPCADTS** and **TP6CADTS**. For the frequency range investigated (20 Hz to 1 MHz), in both cells, a larger semicircle occurred in the lower-frequency range (~20Hz to 1 kHz) and a smaller semicircle occurred in the higher-frequency range. With the bias illumination and voltage applied, the larger semicircle at lower frequencies corresponds to the charge-transfer processes at the TiO_2/dye/electrolyte interface, while the smaller semicircle at higher frequencies corresponds to the charge-transfer processes at the Pt/electrolyte interface. The two cells hardly showed a difference in smaller semicircles at higher frequencies, but the difference in larger semicircles at lower frequencies was significant. The larger width of the lower-frequency semicircle of the **TP6CADTS**-based cell indicates a larger charge-transfer resistance at the TiO_2/dye/electrolyte interface.

Figure 2-5(b) shows the EIS Bode plots (i.e., the phase of the impedance vs the frequency) of the DSSCs based on **TPCADTS** and **TP6CADTS**. For the frequency range investigated, both EIS Bode plots also exhibited two peak features; the one at higher frequencies corresponds to the charge transfer at the Pt/electrolyte interface and the one at lower frequencies corresponds to the charge transfer at the TiO_2/dye/electrolyte interface. Again, the difference in bode plots of both cells mainly occurred in the lower-frequency range. The characteristic frequency of the lower-frequency peak in the Bode plot is related to the charge recombination rate, and its reciprocal is associated with the electron lifetime.[27] As can be seen in Figure 2-5(b), the lower-frequency peak of the **TP6CADTS**-based cell shifted to a lower frequency as compared to that of the **TPCADTS**-based cell, indicating that the electron lifetime was effectively prolonged by the two long hexyloxy chains near the TiO_2/dye/electrolyte interface. The EIS results clearly suggest that the two long hexyloxy chains of **TP6CADTS** act as effective blocking units between the TiO_2 surface and electrolyte, preventing the approach of hydrophilic I_3^- ions to the TiO_2 surface and thereby leading to suppressed charge recombination/dark current and lengthened electron lifetimes.[28] These factors in turn result in the higher V_{oc} (50 mV higher) of the **TP6CADTS**-based cell as compared to the **TPCADTS**-based cell.

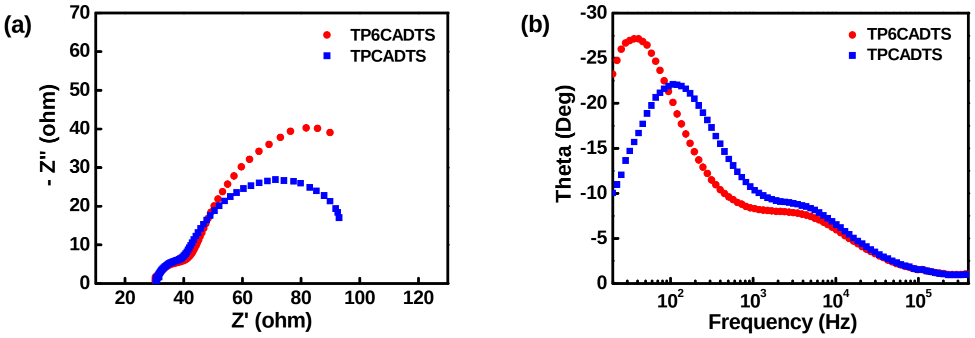

Figure 2-5. EIS (a) Nyquist plots and (b) Bode phase plots for DSSCs based on **TPCADTS** and **TP6CADTS**.

2-3 Organic Donor–Acceptor–Acceptor Dyes Featuring Pyrimidine as the Bridging Acceptor

To realize efficient light harvesting, it is highly desired to develop dyes that possess high molar absorption coefficients that extend throughout the visible and into the NIR regions. Organic D–π–A sensitizers with a long π-conjugation length have been shown to be operative in augmenting the molar extinction coefficients and in realizing bathochromic shifts in absorption.[29] In addition to the length of the π-conjugated framework, the intrinsic electronic characteristics of the π-conjugated spacer, especially the one linked to cyanoacrylic acid, have also significantly affected the spectral response of the dyes. For example, the selenophene-based organic dyes showed red-shifted absorption accompanied by enhanced molar extinction coefficients as compared to their thiophene- and furan-based analogs.[30] Moreover, incorporation of electron-donating or electron-withdrawing substituents directly onto/in the π-spacer has represented another effective way to red-shift the absorption of the dyes. In this regard, it was reported that organic dyes containing 3,4-ethylenedioxythiophene,[31] terephthalonitrile,[32] or thiazole[33] exhibit red-shifted absorption in comparison with their parent counterparts.

In this work, we developed a series of organic dyes (**DPTP**, **OMeDPTP**, and **OHexDPTP**, Scheme 2-4), in which various diaryllthienylamine donor moieties and a cyanoacrylic acid acceptor moiety are bridged by an electron-deficient pyrimidine ring. In order to differentiate our molecular design from the conventional D–π–A system, we referred to this kind of structural arrangement as the donor–acceptor–acceptor (D–A–A) molecular architecture. For a parallel comparison, a D–π–A model dye **M-TP** with phenylene as the π-bridge was also synthesized for assessing the impacts of pyrimidine on optical and electrochemical properties of **DPTP**. In general, the dyes were designed with the following three structural characteristics that are all beneficial to lower the energy of ICT transition: (i) the diarylthienylamine blocks behave as stronger electron-donating moieties than the conventional diarylphenylamine congeners because of their fortified quinoid character;[34] (ii) the diarylthienylamine blocks are connected to the 2-position of pyrimidine, and thus coplanar conformations between thiophene and pyrimidine rings can be easily reached due to the lack of *ortho–ortho* steric interactions.[35] The coplanarity is capable of facilitating π-electron delocalization in the conjugated backbone; (iii) the acceptor moiety and also the TiO_2-anchoring group, cyanoacrylic acid, is directly linked to a highly electron-deficient pyrimidine ring.

2-3-1 Synthesis

The synthetic routes to the dyes **DPTP**, **OMeDPTP**, **OHexDPTP**, and the model dye **M-TP** are illustrated in Scheme 2-4. Palladium-catalyzed Negishi coupling reactions of diarylthienylamines with 5-bromo-2-iodopyrimidine afforded **2-5**, which were then converted to their corresponding carbaldehydes **2-6** by lithiation with *n*-butyl lithium and subsequently quenching with ethyl formate. Finally, the aldehydes **2-6** were condensed with cyanoacetic acid to yield the target compounds **DPTP**, **OMeDPTP**, and **OHexDPTP** via Knöevenagel reaction in the presence of ammonium acetate. The model dye **M-TP** was obtained via a two-step process that the first involves Stille coupling of 5-(*N*,*N*-diphenylamino)-2-(tri-*n*-butylstannyl)thiophene with 4-bromobenzaldehyde, then followed by Knöevenagel condensation with cyanoacetic acid.

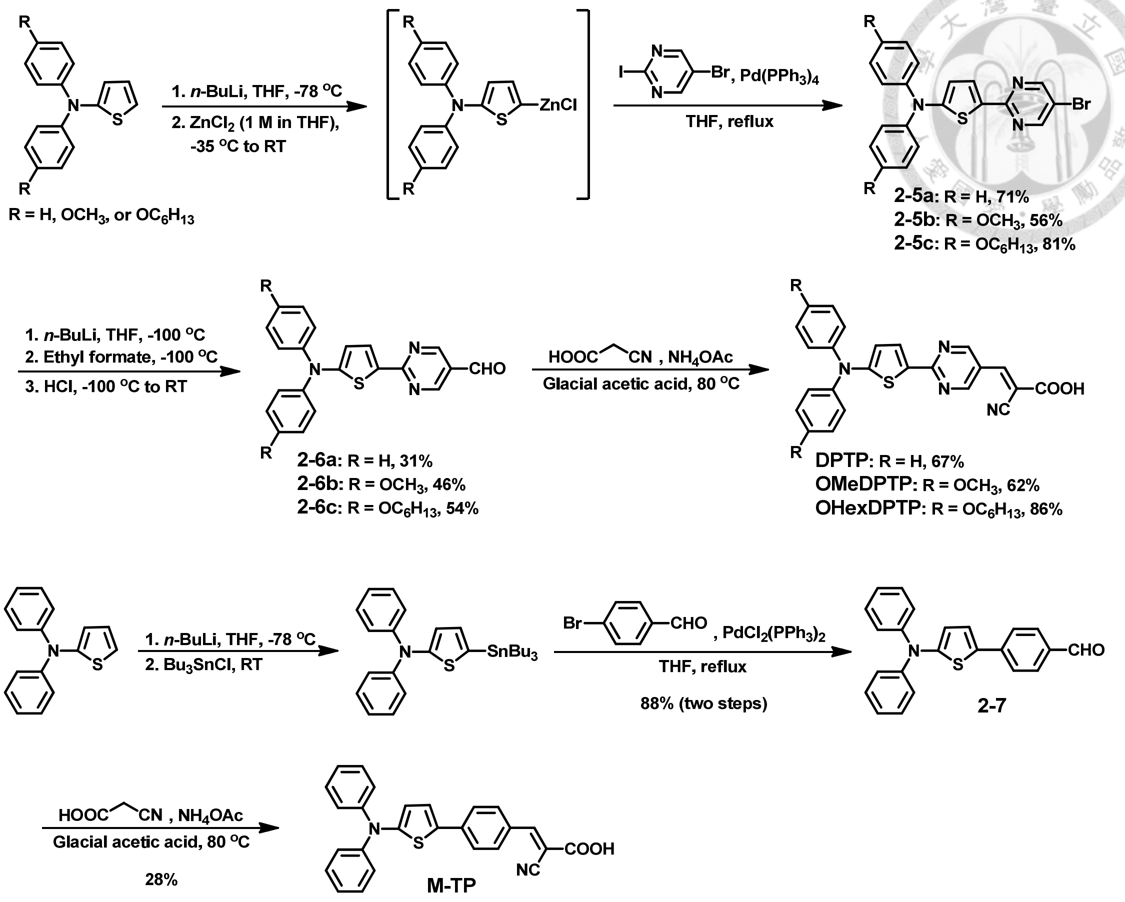

Scheme 2-4. The synthetic routes to the dyes **DPTP**, **OMeDPTP**, **OHexDPTP**, and the model dye **M-TP**.

2-3-2 Optical Properties

The UV–Vis absorption spectra and emission spectra of the dyes in *tert*-butanol–acetonitrile (1:1, v/v) solutions are depicted in Figure 2-6(a). Their related photophysical data are summarized in Table 2-3. The absorption band of **DPTP** in solution showed a λ_{abs} at 484 nm with a ε of 25300 M^{-1} cm^{-1}, which is assigned to the ICT transition. In comparison with **DPTP**, **M-TP** displayed a less intense and blue-shifted absorption band centered at 438 nm (ε = 19800 M^{-1} cm^{-1}). It proves that the D–A–A molecular scaffold shows a better light-harvesting ability than the conventional D–π–A counterpart. Furthermore, the absorption band of **OMeDPTP** and

OHexDPTP exhibited a λ_{abs} at 502 (ε = 31300 M^{-1} cm^{-1}) and 506 nm (ε = 29300 M^{-1} cm^{-1}), respectively, which are red-shifted by ca. 20 nm compared to that of **DPTP**, as a result of the stronger electron-donating nature of the dialkoxy substituents. On the other hand, **DPTP**, **OMeDPTP**, and **OHexDPTP** exhibited emission bands centered at 560, 590, and 594 nm, respectively, when excited on their absorption maxima. Upon anchoring on the 7 μm porous TiO_2 nanoparticle films, the absorption bands of these dyes were blue-shifted in comparison with those in the *tert*-butanol–acetonitrile (1:1, v/v) solutions [Figure 2-6(b)]. The blue shift stems from the deprotonation of carboxylic acid upon adsorption onto the TiO_2 surface, and the resulting carboxylate–TiO_2 unit is a weaker electron acceptor than the carboxylic acid.[21]

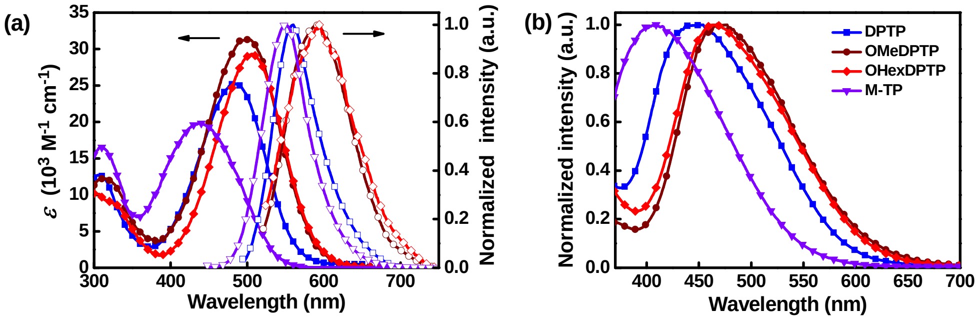

Figure 2-6. (a) Absorption and emission spectra of **DPTP** (squares), **OMeDPTP** (circles), **OHexDPTP** (diamonds), and **M-TP** (triangles) measured in *tert*-butanol–acetonitrile (1:1, v/v) solutions. (b) Absorption spectra of the dyes anchoring on 7 μm porous TiO_2 nanoparticle films.

Table 2-3. Photophysical and electrochemical parameters as well as adsorbed amount on TiO_2 of the dyes **DPTP**, **OMeDPTP**, **OHexDPTP**, and **M-TP**.

dye	λ_{abs} (nm)^a	ε (M^{-1} cm^{-1})^a	λ_{em} (nm)^a	λ_{abs} on TiO_2 (nm)^b	Γ (mol/cm^2)^c	E_{0-0} (eV)^d	E_{ox} (V)^e	E_{ox}^* (V)^f
DPTP	484	25300	560	454	1.8×10^{-7}	2.20	1.09	−1.11
OMeDPTP	502	31300	590	477	1.9×10^{-7}	2.11	0.99	−1.12
OHexDPTP	506	29300	594	467	6.0×10^{-8}	2.11	0.98	−1.13
M-TP	438	19800	549	409	2.5×10^{-7}	2.32	1.01	−1.31

[a] Measured in *tert*-butanol–acetonitrile (1:1, v/v) solutions (10^{-5} M). [b] Obtained through measuring the dyes adsorbed on 7 μm TiO_2 nanoparticle films in chlorobenzene solutions. [c] Γ is the surface density of the dye on the TiO_2 nanoparticle film. [d] Estimated from the onset point of the absorption spectra in *tert*-butanol–acetonitrile (1:1, v/v) solutions. [e] Measured in CH_2Cl_2 solutions with 0.1 M $TBAPF_6$ as a supporting electrolyte; calibrated with Fc/Fc$^+$ as an external reference and converted to NHE by addition of 630 mV.[22] [f] $E_{ox}^* = E_{ox} - E_{0-0}$.

Like many metal-free dyes,[36] the absorption of the dyes exhibited negative solvatochromism, i.e., a blue shift of λ_{abs} in polar solvents (Figure 2-7, taking **DPTP** as an example). This phenomenon may be attributed to the interaction of polar solvent molecules with the carboxylic acid, which in turn decreases the electron-withdrawing strength of the COOH group.

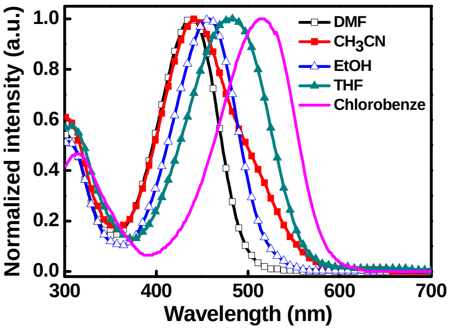

Figure 2-7. Absorption spectra of **DPTP** in different solvents.

2-3-3 Theoretical Calculations

DFT calculations were carried out at the B3LYP/6-31G(d) level to gain more insight into the electronic structures of the dyes. The HOMOs of all the dyes are mainly populated on diarylamine and thiophene moieties, whereas LUMOs are sizably delocalized through pyrimidine and cyanoacrylic acid fragments (Figure 2-8). This result suggests that the HOMO–LUMO excitation shifts the electron density distribution from the diarylamine unit to the cyanoacrylic acid moiety, hence facilitating efficient photoinduced/interfacial electron injection from excited dyes to the TiO_2 electrode.

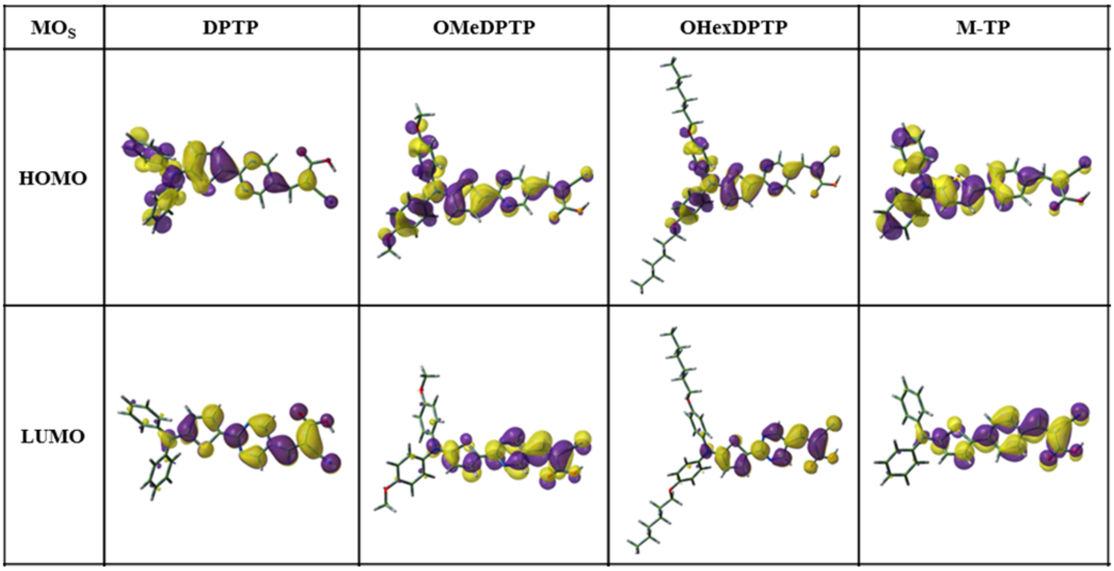

Figure 2-8. HOMOs and LUMOs of the dyes **DPTP**, **OMeDPTP**, **OHexDPTP**, and **M-TP** calculated with DFT.

2-3-4 Electrochemical Properties

As shown in Figure 2-9, one quasi-reversible oxidation wave attributed to the oxidation of the diarylthienylamine donor moieties was observed for all the dyes. The relevant CV data are collected in Table 2-3. The less positive oxidation potentials of **OMeDPTP** and **OHexDPTP** relative to **DPTP** can be ascribed to the presence of stronger electron-donating dialkoxy substituents. The $E_{0\text{–}0}$, which was estimated from the onset point of the absorption spectrum in a *tert*-butanol–acetonitrile (v/v, 1:1) solution, and the E_{ox} were used to calculate the E_{ox}^{*}. It is worth mentioning that both the

E_{ox} and E_{ox}^* of **DPTP** were more positive than those of **M-TP**, yet the degree of the shift in the E_{ox}^* was larger than that in the E_{ox}, thus leading to a narrower energy gap for **DPTP**. The deduced E_{ox}^* values corresponding to the LUMO levels of these dyes were more negative than the conduction band edge of the TiO_2 (−0.5 V vs NHE),[23] indicating that the electron injection process shall be energetically favorable. In addition, the E_{ox} values corresponding to the HOMO levels of the dyes were more positive than the redox potential of the I^-/I_3^- couple (0.4 V vs NHE), suggesting that the oxidized dyes shall be able to accept electrons from I^- thermodynamically for effective dye regeneration.

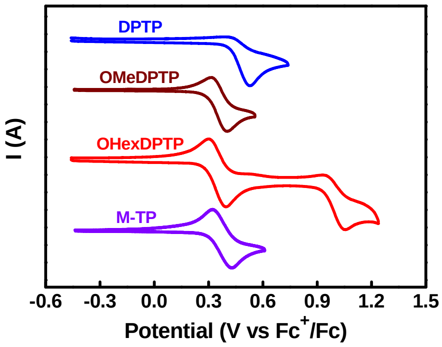

Figure 2-9. Cyclic voltammograms of **DPTP**, **OMeDPTP**, **OHexDPTB**, and **M-TP** recorded in solutions.

2-3-5 Photovoltaic and Electrochemical Impedance Characteristics

The photovoltaic performance of these dyes as the sensitizers for DSSCs was evaluated with a sandwich cell using 0.6 M 1-butyl-3-methylimidazolium iodide, 0.05 M LiI, 0.03 M I_2, 0.5 M 4-TBP, and 0.1 M guanidinium thiocyanate in a mixture of acetonitrile–valeronitrile (85:15, v/v) as the redox electrolyte. The IPCE spectra and the *J*–*V* curves under standard global AM 1.5 solar irradiation of the DSSCs are plotted in

Figure 2-10(a) and Figure 2-10(b), respectively. The DSSCs based on **DPTP**, **OMeDPTP**, and **OHexDPTP** showed IPCEs > 70% from 380–400 nm to 570 nm and reached IPCE maxima of 90–92% around 450 nm, indicative of their highly efficient performance. In agreement with the trend in absorption spectra, the IPCE spectra of **DPTP**-, **OMeDPTP**- and **OHexDPTP**-based DSSCs all exhibited higher peak values and extended to longer wavelengths than that of the model dye **M-TP**. Moreover, IPCE spectra of **OMeDPTP**- and **OHexDPTP**-based DSSCs also extended to longer wavelengths than that of **DPTP**. As listed in Table 2-4, the **OHexDPTP**-based cell gave a J_{sc} of 13.79 mA/cm^2, V_{oc} of 0.77 V, and FF of 0.72, yielding an overall PCE of 7.64%. Although both **DPTP**- and **OMeDPTP**-based cells delivered J_{sc} values that are similar to (or even slightly higher than) that of the **OHexDPTP**-based cell, yet with relatively lower V_{oc} values, they both exhibited inferior PCEs of 6.72% and 7.05%, respectively. In addition, the **M-TP**-based cell delivered the poorest PCE of 5.22% among all the cells. For a fair comparison, the **N719**-sensitized DSSC was also fabricated and tested under similar conditions. The PCE of the **OHexDPTP**-based cell reached ~90% of the **N719**-based cell efficiency.

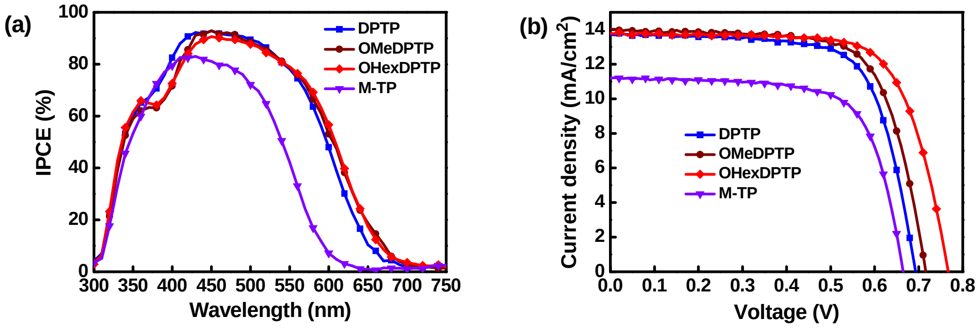

Figure 2-10. (a) IPCE spectra and (b) *J–V* curves of DSSCs based on **DPTP**, **OMeDPTP**, **OHexDPTP**, and **M-TP**.

Table 2-4. Performance parameters of DSSCs sensitized with the dyes **DPTP**, **OMeDPTP**, **OHexDPTP**, **M-TP**, and **N719**.[a]

dye	J_{sc} (mA/cm^2)	V_{oc} (V)	FF	PCE (%)
DPTP	13.72	0.69	0.71	6.72
OMeDPTP	14.01	0.71	0.71	7.05
OHexDPTP	13.79	0.77	0.72	7.64
M-TP	11.19	0.66	0.70	5.22
N719	16.12	0.76	0.70	8.57

[a] The concentration of the organic dyes was maintained at 0.5 mM in a chlorobenzene solution, with 0.5 mM deoxycholic acid as a co-adsorbent [**N719** was fabricated in a *tert*-butanol–acetonitrile (1:1, v/v) solution under the same conditions]. Performance of DSSCs was measured with a working area of 0.125 cm^2.

Interestingly, the **DPTP**- and **OHexDPTP**-based cells showed nearly the same J_{sc} despite the larger molar extinction coefficients and red-shifted absorption of **OHexDPTP**. This is attributed to the smaller density of **OHexDPTP** on the TiO_2 surface, due to the greater steric congestion of the dihexyloxy-substituted diphenylthienylamine donor moiety. By desorbing the dyes from TiO_2 with a basic solution, the adsorbing densities were determined to be 1.8×10^{-7} and 6.0×10^{-8} mol/cm^2 for **DPTP** and **OHexDPTP**, respectively, supporting such a mechanism. On the other hand, the surface density of **OMeDPTP** was similar to that of **DPTP** due to their similar molecular sizes, and thus the highest J_{sc} of **OMeDPTP**-based cell among all the cells can be ascribed to its simultaneously better light-harvesting ability and larger surface density on TiO_2.

Figure 2-11(a) shows the EIS Nyquist plots for DSSCs based on **DPTP**, **OMeDPTP** and **OHexDPTP**. The three cells hardly showed any difference in smaller semicircles at higher frequencies, but the difference in larger semicircles at lower frequencies between the **OHexDPTP**- and **DPTP-** (or **OMeDPTP**-) based cells was significant. The larger width of the lower-frequency semicircle of the **OHexDPTP**-based cell indicates a larger charge-transfer resistance at the

TiO_2/dye/electrolyte interface. Figure 2-11(b) shows the EIS Bode plots of the DSSCs based on **DPTP**, **OMeDPTP**, and **OHexDPTP**. Again, the difference in Bode plots of the three cells mainly occurred in the lower-frequency range, and the lower-frequency peak of the **OHexDPTP**-based cell shifted to a lower frequency as compared to those of the **DPTP**- and **OMeDPTP**-based cells, indicating that the electron lifetime was effectively prolonged by the two long hexyloxy chains near the TiO_2/dye/electrolyte interface. The EIS results clearly suggest that the two long hexyloxy chains of **OHexDPTP** act as effective blocking units between the TiO_2 surface and the electrolyte, preventing the approach of hydrophilic I_3^- ions to the TiO_2 surface and thereby leading to suppressed charge recombination/dark current and lengthened electron lifetimes. These factors in turn lead to the higher V_{oc} of the **OHexDPTP**-based cell relative to the **DPTP**- and **OMeDPTP**-based cells.

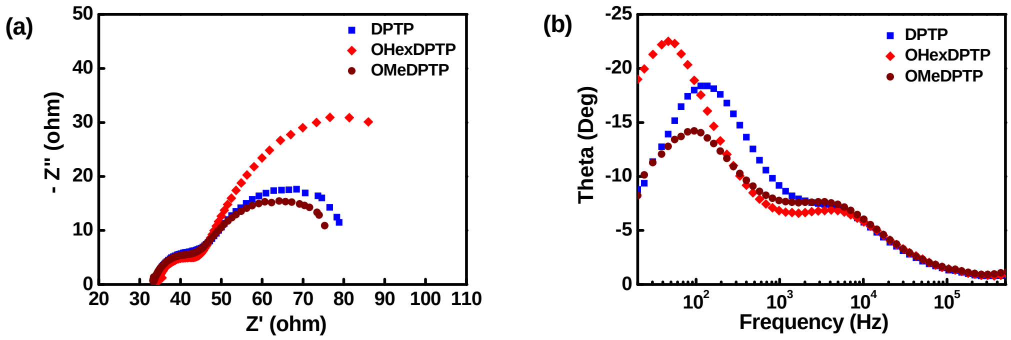

Figure 2-11. EIS (a) Nyquist plots and (b) Bode phase plots for DSSCs based on **DPTP**, **OMeDPTP**, and **OHexDPTP**.

2-4 Organic Donor–Acceptor–Acceptor Dyes Featuring 2,1,3-Benzothiadiazole as the Bridging Acceptor

With the success of the pyrimidine-containing D–A–A dyes, in this work, we further synthesized another series of D–A–A dyes (**DPTB**, **OMeDPTB**, and **OHexDPTB**, Scheme 2-5), in which 2,1,3-benzothiadiazole (BT) is utilized to replace the pyrimidine block. The BT represents one of the most ubiquitous electron-accepting units in the design of optoelectronic materials because of its fascinating features, including low-band-gap character, high absorption coefficient, and appropriate energy levels.[37] Several BT-containing organic DSSC dyes with different configurations were reported and showed distinguished light-harvesting abilities.[34, 38] Therefore, we envisioned that the structural modification would enable these tailor-made dyes to show significant bathochromic shifts in absorption as compared to their pyrimidine-based analogs. This study also provided us with an opportunity to further assess the applicability of our D–A–A molecular design strategy on developing photosensitizers for DSSCs.

2-4-1 Synthesis

The synthetic pathways of the dyes **DPTB**, **OMeDPTB**, and **OHexDPTB** are illustrated in Scheme 2-5. Stille coupling reactions of triarylamine-functionalized tributylstannyl derivatives and 4,7-dibromo-2,1,3-benzothiadiazole afforded the mono-functionalized intermediates **2-8**, which were directly reacted with copper cyanide to yield their corresponding cyano derivatives **2-9** via Rosenmunde–von Braun reaction. Finally, the reduction of **2-9** using diisopropylaluminum hydride followed by Knöevenagel condensation of the resulting aldehydes **2-10** with cyanoacetic acid in the presence of ammonium acetate gave the target compounds in moderate overall yields.

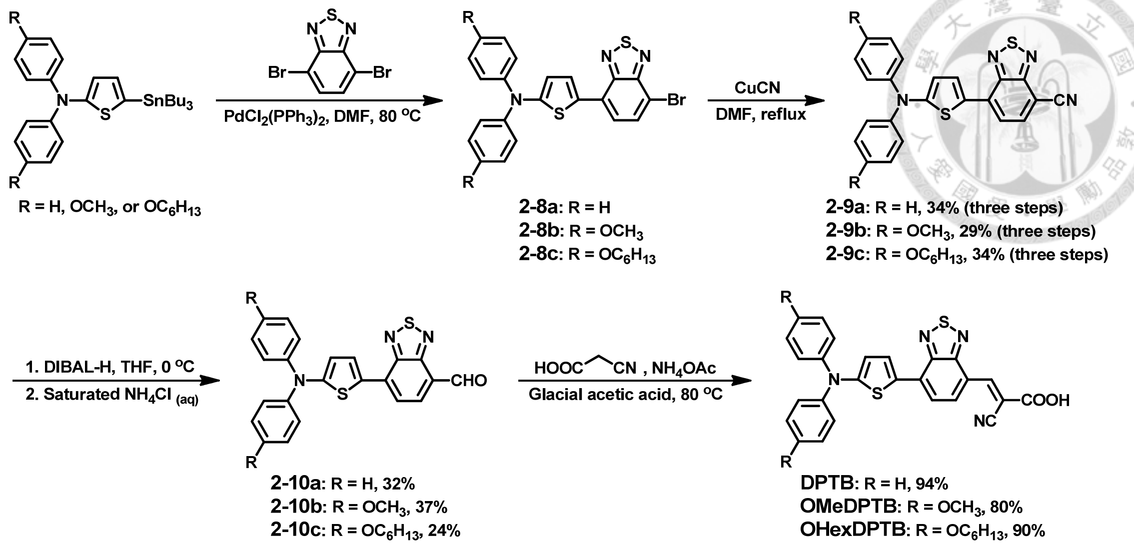

Scheme 2-5. Synthesis of the dyes **DPTB**, **OMeDPTB**, and **OHexDPTB**.

2-4-2 Optical Properties

The UV–vis absorption spectra of the dyes in CH_2Cl_2 solutions are depicted in Figure 2-12(a), and their pertinent photophysical parameters are summarized in Table 2-5. The photoluminescence data of these dyes are not provided here since the dyes were almost non-luminescent. All the three dyes exhibited an intense absorption band in the longer-wavelength region with a λ_{abs} around 613–654 nm and a ε that is higher than 3×10^4 M^{-1} cm^{-1}, which is assigned to the ICT transition. Apparently, the absorption of this series of BT-containing D–A–A dyes effectively extended to the NIR region and was significantly red-shifted as compared to that of their pyrimidine-based analogs. The absorption bands of **OMeDPTB** and **OHexDPTB** were red-shifted compared to that of **DPTB** by ca. 40 nm because of the stronger electron-donating nature of the dialkoxy substituents. This red shift is profitable for photon harvesting and thus photocurrent generation in DSSCs (*vide infra*). Moreover, it is worth mentioning that in comparison to the reported D–A–π–A dye that incorporates thiophene as an extra π-spacer to connect the BT and cyanoacrylic acid blocks (λ_{abs} = 541 nm in a THF solution),[34]

DPTB showed an evident bathochromic shift in absorption, corroborating again that enhanced solar spectral responses can be realized through our D–A–A molecular design concept. Figure 2-12(b) depicts the absorption spectra of the dyes anchoring on 7 μm porous TiO_2 nanoparticle films. The absorption maxima of the three dyes were blue-shifted compared to those observed in CH_2Cl_2 solutions. This phenomenon can be attributed to the deprotonation of carboxylic acid upon adsorption onto the TiO_2 surface, and the resulting carboxylate–TiO_2 unit is a weaker electron acceptor than the corresponding carboxylic acid.[21]

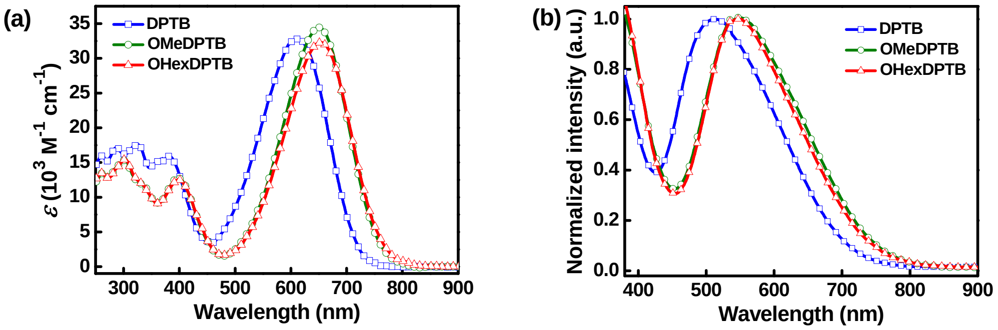

Figure 2-12. Absorption spectra of **DPTB**, **OMeDPTB**, and **OHexDPTB** (a) in CH_2Cl_2 solutions (b) anchoring on 7 μm porous TiO_2 nanoparticle films.

Table 2-5. Photophysical and electrochemical parameters of the dyes **DPTB**, **OMeDPTB**, and **OHexDPTB**.

dye	λ_{abs} (nm)[a]	ε (M^{-1} cm^{-1})[a]	λ_{abs} on TiO_2 (nm)[b]	$E_{0\text{–}0}$ (eV)[c]	E_{ox}^{1} (V)[d]	E_{red} (V)[e]	E_{ox}^{*} (V)[f]
DPTB	613	32800	513	1.74	1.02	−0.66	−0.72
OMeDPTB	650	34442	548	1.65	0.87	−0.70	−0.78
OHexDPTB	654	32292	547	1.64	0.87	−0.69	−0.77

[a]Measured in CH_2Cl_2 solutions (10^{-5} M). [b]Obtained through measuring the dyes adsorbed on 7 μm TiO_2 nanoparticle films in chlorobenzene solutions. [c]Estimated from the onset point of the absorption spectra in CH_2Cl_2 solutions. [d]Measured in CH_2Cl_2 solutions with 0.1 M $TBAPF_6$ as a supporting electrolyte. [e]Measured in THF solutions with 0.1 M TBAP as a supporting electrolyte. [d,e]Calibrated with Fc/Fc^+ as an external reference and converted to NHE by addition of 630 mV.[22] [f]$E_{ox}^{*} = E_{ox}^{1} - E_{0\text{–}0}$.

2-4-3 Theoretical Calculations

To gain more insight into the electronic structures of the dyes, DFT calculations were carried out at the B3LYP/6-31G(d) level for geometry optimization. As shown in Figure 2-13, the HOMOs of the dyes are populated over the whole molecular conjugated backbone with substantial contributions from the diarylamine and thiophene fragments, whereas LUMOs are delocalized through the thiophene, BT, and cyanoacrylic acid blocks with considerable contributions from the latter two. The significant spatial overlap between the HOMO and LUMO as well as the coplanar conformation between the thiophene and BT rings is beneficial to enhance the efficiency of ICT transition, as evidenced in the absorption spectra. Moreover, the HOMO–LUMO excitation shifts the electron density distribution from the diarylamine unit to the cyanoacrylic acid block, thus facilitating efficient electron injection from photoexcited dyes into the TiO_2 electrode.

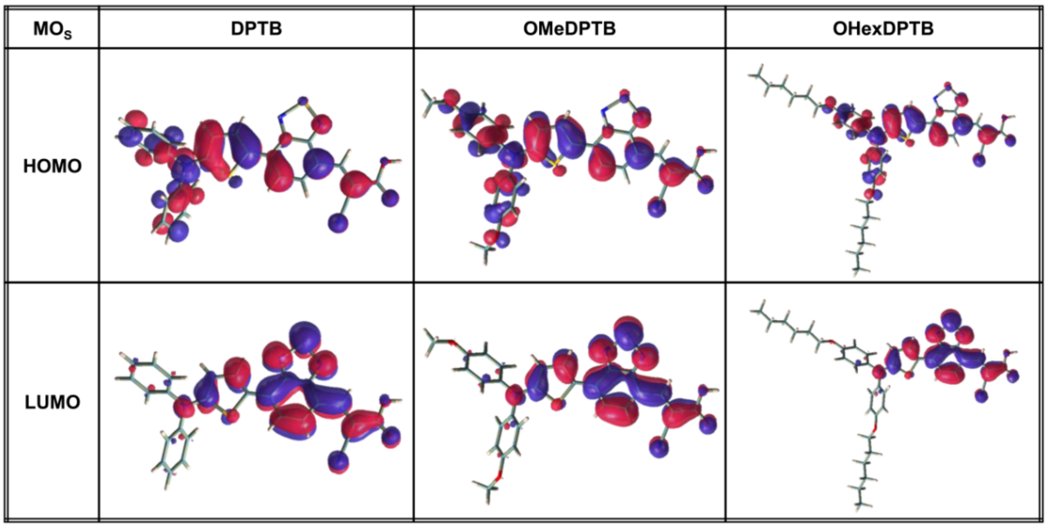

Figure 2-13. HOMOs and LUMOs of the dyes **DPTB**, **OMeDPTB**, and **OHexDPTB** calculated with DFT.

2-4-4 Electrochemical Properties

The electrochemical properties of these dyes were studied by CV. Representative cyclic voltammograms are shown in Figure 2-14 and the relevant CV data are collected in Table 2-5. The three dyes all exhibited one reversible oxidation wave at lower potentials and one irreversible (or quasi-reversible) oxidation wave at higher potentials. The first waves can be ascribed to the oxidation of the diarylthienylamine donor moieties, whereas the second waves can be assigned to the oxidation of the conjugated backbones.[38d] The oxidation potentials of **OMeDPTB** and **OHexDPTB** were less positive than those of **DPTB** due to the presence of the stronger electron-donating dialkoxy substituents. Moreover, the introduction of the dialkoxy substituents on the donor moieties increases the electron density of the conjugated backbones, thus making the second oxidation behaviors of **OMeDPTB** and **OHexDPTB** more reversible. On the other hand, one quasi-reversible reduction wave attributed to the reduction of the cyanoacrylic acid block was observed in the cathodic potential regime for the dyes, which was relatively insensitive to the structural alterations of the donor moieties even though the reduction potentials of **OMeDPTB** and **OHexDPTB** were slightly more negative than that of **DPTB**. The E_{0-0} estimated from the onset point of the absorption spectrum in CH_2Cl_2 and the first oxidation potential (E_{ox}^{1}) was used to calculate the E_{ox}^{*}. The deduced E_{ox}^{*} values corresponding to the LUMO levels of these three dyes were more negative than the conduction band edge of the TiO_2 electrode (−0.5 V vs NHE),[23] indicating that the electron injection from photoexcited dyes into TiO_2 would be energetically favorable. The first oxidation potentials (E_{ox}^{1}) corresponding to the HOMO levels of the dyes were more positive than the redox potential of the I^-/I_3^- couple (0.4 V vs NHE). It suggests that the oxidized dyes formed after electron injection into TiO_2 should be able to thermodynamically accept electrons from I^- ions for effective dye regeneration.

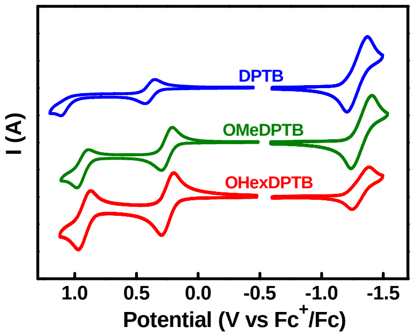

Figure 2-14. Cyclic voltammograms of **DPTB**, **OMeDPTB**, and **OHexDPTB** recorded in solutions.

2-4-5 Photovoltaic Characteristics

In common with the photovoltaic characterization on the pyrimidine-based dyes, the photovoltaic performance of **DPTB**, **OMeDPTB**, and **OHexDPTB** as the photosensitizers for DSSCs was first evaluated with a sandwich cell using 0.6 M 1-butyl-3-methylimidazolium iodide, 0.05 M LiI, 0.03 M I_2, 0.5 M 4-TBP, and 0.1 M guanidinium thiocyanate in a mixture of acetonitrile–valeronitrile (85:15, v/v) as the redox electrolyte (EL1). The performance parameters of the corresponding DSSCs measured under AM 1.5G simulated solar illumination at an intensity of 100 mW/cm^2 are summarized in Table 2-6. The preliminary results showed that the DSSCs exhibit extremely low PCEs (<0.06%). We attribute the poor photovoltaic performance to the addition of 4-TBP into the electrolyte that can negatively shift the conduction band edge of TiO_2 about 0.3 V,[32] thus impeding efficient electron injection from the photoexcited dyes into the TiO_2 electrode.[39] Recently, a few BT-containing sensitizers with similar structural features to our dyes (i.e., the BT block directly adjacent to the cyanoacrylic acid) were also reported to show inferior performance to their analogs even though the origins of the low PCEs were different.[38d–e] For a fair comparison, the **N719**-sensitized DSSC was also fabricated under the same conditions and reached a PCE of 8.57%.

Table 2-6. Performance parameters of DSSCs based on the dyes **DPTB**, **OMeDPTB**, **OHexDPTB**, and **N719**.[a]

dye	J_{sc} (mA/cm^2)	V_{oc} (V)	FF	PCE (%)
DPTB[b]	0.31	0.28	0.45	0.039
OMeDPTB[b]	0.42	0.25	0.45	0.045
OHexDPTB[b]	0.44	0.30	0.45	0.059
N719[b]	16.12	0.76	0.70	8.57
DPTB[c]	9.12	0.41	0.62	2.30
OMeDPTB[c]	13.06	0.39	0.62	3.13
OHexDPTB[c]	11.10	0.45	0.63	3.16
N719[c]	14.05	0.57	0.67	5.39

[a] The concentration of the organic dyes was maintained at 0.5 mM in a chlorobenzene solution, with 0.5 mM deoxycholic acid as a co-adsorbent [**N719** was fabricated in a *tert*-butanol–acetonitrile (1:1, v/v) solution under the same conditions]. Performance of DSSCs was measured with a working area of 0.125 cm^2. [b] The composition for the EL1 electrolyte is: 0.6 M 1-butyl-3-methylimidazolium iodide, 0.05 M LiI, 0.03 M I_2, 0.5 M 4-TBP, and 0.1 M guanidinium thiocyanate in a mixture of acetonitrile and valeronitrile (85/15, v/v). [c] The composition for the EL2 electrolyte is: 0.6 M 1,2-dimethyl-3-propylimidazolium iodide, 0.05 M LiI, and 0.03 M I_2 in acetonitrile.

To improve the poor device performance, the DSSCs were then fabricated in a 4-TBP-free condition by merely using 0.6 M 1,2-dimethyl-3-propylimidazolium iodide, 0.05 M LiI, and 0.03 M I_2 in acetonitrile as the redox electrolyte (EL2). The IPCE spectra and the *J–V* curves of the DSSCs using the EL2 electrolyte are shown in Figure 2-15(a) and Figure 2-15(b), respectively. The DSSCs based on these organic dyes exhibited remarkably improved performance, whereas the **N719**-based cell showed a lower PCE than the parent cell based on the EL1 electrolyte, mainly due to the lower J_{sc} and V_{oc} values (Table 2-6). The decrease in V_{oc} for the **N719**-based cell can be partly attributed to the shift of the conduction band edge of TiO_2 toward a positive potential due to the removal of 4-TBP. Such phenomenon also qualitatively verifies our aforementioned speculation on the poor photovoltaic performance of the DSSCs based on the BT-containing D–A–A dyes in conjunction with the EL1 electrolyte. In agreement with the trend in absorption spectra, the IPCE spectra of the three cells all extended to the NIR region, and those of **OMeDPTB**- and **OHexDPTB**-based devices showed red-shifted responses as compared to that of **DPTB**-based device [Figure 2-15(a)]. In addition, the **OMeDPTB**-based cell exhibited the highest IPCE values among the three cells over the whole spectral range, thus delivering a maximum J_{sc} of 13.06 mA/cm^2. On the other hand, the **OHexDPTB**-based cell gave a higher V_{oc} than the other two cells, benefiting from the presence of two long aliphatic hexyloxy chains on the diarylthienylamine donor. As a whole, the **OHexDPTB**-based cell showed the best PCE of 3.16% among these three DSSCs, with a J_{sc} of 11.10 mA/cm^2, V_{oc} of 0.45 V, and FF of 0.63.

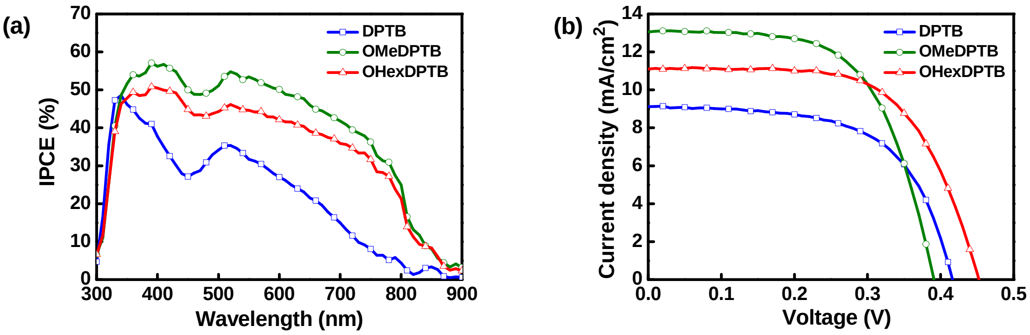

Figure 2-15. (a) IPCE spectra and (b) J–V curves of DSSCs based on **DPTB**, **OMeDPTB**, and **OHexDPTB** in conjunction with the EL2 electrolyte.

2-5 Conclusions

In section 2-2, we developed two organic D–π–A sensitizers (**TPCADTS** and **TP6CADTS**) that contain a coplanar diphenyl-substituted DTS as the π-bridge. Compared to **TPCADTS**, **TP6CADTS** possessed a narrower bandgap and higher HOMO level than **DPTP** due to the presence of the stronger electron-donating hexyloxy substituents on the triphenylamine donor moiety. The aliphatic hexyloxy chains of **TP6CADTS** also benefited the suppression of the charge recombination at the TiO_2/dye/electrolyte interface, thus resulting in the higher V_{oc}, IPCEs, and overall PCE of 7.6% in the corresponding cell.

In section 2-3, we synthesized a series of D–A–A sensitizers (**DPTP**, **OMeDPTP**, and **OHexDPTP**), in which various diarylthienylamine donor moieties are connected to a cyanoacrylic acid acceptor moiety through another electron-deficient pyrimidine block. By taking advantage of the characteristic planarity and electronic deficiency of pyrimidine, **DPTP** showed a better light-harvesting ability than its D–π–A counterpart **M-TP**. The incorporation of the dialkoxy substituents on the donor moiety gave **OMeDPTP** and **OHexDPTP** narrower bandgaps and higher HOMO levels as compared to those of **DPTP**. The introduction of two long hexyloxy chains on the donor moiety of **OHexDPTP** effectively suppressed the charge recombination at the TiO_2/dye/electrolyte interface, leading to the fact that the **OHexDPTP**-based cell delivered the highest V_{oc} and thus the highest PCE of 7.64% among the series of cells.

In section 2-4, another series of D–A–A dyes (**DPTB**, **OMeDPTB**, and **OHexDPTB**) characterized by the adoption of BT as the bridging acceptor were synthesized. These dyes showed better light-harvesting capabilities than not only their pyrimidine-based analogs but also the previously reported D–A–π–A counterpart. The incorporation of the dialkoxy substituents on the donor moiety endowed **OMeDPTB** and **OHexDPTB** with narrower bandgaps and higher HOMO levels than **DPTB**. In photovoltaic characterization, the use of the 4-TBP-containing electrolyte (EL1) that can negatively shift the conduction band edge of TiO_2 about 0.3 V impeded efficient electron injection from the photoexcited dyes into the TiO_2 electrode because of their deep-lying LUMO levels, thus leading to poor photovoltaic performance. In contrast, the DSSCs based on these dyes in conjunction with the 4-TBP-free electrolyte (EL2) showed markedly improved performance with solar spectral responses extending to the NIR region, and the best cell based on **OHexDPTB** reached a PCE of 3.16%.

According to the results of the two series of D–A–A dyes, we conclude that although the D–A–A dyes generally show better light-harvesting abilities than their counterparts, DSSCs sensitized with D–A–A dyes may suffer from a trade-off between the photocurrent and the photovoltage owing to the possibly limited uses of the 4-TBP-containing electrolytes.

2-6 Experimental Details

Synthesis and Materials. Unless otherwise stated, all chemicals and reagents were used as received from commercial sources without purification. Solvents for chemical synthesis were purified by distillation. All chemical reactions were carried out under an argon or nitrogen atmosphere. The 5,5’-bis(trimethylsilyl)-3,3’-diphenylsilylene-2,2’-bithiophene,[16] 4-(*N*,*N*-diphenylamino)phenylboronic acid,[40] tributyl[4-(*N*,*N*-bis(4-hexyloxyphenyl)amino)phenyl]stannane,[41] 5-bromo-2-iodopyrimidine,[42] and 5-(*N*,*N*-diphenylamino)-2-(tri-*n*-butylstannyl)thiophene[43] were synthesized based on the reported procedures.

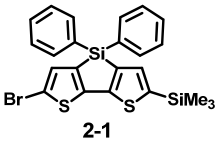

2-1

5-Bromo-5’-trimethylsilyl-3,3’-diphenylsilylene-2,2’-bithiophene (2-1). To a stirring solution of 5,5’-bis(trimethylsilyl)-3,3’-diphenylsilylene-2,2’-bithiophene (13.55 g, 27.60 mmol) in *N*,*N*-dimethylformamide (275 mL) was added dropwise *N*-bromosuccinimide (5.86 g, 33.12 mmol) dissolved in *N*,*N*-dimethylformamide (275 mL) at 0 °C under exclusion of light, and the reaction mixture was then warmed to room temperature. After being stirred for 12 h, the reaction mixture was poured into water and extracted with diethyl ether. The combined extracts were washed with brine, dried over anhydrous magnesium sulfate, and filtered. The solvent of the filtrate was removed by rotary evaporation. The crude product was dissolved in hexane, and the undissolved solid was filtered. The filtrate was evaporated to dryness, and the resulting solid was washed with ethanol to afford **2-1** as a white solid (9.04 g, 66%), mp 140–142 °C; IR (KBr) ν 3065, 2950, 1587, 1427, 1245, 995 cm^{-1}; ^1H NMR ($CDCl_3$, 400 MHz) δ 7.63

(dt, J = 6.4, 1.6 Hz, 4H), 7.45–7.36 (m, 6H), 7.31 (s, 1H), 7.18 (s, 1H), 0.36 (s, 9H); ^{13}C NMR ($CDCl_3$, 100 MHz) δ 154.8, 150.6, 142.5, 140.3, 136.1, 135.2, 132.1, 131.1, 130.3, 128.1, 111.9, 0.3; HRMS (*m/z*, FAB$^+$) calcd for $C_{23}H_{21}BrS_2Si_2$ 495.9807, found 495.9803.

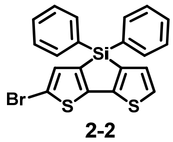

2-2

5-Bromo-3,3'-diphenylsilylene-2,2'-bithiophene (2-2). To a stirring solution of **2-1** (3.30 g, 6.63 mmol) in chloroform (165 mL) was added dropwise trifluoroacetic acid (0.98 mL, 13.26 mmol) at room temperature under exclusion of light. After being stirred for 12 h, the reaction mixture was poured into water and extracted with chloroform. The combined extracts were washed with brine, dried over anhydrous magnesium sulfate, and filtered. The solvent of the filtrate was removed by rotary evaporation to afford **2-2** as a light yellow solid (2.75 g, 98%), mp 173–175 °C; IR (KBr) ν 3090, 3018, 1586, 1427, 1250, 943 cm^{-1}; ^{1}H NMR ($CDCl_3$, 400 MHz) δ 7.64 (d, J = 6.8 Hz, 4H), 7.47–7.37 (m, 6H), 7.30 (d, J = 4.8 Hz, 1H), 7.24 (d, J = 4.8 Hz, 1H), 7.20 (s, 1H); ^{13}C NMR ($CDCl_3$, 100 MHz) δ 150.5, 149.6, 139.9, 138.7, 135.2, 132.0, 130.9, 130.4, 129.5, 128.1, 126.2, 111.8; HRMS (*m/z*, FAB$^+$) calcd for $C_{20}H_{13}BrS_2Si$ 423.9411, found 423.9416.

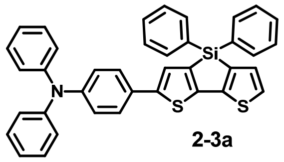

2-3a

5-[*N*,*N*-bis(phenylamino)phenyl]-3,3'-diphenylsilylene-2,2'-bithiophene (2-3a). A mixture of **2-2** (2.33 g, 5.48 mmol), 4-(*N*,*N*-diphenylamino)phenylboronic acid (1.90 g, 6.58 mmol), $Pd(PPh_3)_4$ (316 mg, 0.27 mmol), and potassium carbonate (2 M aqueous solution, 13.7 mL, 27.40 mmol) in toluene (270 mL) was stirred and heated to reflux under argon for 2.5 h. The reaction mixture was poured into water and extracted with dichloromethane. The combined extracts were washed with brine, dried over anhydrous magnesium sulfate, and filtered. The solvent of the filtrate was removed by rotary evaporation, and the crude product was purified by column chromatography on silica gel with dichloromethane/hexane (v/v, 1:5) as eluent to afford **2-3a** as a yellow solid (2.68 g, 83%), mp 230–232 °C; IR (KBr) ν 3059, 3023, 1590, 1494, 1273, 826 cm^{-1}; ^1H NMR ($CDCl_3$, 400 MHz) δ 7.67 (dt, *J* = 6.4, 1.6 Hz, 4H), 7.48–7.22 (m, 15 H), 7.12 (dd, *J* = 8.4, 1.2 Hz, 4H), 7.07–7.02 (m, 4H); ^{13}C NMR ($CDCl_3$, 100 MHz) δ 150.5, 148.4, 147.3, 146.9, 145.7, 141.1, 139.0, 135.3, 131.6, 130.2, 129.5, 129.2, 128.4, 128.1, 126.3, 125.8, 124.6, 124.3, 123.6, 122.9; HRMS (*m/z*, FAB^+) calcd for $C_{38}H_{27}NS_2Si$ 589.1354, found 589.1349.

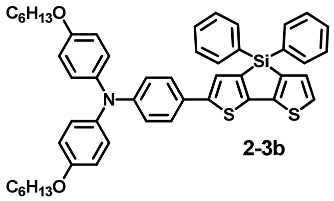

2-3b

5-[*N*,*N*-bis(4-hexyloxyphenylamino)phenyl]-3,3’-diphenylsilylene-2,2’-bithiophene (2-3b). A mixture of **2-2** (2.94 g, 6.91 mmol), tributyl[4-(*N*,*N*-bis(4-hexyloxyphenyl)amino)phenyl]stannane (7.61 g, 10.37 mmol), and $Pd(PPh_3)_4$ (404 mg, 0.35 mmol) in anhydrous toluene (35 mL) was stirred and heated at 100 °C under argon for 24 h. After the mixture was cooled to room temperature, the solvent was removed by rotary evaporation, and the crude product was purified by column chromatography on silica gel with dichloromethane/hexane (v/v, 1:3) as eluent to afford **2-3b** as a yellow solid (3.32 g, 61%), mp 55–57 °C; IR (KBr) ν 3063, 2955, 2853, 1601, 1505, 1475, 1011, 824 cm^{-1}; ^{1}H NMR (DMSO-d_6, 400 MHz) δ 7.71 (s, 1H), 7.66 (d, J = 6.8 Hz, 4H), 7.56 (d, J = 4.4 Hz, 1H), 7.50–7.37 (m, 9H), 6.99 (d, J = 8.8 Hz, 4H), 6.87 (d, J = 8.8 Hz, 4H), 6.75 (d, J = 8.4 Hz, 2H), 3.89 (t, J = 6.2 Hz, 4H), 1.67 (m, 4H), 1.38 (m, 4H), 1.29 (m, 8H), 0.86 (t, J = 6.2 Hz, 6H); ^{13}C NMR (CD_2Cl_2, 100 MHz) δ 156.1, 151.0, 148.7, 148.2, 146.8, 141.6, 140.6, 139.3, 135.7, 132.2, 130.7, 130.0, 128.6, 127.2, 126.6, 126.4, 126.3, 124.4, 120.4, 115.7, 68.8, 32.2, 29.9, 26.4, 23.3, 14.5; HRMS (m/z, FAB$^+$) calcd for $C_{50}H_{51}NO_2S_2Si$ 789.3130, found 789.3133.

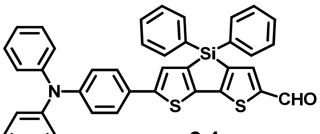

2-4a

5-[*N*,*N*-bis(phenylamino)phenyl]-5’-formyl-3,3’-diphenylsilylene-2,2’-bithiophene (2-4a). To a stirring solution of **2-3a** (826 mg, 1.4 mmol) in anhydrous *N*,*N*-dimethylformamide (30 mL) was added dropwise phosphorus oxychloride (0.22 mL, 2.38 mmol) at −40 °C under argon. The reaction mixture was then heated to 60 °C and stirred for 4 h. After being cooled to room temperature, the reaction mixture was quenched with 10% sodium acetate aqueous solution (210 mL) and extracted with ethyl acetate. The combined extracts were washed with brine, dried over anhydrous magnesium sulfate, and filtered. The solvent of the filtrate was removed by rotary evaporation, and the crude product was purified by column chromatography on silica gel with ethyl acetate/hexane (v/v, 1:10) as eluent to afford **2-4a** as a red solid (553 mg, 64%), mp 235–237 °C; IR (KBr) ν 3031, 2809, 1657, 1589, 1487, 1115, 825 cm^{-1}; ^{1}H

NMR ($CDCl_3$, 400 MHz) δ 9.87 (s, 1H), 7.86 (s, 1H), 7.65 (dd, *J* = 8.0, 1.2 Hz, 4H), 7.49–7.45 (m, 4H), 7.41–7.37 (m, 5H), 7.30–7.26 (m, 4H), 7.12 (dd, *J* = 8.4, 0.8 Hz, 4H), 7.08–7.04 (m, 4H); ^{13}C NMR ($CDCl_3$, 100MHz) δ 182.2, 159.7, 149.9, 147.8, 147.1, 146.7, 145.8, 144.7, 139.9, 139.4, 135.2, 130.7, 130.2, 129.2, 128.3, 127.3, 126.7, 124.9, 124.6, 123.3, 123.1; HRMS (*m/z*, FAB$^+$) calcd for $C_{39}H_{27}NOS_2Si$ 617.1303, found 617.1304.

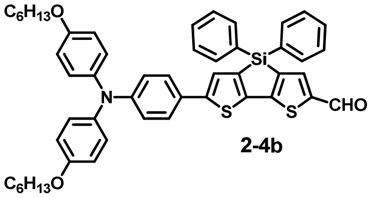

2-4b

5-[*N*,*N*-bis(4-hexyloxyphenylamino)phenyl]-5'-formyl-3,3'-diphenylsilylene-2,2'-bithiophene (2-4b). To a stirring solution of **2-3b** (2 g, 2.53 mmol) in anhydrous *N*,*N*-dimethylformamide (54 mL) was added dropwise phosphorus oxychloride (0.4 mL, 4.3 mmol) at −40 °C under argon. The reaction mixture was then heated to 60 °C and stirred for 3 h. After being cooled to room temperature, the reaction mixture was quenched with 10% sodium acetate aqueous solution (380 mL) and extracted with ethyl acetate. The combined extracts were washed with brine, dried over anhydrous magnesium sulfate, and filtered. The solvent of the filtrate was removed by rotary evaporation, and the crude product was purified by column chromatography on silica gel with ethyl acetate/hexane (v/v, 1:10) as eluent to afford **2-4b** as a red solid (1.62 g, 78%), mp 65–67 °C; IR (KBr) ν 3061, 2953, 2856, 2706, 1664, 1599, 1506, 1237, 1139, 825 cm^{-1}; ^{1}H NMR (DMSO-d_6, 400 MHz) δ 9.87 (s, 1H), 8.40 (s, 1H), 7.86 (s, 1H), 7.70 (d, *J* = 7.2 Hz, 4H), 7.55–7.41 (m, 8H), 7.03 (d, *J* = 8.8 Hz, 4H), 6.90 (d, *J* = 8.8 Hz, 4H), 6.74 (d, *J* = 8.4 Hz, 2H), 3.92 (t, *J* = 6.8 Hz, 4H), 1.69 (m, 4H), 1.39 (m, 4H), 1.30 (m, 8H), 0.87 (t, *J* = 6.8 Hz, 6H); ^{13}C NMR (CD_2Cl_2, 100 MHz) δ 182.6, 159.9, 156.4, 150.9, 149.4, 146.5, 146.4, 145.2, 140.3, 140.2, 139.8, 135.7, 131.1, 130.9, 128.7, 127.5, 126.9, 125.5, 124.7, 119.9, 115.7, 68.8, 32.2, 29.9, 26.3, 23.3, 14.5; HRMS (*m/z*, FAB$^+$) calcd for $C_{51}H_{51}NO_3S_2Si$ 817.3080, found 817.3077.

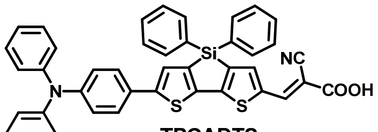

TPCADTS

3-[5-[*N*,*N*-bis(phenylamino)phenyl]-3,3'-diphenylsilylene-2,2'-bithiophene-5'-yl]-2-cyanoacrylic acid (TPCADTS). A mixture of **2-4a** (370 mg, 0.6 mmol), cyanoacetic acid (153 mg, 1.8 mmol), and ammonium acetate (39 mg) in glacial acetic acid (13 mL) was stirred and heated at 120 °C for 12 h. After the reaction mixture was cooled to room temperature, the resulting precipitate was collected by filtration and thoroughly washed with water, methanol, and diethyl ether to afford **TPCADTS** as a black solid (350 mg, 85%), mp 294–296 °C; IR (KBr) ν 3056, 2217, 1718, 1682, 1592, 1429, 824 cm^{-1}; ^{1}H NMR (DMSO-d_6, 400 MHz) δ 8.46 (s, 1H), 8.32 (s, 1H), 7.96 (s, 1H), 7.69–7.64 (m, 6H), 7.52–7.48 (m, 2H), 7.46–7.42 (m, 4H), 7.35–7.31 (m, 4H), 7.11–7.05 (m, 6H), 6.97 (d, *J* = 8.8 Hz, 2H); ^{13}C NMR (DMSO-d_6, 100 MHz) δ 163.8, 158.8, 149.8, 147.5, 146.6, 146.4, 145.5, 143.4, 139.8, 137.3, 135.0, 130.9, 129.9, 129.7, 128.5, 126.9, 126.6, 126.3, 124.6, 123.7, 122.5, 116.9; HRMS (*m/z*, FAB$^+$) calcd for $C_{42}H_{28}N_2O_2S_2Si$ 684.1361, found 684.1357.

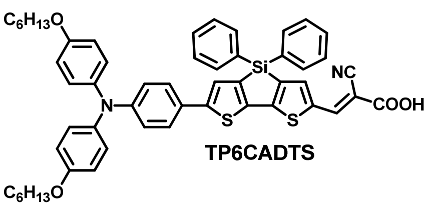

TP6CADTS

3-[5-[*N*,*N*-bis(4-hexyloxyphenylamino)phenyl]-3,3'-diphenylsilylene-2,2'-bithiophene-5'-yl]-2-cyanoacrylic acid (TP6CADTS). A mixture of **2-4b** (327 mg, 0.4 mmol), cyanoacetic acid (102 mg, 1.2 mmol), and ammonium acetate (26 mg) in glacial acetic acid (9mL) was stirred and heated at 120 °C for 12 h. After the reaction mixture was cooled to room temperature, the resulting precipitate was collected by filtration and thoroughly washed with water, methanol, and hexane to afford **TP6CADTS** as a black solid (305 mg, 86%), mp 244–246 °C; IR (KBr) ν 3062, 2930, 2854, 2215, 1719, 1682, 1565, 1373, 822 cm^{-1}; ^{1}H NMR (DMSO-d_6, 400 MHz) δ 8.46 (s, 1H), 8.31 (s, 1H), 7.87 (s, 1H), 7.67 (d, *J* = 7.2 Hz, 4H), 7.56–7.42 (m, 8H), 7.03 (d, *J* = 8.8Hz, 4H), 6.90 (d, *J* = 8.8 Hz, 4H), 6.75 (d, *J* = 8.4 Hz, 2H), 3.92 (t, *J* = 6.8 Hz, 4H), 1.69 (m, 4H), 1.40 (m, 4H), 1.30 (m, 8H), 0.88 (t, *J* = 6.8 Hz, 6H); ^{13}C NMR (DMSO-d_6, 100 MHz) δ 164.5, 156.3, 151.2, 149.4, 147.2, 145.5, 140.3, 139.9, 137.8, 135.7, 131.6, 130.7, 129.2, 127.8, 127.4, 126.2, 124.9, 119.3, 116.2, 68.3, 31.7, 29.4, 25.9, 22.7, 14.6; HRMS (*m/z*, FAB$^+$) calcd for $C_{54}H_{52}N_2O_4S_2Si$ 884.3138, found 884.3146.

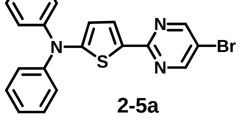

2-5a

[5-(5-Bromo-pyrimidin-2-yl)-thiophen-2-yl]-*N*,*N*-diphenylamine (2-5a). To a stirring solution of 2-(*N*,*N*-diphenylamino)thiophene (5.03 g, 20 mmol) in anhydrous THF (60 mL) was added dropwise *n*-BuLi solution (1.6 M in hexane, 13.13 mL, 21 mmol) at −78 °C under an argon atmosphere. The reaction mixture was warmed to −

35 °C and stirred for 15 min. $ZnCl_2$ (22 mL of 1 M solution in anhydrous THF, 22 mmol) was then added to the reaction mixture in one portion. The reaction mixture was warmed to room temperature and stirred for 30 min. To the above resulting zinc reagent were added 5-bromo-2-iodopyrimidine (5.70 g, 20 mmol), $Pd(PPh_3)_4$ (1.15 g, 1 mmol), and anhydrous THF (80 mL). The whole mixture was heated to reflux under argon for 3 h. After being cooled to room temperature, the reaction mixture was poured into water and extracted with ethyl acetate. The combined extracts were washed with brine, dried over anhydrous magnesium sulfate, and filtered. The solvent of the filtrate was removed by rotary evaporation, and the crude product was purified by column chromatography on silica gel with dichloromethane/hexane (v/v, 1:1) as eluent to afford **2-5a** as a yellow solid (5.83 g, 71%), mp 160–162 °C; IR (KBr) ν 3068, 3028, 1587, 1547, 1468, 1293, 1120, 810 cm^{-1}; ^1H NMR (CD_2Cl_2, 400 MHz) δ 8.59 (s, 2H), 7.74 (d, *J* = 4.0 Hz, 1H), 7.33 (t, *J* = 7.6 Hz, 4H), 7.24 (d, *J* = 7.6 Hz, 4H), 7.14 (t, *J* = 7.6 Hz, 2H), 6.53 (d, *J* = 4.0 Hz, 1H); ^{13}C NMR (CD_2Cl_2, 100 MHz) δ 159.8, 158.0, 157.8, 147.4, 131.6, 129.9, 129.8, 124.9, 124.6, 117.4, 115.9; HRMS (*m/z*, FAB^+) calcd. for $C_{20}H_{14}{}^{79}BrN_3S$ 407.0092, found 407.0102, calcd. for $C_{20}H_{14}{}^{81}BrN_3S$ 409.0071, found 409.0080.

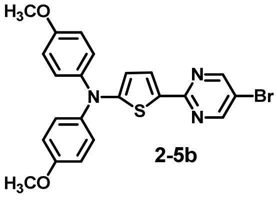

2-5b

[5-(5-Bromo-pyrimidin-2-yl)-thiophen-2-yl]-*N*,*N*-bis(4-methoxyphenyl)amine (2-5b). The synthetic procedure was similar to that of **2-5a**, except that the eluent of column purification was dichloromethane/hexane (v/v, 3:4). **2-5b** was isolated as a yellow solid (56%), mp 145–147 °C; IR (KBr) ν 3071, 3020, 2958, 2837, 1606, 1550, 1298, 1168, 1030, 829 cm^{-1}; ^{1}H NMR (CD_2Cl_2, 400 MHz) δ 8.53 (s, 2H), 7.65 (d, *J* = 4.0 Hz, 1H), 7.21 (dd, *J* = 2.4, 6.8 Hz, 4H), 6.88 (dd, *J* = 2.4, 6.8 Hz, 4H), 6.24 (d, *J* = 4.0 Hz, 1H), 3.80 (s, 6H); ^{13}C NMR (CD_2Cl_2, 100 MHz) δ 160.6, 160.1, 157.7, 157.5, 140.4, 130.5, 127.9, 126.8, 115.1, 115.0, 112.0, 56.0; HRMS (*m/z*, FAB$^+$) calcd. for $C_{22}H_{18}{}^{79}BrN_3O_2S$ 467.0303, found 467.0299, calcd. for $C_{22}H_{18}{}^{81}BrN_3O_2S$ 469.0283, found 469.0281.

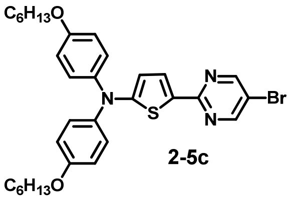

2-5c

[5-(5-Bromo-pyrimidin-2-yl)-thiophen-2-yl]-*N*,*N*-bis(4-hexyloxyphenyl)amine (2-5c). The synthetic procedure was similar to that of **2-5a**, except that the eluent of column purification was dichloromethane/hexane (v/v, 2:3). **2-5c** was isolated as a yellow solid (81%), mp 86–88 °C; IR (KBr) ν 3040, 2954, 2856, 1605, 1547, 1240, 1009, 821 cm^{-1}; ^{1}H NMR ($CDCl_3$, 400 MHz) δ 8.53 (s, 2H), 7.67 (d, *J* = 4.0 Hz, 1H), 7.20 (dd, *J* = 2.0, 6.8 Hz, 4H), 6.85 (dd, *J* = 2.0, 6.8 Hz, 4H), 6.27 (d, *J* = 4.0 Hz, 1H), 3.94 (t, *J* = 6.8 Hz, 4H), 1.79 (m, 4H), 1.47 (m, 4H), 1.35 (m, 8H), 0.93 (t, *J* = 6.8 Hz, 6H); ^{13}C NMR ($CDCl_3$, 100 MHz) δ 160.3, 159.6, 157.1, 156.4, 139.7, 130.1, 127.0, 126.3, 115.2, 114.2, 111.5, 68.2, 31.7, 29.3, 25.8, 22.7, 14.2; HRMS (*m/z*, FAB$^+$) calcd. for $C_{32}H_{38}{}^{79}BrN_3O_2S$ 607.1868, found 607.1862, calcd. for $C_{32}H_{38}{}^{81}BrN_3O_2S$ 609.1848, found 609.1843.

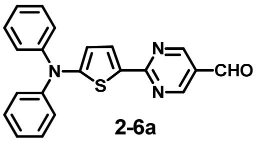

2-6a

2-(5-*N*,*N*-diphenylaminothiophen-2-yl)-pyrimidine-5-carbaldehyde (2-6a). To a stirring solution of **2-5a** (4.90 g, 12 mmol) in 160 mL anhydrous THF was added dropwise *n*-BuLi solution (1.6 M in hexane, 7.73 mL, 12.36 mmol) at −100 °C under an argon atmosphere. The resulting solution was stirred for 20 min, after which time anhydrous ethyl formate (1.03 mL, 12.72 mmol) was added dropwise over 5 min. After being stirred for 20 min, the reaction was quenched with 1.5M HCl in THF solution (8 mL, 12 mmol). The cold bath was removed, and the reaction mixture was stirred for 2 h. The THF was removed under reduced pressure, and the residue was extracted with chloroform. The combined extracts were washed with brine, dried over anhydrous magnesium sulfate, and filtered. The solvent of the filtrate was removed by rotary evaporation, and the crude product was purified by column chromatography on silica gel with dichloromethane/hexane (v/v, 2:1) as eluent to afford **2-6a** as an orange solid (1.33 g, 31% yield), mp 200–202 °C; IR (KBr) ν 3064, 2923, 2821, 1687, 1587, 1445, 1217, 1058, 835 $\mathrm{cm^{-1}}$; ^{1}H NMR (CD_2Cl_2, 400 MHz) δ 9.94 (s, 1H), 8.90 (s, 2H), 7.90 (d, *J* = 4.4 Hz, 1H), 7.39–7.18 (m, 10H), 6.50 (d, *J* = 4.4 Hz, 1H); ^{13}C NMR (CD_2Cl_2, 100 MHz) δ 188.6, 164.4, 161.6, 158.8, 146.9, 133.1, 130.0, 129.7, 125.8, 125.4, 125.2, 115.5; HRMS (*m/z*, FAB^{+}) calcd. for $C_{21}H_{15}N_3OS$ 357.0936, found 357.0935.

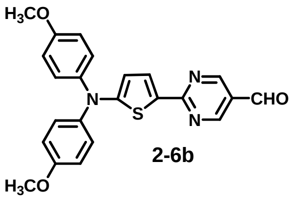

2-6b

2-[5-*N*,*N*-bis(4-methoxyphenyl)aminothiophen-2-yl]-pyrimidine-5-carbaldehyde

(2-6b). The synthetic procedure was similar to that of **2-6a**, except that the eluent used for column purification was dichloromethane. **2-6b** was isolated as an orange solid (46%), mp 183–185 °C; IR (KBr) ν 3061, 3033, 2820, 2734, 1692, 1592, 1503, 1299, 1159, 825 cm^{-1}; ^{1}H NMR (CD$_2$Cl$_2$, 400 MHz) δ 9.89 (s, 1H), 8.84 (s, 2H), 7.84 (d, *J* = 4.4 Hz, 1H), 7.26 (dd, *J* = 2.4, 6.8 Hz, 4H), 6.91 (dd, *J* = 2.4, 6.8 Hz, 4H), 6.25 (d, *J* = 4.4 Hz, 1H), 3.81 (s, 6H); ^{13}C NMR (CD$_2$Cl$_2$, 100 MHz) δ 188.5, 164.5, 164.2, 158.8, 158.1, 139.7, 133.9, 127.4, 126.9, 124.7, 115.3, 111.3, 56.1; HRMS (*m/z*, FAB^{+}) calcd. for $C_{23}H_{19}N_3O_3S$ 417.1147, found 417.1144.

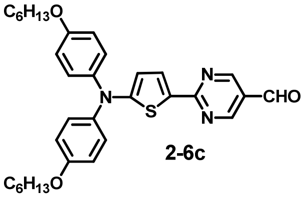

2-6c

2-[5-*N*,*N*-bis(4-hexyloxyphenyl)aminothiophen-2-yl]-pyrimidine-5-carbaldehyde (2-6c). The synthetic procedure was similar to that of **2-6a**, except that the eluent used for column purification was dichloromethane. **2-6c** was isolated as an orange solid (54%), mp 93–95 °C; IR (KBr) ν 3046, 2951, 2854, 2722, 1691, 1587, 1542, 1238, 1067, 831 cm^{-1}; ^{1}H NMR (CD$_2$Cl$_2$, 400 MHz) δ 9.88 (s, 1H), 8.83 (s, 2H), 7.83 (d, *J* = 4.4 Hz, 1H), 7.24 (dd, *J* = 2.0, 6.8 Hz, 4H), 6.89 (dd, *J* = 2.0, 6.8 Hz, 4H), 6.23 (d, *J* = 4.4 Hz, 1H), 3.96 (t, *J* = 6.8 Hz, 4H), 1.78 (m, 4H), 1.47 (m, 4H), 1.37 (m, 8H), 0.93 (t, *J* = 6.8 Hz, 6H); ^{13}C NMR (CD$_2$Cl$_2$, 100 MHz) δ 188.5, 164.5, 164.4, 158.8, 157.7, 139.5, 133.9, 127.4, 126.7, 124.6, 115.8, 111.1, 68.9, 32.2, 29.8, 26.3, 23.3, 14.5; HRMS (*m/z*, FAB^{+}) calcd. for $C_{33}H_{39}N_3O_3S$ 557.2712, found 557.2714.

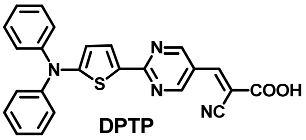
DPTP

2-Cyano-3-[2-(5-*N*,*N*-diphenylaminothiophen-2-yl)-pyrimidin-5-yl] acrylic acid (DPTP). A mixture of **2-6a** (100 mg, 0.28 mmol), cyanoacetic acid (71 mg, 0.84 mmol), and ammonium acetate (14 mg) in glacial acetic acid (5 mL) was stirred and heated at 80 °C for 12 h. After the reaction mixture was cooled to room temperature, the resulting precipitate was collected by filtration and thoroughly washed with water, methanol, and hexane to afford **DPTP** as a black solid (80 mg, 67%), mp 233–235 °C; IR (KBr) ν 3032, 2928, 2229, 1687, 1585, 1491, 1247, 1083, 858 cm^{-1}; ^{1}H NMR (DMSO-d_6, 400 MHz) δ 9.15 (s, 2H), 8.26 (s, 1H), 7.85 (d, *J* = 4.0 Hz, 1H), 7.43 (t, *J* = 7.6 Hz, 4H), 7.30 (d, *J* = 7.6 Hz, 4H), 7.24 (t, *J* = 7.6 Hz, 2H), 6.44 (d, *J* = 4.0 Hz, 1H); ^{13}C NMR (DMSO-d_6, 100 MHz) δ 162.8, 161.4, 160.2, 158.5, 148.3, 146.0, 132.4, 129.9, 128.6, 125.7, 124.9, 121.7, 116.2, 114.4, 104.1; HRMS (*m/z*, FAB$^+$) calcd. for $C_{24}H_{16}N_4O_2S$ 424.0994, found 424.1004.

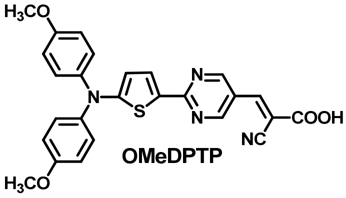
OMeDPTP

2-Cyano-3-{2-[5-*N*,*N*-bis(4-methoxyphenyl)aminothiophen-2-yl]-pyrimidin-5-yl} acrylic acid (OMeDPTP). The synthetic procedure was similar to that of **DPTP**. **OMeDPTP** was synthesized as a black solid (62%), mp 236–238 °C; IR (KBr) ν 3106, 3005, 2927, 2833, 2217, 1713, 1589, 1545, 1076, 860 cm^{-1}; ^{1}H NMR (DMSO-d_6, 400 MHz) δ 9.10 (s, 2H), 8.22 (s, 1H), 7.79 (d, *J* = 4.0 Hz, 1H), 7.32 (d, *J* = 8.8 Hz, 4H), 7.00 (d, *J* = 8.8 Hz, 4H), 6.13 (d, *J* = 4.0 Hz, 1H), 3.78 (s, 6H); ^{13}C NMR (DMSO-d_6, 100 MHz) δ 163.3, 163.0, 161.6, 158.6, 157.5, 148.5, 138.7, 133.4, 127.3, 125.6, 120.9, 116.4, 115.1, 109.9, 102.8, 55.4; HRMS (*m/z*, FAB$^+$) calcd. for $C_{26}H_{20}N_4O_4S$ 484.1205, found 484.1209.

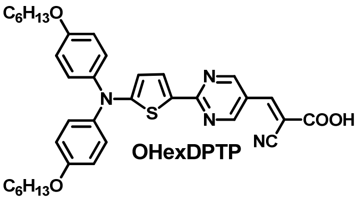

OHexDPTP

2-Cyano-3-{2-[5-*N*,*N*-bis(4-hexyloxyphenyl)aminothiophen-2-yl]-pyrimidin-5-yl} acrylic acid (OHexDPTP). The synthetic procedure was similar to that of **DPTP**. **OHexDPTP** was synthesized as a black solid (86%), mp 142–144 °C; IR (KBr) ν 3067, 2953, 2857, 2226, 1693, 1584, 1537, 1213, 1009, 852 cm^{-1}; ^{1}H NMR (CD_2Cl_2, 400 MHz) δ 9.05 (s, 2H), 8.08 (s, 1H), 7.88 (d, *J* = 4.4 Hz, 1H), 7.25 (d, *J* = 8.8 Hz, 4H), 6.90 (d, *J* = 8.8 Hz, 4H), 6.25 (d, *J* = 4.4 Hz, 1H), 3.96 (t, *J* = 6.4 Hz, 4H), 1.77 (m, 4H), 1.47 (m, 4H), 1.36 (m, 8H), 0.92 (t, *J* = 6.4 Hz, 6H); ^{13}C NMR (CD_2Cl_2, 100 MHz) δ 165.7, 163.2, 159.5, 158.2, 150.1, 139.5, 135.1, 127.7, 126.5, 120.7, 116.1, 111.7, 101.1, 69.0, 32.2, 29.8, 26.3, 23.2, 14.4; HRMS (*m/z*, FAB$^+$) calcd. for $C_{36}H_{40}N_4O_4S$ 624.2770, found 624.2769.

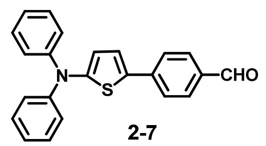

2-7

4-(5-*N*,*N*-diphenylaminothiophen-2-yl)-benzaldehyde (2-7). A mixture of 5-(*N*,*N*-diphenylamino)-2-(tri-*n*-butylstannyl)thiophene (5.40 g, 10.0 mmol), 4-bromobenzaldehyde (1.48 g, 8.0 mmol), and $PdCl_2(PPh_3)_2$ (281 mg, 0.4 mmol) in anhydrous THF (50 mL) was stirred and heated to reflux under argon for 1.5 h. After the reaction mixture was cooled to room temperature, the solvent was removed by rotary evaporation, and the crude product was purified by column chromatography on silica gel with dichloromethane/hexane (v/v, 1:2) as eluent to afford **2-7** as a yellow solid (2.5 g, 88%), mp 122–124 °C; IR (KBr) ν 3061, 3033, 2820, 2734, 1692, 1592, 1503, 1299, 1159, 1061, 825 cm^{-1}; ^{1}H NMR (DMSO-d_6, 400 MHz) δ 9.93 (s, 1H), 7.85 (d, *J* = 8.4 Hz, 2H), 7.73 (d, *J* = 8.4 Hz, 2H), 7.55 (d, *J* = 4.0 Hz, 1H), 7.34 (t, *J* = 7.6 Hz, 4H), 7.14–7.09 (m, 6H), 6.67 (d, *J* = 4.0 Hz, 1H); ^{13}C NMR (CDCl$_3$, 100 MHz) δ 191.1, 153.7, 147.2, 140.2, 134.3, 134.2, 130.3, 129.2, 124.7, 124.1, 123.7, 123.2, 119.9; HRMS (*m/z*, FAB$^+$) calcd. for $C_{23}H_{17}NOS$ 355.1031, found 355.1028.

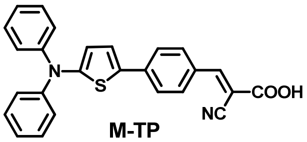

M-TP

2-Cyano-3-[4-(5-*N*,*N*-diphenylaminothiophen-2-yl)-phenyl] acrylic acid (M-TP). The synthetic procedure was similar to that of **DPTP**. **M-TP** was synthesized as a dark red solid (28%), mp 223–225 °C; IR (KBr) ν 3063, 3042, 2228, 1688, 1592, 1504, 1462, 1270, 1184, 1054, 937 cm^{-1}; ^{1}H NMR (DMSO-d_6, 400 MHz) δ 8.26 (s, 1H), 8.02 (d, *J* = 8.4 Hz, 2H), 7.73 (d, *J* = 8.4 Hz, 2H), 7.58 (d, *J* = 4.0 Hz, 1H), 7.35 (t, *J* = 7.6 Hz, 4H), 7.15–7.10 (m, 6H), 6.68 (d, *J* = 4.0 Hz, 1H); ^{13}C NMR (DMSO-d_6, 100 MHz) δ 163.5, 153.3, 153.0, 146.8, 138.2, 133.8, 131.6, 129.7, 129.6, 125.6, 124.7, 124.0, 123.0, 120.2, 116.5, 102.0; HRMS (*m/z*, FAB$^+$) calcd. for $C_{26}H_{18}N_2O_2S$ 422.1089, found 422.1086.

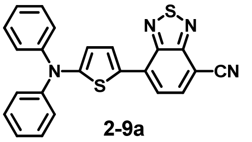

2-9a

[5-(7-Cyano-2,1,3-benzothiadiazol-4-yl)-thiophen-2-yl]-*N*,*N*-diphenylamine

(2-9a). A mixture of 5-(*N*,*N*-diphenylamino)-2-(tri-*n*-butylstannyl)thiophene (10.80 g, 20 mmol), 4,7-dibromo-2,1,3-benzothiadiazole (5.88 g, 20 mmol), and $PdCl_2(PPh_3)_2$ (281 mg, 0.4 mmol) in anhydrous *N*,*N*-dimethylformamide (30 mL) was stirred and heated at 80 °C under an argon atmosphere overnight. After being cooled to room temperature, the reaction mixture was poured into methanol. The resulting precipitate was filtered, washed with methanol, and dried. The crude product mixture consisting of **2-8a** and the disubstituted byproduct was used for the next step without further separation. A mixture of the crude product mixture and copper cyanide (4.48 g, 50 mmol) in *N*,*N*-dimethylformamide (108 mL) was stirred and heated to reflux overnight. The cooled reaction mixture was added into an icy solution of concentrated HCl (12 mL, 12 N), iron (III) chloride (21.87 g), and water (122 mL). The mixture was then heated at 70 °C for 0.5 h, after which time the mixture was extracted with toluene and water. The combined extracts were washed with brine, dried over anhydrous magnesium sulfate, and filtered. The solvent of the filtrate was removed by rotary evaporation, and the crude product was purified by column chromatography on silica gel with dichloromethane/hexane (v/v, 1:1) as eluent to afford **2-9a** as a black solid (2.82 g, 34%), mp 220–222 °C; IR (KBr) ν 3037, 2224, 1584, 1531, 1492, 1461, 1370, 1206, 1054, 898 cm^{-1}; ^1H NMR ($CDCl_3$, 400 MHz) δ 8.15 (d, *J* = 4.0 Hz, 1H), 7.91 (d, *J* = 7.6 Hz, 1H), 7.59 (d, *J* = 7.6 Hz, 1H), 7.37–7.33 (m, 4H), 7.27 (d, *J* = 7.2 Hz, 4H), 7.16 (t, *J* = 7.2 Hz, 2H), 6.64 (d, *J* = 4.0 Hz, 1H); ^{13}C NMR ($CDCl_3$, 100 MHz) δ 157.5, 153.7, 151.0, 146.8, 135.9, 132.6, 131.0, 129.4, 127.7, 124.6, 124.2, 121.2, 117.2, 116.0, 100.7; HRMS (*m/z*, FAB^+) calcd for $C_{23}H_{14}N_4S_2$ 410.0660, found 410.0657.

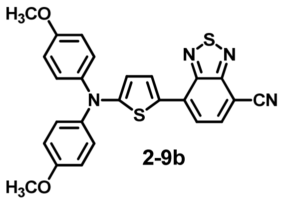

2-9b

[5-(7-Cyano-2,1,3-benzothiadiazol-4-yl)-thiophen-2-yl]-*N*,*N*-bis(4-methoxyphenyl)amine (2-9b). The synthetic procedure was similar to that of **2-9a**, except that the eluent for column purification was dichloromethane/hexane (v/v, 2:1). **2-9b** was isolated as a black solid (29%), mp 156–158 °C; IR (KBr) ν 3040, 2929, 2831, 2225, 1605, 1567, 1541, 1421, 1354, 1241, 1170, 1036, 829 $\mathrm{cm^{-1}}$; ^{1}H NMR ($\mathrm{CDCl_3}$, 400 MHz) δ 8.11 (d, J = 4.4 Hz, 1H), 7.84 (d, J = 7.6 Hz, 1H), 7.46 (d, J = 7.6 Hz, 1H), 7.24 (d, J = 8.8 Hz, 4H), 6.90 (d, J = 8.8 Hz, 4H), 6.37 (d, J = 4.4 Hz, 1H), 3.83 (s, 6 H); ^{13}C NMR ($\mathrm{CDCl_3}$, 100 MHz) δ 159.9, 157.0, 153.8, 150.9, 139.7, 135.9, 132.8, 131.8, 126.3, 124.6, 120.2, 116.2, 114.8, 112.4, 99.4, 55.6, 55.5; HRMS (*m/z*, FAB$^+$) calcd for $\mathrm{C_{25}H_{18}N_4O_2S_2}$ 470.0871, found 470.0868.

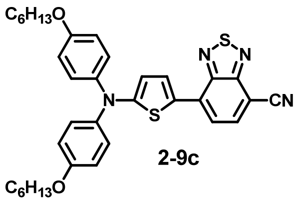

2-9c

[5-(7-Cyano-2,1,3-benzothiadiazol-4-yl)-thiophen-2-yl]-*N*,*N*-bis(4-hexyloxyphenyl)amine (2-9c). The synthetic procedure was similar to that of **2-9a**. The crude product was purified by column chromatography on silica gel twice using dichloromethane/hexane (v/v, 1:1) and then ethyl acetate/hexane (v/v, 1:12) as eluent to afford **2-9c** as a black solid (34%), mp 107–109 °C; IR (KBr) ν 3043, 2957, 2854, 2222, 1605, 1543, 1470, 1352, 1233, 1178, 1025, 835 $\mathrm{cm^{-1}}$; ^{1}H NMR ($\mathrm{CDCl_3}$, 400 MHz) δ 8.11 (d, J = 4.4 Hz, 1H), 7.83 (d, J = 8.0 Hz, 1H), 7.44 (d, J = 8.0 Hz, 1H), 7.23 (dd, J =

2.4, 7.2 Hz, 4H), 6.88 (dd, $J = 2.4, 7.2$ Hz, 4H), 6.36 (d, $J = 4.4$ Hz, 1H), 3.96 (t, $J = 6.8$ Hz, 4H), 1.82–1.78 (m, 4H), 1.50–1.46 (m, 4H), 1.39–1.34 (m, 8H), 0.95–0.91 (m, 6H); ^{13}C NMR ($CDCl_3$, 100 MHz) δ 160.1, 156.6, 153.7, 150.8, 139.4, 135.8, 132.8, 131.9, 126.3, 124.2, 119.9, 116.2, 115.2, 112.1, 99.1, 68.2, 31.6, 29.3, 25.8, 22.7, 14.1; HRMS (*m/z*, FAB$^+$) calcd for $C_{35}H_{38}N_4O_2S_2$ 610.2436, found 610.2435.

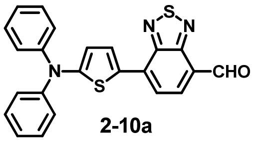

2-10a

7-(5-*N*,*N*-diphenylaminothiophen-2-yl)-2,1,3-benzothiadiazole-4-carbaldehyde (2-10a). To a stirring solution of **2-9a** (616 mg, 1.5 mmol) in anhydrous THF (30 mL) was added dropwise diisopropylaluminum hydride solution (1M in THF, 3.75 mL, 3.75 mmol) at 0 °C under an argon atmosphere. After being stirred at this temperature for 2 h, the reaction was quenched with saturated aqueous ammonium chloride solution (15 mL), and the cooling bath was removed. After being stirred at ambient temperature for another 1 h, the reaction mixture was poured into water and extracted with ethyl acetate. The combined extracts were washed with brine, dried over anhydrous magnesium sulfate, and filtered. The solvent of the filtrate was removed by rotary evaporation, and the crude product was purified by column chromatography on silica gel with dichloromethane/hexane (v/v, 2:1) as eluent to afford **2-10a** as a black solid (200 mg, 32%), mp 175–177 °C; IR (KBr) ν 3035, 2839, 2729, 1690, 1587, 1537, 1490, 1369, 1265, 1154, 1058, 837 cm^{-1}; ^{1}H NMR ($CDCl_3$, 400 MHz) δ 10.59 (s, 1H), 8.16 (d, $J =$ 4.0 Hz, 1H), 8.09 (d, $J = 7.6$ Hz, 1H), 7.68 (d, $J = 7.6$ Hz, 1H), 7.34–7.30 (m, 4H), 7.26–7.23 (m, 4H), 7.15–7.11 (m, 2H), 6.63 (d, $J = 4.0$ Hz, 1H); ^{13}C NMR ($CDCl_3$, 100 MHz) δ 188.1, 157.4, 153.6, 151.9, 146.8, 133.3, 133.0, 130.9, 129.4, 128.4, 124.6, 124.2, 123.9, 121.6, 117.3; HRMS (*m/z*, FAB$^+$) calcd for $C_{23}H_{15}N_3OS_2$ 413.0657, found 413.0658.

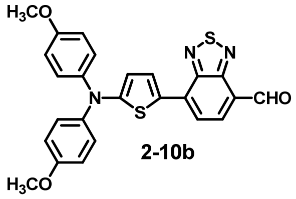
2-10b

7-[5-*N*,*N*-bis(4-methoxyphenyl)aminothiophen-2-yl]-2,1,3-benzothiadiazole-4-carbaldehyde (2-10b). The synthetic procedure was similar to that of **2-10a**. The crude product was purified by column chromatography on silica gel twice using ethyl acetate/toluene (v/v, 1:40) and then ethyl acetate/hexane (v/v, 1:3) as eluent to afford **2-10b** as a black solid (37%), mp 150–152 °C; IR (KBr) ν 3070, 2960, 2837, 1665, 1604, 1546, 1418, 1349, 1235, 1182, 1008, 840 cm^{-1}; ^{1}H NMR ($CDCl_3$, 400 MHz) δ 10.55 (s, 1H), 8.15 (d, *J* = 4.4 Hz, 1H), 8.04 (d, *J* = 8.0 Hz, 1H), 7.56 (d, *J* = 8.0 Hz, 1H), 7.24 (dd, *J* = 2.4, 6.8 Hz, 4H), 6.90 (dd, *J* = 2.4, 6.8 Hz, 4H), 6.38 (d, *J* = 4.4 Hz, 1H), 3.83 (s, 6 H); ^{13}C NMR ($CDCl_3$, 100 MHz) δ 187.9, 160.0, 157.0, 153.7, 151.8, 139.7, 133.7, 133.3, 131.9, 126.3, 125.3, 123.1, 120.5, 114.7, 112.6, 55.5; HRMS (*m/z*, FAB$^+$) calcd for $C_{25}H_{19}N_3O_3S_2$ 473.0868, found 473.0875.

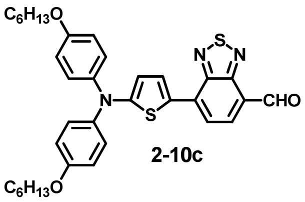
2-10c

7-[5-*N*,*N*-bis(4-hexyloxypheny)aminothiophen-2-yl]-2,1,3-benzothiadiazole-4-carbaldehyde (2-10c). The synthetic procedure was similar to that of **2-10a**, except that the eluent for column purification was toluene. **2-10c** was isolated as a black solid

(24%), mp 106–108 °C; IR (KBr) ν 3066, 2956, 2854, 1673, 1605, 1538, 1435, 1346, 1239, 1179, 1051, 832 cm^{-1}; ^{1}H NMR (CD_2Cl_2, 400 MHz) δ 10.57 (s, 1H), 8.13 (d, *J* = 4.4 Hz, 1H), 8.05 (d, *J* = 7.6 Hz, 1H), 7.62 (d, *J* = 7.6 Hz, 1H), 7.23 (d, *J* = 8.8 Hz, 4H), 6.90 (d, *J* = 8.8 Hz, 4H), 6.36 (d, *J* = 4.4 Hz, 1H), 3.97 (t, *J* = 6.4 Hz, 4H), 1.83–1.76 (m, 4H), 1.50–1.45 (m, 4H), 1.38–1.36 (m, 8H), 0.93 (t, *J* = 6.8 Hz, 6H); ^{13}C NMR ($CDCl_3$, 100 MHz) δ 187.9, 160.2, 156.6, 153.7, 151.8, 139.5, 133.7, 133.3, 132.0, 126.3, 125.1, 123.2, 120.4, 115.2, 112.4, 68.3, 31.7, 29.3, 25.8, 22.7, 14.2; HRMS (*m/z*, FAB$^+$) calcd for $C_{35}H_{39}N_3O_3S_2$ 613.2433, found 613.2432.

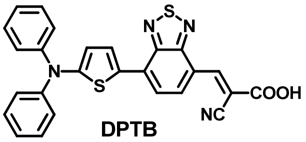

DPTB

2-Cyano-3-[7-(5-*N*,*N*-diphenylaminothiophen-2-yl)-2,1,3-benzothiadiazol-4-yl] acrylic acid (DPTB). A mixture of **2-10a** (207 mg, 0.5 mmol), cyanoacetic acid (128 mg, 1.5 mmol), and ammonium acetate (27 mg) in glacial acetic acid (9 mL) was stirred and heated at 80 °C for 2 h. After the reaction mixture was cooled to room temperature, the resulting precipitate was collected by filtration and thoroughly washed with water, methanol, and hexane to afford **DPTB** as a black solid (225 mg, 94%), mp 255–257 °C; IR (KBr) ν 3023, 2225, 1694, 1588, 1533, 1490, 1377, 1235, 1153, 1053, 904, 812 cm^{-1}; ^{1}H NMR (Acetone-d_6, 400 MHz) δ 9.13 (s, 1H), 8.77 (d, *J* = 8.0 Hz, 1H), 8.23 (d, *J* = 4.4 Hz, 1H), 8.04 (d, *J* = 8.0 Hz, 1H), 7.41 (t, *J* = 8.0 Hz, 4H), 7.31–7.29 (m, 4H), 7.21 (t, *J* = 7.2 Hz, 2H), 6.66 (d, *J* = 4.4 Hz, 1H); ^{13}C NMR (DMSO-d_6, 100 MHz) δ 163.3, 158.0, 154.3, 150.2, 146.5, 146.1, 131.1, 130.5, 130.0, 129.8, 127.5, 125.0, 124.2, 122.5, 120.1, 116.5, 102.5; HRMS (*m/z*, FAB$^+$) calcd for $C_{26}H_{16}N_4O_2S_2$ 480.0715, found 480.0712.

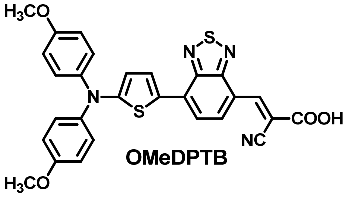

2-Cyano-3-{7-[5-*N*,*N*-bis(4-methoxyphenyl)aminothiophen-2-yl]-2,1,3-benzothiadiazol-4-yl} acrylic acid (OMeDPTB). The synthetic procedure was similar to that of **DPTB**. **OMeDPTB** was synthesized as a black solid (80%), mp 235–237 °C; IR (KBr) ν 3047, 2951, 2219, 1693, 1582, 1536, 1454, 1324, 1213, 1149, 1070, 817 cm^{-1}; ^{1}H NMR (DMSO-d_6, 400 MHz) δ 8.92 (s, 1H), 8.61 (d, *J* = 8.0 Hz, 1H), 8.14 (d, *J* = 4.4 Hz, 1H), 8.00 (d, *J* = 8.0 Hz, 1H), 7.29 (d, *J* = 8.8 Hz, 4H), 7.00 (d, *J* = 8.8 Hz, 4H), 6.30 (d, *J* = 4.4 Hz, 1H), 3.78 (s, 6 H); ^{13}C NMR (DMSO-d_6, 100 MHz) δ 163.6, 161.4, 157.2, 154.5, 150.0, 146.0, 139.2, 131.7, 130.0, 126.9, 124.1, 121.1, 118.8, 116.7, 115.1, 111.0, 101.0, 55.3; HRMS (*m/z*, FAB^{+}) calcd for $C_{28}H_{20}N_4O_4S_2$ 540.0926, found 540.0933.

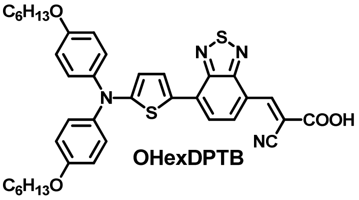

2-Cyano-3-{7-[5-*N*,*N*-bis(4-hexyloxypheny)aminothiophen-2-yl]-2,1,3-benzothiadiazol-4-yl} acrylic acid (OHexDPTB). The synthetic procedure was similar to that of **DPTB**. **OHexDPTB** was synthesized as a black solid (90%), mp 152–154 °C; IR (KBr) ν 3058, 2928, 2860, 2219, 1692, 1579, 1534, 1439, 1349, 1228, 1061, 828 cm^{-1}; ^{1}H NMR (CD_2Cl_2, 400 MHz) δ 9.05 (s, 1H), 8.66 (d, *J* = 8.4 Hz, 1H), 8.08 (d, *J* = 4.0 Hz, 1H), 7.55 (d, *J* = 8.4 Hz, 1H), 7.22 (d, *J* = 8.8 Hz, 4H), 6.90 (d, *J* = 8.8 Hz, 4H), 6.32 (d, *J* = 4.0 Hz, 1H), 3.97 (t, *J* = 6.4 Hz, 4H), 1.83–1.76 (m, 4H), 1.48 (m, 4H), 1.38–1.36 (m, 8H), 0.93 (t, *J* = 6.8 Hz, 6H); ^{13}C NMR (CD_2Cl_2, 100 MHz) δ 162.5, 157.9, 156.0, 151.5, 148.7, 140.0, 133.8, 133.1, 131.8, 127.4, 125.6, 121.4, 119.6, 117.0, 116.0, 112.5, 69.0, 32.2, 29.8, 26.3, 23.2, 14.4; HRMS (*m/z*, FAB$^+$) calcd for $C_{38}H_{40}N_4O_4S_2$ 680.2491, found 680.2491.

Measurement of Electronic Absorption Spectra of Organic Dyes in solutions. Electronic absorption spectra of organic dyes in solutions were recorded with a spectrophotometer (JASCO V-670).

Measurement of Electronic Absorption Spectra of Dye-Loaded Nanoporous TiO_2 films. A 7-μm-thick transparent porous TiO_2 nanoparticle layer (adopting 20-nm anatase TiO_2 nanoparticles) was coated on a glass plate by the doctor-blade method. After being sintered at 500 °C for 30 min, the TiO_2 film was immersed into a dye solution (0.5 mM) at room temperature for 24 h. The electronic absorption spectrum of the dye-loaded TiO_2 film was then recorded on a spectrophotometer.

Solvent Effect Measurement. The absorption spectra of **DPTP** were measured in different organic solvents while maintaining the concentration of the dye solutions below 1×10^{-5} M.

Theoretical Calculations. Density functional theory (DFT) calculations were conducted by using the hybrid B3LYP function for geometry optimization. The molecular orbital levels of HOMO and LUMO were achieved with the 6-31G(d) basis set implemented in the Gaussian 03 package.

Cyclic Voltammetry Measurement. The electrochemical properties of dyes were investigated by cyclic voltammetry (CV). The measurement of oxidation potentials was carried out in an anhydrous DMF or CH_2Cl_2 solution (1.0 mM) containing 0.1 M tetrabutylammonium hexafluorophosphate ($TBAPF_6$) as a supporting electrolyte, while the measurement of the reduction potentials was conducted in an anhydrous THF solution (1.0 mM) containing 0.1 M tetrabutylammonium perchlorate (TBAP) as a supporting electrolyte, purged with argon prior to conduct the experiments. A glassy carbon electrode and a platinum wire was used as the working electrode and counter electrode, respectively. All potentials were recorded versus Ag/AgCl (saturated) as a reference electrode and calibrated with the ferrocene/ferrocenium (Fc/Fc^+) redox couple. All measurements were performed at a scan rate of 100 mV s^{-1}.

Fabrication of Dye-Sensitized Solar Cells. To prepare the DSSC working electrodes, the FTO glass plates were first cleaned in a detergent solution under ultrasonication for 15 min, and then sequentially rinsed with water and ethanol. A layer of 20-nm-sized anatase TiO_2 nanoparticles as the transparent nanocrystalline layer was first coated on the FTO glass plates by the doctor-blade method. After drying the film at 120 °C, another layer of 400-nm-sized anatase TiO_2 nanoparticles was then deposited as the light-scattering layer. The resulting working electrode was composed of a 12-μm-thick (7-μm-thick for the **TPCADTS**- and **TP6CADTS**-based DSSC) transparent TiO_2 nanoparticle layer (particle size: 20 nm) and a 4-μm-thick (5-μm-thick for the **TPCADTS**- and **TP6CADTS**-based DSSC) TiO_2 scattering layer (particle size: 400 nm). The nanoporous TiO_2 electrodes were then sequentially heated at 150 °C for 10 min, at 300 °C for 10 min, at 400 °C for 10 min, and finally, at 500 °C for 30 min. After cooling, the nanoporous TiO_2 electrodes were immersed into a solution containing organic dyes (0.5 mM) or **N719** (0.5 mM) with deoxycholic acid (0.5 mM) as a co-adsorbent at room temperature for 24 h. Counter electrodes of the DSSC were prepared by depositing 40-μm-thick Pt films on the FTO glass plates by e-beam evaporation. The dye-adsorbed TiO_2 working electrode and the counter electrode were then assembled into a sealed DSSC cell with a sealant spacer between the two electrode plates. A drop of electrolyte solution was injected into the cell through a drilled hole. Finally, the hole was sealed using the sealant and a cover glass. An anti-reflection coating film was adhered to the DSSC (only for the DSSCs described in Section 2-3 and 2-4). A mask with an aperture area of 0.125 cm^2 was covered on a testing cell during photocurrent–voltage and incident monochromatic photon-to-current conversion efficiency measurements.

Photocurrent–Voltage Measurement. The photocurrent–voltage characteristics of the DSSCs were measured under illumination of AM1.5G solar light from a 300-W xenon lamp solar simulator. The incident light intensity was calibrated as 100 mW/cm^2. Photocurrent–voltage curves were obtained by applying an external bias voltage to the cell and measuring the generated photocurrent.

Incident Monochromatic Photon-to-Current Conversion Efficiency Measurement. The incident monochromatic photon-to-current conversion efficiency (IPCE) spectra were measured by using a 75-W xenon arc lamp as the light source coupled to a monochromator. The IPCE data were taken by illuminating monochromatic light on the solar cells (with a wavelength sampling interval of 10 nm) and measuring the short-circuit current density of the solar cells. The IPCE measurement was performed with a lock-in amplifier, a low speed chopper, and a bias light source under the full computer control.

Electrochemical Impedance Spectroscopy Measurement. The electrochemical impedance spectroscopy (EIS) of the cells was measured by using an impedance analyzer with a frequency range of 20 Hz to 1 MHz. In this study, during the impedance measurement, the cell was under the constant AM1.5G 100mW/cm^2 illumination. The impedance of the cell (throughout the frequency range of 20 Hz to 1 MHz) was then measured by applying a bias at the open-circuit voltage of the cell (namely, under the condition of no dc electric current) and by using an ac amplitude of 10 mV.

2-7 References

---

[1] O'Reagen, B.; Grätzel, M. *Nature* **1991,** *353,* 737.

[2] (a) Giribabu, L.; Kanaparthi, R. K.; Velkannan, V. *Chemical Record* **2012,** *12,* 306. (b) Mishra, A.; Fischer, M. K. R.; Bäuerle, P. *Angew. Chem., Int. Ed.* **2009,** *48,* 2474. (c) Yen, Y.-S.; Chou, H.-H.; Chen, Y.-C.; Hsu, C.-Y.; Lin, J. T. *J. Mater. Chem.* **2012,** *22,* 8734. (d) Clifford, J. N.; Planellsb, M.; Palomares, E. *J. Mater. Chem.* **2012,** *22,* 24195. (e) Liang, M.; Chen, J. *Chem. Soc. Rev.* **2013,** *42,* 3453.

[3] Wang, M.; Grätzel, C.; Zakeeruddin, S. M.; Grätzel, M. *Energy Environ. Sci.* **2012,** *5,* 9394.

[4] Hardin, B. E.; Snaith, H. J.; McGehee, M. D. *Nat. Photonics* **2012,** *6,* 162.

[5] (a) Nazeeruddin, M. K.; Kay, A.; Rodicio, L.; Humphry-Baker, R.; Müller, E.; Liska, P.; Vlachopoulos, N.; Grätzel, M. *J. Am. Chem. Soc.* **1993,** *115,* 6382. (b) Grätzel, M. *J. Photochem.Photobiol. A* **2004,** *164,* 3.

[6] (a) Nazeeruddin, M. K.; Splivallo, R.; Liska, P.; Comte, P.; Grätzel, M. *Chem. Commun.* **2003,** 1456. (b) Nazeeruddin, M. K.; De Angelis, F.; Fantacci, S.; Selloni, A.; Viscardi, G.; Liska, P.; Ito, S.; Takeru, B.; Grätzel, M. *J. Am. Chem. Soc.* **2005,** *127,* 16835.

[7] (a) Nazeeruddin, M. K.; Péchy, P.; Grätzel, M. *Chem. Commun.* **1997,** 1705. (b) Nazeeruddin, M. K.; Péchy, P.; Renouard, T.; Zakeeruddin, S. M.; Humphry-Baker, R.; Comte, P.; Liska, P.; Cevey, L.; Costa, E.; Shklover, V.; Spiccia, L.; Deacon, G. B.; Bignozzi, C. A.; Grätzel, M. *J. Am. Chem. Soc.* **2001,** *123,* 1613. (c) Chiba, Y.; Islam, A.; Watanabe, Y.; Komiya, R.; Koide, N.; Han, L. *Jpn. J. Appl. Phys.* **2006,** *45* (Part 2), L638.

[8] (a) Cao, Y.; Bai, Y.; Yu, Q.; Cheng, Y.; Liu, S.; Shi, D.; Gao, F.; Wang, P. *J. Phys.*

Chem. C **2009,** *113,* 6290. (b) Yu, Q.; Wang, Y.; Yi, Z.; Zu, N.; Zhang, J.; Zhang, M.; Wang, P. *ACS Nano* **2010,** *4,* 6032.

[9] Zeng, W.; Cao, Y.; Bai, Y.; Wang, Y.; Shi, Y.; Zhang, M.; Wang, F.; Pan, C.; Wang, P. *Chem. Mater.* **2010,** *22,* 1915.

[10] Yella, A.; Lee, H.-W.; Tsao, H. N.; Yi, C.; Chandiran, A. K.; Nazeeruddin, M. K.; Diau, E. W.-G.; Yeh, C.-Y.; Zakeeruddin, S. M.; Grätzel, M. *Science* **2011,** *334,* 629.

[11] Tsao, H. N.; Yi, C.; Moehl, T.; Yum, J.-H.; Zakeeruddin, S. M.; Nazeeruddin, M. K.; Grätzel, M. *ChemSusChem* **2011,** *4,* 591.

[12] Cai, N.; Moon, S.-J.; Cevey-Ha, L.; Moehl, T.; Humphry-Baker, R.; Wang, P.; Zakeeruddin, S. M.; Grätzel, M. *Nano Lett.* **2011,** *11,* 1452.

[13] (a) Shirota, Y. *J. Mater. Chem.* **2000,** *10,* 1. (b) Shirota, Y. *J. Mater. Chem.* **2005,** *15,* 75.

[14] Xu, M.; Li, R.; Pootrakulchote, N.; Shi, D.; Guo, J.; Yi, Z.; Zakeeruddin, S. M.; Grätzel, M.; Wang, P. *J. Phys. Chem. C* **2008,** *112,* 19770.

[15] Ohshita, J.; Nodono, M.; Watanabe, T.; Ueno, Y.; Kunai, A.; Harima, Y.; Yamashita, K.; Ishikawa, M. *J. Organomet. Chem.* **1998,** *553,* 487.

[16] Ohshita, J.; Nodono, M.; Kai, H.; Watanabe, T.; Kunai, A.; Komaguchi, K.; Shiotani, M.; Adachi, A.; Okita, K.; Harima,Y.; Yamashita, K.; Ishikawa, M. *Organometallics* **1999,** *18,* 1453.

[17] Yamaguchi, S.; Tamao, K. *Bull. Chem. Soc. Jpn.* **1996,** *69,* 2327.

[18] Liu, D.; Fessenden, R. W.; Hug, G. L.; Kamat, P. V. *J. Phys. Chem. B* **1997,** *101,* 2583.

[19] Khazraji, A. C.; Hotchandani, S.; Das, S.; Kamat, P. V. *J. Phys. Chem. B* **1999,** *103,* 4693.

---

[20] Ko, S.; Choi, H.; Kang, M. S.; Hwang, H.; Ji, H.; Kim, J.; Ko, J.; Kang, Y. *J. Mater. Chem.* **2010,** *20,* 2391.

[21] Wang, Z.-S.; Cui, Y.; Dan-oh, Y.; Kasada, C.; Shinpo, A.; Hara, K. *J. Phys. Chem. C* **2007,** *111,* 7224.

[22] Hao, Y.; Yang, X.; Cong, J.; Tian, H.; Hagfeldt, A.; Sun, L. *Chem. Commun.* **2009,** 4031.

[23] Klein, C.; Nazeeruddin,M. K.; Censo, D. D.; Liska, P.; Grätzel, M. *Inorg. Chem.* **2004,** *43,* 4216.

[24] (a) Hara, K.; Dan-oh, Y.; Kasada, C.; Ohga, Y.; Shinpo, A.; Suga, S.; Sayama, K.; Arakawa, H. *Langmuir* **2004,** *20,* 4205. (b) Boschloo, G.; Ha1ggman, L.; Hagfeldt, A. *J. Phys. Chem. B* **2006,** *110,* 13144.

[25] Zhang, C.; Huang, Y.; Huo, Z.; Chen, S.; Dai, S. *J. Phys. Chem. C* **2009,** *113,* 21779.

[26] (a) Andrade, L.; Zakeeruddin, S. M.; Nazeeruddin, M. K.; Ribeiro, H. A.; Mendes, A.; Grätzel, M. *ChemPhysChem* **2009,** *10,* 1117. (b) Fabregat-Santiago, F.; Bisquert, J.; Palomares, E.; Otero, L.; Kuang, D.; Zakeeruddin, S. M.; Grätzel, M. *J. Phys. Chem. C* **2007,** *111,* 6550.

[27] (a) Adachi, M.; Sakamoto, M.; Jiu, J.; Ogata, Y.; Isoda, S. *J. Phys. Chem. B* **2006,** *110,* 13872. (b) Wang, Q.; Moser, J.; Grätzel, M. *J. Phys. Chem. B* **2005,** *109,* 14945.

[28] (a) Koumura, N.; Wang, Z.-S.; Mori, S.; Miyashita, M.; Suzuki, E.; Hara, K. *J. Am. Chem. Soc.* **2006,** *128,* 14256. (b) Kim, S.; Kim, D.; Choi, H.; Kang, M. S.; Song, K.; Kang, S. O.; Ko, J. *Chem. Commun.* **2008,** 4951.

[29] (a) Zhang, G.; Bai, Y.; Li, R.; Shi, D.; Wenger, S.; Zakeeruddin, S. M.; Grätzel, M.; Wang, P. *Energy Environ. Sci.* **2009,** *2,* 92. (b) Zhang, G.; Bala, H.; Cheng, Y.; Shi, D.; Lv, X.; Yu, Q.; Wang., P. *Chem. Commun.* **2009,** 2198.

---

[30] Li, R.; Lv, X.; Shi, D.; Zhou, D.; Cheng, Y.; Zhang, G.; Wang, P. *J. Phys. Chem. C* **2009,** *113,* 7469.

[31] Liu, W.-H.; Wu, I-C.; Lai, C.-H.; Lai, C.-H.; Chou, P.-T.; Li, Y.-T.; Chen, C.-L.; Hsub, Y.-Y.; Chi, Y. *Chem. Commun.* **2008,** 5152.

[32] Tian, H.; Yang, X.; Chen, R.; Zhang, R.; Hagfeldt, A.; Sun, L. *J. Phys. Chem. C* **2008,** *112,* 11023.

[33] Chen, C.-H.; Hsu, Y.-C.; Chou, H.-H.; Thomas, K. R. J.; Lin, J. T.; Hsu, C.-P. *Chem. Eur. J.* **2010,** *16,* 3184.

[34] Velusamy, M.; Thomas, K. R. J.; Lin, J. T.; Hsu, Y.-C.; Ho, K.-C. *Org. Lett.* **2005,** *7,* 1899.

[35] (a) Wong, K.-T.; Hung, T. S.; Lin, Y.; Wu, C.-C.; Lee, G.-H.; Peng, S.-M.; Chou, C. H.; Su, Y. O. *Org. Lett.* **2002,** *4,* 513. (b) Fang, Y.-Q.; Taylor, N. J.; Hanan, G. S.; Loiseau, F.; Passalacqua, R.; Campagna, S.; Nierengarten, H.; Dorsselaer, A. V. *J. Am. Chem. Soc.* **2002,** *124,* 7912.

[36] Huang, S.-T.; Hsu, Y.-C.; Yen, Y.-S.; Chou, H. H.; Lin, J. T.; Chang, C.-W.; Hsu, C.-P.; Tsai, C.; Yin, D.-J. *J. Phys. Chem. C* **2008,** *112,* 19739.

[37] Neto, B. A. D.; Lapis, A. A. M.; da Silva Júnior, E. N.; Dupont, J. *Eur. J. Org. Chem.* **2013,** 228.

[38] (a) Kim, J.-J.; Choi, H.; Lee, J.-W.; Kang, M.-S.; Song, K.; Kang, S. O.; Ko, J. *J. Mater. Chem.* **2008,** *18,* 5223. (b) Tang, Z.-M.; Lei, T.; Jiang, K.-J.; Song, Y.-L.; Pei, J. *Chem. Asian J.* **2010,** *5,* 1911. (c) Zhu, W.; Wu, Y.; Wang, S.; Li, W.; Li, X.; Chen, J.; Wang, Z.-S.; Tian, H. *Adv. Funct. Mater.* **2011,** *21,* 756. (d) Haid, S.; Marszalek, M.; Mishra, A.; Wielopolski, M.; Teuscher, J.; Moser, J.-E.; Humphry-Baker, R.; Zakeeruddin, S. M.; Grätzel, M.; Bäuerle, P. *Adv. Funct. Mater.* **2012,** *22,* 1291. (e)

Kim, B.-G.; Zhen, C.-G.; Jeong, E. J.; Kieffer, J.; Kim, J. *Adv. Funct. Mater.* **2012,** *22,* 1606. (f) Lin, R. Y.-Y.; Lee, C.-P.; Chen, Y.-C.; Peng, J.-D.; Chu, T.-C.; Chou, H.-H.; Yang, H.-M.; Lin, J. T.; Ho, K.-C. *Chem. Commun.* **2012,** *48,* 12071.

[39] Hara, K.; Tachibana, Y.; Ohga, Y.; Shinpo, A.; Suga, S.; Sayama, K.; Sugihara, H.; Arakawa, H. *Sol. Energy Mater. Sol. Cells* **2003,** *77,* 89.

[40] Li, Z. H.; Wong, M. S. *Org. Lett.* **2006,** *8,* 1499.

[41] Qian, G.; Dai, B.; Luo, M.; Yu, D.; Zhan, J.; Zhang, Z.; Ma, D.; Wang, Z. Y. *Chem. Mater.* **2008,** *20,* 6208.

[42] Vlád, G.; Horváth, I. T. *J. Org. Chem.* **2002,** *67,* 6550.

[43] Wu, I.-Y.; Lin, J. T.; Tao, Y.-T.; Balasubramaniam, E.; Su, Y. Z.; Ko, C.-W. *Chem. Mater.* **2001,** *13,* 2626.

Chapter 3. Development of Donor Materials for Vacuum-Deposited Small-Molecule Organic Solar Cells

3-1 Introduction

Organic solar cells (OSCs) are under intensive interdisciplinary investigation in both academia and industry worldwide because of their potential to enable mass production of cost-effective and flexible solar energy conversion devices.[1] During the history of their development, small-molecule organic solar cells (SMOSCs)[2] featuring small-molecule semiconductors as donor materials have received less attention than solution-processed polymer bulk heterojunction (BHJ) solar cells due to their inferior device performance. However, SMOSCs are still of great interest to the research community because of the unique advantages of small molecules over polymers, including well-defined molecular structures, easier purification, amenability to large-scale production, and better batch-to-batch reproducibility. As such, ever-increasing research endeavors have been dedicated to developing SMOSCs over the past few years, and their efficiencies have dramatically improved within the past three years.[3]

On the other hand, one notable merit of small-molecule semiconductors is that they can be fabricated by both the two processing techniques, solution processing and vacuum deposition, as a result of their low molecular weight. Although solution processing is generally considered to be more cost-effective and more feasible for large-scale roll-to-roll production than vacuum deposition, the latter remains attractive in terms of great diversity in the selection of device architectures. Specifically, the vacuum deposition technique is not only suitable for the fabrication of the BHJ structure but also for the bilayer planar heterojunction (PHJ) and even the more advanced hybrid planar-mixed heterojunction (PMHJ)[4] structure. Moreover, the multi-junction tandem cells can also be easily prepared through vacuum deposition; these may constitute one of the promising approaches to breaking through the 10% theoretical limit for single-junction OSCs.[5] In this context, a world record PCE of 12.0% has been released for a double-junction tandem device by Heliatek GmbH.[6] This current advance has clearly demonstrated that SMOSCs can indeed compete with or even surpass their polymeric counterparts.

Some representative solution-processed molecular donors achieving PCEs in excess of 5% in simple conventional SMOSCs without any interlayers are shown in Scheme 3-1, with a maximum PCE of 7.03% for **DTS(PTTh$_2$)$_2$**,[7] 7.0%[8] (7.88% in an inverted device with a special interlayer)[9] for **p-DTS(FBTTh$_2$)$_2$**, 7.38% for **DR3TBDT**,[10] 5.2% for **BP**,[11] 5.5% for **SQ**,[12] and 5.29% for **BDT-DPP**.[13]

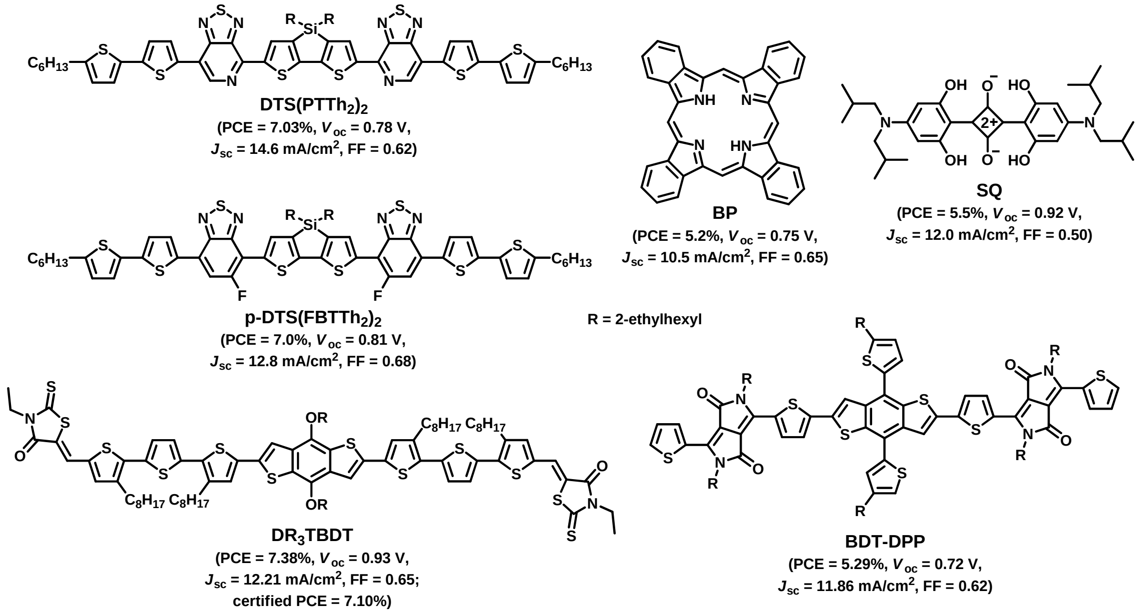

Scheme 3-1. Solution-processed molecular donors with PCEs of over 5%.

Among the p-type semiconductors employed as electron donors for the fabrication of vacuum-deposited SMOSCs, metal phthalocyanines (**MPcs**) represent the earliest and most thoroughly studied molecular donors because of their intense absorption in the red and NIR spectral regions with molar extinction coefficients as high as 2×10^5 M^{-1} cm^{-1} as well as excellent thermal and chemical stability.[14] The optoelectronic properties, molecular shape, and solid-state stacking of these two-dimensional macrocycles can be tuned by changing the metal atoms in the central cavity. In the respect, **CuPc** (Scheme 3-2) and **ZnPc** have been the most common choices due to their longer exciton diffusion length than that of other **MPcs**,[15] and PCEs of up to 5.0% (AM1.5, 120 mW/cm^2) was achieved for the **CuPc**:C_{60} PMHJ devices.[16] However, the high-lying HOMO level of **CuPc** leading to moderate V_{oc} values (generally less than 0.6V) in the corresponding devices is the main impediment to further efficiency improvement.

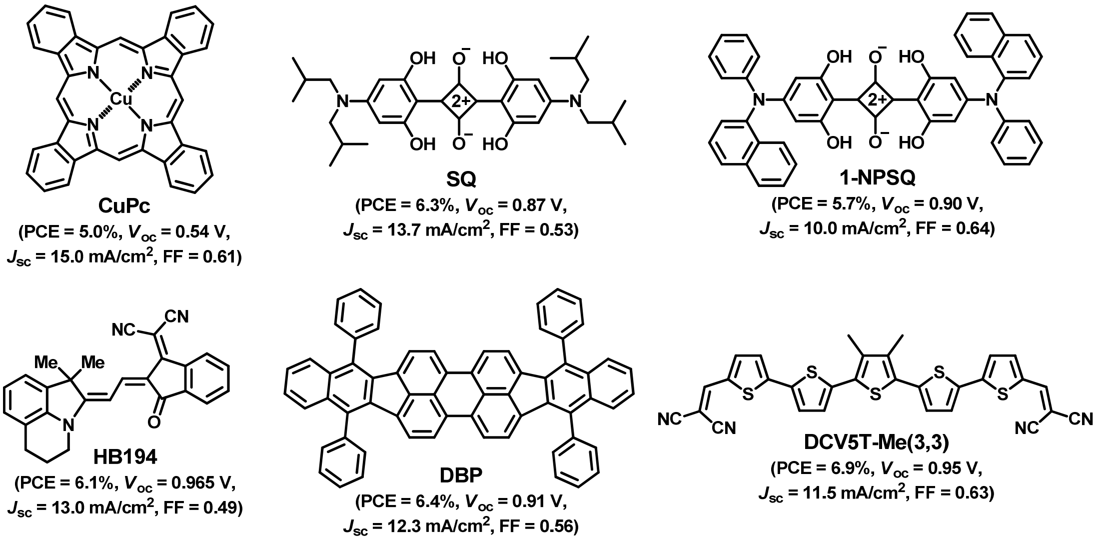

Scheme 3-2. High-performance vacuum-processed molecular donors.

Squaraine dyes that are notable for their exceptionally high molar extinction coefficients of over 10^5 M^{-1} cm^{-1} extending from the green to the NIR region have been effectively utilized as molecular donors for SMOSCs.[17] The isobutylamine-based **SQ** and the arylamine-substituted **1-NPSQ** displayed PCEs of 3.6%[17b] and 4.6%[17c], respectively, in vacuum-processed PHJ devices employing as C_{60} the acceptor. Note that the active layers were deposited by spin-coating the donor solution followed by vacuum thermal evaporation of C_{60}. After thermal annealing of the neat donor layer, the PCEs were further increased to 4.6%[17b] and 5.7%[17c] for the **SQ** and **1-NPSQ**-based cells, respectively. The superior efficiency of **1-NPSQ** was rationalized by its deeper-lying HOMO level (resulting in increased V_{oc}) and improved intermolecular stacking that facilitates hole charge transport (leading to enhanced FF)[17d–e] as compared to those of **SQ**. Recently, an even higher PCE of 6.3% was achieved for co-evaporated **SQ**:C_{70} BHJ solar cells.[18] The efficiency enhancement was due to not only stronger absorption of C_{70} relative to C_{60} but also the better light harvesting of the BHJ cells as compared to the PHJ cells that results in higher external quantum efficiencies corresponding to the absorption of **SQ**.

The class of dipolar push–pull merocyanine dyes with easily tunable optoelectronic properties has also shown promising photovoltaic performance in solution-[19] and vacuum-processed SMOSCs,[20] among which the **HB194** dye possessing a planar geometry exhibited the best PCE of 4.9% (AM1.5, 88 mW/cm^2) in vacuum-processed BHJ devices utilizing C_{60} as the acceptor.[20a] Later on, the PCE was improved to 6.1% by using MoO_3 as a hole-transporting layer instead of poly(3,4-ethylenedioxythiophene):poly(4-styrene sulfonate) (PEDOT:PSS).[20b] It is worth mentioning that **HB194** showed a high space-charge limited current mobility of 2×10^{-4} cm^2 V^{-1} s^{-1}, irrespective of its high ground-state dipole moment that is unfavorable for efficient charge transport.

Tetraphenyldibenzoperiflanthene (**DBP**) is another highly efficient donor material for vacuum-deposited SMOSCs, and a PCE of 3.6% was obtained in a simple **DBP**/C_{60} PHJ device.[21] By incorporation of the PEDOT:PSS thin film as an anodic buffer layer and the tris[4-(5-phenylthiophen-2-yl)phenyl]amine[22] layer between the **DBP** and the PEDOT:PSS layer for prevention of exciton quenching, the PCE was increased to 5.25%.[23] Later, a PCE of 6.4% was achieved for a **DBP**:C_{70} PMHJ cell.[24] This high photovoltaic performance of **DBP** was attributed to its several attractive properties including intense thin-film absorption in the red region with the longest wavelength absorption peak at 610 nm, a low-lying HOMO level of −5.5 eV (measured by CV),[21] a high space-charge limited current mobility of 10^{-4} cm^2 V^{-1} s^{-1},[23] and preferred horizontal molecular orientation in the neat film and even the blend film.[25]

The terminally dicyanovinylene-substituted oligothiophenes are among the best-studied vacuum-processed donor materials.[26] One distinctive feature of this class of materials is that they possess deep-lying HOMO energy levels and thus afford the resulting devices with extraordinary V_{oc} of ~1 V. Tailoring of the conjugation length of the oligothiophene core unit as well as the length and location of pendant alkyl side chains has enabled these active materials to demonstrate reliable PCEs. The PMHJ solar cells prepared by co-evaporation of **DCV5T-Me(3,3)** and C_{60} on heated substrates (75 °C) exhibited PCEs of up to 6.9%, which is the highest reported to date for vacuum-deposited single-junction SMOSCs.[26c]

In this chapter, eight small-molecule donor materials would be described. Their corresponding vacuum-deposited solar cell devices were fabricated and tested by the Prof. Hao-Wu Lin research group at the Department of Materials Science and Engineering, National Tsing Hua University.

3-2 A Donor–π-Bridge–Acceptor Molecular Donor Bearing a Coplanar Diphenyl-Substituted Dithienosilole as the π-Bridge

Encouraged by the promising results of the diphenyl-substituted DTS-based sensitizers that were introduced in Chapter 2, in this work, we further synthesized a D–π–A molecular donor **TPDCDTS** (Scheme 3-3) by replacing cyanoacrylic acid of **TPCADTS** with dicyanovinylene, one of the most utilized electron acceptor moiety in organic optoelectronic materials. The stronger electron-withdrawing ability of dicyanovinylene relative to cyanoacrylic acid is beneficial to lower the energy of the ICT transition, and thus the introduction of dicyanovinylene is able to endow the resulting molecules with a better light-harvesting ability. Besides, the dicyanovinylene groups are stable under vacuum sublimation conditions, a crucial prerequisite for device fabrication via vacuum thermal evaporation. On the other hand, it should be pointed out that the adoption of the diphenyl-substituted DTS as a building block to construct molecular donors provides additional advantages: (i) the HOMO level of DTS is lower than that of cyclopentadithiophene,[27] and the DTS-containing polymer possesses a lower-lying HOMO level than its carbon-bridged counterpart.[28] Therefore, the introduction of DTS can probably lower the HOMO level of the resulting molecules and in turn afford high V_{oc} values in the corresponding devices; (ii) the tetrahedral silicon center of the diphenyl-substituted DTS does not distort the coplanarity of the π-conjugated system. Instead, the C_{sp^2}–Si bond of DTS is significantly longer than the C_{sp^2}–C_{sp^3} bond of cyclopentadithiophene, allowing for more efficient π–π stacking of conjugated backbones due to the reduced steric hindrance between the pendant groups and thiophene rings.[29] It was also reported that the DTS-containing polymer shows a higher field effect hole mobility (3-fold higher) than its carbon-bridged counterpart.[30]

3-2-1 Synthesis

The synthetic rout to **TPDCDTS** is shown in Scheme 3-3. Compound **2-4a** was condensed with malononitrile to give the target compound **TPDCDTS** in 72% yield via Knöevenagel reaction in the presence of basic aluminum oxide.

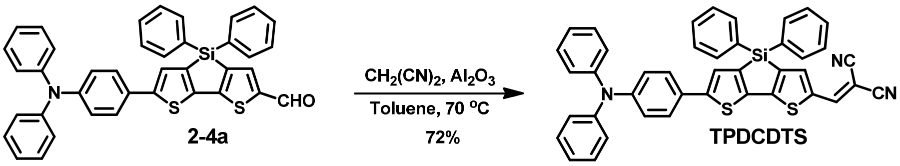

Scheme 3-3. Synthesis of **TPDCDTS**.

3-2-2 Optical Properties

The absorption spectra of **TPDCDTS** in a CH_2Cl_2 solution and as a thin film are shown in Figure 3-1. The absorption spectrum in CH_2Cl_2 showed a band centered at 537 nm (ε = 45800 M^{-1} cm^{-1}), while the thin-film absorption band exhibited a λ_{abs} = 542 nm. Compared to the solution absorption spectrum, the thin-film spectrum was red-shifted and broadened presumably due to intermolecular π–π stacking in the solid state, which benefits light harvesting.

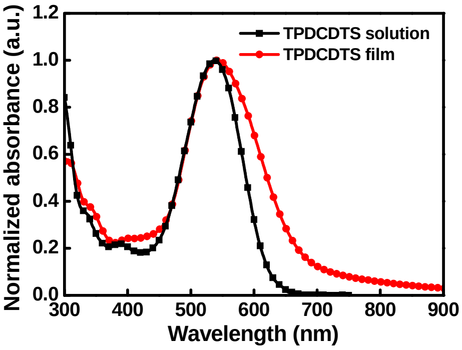

Figure 3-1. Absorption spectra of **TPDCDTS** in a CH_2Cl_2 solution and as a thin film.

Variable angle spectroscopic ellipsometry was used to study the optical constants (refractive index, *n*, and extinction coefficient, *k*) of the vacuum-deposited **TPDCDTS** thin film. As shown in Figure 3-2(a), the ordinary (*o*, in-plane or parallel) refractive index and extinction coefficient were much larger than the extraordinary (*e*, out-of-plane or perpendicular) ones, indicative of optical anisotropy. In general, for conjugated molecules with a linear π-system, the transition dipole moment of the lowest energy excited state is along their molecular backbone. Accordingly, this kind of optical anisotropy (ordinary optical constants larger than extraordinary ones) indicates that **TPDCDTS** molecules are horizontally oriented in the film deposited by thermal evaporation. This horizontal molecular orientation in films is able to increase the absorption of the normal incident light and facilitate the charge carrier transport along the vertical direction,[31] both of which are beneficial for OSCs device performance.

Figure 3-2(b) shows the optical constants of the vacuum-deposited thin films of the commonly used fullerene acceptors C_{60} and C_{70}, revealing that the extinction coefficients of C_{70} in the range of 370–700 nm are significantly larger than those of C_{60}.

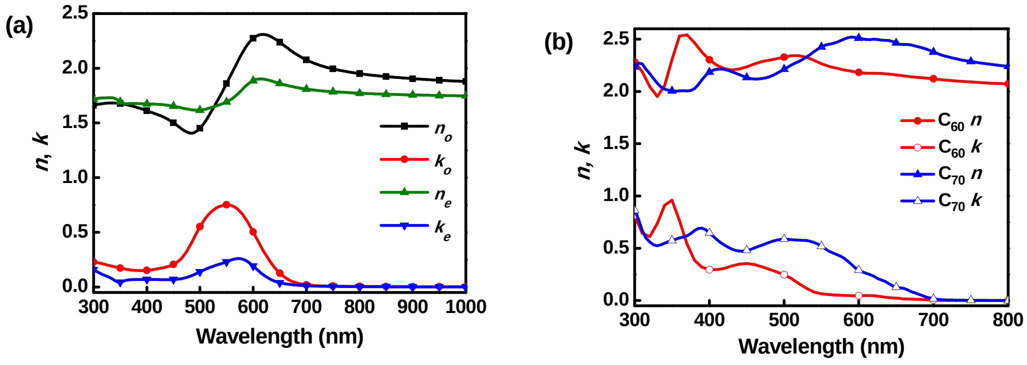

Figure 3-2. (a) Ordinary and extraordinary optical constants of **TPDCDTS** thin-film spectra. (b) Optical constants of C_{60} and C_{70} thin-film spectra.

3-2-3 Electrochemical Properties

The electrochemical characteristics of **TPDCDTS** were probed by CV. As shown in Figure 3-3, **TPDCDTS** exhibited two quasi-reversible oxidation waves with potentials at 0.43 and 0.84 V (vs Fc/Fc$^+$), respectively. The less positive oxidation wave can be attributed to the oxidation of the triphenylamine donor moiety, whereas the second oxidation wave can be assigned to the DTS core according to the previous reports on electrochemical behaviors of DTS derivatives.[32] Considering energy level shifts due to intermolecular interactions, the HOMO level of the **TPDCDTS** thin film was determined by ultraviolet photoelectron spectroscopy (UPS) to have a value of −5.40 eV. The fairly low-lying HOMO level would result in a large energy level offset to the LUMO level of fullerenes and thus relatively large V_{oc} values in the corresponding devices.

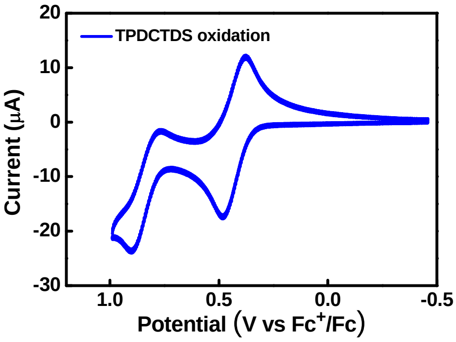

Figure 3-3. Cyclic voltammogram of **TPDCDTS** measured in a CH_2Cl_2 solution.

3-2-4 Photovoltaic Characteristics

The photovoltaic performance of **TPDCDTS** was studied in vacuum-deposited PMHJ devices, where the active layers were composed of a BHJ layer sandwiched between a homogeneous donor and acceptor layer. This kind of device architecture can provide not only efficient photon harvesting but also good photogenerated charge carrier transport to the respective electrodes. The device structures were fabricated with a configuration of ITO/hole-transporting layer (HTL)/**TPDCDTS** (3 nm)/1:1 (v/v) **TPDCDTS**:C_{60} or C_{70} (35 nm)/C_{60} (20 nm) or C_{70} (10 nm)/2,9-dimethyl-4,7-diphenyl-1,10-phenanthroline (BCP) (10 nm)/Ag (120 nm), in which the BCP thin film serves as the electron-transporting layer with an exciton blocking character. Initially, various hole-transporting materials including hexaazatriphenylenehexacarbonitrile [$HAT(CN)_6$], MoO_3, PEDOT:PSS , PEDOT:PSS/$HAT(CN)_6$, and PEDOT:PSS/MoO_3 were tested to optimize the photovoltaic performance (Figure 3-4 and Table 3-1). It was found that the devices with MoO_3 as the HTL exhibit superior performance to those based on other HTLs. Accordingly, MoO_3 was chosen as the hole-transporting material for further device fabrication.

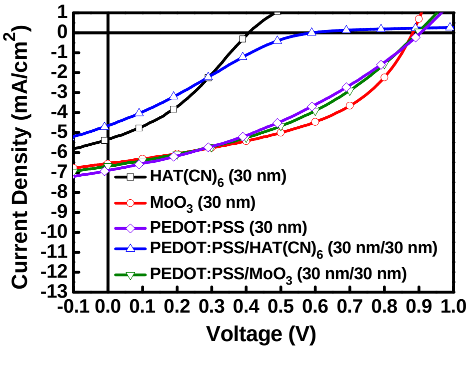

Figure 3-4. *J–V* characteristics of **TPDCDTS**:C_{60} PMHJ solar cells with different hole-transporting layers.

Table 3-1. Photovoltaic parameters of **TPDCDTS**:C_{60} PMHJ solar cells with different hole-transporting layers.

device	V_{oc} (V)	J_{sc} (mA/cm^2)	FF	PCE (%)
HAT(CN)$_6$	0.41	5.33	0.35	0.76
MoO_3	0.88	6.56	0.46	2.69
PEDOT:PSS	0.91	6.90	0.36	2.24
PEDOT:PSS/HAT(CN)$_6$	0.59	4.66	0.24	0.66
PEDOT:PSS/MoO_3	0.90	6.68	0.40	2.37

Figure 3-5(a) shows the *J–V* characteristics of **TPDCDTS**:fullerene PMHJ solar cells with MoO_3 (30 nm) as the HTL. The **TPDCDTS**:C_{60} PMHJ device gave a V_{oc} of 0.88 V, a J_{sc} of 6.56 mA/cm^2, and a FF of 0.46, yielding a PCE of 2.69% under AM 1.5 G, 1 sun (100 mW/cm^2) simulated solar illumination. Furthermore, the **TPDCDTS**:C_{70} PMHJ device delivered a higher PCE of 3.82%, with a V_{oc} of 0.83 V, J_{sc} of 9.53 mA/cm^2, FF of 0.48. Interestingly, the FF values of **TPDCDTS**:C_{60} and **TPDCDTS**:C_{70} PMHJ devices were close to each other, suggesting similar blend layer morphologies and charge carrier percolation networks in both devices.

The difference in J_{sc} between the two cells can be explained by the broader and larger extinction coefficients of C_{70} relative to C_{60} [Figure 3-2(b)], which was also reflected in the external quantum efficiency (EQE) spectra shown in Figure 3-5(b). Both devices showed high EQE values around 500–650 nm closely corresponding to the absorption of **TPDCDTS**. However, due to the stronger absorption of C_{70} in the range of 370–700 nm, the **TPDCDTS**:C_{70} PMHJ device demonstrated higher EQE values over the entire visible region, thus leading to a higher J_{sc} value.

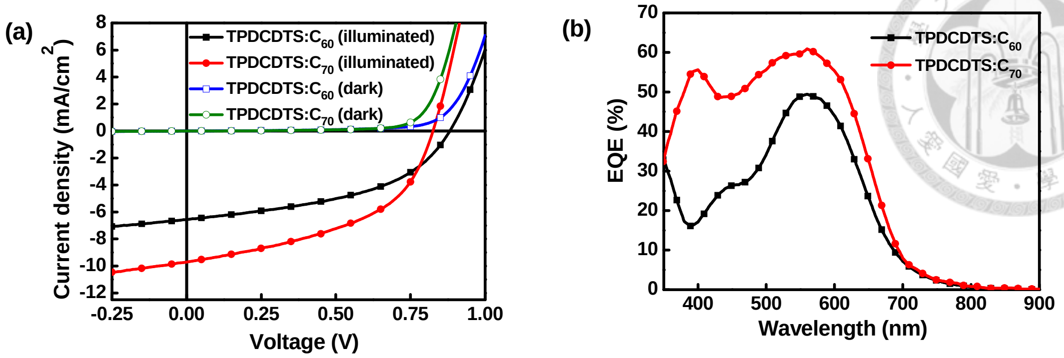

Figure 3-5. (a) *J–V* characteristics and (b) EQE spectra of **TPDCDTS**:C_{60} PMHJ (square) and **TPDCDTS**:C_{70} PMHJ (circle) solar cells.

3-3 A Donor–Acceptor–Acceptor Molecular Donor Featuring 2,1,3-Benzothiadiazole as the Bridging Acceptor

From our earlier study of DSSCs, we learned that the pyrimidine-based D–A–A sensitizer **DPTP** possesses a smaller bandgap and a lower-lying HOMO level than its D–π–A counterpart **M-TP** that adopts phenylene as the π-spacer. In addition, our study also revealed that, as compared to the previously reported D–A–π–A sensitizer **S3**, the BT-containing D–A–A sensitizer **DPTB** has both a narrower bandgap and a deeper-lying HOMO level as well, even though its effective conjugation length is shorter than that of **S3** (Scheme 3-4, Table 3-2, and Table 3-3). Consequently, we argued that such D–A–A molecules could show the potential to concurrently enhance the J_{sc} and V_{oc}, as utilized as donors for SMOSCs. On the basis of this consideration, we developed a D–A–A donor molecule **DTDCTB**, in which an electron-donating ditolylthienylamine moiety is connected to an electron-withdrawing dicyanovinylene moiety through another electron-deficient BT block (Scheme 3-5).

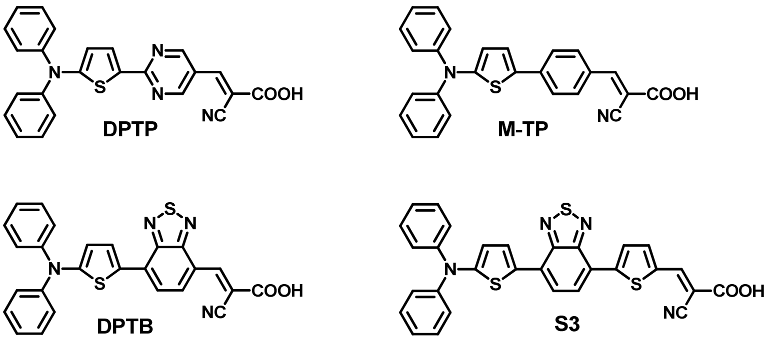

Scheme 3-4. Molecular Structures of D–A–A sensitizers and their counterparts.

Table 3-2. Photophysical and electrochemical parameters for **DPTP** and **M-TP**.

compd	molecular configuration	λ_{abs} soln (nm)[a]	HOMO (eV)[b]	LUMO (eV)[c]	ΔE (eV)[d]
DPTP	D–A–A	484	−5.26	−3.06	2.20
M-TP	D–π–A	438	−5.18	−2.86	2.32

[a]Measured in *tert*-butanol–acetonitrile (1 : 1, v/v) solutions. [b]Calculated from electrochemical measurements. [c]LUMO = HOMO + ΔE. [d]Estimated from the onset point of the absorption spectra.

Table 3-3. Photophysical and electrochemical parameters for **DPTB** and **S3**.

compd	molecular configuration	λ_{abs} soln (nm)[b]	HOMO (eV)[c]	LUMO (eV)[c]	ΔE (eV)[c]
DPTB	D–A–A	582	−5.19	−3.51	1.68
S3[a]	D–A–π–A	541	−5.12	−3.26	1.86

[a]The data were taken from the literature.[33] [b]Measured in THF solutions. [c]Calculated from electrochemical measurements.

3-3-1 Synthesis

Since the synthetic pathway toward the preparation of the BT-based sensitizers introduced in Chapter 2 was tedious and the overall chemical yield was low, we developed a new synthetic route to **DTDCTB** (Scheme 3-5). Benzylic bromination of 4-bromo-7-methyl-2,1,3-benzothiadiazole with *N*-bromosuccinimide afforded **3-1**. Silver nitrate-promoted hydrolysis of **3-1** gave aldehyde **3-2**, which was then condensed with malononitrile to give the key intermediate **3-3** via Knöevenagel reaction in the presence of basic aluminum oxide. Finally, Stille coupling of 5-(*N*,*N*-ditolylamino)-2-(tri-*n*-butylstannyl)thiophene and **3-3** yielded **DTDCTB** in good yield. It is noteworthy that this newly developed synthetic route provides a versatile method for further engineering of the molecular structure through the combination of the unsymmetrical intermediate **3-3** and other electron-donating groups.

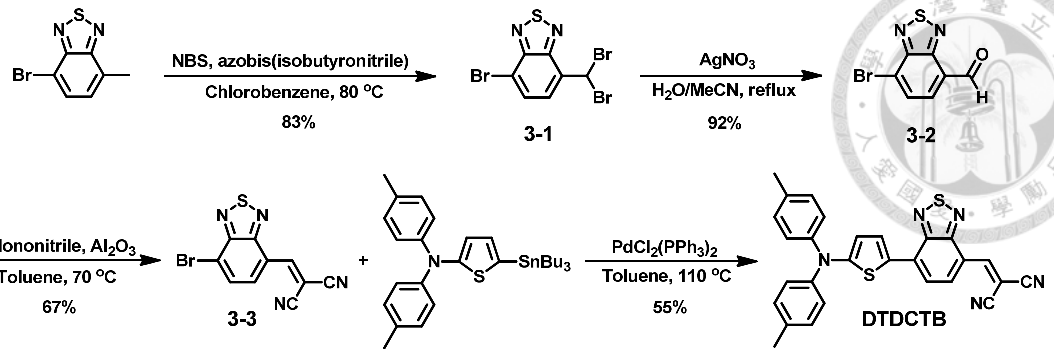

Scheme 3-5. Synthetic route to **DTDCTB**.

3-3-2 Crystal Structure and Packing

The molecular structure of **DTDCTB** was analyzed by single-crystal X-ray crystallography. As shown in Figure 3-6, **DTDCTB** displayed an almost coplanar conformation between the thiophene and BT rings with a dihedral angle of 5.5°. This coplanarity facilitates the electronic coupling between the electron-donating and electron-withdrawing blocks, enhancing the ICT efficiency and thus ensuring a distinctive bathochromic shift of the spectral responses. The highly polar nature of the heteroaryl components leads **DTDCTB** molecules to pack in an antiparallel manner and self-assemble into centrosymmetric dimers. Such a supramolecular arrangement is similar to those observed in some highly dipolar dyes reported by Würthner and Meerholz et al. and has been proposed to effectively eliminate molecular dipole moments in the solid state and, thus, avoid the large energetic disorder that is thought to be detrimental to efficient charge carrier transport.[19b–d,34] In addition, the cofacial arrangement of two neighboring BT rings with a shortest point-to-point (N1–C3) distance of 3.55 Å indicates non-negligible π–π interactions.

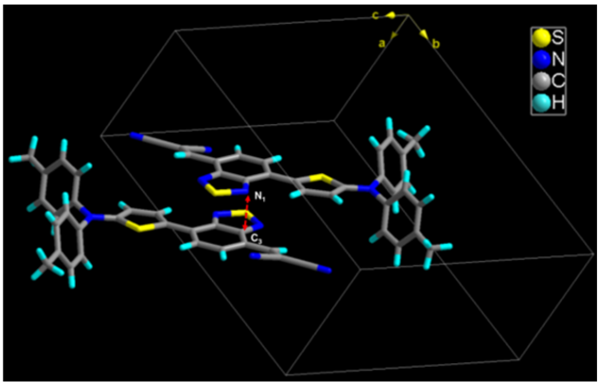

Figure 3-6. X-ray-determined molecular structure and crystal packing of **DTDCTB**.

3-3-3 Electrochemical Properties

The electrochemical properties of **DTDCTB** were probed by CV in solution. As shown in Figure 3-7, **DTDCTB** exhibited one reversible oxidation wave with a potential at 0.35 V (vs Fc/Fc^+), corresponding to oxidation of the ditolylthienylamine donor moiety. On the other hand, two reversible reduction waves at −1.09 and −1.74 V (vs Fc/Fc^+) were observed in the cathodic potential regime. The first reduction wave can be ascribed to the reduction of the dicyanovinylene block and the second to the reduction of the BT fragment. By reference to the Fc/Fc^+ redox couple, where the HOMO level of Fc is assigned to be 4.8 eV below the vacuum level, the HOMO and LUMO energy levels of **DTDCTB** were calculated to be −5.15 and −3.71 eV on the basis of the oxidation potential and the first reduction potential, respectively. In spite of the presence of the strong ditolylthienylamine donor moiety, **DTDCTB** shows a fairly low-lying HOMO level because of the strong electron-withdrawing character of the BT and dicyanovinylene blocks. Considering energy level shifts due to intermolecular interactions in the solid state, the HOMO level of the **DTDCTB** thin film was determined to be −5.30 eV by UPS.

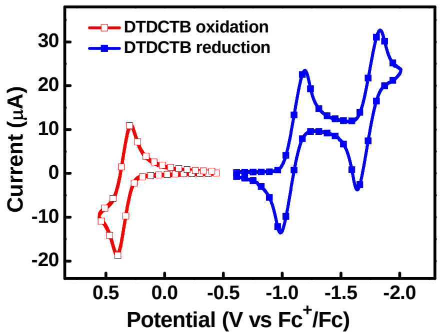

Figure 3-7. Cyclic voltammograms of **DTDCTB** in solution.

3-3-4 Optical Properties

Figure 3-8(a) shows the absorption spectra of **DTDCTB** in a CH_2Cl_2 solution and as a vacuum-deposited thin film. Surprisingly, with such a short effective conjugation length, **DTDCTB** showed an intense absorption band at λ_{abs} = 663 nm accompanied by a high ε of 41660 M^{-1} cm^{-1} in CH_2Cl_2. On the other hand, the thin-film absorption band of **DTDCTB** exhibited a red-shifted λ_{abs} = 684 nm. The significant broadening of the thin-film absorption band is possibly due to intermolecular π–π stacking as evidenced in the crystal packing. Apparently, the thin-film absorption of **DTDCTB** effectively extends the useful photon-harvesting range down to the NIR region.

Optical constants of vacuum-deposited thin films of **DTDCTB**, C_{60}, and C_{70} are shown in Figure 3-8(b). The **DTDCTB** thin film exhibited high k values across the 550–800 nm wavelength range, with $k_{max} \approx 0.95$ at λ = 670 nm, which is coincident with the absorption spectra shown in Figure 3-8(a). Notably, the k_{max} value is among the highest reported for solar-absorbing organic thin films, as compared with the commonly used polymeric donor poly(3-hexylthiophene) (**P3HT**) or molecular donor **CuPc**, which show k_{max} values of ~0.65 and ~0.95, respectively.[35,36] This result indicates that the efficient ICT gives the **DTDCTB** molecule highly polar character, which favors the formation of ultracompact absorption dipole packing in the thin film upon vacuum deposition. In addition, the *k* spectra of the commonly used acceptor molecules C_{60} and C_{70} showed complementary wavelength coverage (<550 nm) with respect to the **DTDCTB** thin film. As a result, fullerenes C_{60} and C_{70} were selected as acceptor materials to be paired with **DTDCTB** for subsequent device fabrication.

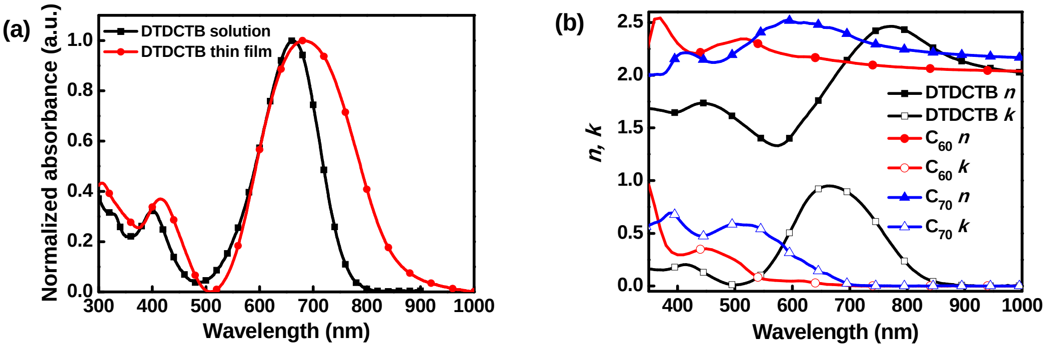

Figure 3-8. (a) Normalized absorption spectra of **DTDCTB** in CH_2Cl_2 and as a thin film. (b) Optical constants of **DTDCTB**, C_{60}, and C_{70} thin-film spectra.

3-3-5 Quantum Mechanical Calculations

To gain more insight into the electronic and optical properties of **DTDCTB**, DFT and time-dependent DFT calculations (TDDFT) were performed for the molecule in a CH_2Cl_2 solution. The distributions of the frontier molecular orbitals are similar to those described previously for the BT-based sensitizers (Figure 3-9). The first electronic transition corresponds to a charge-transfer excitation from the HOMO to the LUMO, whereas the second and third transitions may stem from two different π–π^* excitations, from the HOMO－1 to the LUMO and from the HOMO to the LUMO+1 (Table 3-4). The excitation energy of the first transition was calculated to be 1.84 eV, and its corresponding computed λ_{abs} was 673 nm that is close to the experimental results

(Figure 3-10). In addition, the high oscillator strength for this transition also coincides with the observed high extinction coefficients.

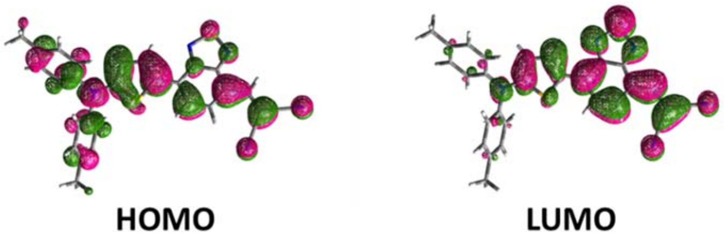

Figure 3-9. Isodensity surface plots of the HOMO and LUMO of **DTDCTB**.

Table 3-4. Calculated TDDFT vertical excitation energies (E), oscillator strengths, composition in terms of molecular orbital contributions, and transition characters for **DTDCTB**.[a]

electronic transition	E (eV, nm)	oscillator strength	composition	character
$S0 \rightarrow S1$	1.84 (673.2)	1.06	70% HOMO → LUMO	charge-transfer
$S0 \rightarrow S2$	2.74 (454.2)	0.09	42% HOMO − 1 → LUMO, 56% HOMO → LUMO+1	π–π*
$S0 \rightarrow S3$	2.92 (424.4)	0.39	56% HOMO → LUMO+1, 41% HOMO − 1 → LUMO	π–π*

[a] Within the considered energy range, we selectively calculate three transitions with moderate intensity (oscillator strength > 0.09).

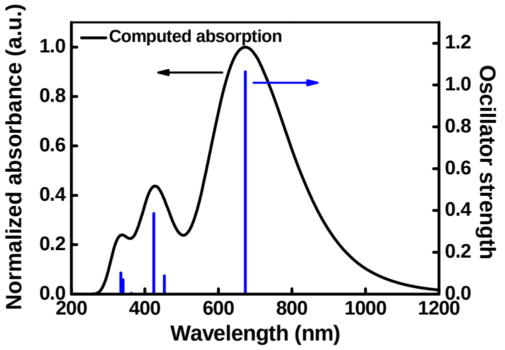

Figure 3-10. Computed absorption spectrum of **DTDCTB** in CH_2Cl_2 (oscillator strengths > 0.06).

3-3-6 Photovoltaic Characteristics

The vacuum-deposited PMHJ structure was adopted to study the photovoltaic performance of **DTDCTB**. The optimized device structures were configured as follows: Device I: ITO/MoO_3 (30 nm)/**DTDCTB** (7 nm)/1:1 (v/v) **DTDCTB**:C_{60} (40 nm)/C_{60} (20 nm)/BCP (10 nm)/Ag (150 nm). Device II: ITO/MoO_3 (5 nm)/**DTDCTB** (7 nm)/1:1 (v/v) **DTDCTB**:C_{70} (40 nm)/C_{70} (7 nm)/BCP (10 nm)/Ag (150 nm). Figure 3-11(a) shows the *J–V* characteristics of **DTDCTB**:fullerene PMHJ solar cells. The **DTDCTB**:C_{60} PMHJ device gave a V_{oc} of 0.80 V, a J_{sc} of 11.40 mA/cm^2, and a FF of 0.48, yielding a PCE of 4.41% under AM 1.5 G 1 sun (100 mW/cm^2) simulated solar illumination. Remarkably, the **DTDCTB**:C_{70} device delivered higher performance, with a V_{oc} of 0.79 V, J_{sc} of 14.68 mA/cm^2, FF of 0.50, and PCE of 5.81%. The moderate V_{oc} values (~0.8 V) of these two devices are due to the fairly low-lying HOMO level of **DTDCTB**, but still leave room for future improvement. The FF values of the **DTDCTB**:C_{60} and **DTDCTB**:C_{70} devices are similar, suggesting similar blend layer morphologies and charge carrier percolation networks in the two devices. The higher J_{sc} of the **DTDCTB**:C_{70} device can be attributed to the stronger absorption of C_{70} relative to C_{60}, which is fully consistent with the EQE spectra shown in Figure 3-11(b). The **DTDCTB**:C_{70} device showed impressively high EQE values of ~50% throughout the UV–vis to NIR region (350–770 nm), thus resulting in the high J_{sc}. It is noteworthy that the calculated J_{sc} values obtained by integrating the EQE spectra with the standard AM 1.5G solar spectrum are in good agreement with the measured J_{sc} ones (within 3–5% error).

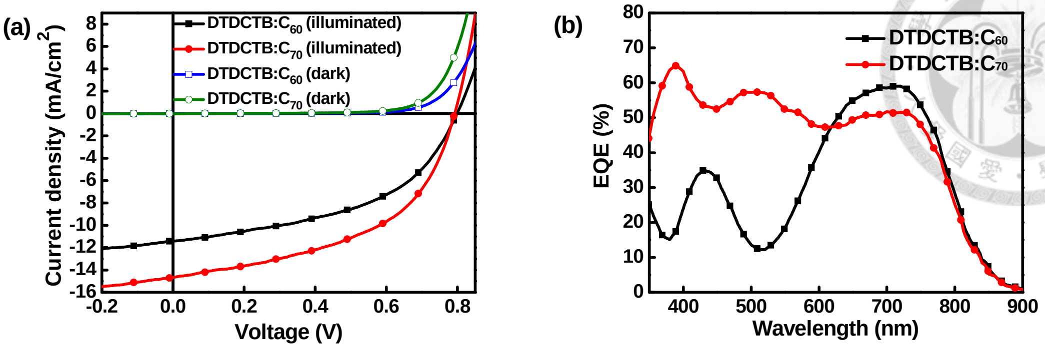

Figure 3-11. (a) *J–V* characteristics and (b) EQE spectra of **DTDCTB**:C$_{60}$ PMHJ (squares) and **DTDCTB**:C$_{70}$ PMHJ (circles) solar cells.

3-4 A Donor–Acceptor–Acceptor Molecular Donor Featuring Pyrimidine as the Bridging Acceptor

Although the vacuum-processed **DTDCTB**:C_{70} PMHJ devices had achieved a high PCE of 5.81%, the moderate V_{oc} value of -0.79 V still left room for improvement. Careful inspection of the energy levels for the D–A–A sensitizers **DPTP** and **DPTB** (Table 3-2 and Table 3-3) revealed that the HOMO level of **DPTP** is deeper than that of **DPTB**. Accordingly, we further synthesized another D–A–A donor molecule **DTDCTP**, in which the pyrimidine acceptor is employed to replace the BT block (Scheme 3-6). We envisaged that the HOMO level of **DTDCTP** would be lower than that of **DTDCTB** and thus an augmented V_{oc} value can be anticipated in the corresponding devices, even though an inevitable loss of photocurrent is foreseeable.

3-4-1 Synthesis

The synthetic pathway of **DTDCTP** is shown in Scheme 3-6. Negishi coupling of 2-[*N*,*N*-ditolylamino]thiophene with 5-bromo-2-iodopyrimidine afforded **3-4**, which was then converted to the corresponding carbaldehyde **3-5** by lithiation with *n*-butyl lithium and subsequently quenching with ethyl formate. Finally, the aldehyde **3-5** was condensed with malononitrile to yield **DTDCTP** via Knöevenagel reaction.

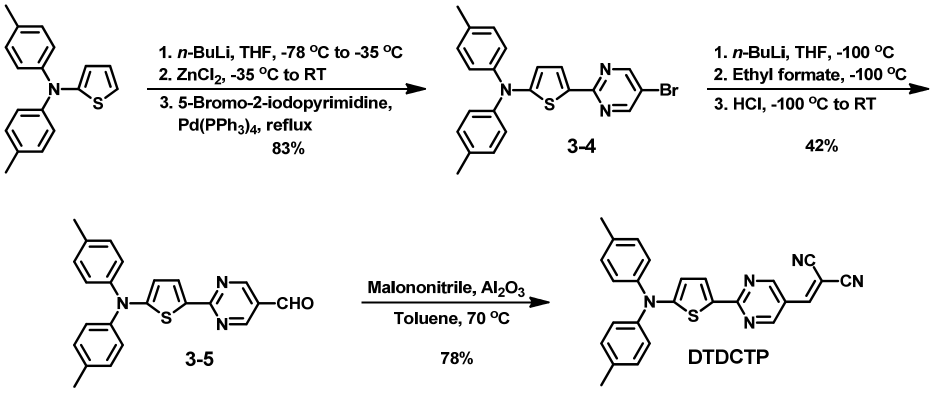

Scheme 3-6. Synthetic route to **DTDCTP**.

3-4-2 Crystal Structure and Packing

The molecular structure of **DTDCTP** was analyzed by X-ray crystallography. As shown in Figure 3-12, **DTDCTP** displayed a nearly coplanar conformation between thiophene and pyrimidine with a dihedral angle of 5.81° due to the lack of *ortho–ortho* steric interactions. This coplanarity facilitates the electronic coupling between the electron-donating and electron-withdrawing blocks, thus enhancing the ICT efficiency so as to increase the light-harvesting range. Like **DTDCTB**, the highly polar character of the heteroaryl components leads **DTDCTP** molecules to pack in an antiparallel manner and self-assemble into centrosymmetric dimers. The cofacial arrangement of two pyrimidine rings of neighboring **DTDCTP** molecules with a shortest distance of around 3.3 Å indicates significant π–π interactions.

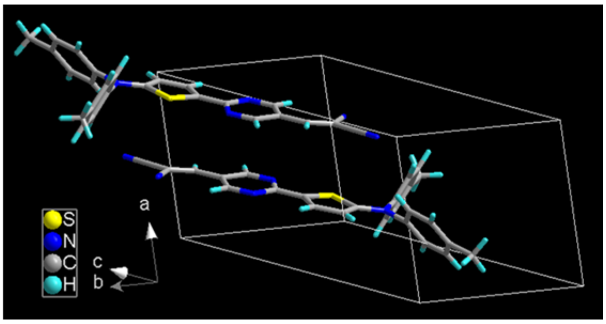

Figure 3-12. The X-ray analyzed molecular structure and crystal packing of **DTDCTP**.

3-4-3 Optical Properties

The absorption band of **DTDCTP** in CH_2Cl_2 exhibited a maximum at 556 nm ($\varepsilon = 53900\ M^{-1}\ cm^{-1}$), which broadened in the thin-film spectrum, possibly due to π–π stacking in the solid state [Figure 3-13(a)]. The k spectrum of the **DTDCTP** thin film (60 nm) is depicted in Figure 3-13(b). The film showed high k in the range of 470–630 nm, with a $k_{max} \sim 1$ at 550 nm. Again, like the k_{max} of the **DTDCTB** thin film, the observed k_{max} value is among the highest reported for organic solar-absorbing thin films,[35,36] implying the existence of compact-packing absorption dipoles in the **DTDCTP** thin film that may substantially increase the absorption efficiency.

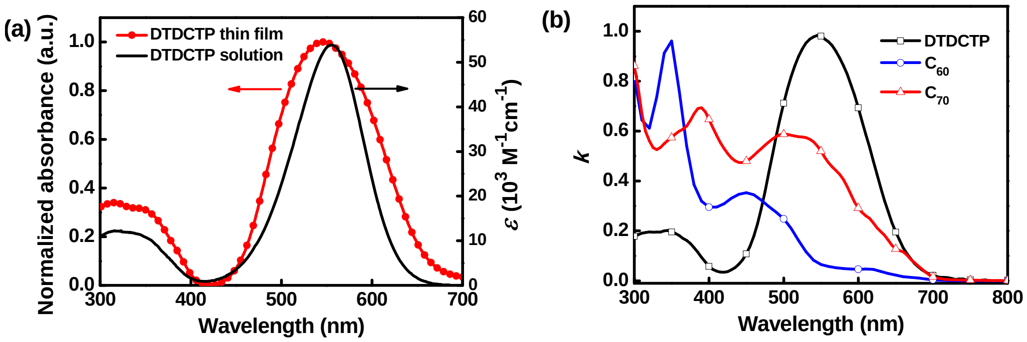

Figure 3-13. (a) Absorption spectra of **DTDCTP** in CH_2Cl_2 and as a thin film. (b) k spectra of **DTDCTP**, C_{60}, and C_{70} thin films.

3-4-4 Photovoltaic and Mobility Characteristics

The photovoltaic properties of **DTDCTP** were investigated with vacuum-processed PMHJ devices. The optimized device structures were configured as follows: (i) device **DTDCTP**:C_{60}: ITO/MoO_3 (20 nm)/**DTDCTP** (7nm)/1:1 (v/v) **DTDCTP**:C_{60} (40 nm)/C_{60} (20 nm)/BCP (10 nm)/Ag, and (ii) device **DTDCTP**:C_{70}: ITO/MoO_3 (20 nm)/**DTDCTP** (7 nm)/1:1 (v/v) **DTDCTP**:C_{70} (40 nm)/C_{70} (6 nm)/BCP (10 nm)/Ag. Figure 3-14(a) shows the J–V curves of **DTDCTP**:fullerene solar cells. The **DTDCTP**:C_{60} device gave a V_{oc} of 0.95 V, a J_{sc} of 8.3 mA/cm^2, and a FF of 0.54, leading to a PCE of 4.3% under AM 1.5G, 1 sun (100 mW/cm^2) simulated solar illumination. Moreover, the **DTDCTP**:C_{70} device delivered a markedly high spectra-mismatch-corrected PCE of 6.4%, with a V_{oc} of 0.95 V, J_{sc} of 12.1 mA/cm^2, and FF of 0.56. The high V_{oc} values of the devices stem from the low-lying HOMO level of

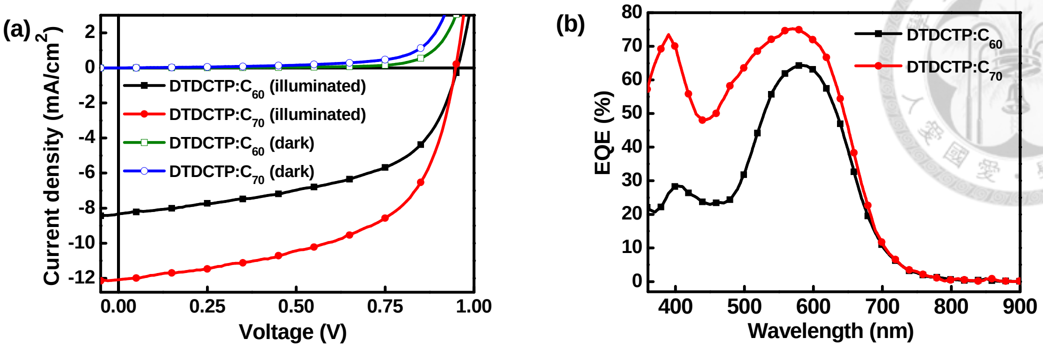

Figure 3-14. (a) *J*–*V* curves and (b) EQE spectra of **DTDCTP**:C_{60} PMHJ (squares) and **DTDCTP**:C_{70} PMHJ (circles) solar cells.

DTDCTP (−5.46 eV) acquired by using UPS, which is deeper than that of **DTDCTB** (−5.30 eV). It is worth noting that this difference in HOMO levels significantly contributes to the increase in V_{oc} for **DTDCTP**-based devices. Apparently, an enhanced V_{oc} value can be successfully achieved through molecular structure modification. Again, the larger J_{sc} obtained in the **DTDCTP**:C_{70} device can be ascribed to larger and broader extinction coefficients of C_{70} relative to C_{60} shown in Figure 3-13(b). The better light-harvesting capability of C_{70} significantly led to the higher EQE values of the **DTDCTP**:C_{70} device as compared to the **DTDCTP**:C_{60} counterpart [Figure 3-14(b)]. Note that the integrated values of EQE spectra with the standard AM 1.5G solar spectrum always agree with the J_{sc} values, with deviation less than 5%. The FF values are comparable for **DTDCTP**:C_{60} and **DTDCTP**:C_{70} devices, suggesting similar blend layer morphologies and charge carrier percolated networks in both devices. In addition, the balanced electron and hole mobilities in the **DTDCTP**:C_{70} mixed layer (~3×10^{-5} cm^2 V^{-1} s^{-1} at 700 $(V/cm)^{1/2}$), which were extracted using the space-charge limited current (SCLC) model (Figure 3-15 and Table 3-5), may account for the relatively high FF values of up to 0.56 in the corresponding solar cells.

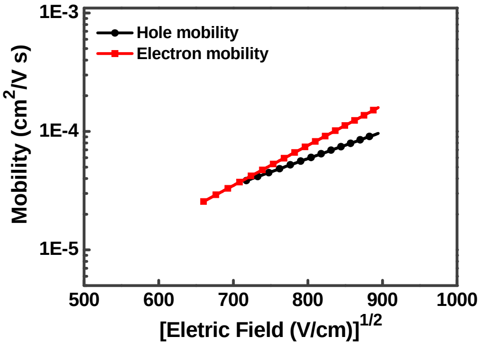

Figure 3-15. Electron and hole mobilities in the **DTDCTP**:C_{70} mixed layer.

Table 3-5. Performance parameters of the **DTDCTP**:C_{70} SCLC device.

device	**zero-field mobility (cm^2/V s)**	**β (cm$^{0.5}$V$^{-0.5}$)**
Hole[a]	9.20631E−7	5.843E−3
Electron[b]	1.49738E−7	8.753E−3

[a] The hole mobility device was configured as: ITO/MoO_3 (1 nm)/1:1 (v/v) **DTDCTP**:C_{70} (100 nm)/MoO_3 (10 nm)/Al (100 nm). [b] The electron mobility device was configured as: ITO/Mg (5 nm)/1:1 (v/v) **DTDCTP**:C_{70} (100 nm)/Ca (5 nm)/Al (100 nm).

3-5 Structural Modification of Donor Moieties of 2,1,3-Benzothiadiazole-Containing Donor–Acceptor–Acceptor Molecular Donors

Our earlier study on D–A–A sensitizers revealed that their bandgaps and HOMO levels can be easily fine-tuned through structural modification of their donor moieties, where their HOMOs are mainly populated, and thereby, alteration of donor moieties has a significant impact on the HOMO level but a limited effect on the LUMO level. More specifically, the D–A–A sensitizers bearing weaker electron-donating groups had a larger bandgap and a lower-lying HOMO level than their analogs containing stronger electron-donating moieties (see Chapter 2). Inspired by this observation, we envisioned that the PCEs of SMOSCs adopting the D–A–A molecules as donors could be further enhanced through delicately manipulating a trade-off between an extended spectral coverage (giving J_{sc}) and an augmented energy offset between the HOMO level of the donor and the LUMO level of the acceptor (giving V_{oc}). Because **DTDCTP** showed a deep-lying enough HOMO level of －5.46 eV and only a moderate light-harvesting ability with an absorption maximum at around 550 nm, **DTDCTB** was chosen as the basis for further structural fine-tuning. In this work, another three BT-containing donor molecules (**DPDCTB**, **DPDCPB**, and **DTDCPB**; Scheme 3-7) were further synthesized, in which the ditolylthienylamine donor moiety of **DTDCTB** is respectively replaced by three relatively weaker electron-donating groups.

3-5-1 Synthesis

The synthesis of the four donor molecules is depicted in Scheme 3-7. With the key asymmetric building block **3-3**, all target compounds were convergently prepared in gram quantities and moderate yields through Stille coupling reactions with triarylamine-based tributylstannyl derivatives.

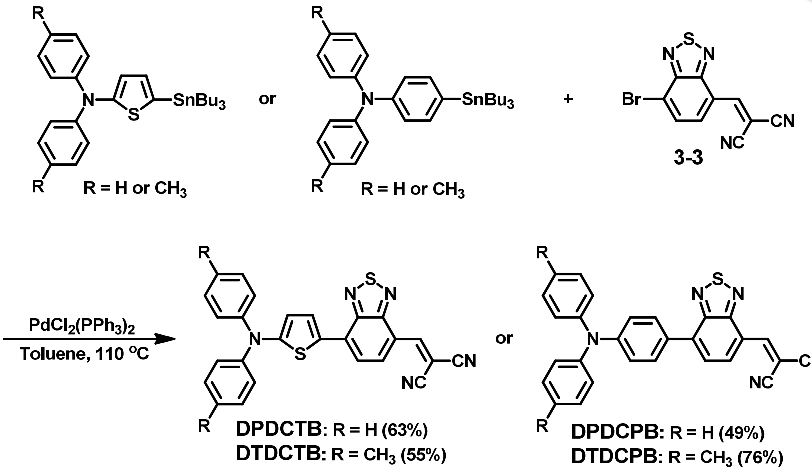

Scheme 3-7. Synthetic route for D–A–A donors **DPDCTB**, **DTDCTB**, **DPDCPB**, and **DTDCPB**.

3-5-2 Crystal Structures and Packings

The molecular structures and crystal packings of **DTDCTB** and **DTDCPB** were characterized by X-ray crystallography (Figure 3-16). Suitable crystals for X-ray analyses were obtained by slow diffusion of orthogonal solvents (dichloromethane/hexane or methanol). In contrast to **DTDCTB**, which displayed an almost coplanar conformation between the thiophene and BT rings with a dihedral angle of 5.5°, **DTDCPB** was highly distorted from planarity with a dihedral angle between the phenylene and BT rings of 24.7°, due to the presence of *ortho–ortho* steric interactions. Like **DTDCTB**, the highly polar nature of the heteroaryl components leads **DTDCPB** molecules to pack in an antiparallel manner and self-assemble into centrosymmetric dimers. The average distance between two neighboring BT rings was smaller for **DTDCTB** (ca. 3.4 Å) than for **DTDCPB** (ca. 3.5 Å), accordingly resulting in a denser packing [d = 1.364 g/cm^3 for **DTDCTB** vs 1.308 g/cm^3 for **DTDCPB**]. The degree of bond length alteration (BLA), calculated as the difference between the bond length of C4−C5 and the average bond length of C3−C4 and C5−C6 of the invariable BT acceptor, amounted to 0.001 Å for **DTDCTB** and 0.030 Å for **DTDCPB** (Table 3-6). The bond length between the triarylamine donors and the BT acceptor (i.e., bond length of C6−C7) for **DTDCTB** was shorter than that for **DTDCPB** (1.434 Å vs 1.472 Å). The smaller BLA of the BT acceptor and the shorter bond length of C6−C7 for **DTDCTB** indicate that the incorporation of thiophene at the donor moiety facilitates π-electron delocalization and imparts an enhanced quinoid character to the conjugated backbone. In other words, the adoption of the ditolylthienylamine donor moiety promotes efficient ICT from the donor side to the acceptor side of **DTDCTB**, thus leading to the easy formation of mesomeric structures ($D–A \leftrightarrow D^{+}=A^{-}$).[37]

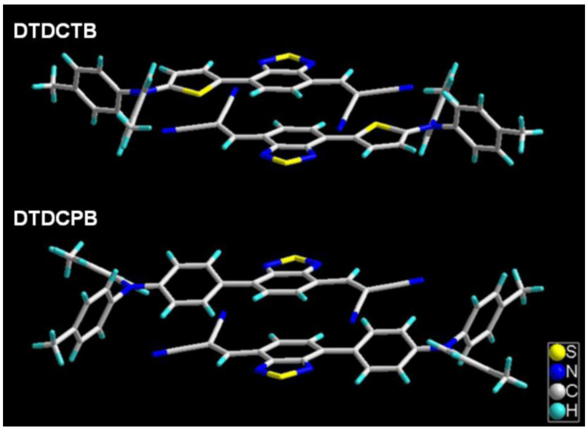

Figure 3-16. X-ray-determined molecular structures and crystal packings of **DTDCTB** and **DTDCPB**.

Table 3-6. Selected bond lengths for **DTDCTB** and **DTDCPB**.[a]

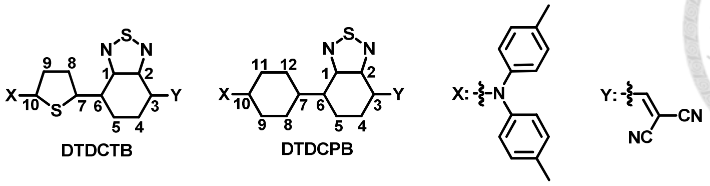

compd	C3−C4	C4−C5	C5−C6	BLA[b]	C6−C7
DTDCTB	1.393	1.395	1.395	0.001	1.434
DTDCPB	1.379	1.407	1.376	0.030	1.472

[a] Bond lengths are given in angstroms. [b] BLA: bond length alternation; BLA = (C4−C5) − [(C3−C4)+(C5−C6)]/2

3-5-3 Thermal Properties

Thermal stabilities and morphological properties of these compounds were investigated by thermogravimetric analysis (TGA) and differential scanning calorimetry (DSC), respectively. The decomposition temperatures (T_d) (referring to 5% weight loss) were in the range of 279−316 °C (Table 3-7), indicating good thermal stability, which is an important prerequisite for device fabrication via vacuum deposition. In DSC, a melting transition manifested from one sharp endothermic peak was observed for each compound (Table 3-7).

Table 3-7. Thermal parameters for **DPDCTB**, **DTDCTB**, **DPDCPB**, and **DTDCPB**.

thermal parameters	**DPDCTB**	**DTDCTB**	**DPDCPB**	**DTDCPB**
T_d (°C)[a]	314	316	279	308
T_m (°C)[b]	187	234	208	288

[a] Temperature corresponding to 5% weight loss obtained from TGA analysis. Under N_2 at a heating rate of 10 °C/min. [b] Temperature obtained from DSC analysis. Under N_2 at a heating rate of 10 °C/min.

3-5-4 Electrochemical Properties

Figure 3-17 shows the cyclic voltammograms of the four donor molecules recorded in solution. Pertinent electrochemical data are summarized in Table 3-8. All four molecules exhibited one quasi-reversible oxidation wave corresponding to the oxidation of the diarylthienylamine or diarylphenylamine donor moieties. The less positive oxidation potentials of **DTDCPB** and **DTDCTB** relative to **DPDCPB** and **DPDCTB** can be rationally ascribed to the presence of the stronger electron-donating *p*-tolyl substituents, while **DPDCTB** and **DTDCTB** showed less positive oxidation potentials than **DPDCPB** and **DTDCPB** due to the electron-rich nature of thiophene. On the other hand, two reversible reduction waves were observed in the cathodic potential regime. The first wave can be assigned to the reduction of the dicyanovinylene block, whereas the second wave can be attributed to the reduction of the BT fragment. In contrast to the oxidation behaviors, the reduction potentials of these four molecules were relatively insensitive to the structural variations of the donor moieties, even though the reduction potentials of **DPDCTB** and **DTDCTB** were slightly less negative than those of **DPDCPB** and **DTDCPB**. Furthermore, the solid-state thin-film HOMO levels of the four molecules were determined using UPS. The HOMO and corresponding calculated LUMO levels are summarized in Table 3-8. The trend observed in the HOMO levels is in good agreement with that of the oxidation potentials. Specifically, the donor molecules bearing *p*-tolyl substituents and/or thiophene showed less positive oxidation potentials and possessed higher-lying HOMO levels than their counterparts. Apparently, the HOMO levels of our D−A−A molecules can be strategically fine-tuned through structural modification of the donor moieties, and solar cell devices based on these three new donors are anticipated to offer higher V_{oc} values than the **DTDCTB**-based device (*vide infra*).

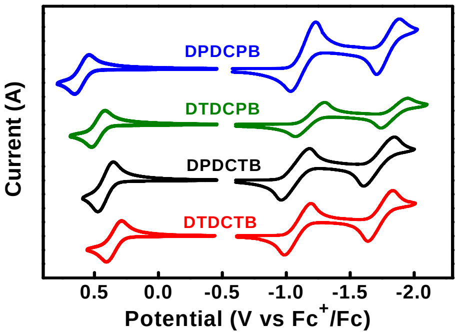

Figure 3-17. Cyclic voltammograms of **DPDCPB**, **DTDCPB**, **DPDCTB**, and **DTDCTB** recorded in solution.

Table 3-8. Photophysical and electrochemical parameters for **DPDCPB**, **DTDCPB**, **DPDCTB**, and **DTDCTB**.

compd	λ_{abs} soln (nm)[a] (ε, M^{-1} cm^{-1})	λ_{abs} film (nm)[b]	ΔE^{opt} film (eV)[c]	E_{ox} (V)[d]	E_{red}^{1} (V)[e]	ΔE^{CV} (eV)[f]	HOMO (eV)[g]	LUMO (eV)[h]
DPDCPB	549 (24365)	577	2.14	0.60	−1.13	1.73	−5.50	−3.36
DTDCPB	570 (27445)	595	2.08	0.47	−1.19	1.66	−5.43	−3.35
DPDCTB	639 (35856)	670	1.91	0.41	−1.07	1.48	−5.35	−3.44
DTDCTB	663 (41660)	684	1.86	0.35	−1.09	1.44	−5.30	−3.44

[a]Measured in CH_2Cl_2 solutions (10^{-5} M). [b]Thin films prepared by vacuum deposition onto fused-silica substrates. [c]Estimated from the extinction coefficient maxima of thin films [Figure 3-19(a)]. [d]Measured in CH_2Cl_2 solutions with 0.1 M $TBAPF_6$ as a supporting electrolyte. [e]Measured in THF solutions with 0.1 M TBAP as a supporting electrolyte. [f]Calculated from the difference between E_{ox}^{1} and E_{red}^{1}. [g]Determined by UPS. [h]LUMO = HOMO + ΔE_{opt} film.

3-5-5 Optical Properties

The absorption spectra of the four molecules in CH_2Cl_2 are depicted in Figure 3-18(a). All showed an intense and broad absorption band in the long-wavelength region, which is assigned to the ICT transition. Compared to **DPDCPB** and **DTDCPB**, significant bathochromic shifts in absorption bands together with increases in ε were found for **DPDCTB** and **DTDCTB** because of the electron-rich and fortified quinoid characters of thiophene as well as the coplanar conformation between the thiophene and BT rings, which are all beneficial in lowering the energy and augmenting the oscillator strength of the ICT transition. In addition, the absorption peaks of **DTDCPB** and **DTDCTB** were red-shifted by ca. 20 nm as compared to those of **DPDCPB** and **DPDCTB** by virtue of the stronger electron-donating nature of the *p*-tolyl substituents. On the other hand, the thin-film absorption bands of these molecules were broadened and red-shifted in comparison to those observed in solution [Figure 3-18(b)], likely due to the intermolecular $\pi-\pi$ stacking of the molecules in the solid state as manifested in the crystal packings.

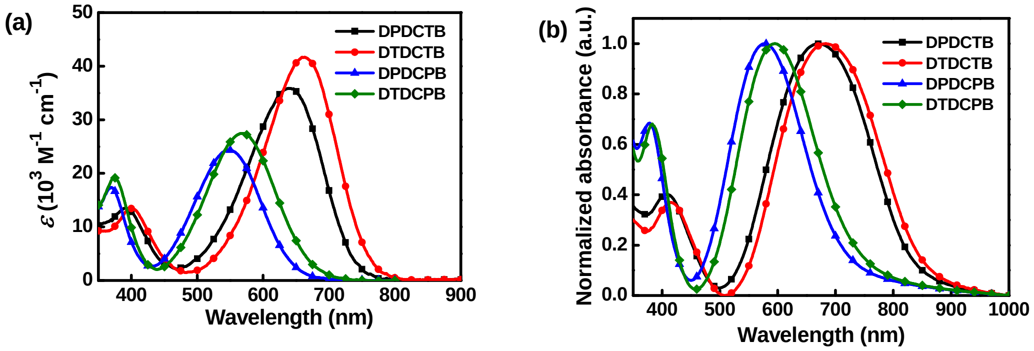

Figure 3-18. Absorption spectra of **DPDCTB** (squares), **DTDCTB** (circles), **DPDCPB** (triangles), and **DTDCPB** (diamonds) (a) in CH_2Cl_2 solutions and (b) as vacuum-deposited thin films.

Optical constants of vacuum-deposited thin films of the four molecules are shown in Figure 3-19(a). The trend in the maximum extinction coefficients is well coincident with that in the absorption maxima. Both **DPDCTB** and **DTDCTB** thin films can be modeled as isotropic layers and showed high k_{max} values of ~1 that are among the highest reported for organic solar-active materials.[35,36] However, the optical isotropic model cannot be adopted to describe the behavior of the two phenylene-containing molecules (**DPDCPB** and **DTDCPB**) thin-films. Therefore, the **DPDCPB** and

DTDCPB films were treated as uniaxially anisotropic with the optical axis along the surface normal. That means the optical constants are distinguished by those for the ordinary polarization, $n_o + ik_o$ and those for the extraordinary polarization, $n_e + ik_e$. The uniaxial model can be successfully fitted to the experimental data, and the extracted optical constants are shown in Figure 3-19(b). The larger k_o relative to k_e for **DPDCPB** and **DTDCPB** indicates preferred orientations parallel to the surface plane upon vacuum deposition onto substrates, as the transition dipole moment of the lowest energy excited state is usually along the molecular backbone for molecules with linear π-systems.[31] This uniaxial anisotropy property generally contributes to stronger absorption for horizontally polarized incident light and therefore may favor high J_{sc} (*vide infra*).

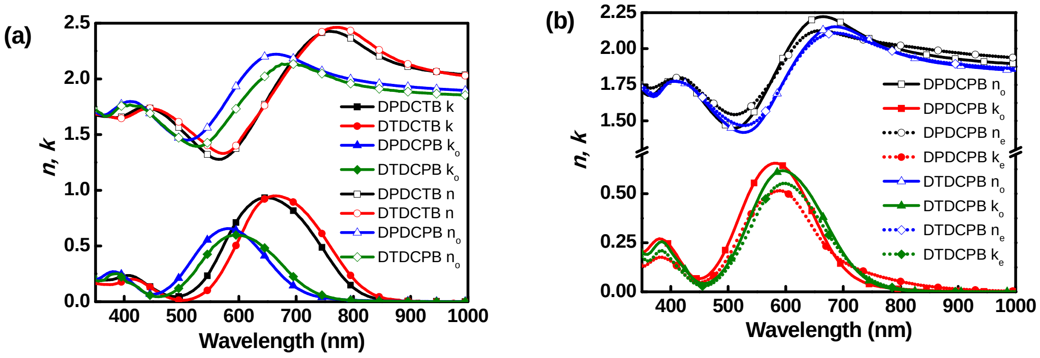

Figure 3-19. (a) Optical constants of **DPDCTB** (squares), **DTDCTB** (circles), **DPDCPB** (triangles), and **DTDCPB** (diamonds) thin-film spectra. (b) Ordinary and extraordinary optical constants of **DPDCPB** and **DTDCPB** thin-film spectra.

3-5-6 Photovoltaic and Mobility Characteristics

In common with the photovoltaic characterization of **DTDCTB**, the vacuum-deposited PMHJ structure was adopted in this study. Fullerene C_{70} was chosen as the electron-accepting counterpart owing to not only its broader and larger extinction coefficients relative to C_{60} but also the superior photovoltaic performance of the **DTDCTB**:C_{70} PMHJ devices as compared to their C_{60}-based counterparts (see Section 3-3). Generally, the devices were fabricated with a configuration of ITO/MoO_3 (5 nm)/donor (7nm)/donor:C_{70}/C_{70} (7 nm)/BCP (10 nm)/Ag (150 nm). The optimal thicknesses of the active layers (the donor layer, donor:C_{70} BHJ layer, and C_{70} layer) are dependent on the optical field distribution as well as exciton diffusion lengths and carrier recombination rates in the thin films. The optimized thicknesses of the BHJ layer in **DPDCTB-**, **DTDCTB-**, **DPDCPB-**, and **DTDCPB**-based devices were found to be 50, 40, 40, and 40 nm, respectively. In addition, the donor:C_{70} blended volume ratio in the BHJ layer was also systematically fine-tuned. The devices fabricated with a donor:C_{70} ratio of 1:1.6 in the BHJ layer gave the best results, except for the **DPDCPB**:C_{70} device that showed the best performance at a ratio of 1:1.

Device performance measurements were carried out under ambient atmosphere using 100 mW/cm^2 AM 1.5G simulated solar illumination. Spectral mismatch-corrected J–V characteristics of the donor:C_{70} (1:1.6) and **DPDCPB**:C_{70} (1:1) PMHJ devices are shown in Figure 3-20(a), and the corresponding solar cell characteristics derived from these curves are summarized in Table 3-9. As expected, the V_{oc} values obtained in these devices are consistent with the magnitudes of the HOMO levels of the donors in spite of the various donor:C_{70} blended ratios. The **DPDCPB**:C_{70} device gave a maximum V_{oc} value of 1.00 ± 0.02 V, reflecting the fact that **DPDCPB** possesses the lowest-lying HOMO level. Moreover, the differences in V_{oc} values are closely correlated to those in the HOMO levels. On the other hand, the J_{sc} values generally follow the trend in donor bandgaps, with a maximum value of 15.08 ± 0.30 mA/cm^2 generated in the **DTDCTB**:C_{70} (1:1.6) device. Interestingly, the J_{sc} value of the **DPDCTB**:C_{70} device is

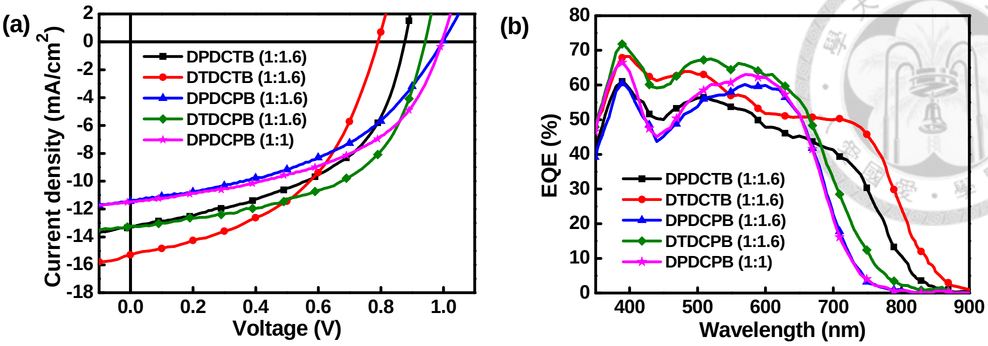

Figure 3-20. (a) Mismatch-corrected *J*−*V* characteristics (under 1 sun, AM 1.5G illumination) and (b) EQE spectra of **DPDCTB**:C_{70} (1:1.6) (squares), **DTDCTB**:C_{70} (1:1.6) (circles), **DPDCPB**:C_{70} (1:1.6) (triangles), **DTDCPB**:C_{70} (1:1.6) (diamonds), and **DPDCPB**:C_{70} (1:1) (stars) PMHJ solar cells.

slightly lower than that of the **DTDCPB**:C_{70} device, even though **DPDCTB** exhibits larger extinction coefficients and a smaller bandgap than **DTDCPB**. This can possibly be attributed to beneficial impact from the uniaxial anisotropy character of **DTDCPB**. The EQE spectra of the PMHJ solar cells are shown in Figure 3-20(b). Both EQE spectra of the **DPDCTB**:C_{70} and **DTDCTB**:C_{70} devices exhibited high plateaus of ~50% (or even higher) throughout the UV−vis range and extend to the NIR region, whereas the **DTDCPB**:C_{70} cell delivered the highest EQEs over the UV−vis range among this series of devices. The calculated J_{sc} values obtained by integrating the EQE spectra with the standard AM 1.5G solar spectrum match the measured J_{sc} values within 3−5%. It is worthwhile to mention that the structural modulation of the donor moieties in the four D−A−A donors and consequent shift of their HOMO levels and adjustment of their bandgaps clearly lead to a trade-off between the V_{oc} and J_{sc} values. Remarkably, the **DTDCPB**:C_{70} device exhibited the best performance through striking a balance between the photovoltage and photocurrent, thus resulting in a PCE of 6.6 ± 0.2% (the highest of 6.8%), with a V_{oc} of 0.93 ± 0.02 V, J_{sc} of 13.48 ± 0.27 mA/cm^2, and FF of 0.53 ± 0.02. The **DTDCPB**:C_{70} (1:1.6) device was further certified by the Photovoltaic Metrology Laboratory, Industrial Technology Research Institute (ITRI) to have a PCE of 6.68% (Figure 3-21).

Table 3-9. Photovoltaic parameters of **DXDCXB**:C_{70} [1:1(1.6)] PMHJ solar cells.[a]

device type	J_{sc} (mA/cm^2)	V_{oc} (V)	FF	PCE [Highest] (%)	R_{Series} (Ω-cm^2)	R_{Shunt} (Ω-cm^2)
DPDCPB:C_{70} (1:1.6)	11.28 ± 0.29	1.00 ± 0.02	0.45 ± 0.02	5.0 ± 0.1 [5.1]	27.0	322.8
DTDCPB:C_{70} (1:1.6)	13.48 ± 0.27	0.93 ± 0.02	0.53 ± 0.02	6.6 ± 0.2 [6.8]	10.6	413.0
DPDCTB:C_{70} (1:1.6)	12.99 ± 0.42	0.88 ± 0.02	0.49 ± 0.01	5.6 ± 0.2 [5.8]	8.3	234.5
DTDCTB:C_{70} (1:1.6)	15.08 ± 0.30	0.79 ± 0.02	0.48 ± 0.01	5.7 ± 0.1 [5.8]	13.5	187.0
DPDCPB:C_{70} (1:1)	11.45 ± 0.23	1.00 ± 0.02	0.49 ± 0.01	5.5 ± 0.1 [5.6]	15.4	396.3
DTDCPB:C_{70} (1:1)	12.72 ± 0.40	0.92 ± 0.02	0.53 ± 0.01	6.2 ± 0.2 [6.4]	12.5	418.8
DPDCTB:C_{70} (1:1)	12.56 ± 0.45	0.85 ± 0.02	0.42 ± 0.02	4.5 ± 0.2 [4.7]	19.8	174.6
DTDCTB:C_{70} (1:1)	14.72 ± 0.25	0.79 ± 0.02	0.49 ± 0.01	5.7 ± 0.1 [5.8]	7.9	205.9

[a] The deviation values were obtained from device-to-device variations of 4-8 devices.

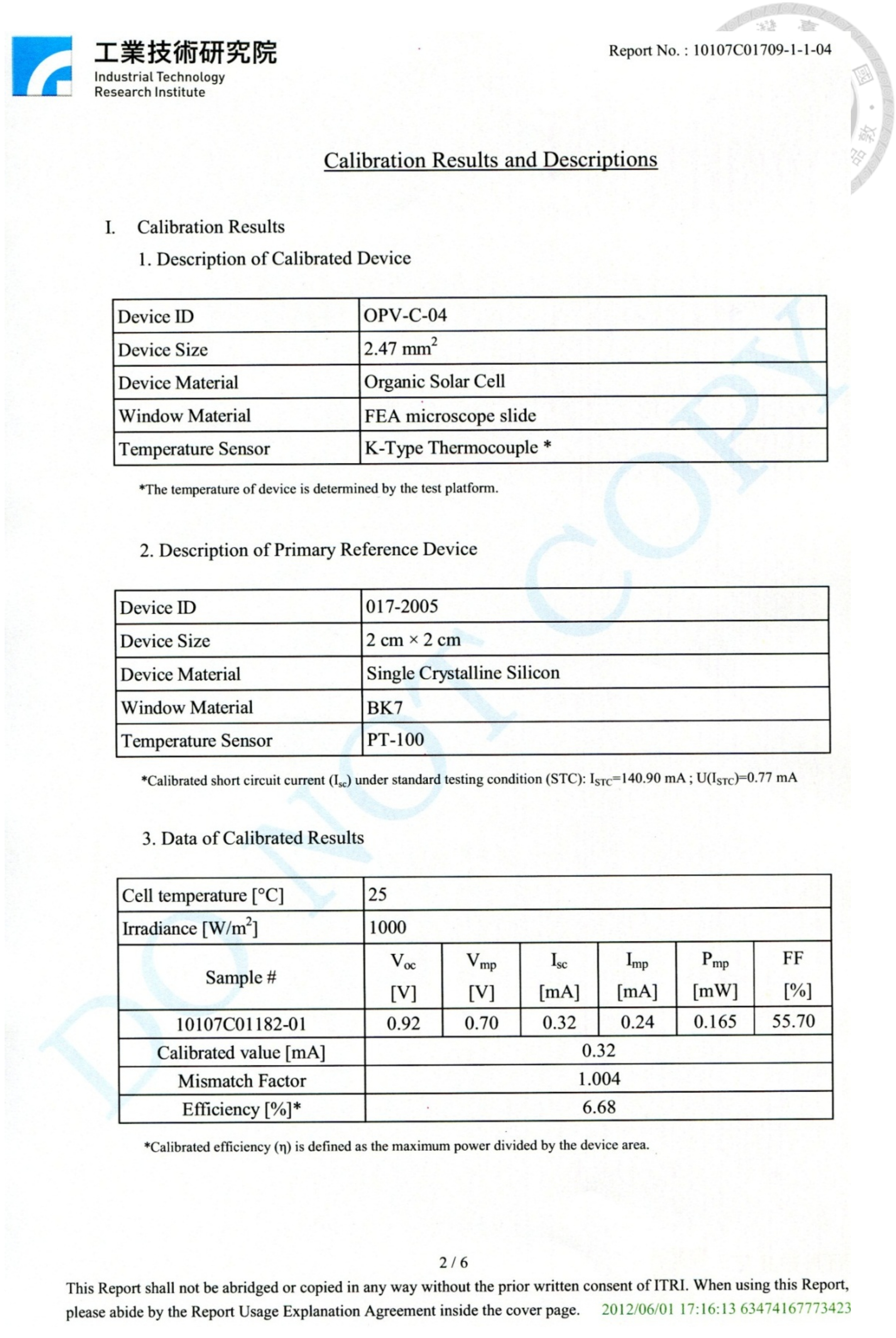

工業技術研究院
Industrial Technology
Research Institute

Report No. : 10107C01709-1-1-04

Calibration Results and Descriptions

I. Calibration Results

1. Description of Calibrated Device

Device ID	OPV-C-04
Device Size	2.47 mm^2
Device Material	Organic Solar Cell
Window Material	FEA microscope slide
Temperature Sensor	K-Type Thermocouple *

*The temperature of device is determined by the test platform.

2. Description of Primary Reference Device

Device ID	017-2005
Device Size	2 cm × 2 cm
Device Material	Single Crystalline Silicon
Window Material	BK7
Temperature Sensor	PT-100

*Calibrated short circuit current (I_{sc}) under standard testing condition (STC): I_{STC}=140.90 mA ; U(I_{STC})=0.77 mA

3. Data of Calibrated Results

Cell temperature [°C]	25					
Irradiance [W/m^2]	1000					
Sample #	V_{oc} [V]	V_{mp} [V]	I_{sc} [mA]	I_{mp} [mA]	P_{mp} [mW]	FF [%]
10107C01182-01	0.92	0.70	0.32	0.24	0.165	55.70
Calibrated value [mA]	0.32					
Mismatch Factor	1.004					
Efficiency [%]*	6.68					

*Calibrated efficiency (η) is defined as the maximum power divided by the device area.

2 / 6

Figure 3-21. Certification report for the **DTDCPB**:C_{70} (1:1.6) PMHJ device.

To gain insight into the differences in the performance of **DTDCPB**:C_{70} PMHJ devices at various blended ratios, carrier mobilities, which were measured using the SCLC method, were examined. The hole and electron mobilities for the **DTDCPB**:C_{70} (1:1.6) blend film are 6.49×10^{-5} and 4.32×10^{-4} cm^2 V^{-1} s^{-1} at 700 $(V/cm)^{0.5}$, respectively, which are higher and more balanced than those for the **DTDCPB**:C_{70} (1:1) film (Figure 3-22 and Table 3-10), thus contributing to the higher device performance for the **DTDCPB**:C_{70} (1:1.6) device. Although significant achievements have already been realized in our system, further improvements in PCEs are still in high demand. In this respect, the moderate FF values of ~0.5 obtained in our devices represent a potential area for further optimization to obtain even better performance. Specifically, the shunt resistances (R_{shunt}) in our devices, calculated from the inverse slopes of the *J*-*V* curves in the fourth quadrant, are several orders of magnitude lower than those in optimized polymer solar cells (Table 3-9).[38] In general, both a high R_{shunt} and a low series resistance (R_{series}) are desirable for producing high FF, and a low R_{shunt} actually stems from more charge recombination and leakage current.[39] Accordingly, increasing hole mobility and thus realizing more balanced carrier transport, to improve the R_{shunt} and the resulting FF values, will be our future research focus.[40]

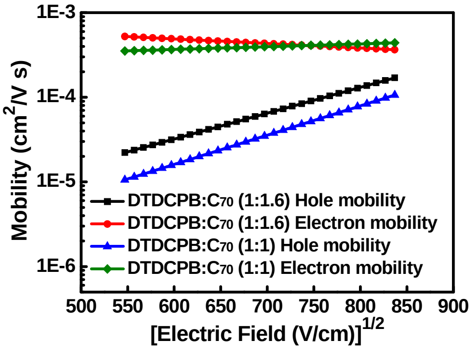

Figure 3-22. Electron and hole mobilities for the **DTDCPB**:C_{70} (1:1.6) and **DTDCPB**:C_{70} (1:1) blend films.

Table 3-10. Performance parameters of **DTDCPB**:C_{70} SCLC devices.

Devices	**zero-field mobility(cm^2/V s)**	**β (cm$^{0.5}$V$^{-0.5}$)**
DTDCPB:C_{70} (1:1.6) Hole[a]	4.76E−7	7.02E−3
DTDCPB:C_{70} (1:1.6) Electron[b]	1.03E−3	−1.24E−3
DTDCPB:C_{70} (1:1) Hole[a]	1.35E−7	7.96E−3
DTDCPB:C_{70} (1:1) Electron[b]	2.33E−4	7.60E−4

[a] The hole-only device was configured as: ITO/MoO_3 (1 nm)/**DTDCPB**:C_{70} (100 nm)/MoO_3 (10 nm)/Al (80 nm). [b] The electron-only device was configured as: ITO/Mg (5 nm)/**DTDCPB**:C_{70} (100 nm)/Ca (5 nm)/Al (80 nm).

3-6 Acceptor−Acceptor−Donor−Acceptor−Acceptor Molecular Donors

Inspired by the highly efficient vacuum-processed acceptor−donor−acceptor (A−D−A) donor materials in the literature,[26,41] in this work, we developed two acceptor−acceptor−donor−acceptor−acceptor (A−A−D−A−A) donor molecules (**BCNDTS** and **BDCDTS**, Scheme 3-8), in which two terminal electron-withdrawing cyano or dicyanovinylene moieties are connected to a central DTS core through another electron-accepting BT blocks. Several advantages of the DTS moiety required for efficient donor materials for OSCs have been introduced in Section 3-2. We envisioned that the A–A–D–A–A molecules would not only exhibit better light-harvesting abilities but also possess deeper-lying HOMO energy levels than their A−D−A counterparts due to the extension of conjugated π-systems and the fortified quinoid character of conjugated backbones that originates from the enhanced acceptor strength.

3-6-1 Synthesis

The synthetic routes to the building block **3-6** as well as the target compounds **BCNDTS** and **BDCDTS** are depicted in Scheme 3-8. Treatment of **3-2** with hydroxylamine hydrochloride gave the corresponding cyano derivative **3-6** in 80% yield. Stille coupling of 5,5’-bis(tri-*n*-butylstannyl)-3,3’-di-*n*-octylsilylene-2,2’-bithiophene with **3-6** afforded **BCNDTS** in 43% yield. **BDCDTS** was obtained in a yield of 38% via a two-step process where the first involves Stille coupling of 5,5’-bis(tri-*n*-butylstannyl)-3,3’-di-*n*-octylsilylene-2,2’-bithiophene with **3-2**, subsequently followed by Knöevenagel condensation with malononitrile.

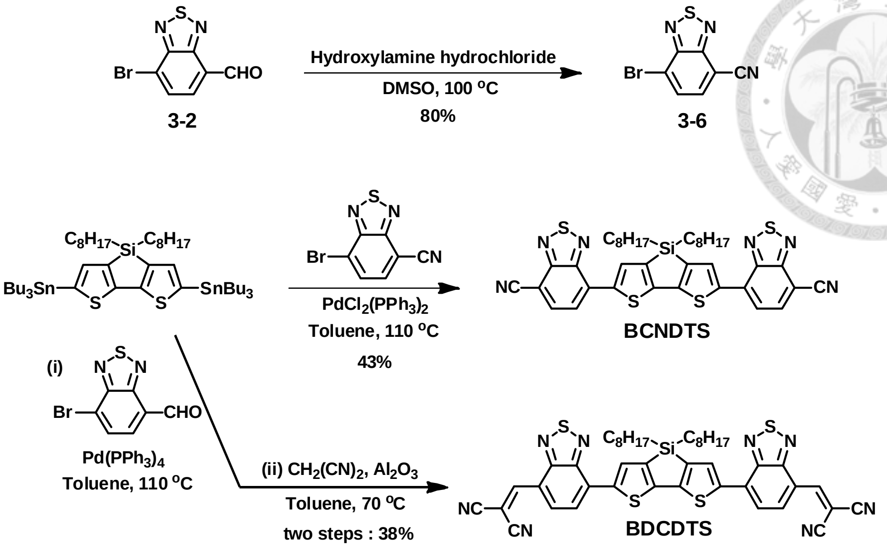

Scheme 3-8. Synthesis of **BCNDTS**, **BDCDTS**, and their building blocks.

3-6-2 Thermal Properties

The thermal stabilities of **BCNDTS** and **BDCDTS** were investigated by TGA, which showed the T_d (5% weight loss) to be 389 and 373 °C for **BCNDTS** and **BDCDTS**, respectively. The inferior thermal stability for **BDCDTS** is attributed to the presence of the relatively fragile dicyanovinylene moieties.

3-6-3 Electrochemical Properties

The electrochemical properties of **BCNDTS** and **BDCDTS** were probed by CV. As shown in Figure 3-23, both compounds exhibited one quasi-reversible oxidation wave with similar potentials at ~0.7 V (vs Fc/Fc^+), corresponding to the oxidation of the central DTS donor moiety. In the cathodic potential regime, four quasi-reversible reduction waves were observed for **BCNDTS**. The first two waves can be attributed to the stepwise reduction of the cyano groups (inset of Figure 3-23), whereas the third wave can be assigned to the reduction of the BT fragments. On the other hand, **BDCDTS** showed three quasi-reversible reduction waves, and the first and second wave can be ascribed to the reduction of the dicyanovinylene and BT blocks, respectively. Moreover, it is worthy to note that the respective reduction potentials of **BDCDTS** were less negative than those of **BCNDTS** (Table 3-11), reflecting the stronger electron-withdrawing nature of dicyanovinylene. The HOMO levels of **BCNDTS** and **BDCDTS** thin films were determined to be −5.40 and −5.80 eV, respectively, by using UPS. This result is quite different from what we expected previously since **BCNDTS** and **BDCDTS** show similar oxidation potentials.

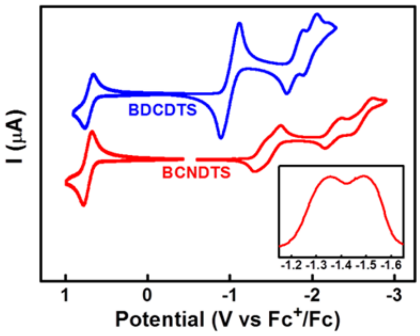

Figure 3-23. Cyclic voltammograms of **BCNDTS** and **BDCDTS** recorded in solution. Inset: the selected reduction region of the differential pulse voltammogram of **BCNDTS**.

Table 3-11. Photophysical and electrochemical parameters for **BCNDTS** and **BDCDTS**.

compd	λ_{abs} soln (nm)^{a} (ε, M^{-1} cm^{-1})	λ_{abs} film (nm)^{b}	ΔE^{opt} film (eV)^{c}	E_{ox} (V)^{d}	E_{red}^{1} (V)^{e}	ΔE^{CV} (eV)^{f}	HOMO (eV)^{g}	LUMO (eV)^{h}
BCNDTS	553 (49984)	572	2.17	0.73	−1.36	2.09	−5.40	−3.23
BDCDTS	643 (78466)	659	1.88	0.71	−0.99	1.70	−5.80	−3.92

[a] Measured in CH_2Cl_2 solutions (10^{-5} M). [b] Thin films on fused-silica substrate. [c] Estimated from λ_{abs} film. [d] Measured in CH_2Cl_2 solutions with 0.1M $TBAPF_6$ as a supporting electrolyte. [e] Measured in THF solutions with 0.1 M TBAP as a supporting electrolyte. [f] Estimated from the difference between E_{ox}^{1} and E_{red}^{1}. [g] Determined by UPS. [h] LUMO = HOMO + ΔE^{opt} film.

3-6-4 Optical Properties

Normalized absorption spectra of **BCNDTS** and **BDCDTS** in CH_2Cl_2 solutions and as thin films are shown in Figure 3-24. In CH_2Cl_2, **BCNDTS** and **BDCDTS** each showed a featureless absorption band with a maximum at 553 and 643 nm, respectively. The red-shifted absorption peak and larger ε of **BDCDTS** relative to **BCNDTS** is attributed to its longer π-conjugation length and the enhanced D−A interaction (Table 3-11). In comparison to the reported A−D−A molecule that is composed of a DTS donor end-capped with BT acceptors (λ_{abs} = 503 nm),[42] these two tailor-made molecules exhibited evident bathochromic shifts in absorption, corroborating that enhanced solar spectral responses can be realized through our molecular design. In contrast, the thin-film absorption bands of **BCNDTS** and **BDCDTS** were broadened and red-shifted, which probably stem from intermolecular π−π stacking of the molecules in the solid states.

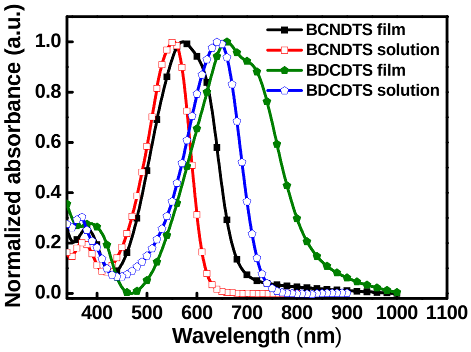

Figure 3-24. Normalized absorption spectra of **BCNDTS** and **BDCDTS** in CH_2Cl_2 solutions and as thin films.

3-6-5 Photovoltaic Characteristics

PHJ solar cells were first fabricated to evaluate the photovoltaic performance of these two molecules. The optimized devices were configured as follows: (i) **BCNDTS**/C_{60} cell: ITO/MoO_3 (5 nm)/**BCNDTS** (10 nm)/C_{60} (35 nm)/BCP (10 nm)/Ag, (ii) **BDCDTS**/C_{60} cell: ITO/PEDOT:PSS (30 nm)/**BDCDTS** (10 nm)/C_{60} (35 nm)/BCP (10 nm)/Ag, (iii) **BCNDTS**/C_{70} cell: ITO/MoO_3 (5 nm)/**BCNDTS** (8 nm)/C_{70} (15 nm)/BCP (10 nm)/Ag. The J–V characteristics under AM 1.5G simulated solar illumination at an intensity of 100 mW/cm^2 and corresponding EQE spectra are shown in Figure 3-25. The **BDCDTS**/C_{60} cell gave a low PCE of 0.07% (Table 3-12), which can be ascribed to the inefficient electron transfer between **BDCDTS** and C_{60} due to the deep-lying LUMO level of **BDCDTS** (Table 3-11). In contrast, the **BCNDTS**/C_{60} device showed superior performance with a V_{oc} of 1.02 V, J_{sc} of 4.17 mA/cm^2, and FF of 0.54, thus improving the PCE to 2.3%. In addition, utilizing C_{70} as the acceptor led to an increase in J_{sc} due to its larger and broader absorption. However, the **BCNDTS**/C_{70} cell delivered a lower PCE of 1.9% due to the inferior V_{oc} and FF. It is noteworthy that both **BCNDTS**/C_{60} and **BCNDTS**/C_{70} devices exhibit high V_{oc} values (up to 1.02 V), which can be ascribed to the deep-lying HOMO level (−5.40 eV) of the **BCNDTS** thin film.

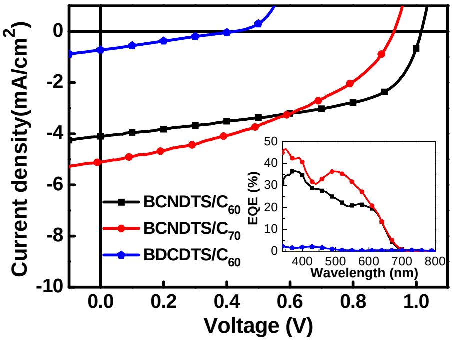

Figure 3-25. J–V curves and EQE spectra (inset) of **BCNDTS** (**BDCDTS**)/C_{60} (C_{70}) PHJ devices.

Table 3-12. Photovoltaic parameters of **BCNDTS** (**BDCDTS**)/C_{60} (C_{70}) PHJ^{a} and **BCNDTS**:C_{60} (C_{70}) PMHJ^{b} solar cells.

device type	J_{sc} (mA/cm^2)	V_{oc} (V)	FF	PCE (%)
BDCDTS/C_{60}^{a}	0.73	0.43	0.24	0.07
BCNDTS/C_{60}^{a}	4.17	1.02	0.54	2.3
BCNDTS/C_{70}^{a}	5.11	0.93	0.41	1.9
BCNDTS:C_{60} (1:1)^{b}	5.80	1.05	0.38	2.3
BCNDTS:C_{70} (1:1)^{b}	7.81	1.03	0.34	2.8
BCNDTS:C_{70} (1:1.5)^{b}	9.79	1.01	0.38	3.7

Encouraged by the promising performance of PHJ cells based on **BCNDTS**, we further adopted the PMHJ structures, which were fabricated with a configuration of ITO/MoO_3 (5 nm)/**BCNDTS** (7 nm)/**BCNDTS**:C_{60} or **BCNDTS**:C_{70} (40 nm)/C_{60} (20 nm) or C_{70} (7 nm)/BCP (10 nm)/Ag, to optimize the device efficiency. Initially, the PMHJ devices were fabricated at a **BCNDTS**: C_{60} or C_{70} blended volume ratio of 1:1. Figure 3-26 shows the J–V characteristics and EQE spectra of the corresponding PMHJ devices. The **BCNDTS**:C_{70} device exhibited a higher J_{sc} and thus a higher PCE of 2.8% than the **BCNDTS**:C_{60} device due to the better light-harvesting ability of C_{70}. The similar FF values of these two cells can be ascribed to the similar field-dependent carrier transport and recombination properties in the BHJ layers (Table 3-12). Moreover, by fine-tuning the **BCNDTS**:C_{70} blended ratio from 1:1 to 1:1.5, the PCE was further improved to 3.7%, with a V_{oc} of 1.01 V, J_{sc} of 9.79 mA/cm^2, and FF of 0.38. The results may indicate that a preferred morphology in the BHJ layer is realized at this blended ratio, thus leading to the increases in J_{sc} and FF.

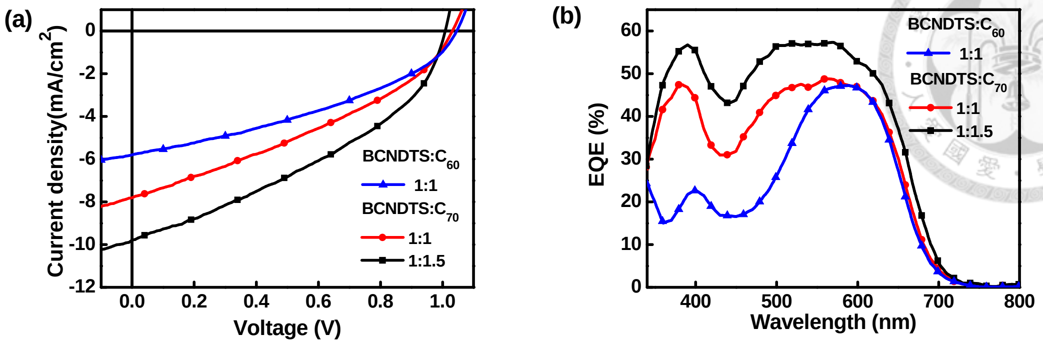

Figure 3-26. (a) *J*–*V* curves and (b) EQE spectra of **BCNDTS**:C$_{60}$ (C$_{70}$) PMHJ devices.

3-7 Conclusions

In section 3-2, a D−π−A small-molecule **TPDCDTS** was synthesized and applied in the fabrication of vacuum-deposited SMOSCs. The intrinsic structural features including a fairly low-lying HOMO level, a moderate light-harvesting ability, and preferred horizontal molecular orientation made **TPDCDTS** a decent donor material for SMOSCs. A vacuum-deposited PMHJ device based on **TPDCDTS** and C_{70} as the electron acceptor exhibited a PCE of 3.82%.

In section 3-3, a D−A−A donor material **DTDCTB**, in which an electron-donating ditolylthienylamine moiety is connected to an electron-withdrawing dicyanovinylene moiety through another electron-accepting BT block, was synthesized. The innovative structural design strategy enabled **DTDCTB** to exhibit a distinguished light-harvesting capability with spectral responses extending to the NIR region. A vacuum-deposited PMHJ device employing **DTDCTB** and C_{70} demonstrated a high J_{sc} and a PCE of 5.81%.

In section 3-4, a D−A−A donor molecule **DTDCTP** characterized by the adoption of pyrimidine as the bridging acceptor was synthesized. Through this structural modification, **DTDCTP** possessed a lower-lying HOMO level than **DTDCTB**. Accordingly, the **DTDCTP**:C_{70} PMHJ device showed a higher V_{oc} and reached a higher PCE of 6.4% than the **DTDCTB**-based device.

In section 3-5, another three new BT-containing D−A−A donor molecules (**DPDCTB**, **DPDCPB**, and **DTDCPB**) with various donor moieties were synthesized in a facile fashion by taking advantage of the asymmetric building block **3-3**. X-ray structure analyses revealed the tendency of these highly dipolar molecules to pack in an antiparallel manner and self-assemble into centrosymmetric dimers in the solid state.

The adoption of thiophene-based donor moieties facilitated π-electron delocalization and easy formation of quinoid mesomeric structures over the conjugated backbone. Compared to **DTDCTB** bearing the strongest ditolylthienylamine donor moiety among this series of molecules, the three newly synthesized molecules possessed lower HOMO levels and exhibited hypsochromic shifts in absorption. Through judicious molecular design and device optimizations, including fine-tuning the layers' thicknesses as well as the blended ratio in the BHJ layer, vacuum-deposited PMHJ devices based on this series of molecules and C_{70} showed PCEs in excess of 5.6%. Notably, the **DTDCPB**:C_{70} (1:1.6) device achieved an impressively high PCE of 6.8% through striking a balance between the photovoltage and the photocurrent.

In section 3-6, two donor molecules (**BCNDTS** and **BDCDTS**) with an A−A−D−A−A molecular architecture were synthesized. The side-by-side combination of two electron-withdrawing groups endowed **BCNDTS** and **BDCDTS** with better light-harvesting abilities than their reported A−D−A counterpart. However, the over-tuned LUMO level prohibited **BDCDTS** as an effective donor material in fullerene-based solar cells. In contrast, the suitable energy levels of **BCNDTS** enabled it to be an efficient donor material for SMOSCs. A PCE of 2.3% was obtained with a simple **BCNDTS**/C_{60} PHJ structure. By adopting PMHJ device structures as well as utilizing C_{70} as the electron acceptor and fine-tuning the donor:acceptor blended ratio in the BHJ layer, the PCE value was further improved to 3.7%.

3-8 Experimental Details

Synthesis and Materials. Unless otherwise stated, all chemicals and reagents were used as received from commercial sources without purification. Solvents for chemical synthesis were purified by distillation. All chemical reactions were carried out under an argon or nitrogen atmosphere. The 4-bromo-7-methyl-2,1,3-benzothiadiazole[43] was synthesized based on the reported procedures.

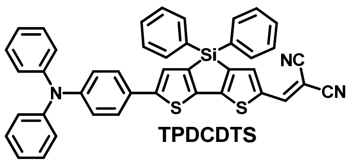

TPDCDTS

5-[*N*,*N*-bis(phenylamino)phenyl]-5’-dicyanomethylidenemethyl-3,3’-diphenylsilylene-2,2’-bithiophene (TPDCDTS). A mixture of **2-4a** (1.03 g, 1.66 mmol), malononitrile (220 mg, 3.32 mmol), and basic aluminum oxide (830 mg) in toluene (40 mL) was stirred and heated at 70 °C for 1 h. After the reaction mixture was cooled to room temperature, the aluminum oxide residue was removed by filtration and thoroughly washed with toluene. The solvent of the filtrate was removed by rotary evaporation, and the crude product was purified by column chromatography on silica gel with ethyl acetate/dichloromethane/hexane (v/v/v, 1:2:10) as eluent to afford **TPDCDTS** as a black solid (800 mg, 72% yield), mp 294 °C (DSC); IR (KBr) ν 3052, 3027, 2216, 1592, 1514, 1488, 1384, 1255, 1114, 926, 830 cm^{-1}; ^{1}H NMR (CD_2Cl_2, 400 MHz) δ 7.82 (s, 1H), 7.80 (s, 1H), 7.65 (d, *J* = 7.2 Hz, 4H), 7.52–7.47 (m, 5H), 7.41 (t, *J* = 7.2 Hz, 4H), 7.30 (t, *J* = 7.8 Hz, 4H), 7.13–7.03 (m, 8H); ^{13}C NMR (CD_2Cl_2, 100 MHz) δ 162.8, 152.5, 150.6, 148.7, 148.2, 147.4, 146.5, 142.7, 141.2, 137.3, 135.7, 131.4, 130.1, 129.8, 128.8, 127.2, 125.6, 125.4, 124.1, 123.0, 115.3, 114.7, 73.8; HRMS (*m/z*, FAB$^+$) calcd for $C_{42}H_{27}N_3S_2Si$ 665.1416, found 665.1416.

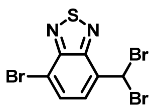

3-1

4-Bromo-7-dibromomethyl-2,1,3-benzothiadiazole (3-1). A mixture of 4-bromo-7-methyl-2,1,3-benzothiadiazole (45.82 g, 200 mmol), azobisisobutyronitrile (6.57 g, 40 mmol), and *N*-bromosuccinimide (106.2 g, 600 mmol) in chlorobenzene (400 mL) was stirred and heated at 80 °C for 4h. After being cooled to room temperature, the reaction mixture was filtered to remove the solid succinimide, and then the filtrate was washed with water and brine, dried over anhydrous magnesium sulfate, and filtered. The solvent of the filtrate was removed by rotary evaporation, and the crude product was purified by column chromatography on silica gel with dichloromethane /hexane (v/v, 1:3) as eluent to afford **3-1** as a white solid (56.1 g, 83%), mp 119–120 °C; IR (KBr) ν 3001, 2922, 1524, 1481, 1315, 1274, 1185, 1097, 937, 880 $\mathrm{cm^{-1}}$; ^{1}H NMR ($CDCl_3$, 400 MHz) δ 7.97–7.90 (m, 2H), 7.40 (s, 1H); ^{13}C NMR ($CDCl_3$, 100 MHz) δ 152.8, 149.6, 133.4, 131.8, 129.4, 115.8, 33.9; HRMS (*m/z*, FAB$^+$) calcd for $C_7H_3{}^{79}Br_3N_2S$ 383.7567, found 383.7542, calcd for $C_7H_3{}^{79}Br_2{}^{81}Br_1N_2S$ 385.7547, found 385.7553, calcd for $C_7H_3{}^{79}Br_1{}^{81}Br_2N_2S$ 387.7526, found 387.7524, calcd for $C_7H_3{}^{81}Br_3N_2S$ 389.7506, found 389.7536.

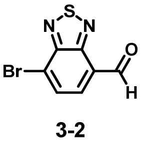

3-2

7-Bromo-2,1,3-benzothiadiazole-4-carbaldehyde (3-2). To a stirring solution of **3-1** (260 mg, 0.67 mmol) in acetonitrile (8 mL) was added silver nitrate aqueous solution (285 mg, 1.68 mmol, water 1.7 mL) and then heated to reflux for 2h. After being cooled to room temperature, the reaction mixture was filtered to remove the AgBr precipitate, and the filtrate was then extracted with dichloromethane. The combined extracts were washed with brine, dried over anhydrous magnesium sulfate, and filtered. The solvent of the filtrate was removed by rotary evaporation to afford **3-2** as a white solid (147 mg, 92%), mp 185–186 °C; IR (KBr) ν 3078, 3021, 2835, 2728, 1702, 1526, 1268, 1102, 937, 879 cm^{-1}; ^{1}H NMR (CDCl$_3$, 400 MHz) δ 10.71 (s, 1H), 8.09–8.03 (m, 2H); ^{13}C NMR (CDCl$_3$, 100 MHz) δ 188.0, 153.8, 152.1, 131.9, 131.5, 126.7, 121.7; HRMS (*m/z*, FAB^{+}) calcd for $C_7H_3{}^{79}BrN_2OS$ 241.9149, found 241.9149, calcd for $C_7H_3{}^{81}BrN_2OS$ 243.9129, found 243.9137.

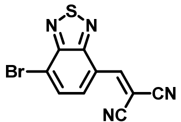

3-3

4-Bromo-7-dicyanovinyl-2,1,3-benzothiadiazole (3-3). A mixture of **3-2** (150 mg, 0.62 mmol), malononitrile (82 mg, 1.24 mmol), and basic aluminum oxide (310 mg) in anhydrous toluene (7 mL) was stirred and heated at 70 °C for 2h. After the reaction mixture was cooled to room temperature, the basic aluminum oxide residue was removed by filtration and thoroughly washed with toluene. The solvent of the filtrate was removed by rotary evaporation, and the crude product was purified by column chromatography on silica gel with dichloromethane/hexane (v/v, 1:1) as eluent to afford **3-3** as a yellow solid (120 mg, 67%), mp 179–180 °C; IR (KBr) ν 3097, 3032, 2229, 1573, 1517, 1380, 1126, 1044, 933, 884 cm^{-1}; ^{1}H NMR (CDCl$_3$, 400 MHz) δ 8.73 (s, 1H), 8.53 (d, J = 7.6 Hz, 1H), 8.05 (d, J = 7.6 Hz, 1H); ^{13}C NMR (CDCl$_3$, 100 MHz) δ 153.0, 152.5, 152.2, 132.0, 130.0, 123.0, 121.8, 113.1, 112.3, 85.2; HRMS (*m/z*, FAB^{+}) calcd for $C_{10}H_3{}^{79}BrN_4S$ 289.9262, found 289.9263, calcd for $C_{10}H_3{}^{81}BrN_4S$ 291.9241, found 291.9237.

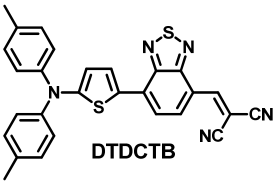

DTDCTB

2-{[7-(5-*N*,*N*-ditolylaminothiophen-2-yl)-2,1,3-benzothiadiazol-4-yl]methylene}-malononitrile (DTDCTB). A mixture of **3-3** (1.46 g, 5 mmol), 5-(*N*,*N*-ditolylamino)-2-(tri-*n*-butylstannyl)thiophene (3.55 g, 6.25 mmol), and $PdCl_2(PPh_3)_2$ (175 mg, 0.25 mmol) in anhydrous toluene (25 mL) was stirred and heated at 110 °C under argon for 2h. After the reaction mixture was cooled to room temperature, the solvent was removed by rotary evaporation, and the crude product was purified by column chromatography on silica gel with dichloromethane/hexane (v/v, 1:1) as eluent to afford **DTDCTB** as a black solid (1.34, 55%), mp 234 °C (DSC); IR (KBr) ν 3033, 2917, 2217, 1566, 1454, 1329, 1265, 1153, 1062, 921, 827 cm^{-1}; ^{1}H NMR ($CDCl_3$, 400 MHz) δ 8.66 (s, 1H), 8.60 (d, *J* = 8.0 Hz, 1H), 8.22 (d, *J* = 4.4 Hz, 1H), 7.57 (d, *J* = 8.0 Hz, 1H), 7.22–7.17 (m, 8H), 6.50 (d, *J* = 4.4 Hz, 1H), 2.39 (s, 6H); ^{13}C NMR ($CDCl_3$, 100 MHz) δ 161.0, 154.6, 151.5, 150.6, 143.8, 135.5, 134.0, 133.2, 130.8, 130.2, 126.0, 124.9, 120.9, 118.9, 114.6, 114.3, 113.8, 78.5, 21.1; HRMS (*m/z*, FAB$^+$) calcd for $C_{28}H_{19}N_5S_2$ 489.1082, found 489.1083.

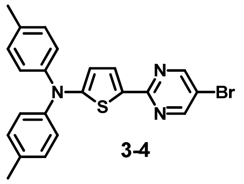

3-4

[5-(5-Bromo-pyrimidin-2-yl)-thiophen-2-yl]-*N*,*N*-ditolylamine (3-4). To a stirring solution of 2-[*N*,*N*-ditolylamino]thiophene (8.31 g, 30 mmol) in anhydrous THF (90 mL) was added dropwise *n*-BuLi solution (1.6 M in hexane, 19.69 mL, 31.5 mmol) at −78

°C under argon. The reaction mixture was warmed to −35 °C and stirred for 15 min. $ZnCl_2$ (33 mL of 1 M solution in anhydrous THF, 33 mmol) was then added to the reaction mixture in one portion, after which the reaction mixture was warmed to room temperature and stirred for 30 min. To the above resulting zinc reagent were added 5-bromo-2-iodopyrimidine (8.55 g, 30 mmol), $Pd(PPh_3)_4$ (1.73 g, 1.5 mmol), and anhydrous THF (120 mL). The whole mixture was heated to reflux under argon for 2 h. After being cooled to room temperature, the reaction mixture was poured into water and extracted with ethyl acetate. The combined extracts were washed with brine, dried over anhydrous magnesium sulfate and filtered. The solvent of the filtrate was removed by rotary evaporation, and the crude product was purified by column chromatography on silica gel with dichloromethane/hexane (v/v, 1:2) as eluent to afford **3-4** as a yellow solid (10.84 g, 83%), mp 173–174 °C; IR (KBr) ν 3028, 2916, 1605, 1551, 1374, 1119, 1056, 928 cm^{-1}; ^{1}H NMR ($CDCl_3$, 400 MHz) δ 8.55 (s, 2H), 7.71 (d, J = 4.4 Hz, 1H), 7.16–7.10 (m, 8H), 6.43 (d, J = 4.4 Hz, 1H), 2,34 (s, 6H); ^{13}C NMR ($CDCl_3$, 100 MHz) δ 159.5, 158.9, 157.2, 144.4, 134.3, 130.0, 129.8, 128.9, 124.4, 114.7, 114.5, 21.0; HRMS (*m/z*, FAB^+) Calcd. for $C_{22}H_{18}{}^{79}BrN_3S$ 435.0405, found 435.0411, calcd. for $C_{22}H_{18}{}^{81}BrN_3S$ 437.0384, found 437.0391.

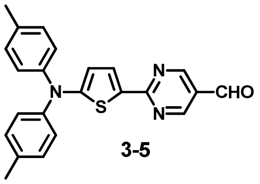

3-5

2-[5-*N*,*N*-ditolylaminothiophen-2-yl]-pyrimidine-5-carbaldehyde (3-5). To a stirring solution of **3-4** (8.73 g, 20 mmol) in 350 mL anhydrous THF was added dropwise *n*-BuLi solution (1.6 M in hexane, 13.13 mL, 21 mmol) at −100 °C under argon. The resulting solution was stirred for 30 min, after which time dry ethyl formate (16.15 mL, 200 mmol) was added dropwise over 5 min. After being stirred for 30 min, the reaction mixture was quenched with 1.5 M HCl in THF solution (15 mL, 22.5 mmol). The cold bath was removed, and the reaction mixture was stirred for 2 h. The solvent was removed by rotary evaporation, and the residue was extracted with chloroform. The combined extracts were washed with brine, dried over anhydrous magnesium sulfate and filtered. The solvent of the filtrate was removed by rotary evaporation, and the crude product was purified by column chromatography on silica gel with dichloromethane as eluent to afford **3-5** as an orange solid (3.27 g, 42%), mp 176–177 °C; IR (KBr) ν 3027, 2918, 2825, 2719, 1694, 1593, 1547, 1209, 1071 cm^{-1}; ^{1}H NMR ($CDCl_3$, 400 MHz) δ 9.92 (s, 1H), 8.88 (s, 2H), 7.88 (d, J = 4.4 Hz, 1H), 7.20-7.14 (m, 8H), 6.40 (d, J = 4.4 Hz, 1H), 2.36 (s, 6H); ^{13}C NMR ($CDCl_3$, 100 MHz) δ 187.9, 164.1, 162.7, 158.4, 143.7, 135.4, 133.4, 130.2, 127.3, 125.1, 124.1, 113.1, 21.1; HRMS (*m/z*, FAB^{+}) calcd. for $C_{23}H_{19}N_3OS$ 385.1249, found 385.1252.

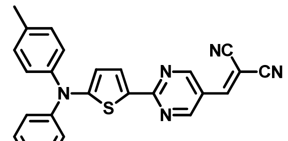

DTDCTP

2-{[2-(5-*N*,*N*-ditolylaminothiophen-2-yl)-pyrimidin-5-yl]methylene}malononitrile (DTDCTP). A mixture of **3-5** (1.54 g, 4.00 mmol), malononitrile (528 mg, 8.00 mmol), and basic aluminum oxide (2.00 g) in dry toluene (60 mL) was stirred and heated at 70 °C for 1 h. After the reaction mixture was cooled to room temperature, the basic aluminum oxide residue was removed by filtration and thoroughly washed with toluene. The solvent of the filtrate was removed by rotary evaporation, and the crude product was purified by column chromatography on silica gel with dichloromethane as eluent to afford **DTDCTP** as a black solid (1.36 g, 78%), mp 209 °C (DSC); IR (KBr) ν 3024, 2921, 2221, 1587, 1542, 1286, 1107, 1071, 814 cm^{-1}; ^{1}H NMR (CDCl$_3$, 400 MHz) δ 8.93 (s, 2H), 7.91 (d, J = 4.4 Hz, 1H), 7.47 (s, 1H), 7.22–7.16 (m, 8H), 6.39 (d, J = 4.4 Hz, 1H), 2.37 (s, 6H); ^{13}C NMR (CDCl$_3$, 100 MHz) δ 164.5, 163.0, 158.2, 152.7, 143.3, 136.1, 135.1, 130.3, 126.6, 125.4, 119.8, 113.7, 112.9, 112.8, 80.1, 21.1; HRMS (*m/z*, FAB^{+}) calcd. for C$_{26}$H$_{19}$N$_5$S 433.1361, found 433.1358.

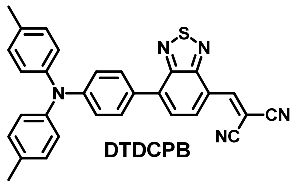

DTDCPB

2-{[7-(4-*N*,*N*-ditolylaminophenylen-1-yl)-2,1,3-benzothiadiazol-4-yl]methylene}-malononitrile (DTDCPB). A mixture of **3-3** (3.49 g, 12 mmol), 4-(*N*,*N*-ditolylamino)-1-(tri-*n*-butylstannyl)phenylene (8.1 g, 14.4 mmol), and PdCl$_2$(PPh$_3$)$_2$ (421 mg, 0.6 mmol) in anhydrous toluene (60 mL) was stirred and heated to 110 °C under argon for 5 h. After the reaction mixture was cooled to room temperature, the solvent was removed by rotary evaporation, and the crude product was purified by column chromatography on silica gel with dichloromethane/hexane (v/v, 4:3) as eluent, to afford **DTDCPB** as a black solid (4.43 g, 76%), mp 288 °C (DSC); IR (KBr) ν 3031, 2918, 2858, 2218, 1592, 1505, 1471, 1328, 1264, 1189, 1102, 946, 826 cm^{-1}; ^{1}H NMR (CDCl$_3$, 400 MHz) δ 8.82 (s, 1H), 8.78 (d, J = 7.6 Hz, 1H), 7.95 (d, J = 9.2 Hz, 2H), 7.84 (d, J = 7.6 Hz, 1H), 7.15–7.09 (m, 10H), 2.36 (s, 6H); ^{13}C NMR (CDCl$_3$, 100 MHz) δ 154.4, 152.6, 152.5, 150.0, 143.9, 140.0, 134.0, 130.7, 130.4, 130.0, 127.3, 125.7, 125.5, 121.1, 120.1, 113.9, 113.1, 81.8, 21.1; HRMS (*m/z*, FAB^{+}) calcd for C$_{30}$H$_{21}$N$_5$S, 483.1518, found, 483.1516.

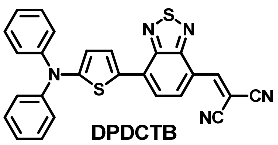

DPDCTB

2-{[7-(5-*N*,*N*-diphenylaminothiophen-2-yl)-2,1,3-benzothiadiazol-4-yl]methylene}malononitrile (DPDCTB). The synthetic procedure was similar to that of **DTDCPB**, except that the eluent for column purification was dichloromethane/hexane (v/v, 1:1). **DPDCTB** was isolated as a black solid (63%), mp 187 °C (DSC); IR (KBr) ν 3034, 2218, 1579, 1532, 1487, 1296, 1059, 756 cm^{-1}; ^{1}H NMR (CDCl$_3$, 400 MHz) δ 8.69 (s, 1H), 8.64 (d, J = 8.0 Hz, 1H), 8.22 (d, J = 4.0 Hz, 1H), 7.65 (d, J = 8.0 Hz, 1H), 7.40–7.36 (m, 4H), 7.32–7.29 (m, 4H), 7.21 (t, J = 7.2 Hz, 2H), 6.61 (d, J = 4.0 Hz, 1H); ^{13}C NMR (CDCl$_3$, 100 MHz) δ 159.7, 154.5, 151.7, 150.7, 146.4, 133.7, 132.5, 130.8, 129.6, 127.3, 125.3, 124.7, 121.5, 119.4, 116.2, 114.4, 113.6, 79.4; HRMS (*m/z*, FAB$^+$) calcd for $C_{26}H_{15}N_5S_2$, 461.0769, found, 461.0760.

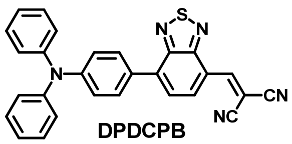

DPDCPB

2-{[7-(4-*N*,*N*-diphenylaminophenylen-1-yl)-2,1,3-benzothiadiazol-4-yl]methylene}malononitrile (DPDCPB). The synthetic procedure was similar to that of **DTDCPB**, except that the eluent for column purification was dichloromethane/hexane (v/v, 1:1). **DPDCPB** was isolated as a black solid (49%), mp 208 °C (DSC); IR (KBr) ν 3047, 2223, 1584, 1524, 1474, 1370, 1336, 1270, 1192, 1044, 931, 821 cm^{-1}; ^{1}H NMR (CDCl$_3$, 400 MHz) δ 8.83 (s, 1H), 8.79 (d, J = 7.6 Hz, 1H), 7.98 (d, J = 8.8 Hz, 2H), 7.86 (d, J = 7.6 Hz, 1H), 7.35–7.31 (m, 4H), 7.22–7.18 (m, 6H), 7.13 (t, J = 7.2 Hz, 2H); ^{13}C NMR (CDCl$_3$, 100 MHz) δ 154.4, 152.6, 152.5, 149.6, 146.6, 139.9, 130.7, 130.5, 129.4, 128.2, 125.8, 125.5, 124.2, 121.4, 121.3, 113.9, 113.1, 82.2; HRMS (*m/z*, FAB$^+$)

calcd for $C_{28}H_{17}N_5S$, 455.1205, found, 455.1204.

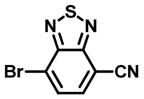

3-6

4-Bromo-7-cyano-2,1,3-benzothiadiazole (3-6). A mixture of **3-2** (16.3 g, 67.1 mmol) and hydroxylamine hydrochloride (9.32 g, 134.1 mmol) in dimethyl sulfoxide (250 mL) was stirred and heated at 100 °C for 2h. After the reaction mixture was cooled to room temperature, the resulting precipitate was collected by filtration, and the crude product was washed with methanol and then dichloromethane to afford **3-6** as a yellow solid (12.96 g, 80%), mp 259–260 °C; IR (KBr) ν 3080, 3040, 2232, 1528, 1480, 1375, 1102, 1032, 942, 876 cm^{-1}; ^1H NMR ($CDCl_3$, 400 MHz) δ 7.97–7.90 (m, 2H); ^{13}C NMR ($CDCl_3$, 100 MHz) δ 153.1, 152.3, 135.8, 131.4, 121.3, 114.7, 105.3. HRMS (*m/z*, FAB^+, $[M+H]^+$) calcd for $C_7H_3{}^{79}BrN_3S$ 239.9231, found 239.9225, calcd for $C_7H_3{}^{81}BrN_3S$ 241.9211, found 241.9207.

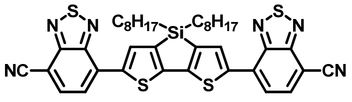

BCNDTS

BCNDTS. A mixture of **3-6** (2.52 g, 10.5 mmol), $PdCl_2(PPh_3)_2$ (351 mg, 0.5 mmol), and 5,5'-bis(tri-*n*-butylstannyl)-3,3'-di-*n*-octylsilylene-2,2'-bithiophene (5 mmol) in anhydrous toluene (50 mL) was stirred and heated at 110 °C under argon for 12 h. After the reaction mixture was cooled to room temperature, the solvent was removed by rotary evaporation. The resulting sticky mixture was added pentane and was then sonicated to generate the crude product, which was collected by filtration and purified by column chromatography on silica gel with chloroform as eluent to afford **BCNDTS**

as a black solid (1.60 g, 43%), mp 228 °C (DSC); IR (KBr) ν 3086, 3046, 2953, 2926, 2848, 2224, 1537, 1496, 1346, 1167, 1095, 882 cm^{-1}; ^{1}H NMR ($CDCl_3$, 400 MHz) δ 8.31 (s, 2H), 8.03 (d, *J* = 8.0 Hz, 2H), 7.90 (d, *J* = 8.0 Hz, 2H), 1.50–1.44 (m, 4H), 1.37–1.33 (m, 4H), 1.23 (m, 16H), 1.09–1.05 (m, 4H), 0.84–0.81 (m, 6H); ^{13}C NMR ($CDCl_3$, 100 MHz) δ 153.6, 152.7, 151.0, 145.3 140.3, 135.8, 133.0, 132.4, 122.9, 115.6, 102.4, 33.2, 31.9, 29.3, 29.2, 24.3, 22.7, 14.2, 11.9; HRMS (*m/z*, FAB$^+$) calcd for $C_{38}H_{40}N_6S_4Si$ 736.1967, found 736.1953.

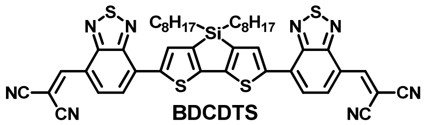

BDCDTS

BDCDTS. A mixture of **3-2** (2.55 g, 10.5 mmol), $Pd(PPh_3)_4$ (288 mg, 0.25 mmol), and 5,5’-bis(tri-*n*-butylstannyl)-3,3’-di-*n*-octylsilylene-2,2’-bithiophene (5 mmol) in anhydrous toluene (50 mL) was stirred and heated at 110 °C under argon for 12 h. After the reaction mixture was cooled to room temperature, the solvent was removed by rotary evaporation. The resulting sticky mixture was added pentane and was then sonicated to generate the crude product, which was collected by filtration and used for the next step without further purification. A mixture of the crude carbaldehyde product (2.50 g), malononitrile (887 mg, 13.44 mmol), and basic aluminum oxide (4 g) in anhydrous toluene (120 mL) was stirred and heated at 70 °C for 1 h. After the reaction mixture was cooled to room temperature, the basic aluminum oxide residue was removed by filtration and thoroughly washed with toluene. The solvent of the filtrate was removed by rotary evaporation, and the crude product was purified by column chromatography on silica gel with dichloromethane/hexane (v/v, 2:1) as eluent to afford **BDCDTS** as a black solid (1.59 g, 38%), mp 246 °C (DSC); IR (KBr) ν 3096, 3033, 2957, 2927, 2848, 2224, 1577, 1529, 1368, 1179, 1104, 1039, 885 cm^{-1}; ^{1}H NMR ($CDCl_3$, 400 MHz) δ 8.75–8.72 (m, 4H), 8.37 (s, 2H), 7.99 (d, *J* = 8.0 Hz, 2H), 1.53–1.47 (m, 4H), 1.40–1.35 (m, 4H), 1.28–1.24 (m, 16H), 1.13–1.09 (m, 4H), 0.85–0.82 (m, 6H); ^{13}C NMR ($CDCl_3$, 100 MHz) δ 154.1, 153.9, 151.6, 150.7, 146.2, 141.4, 133.6, 133.0, 130.4, 123.6, 121.2, 113.9, 113.2, 81.8, 33.3, 31.9, 29.3, 24.3, 22.7, 14.2, 11.9; HRMS (*m/z*, FAB^{+}) calcd for $C_{44}H_{42}N_8S_4Si$ 838.2185, found 838.2187.

Measurement of Electronic Absorption Spectra of Molecular Donors. Electronic absorption spectra of molecular donors in solutions and as thin films were recorded with spectrophotometers JASCO V-670 and PerkinElmer, respectively.

Crystal Structure Determinations. Crystallographic data were collected at 295(2) K on an Oxford Gemini A CCD diffractometer using graphite-monochromatized Cu-Kα radiation (λ = 1.54178 Å). Cell parameters were retrieved and refined using CrysAlis Pro software on all observed reflections. Data reduction was performed with the CrysAlis Pro software. The structures were solved and refined with SHELXL programs.[44] The hydrogen atoms were included in calculated positions and refined using a riding mode.

Cyclic Voltammetry Measurement. The electrochemical properties of molecular donors were investigated by cyclic voltammetry (CV). The measurement of oxidation potentials was carried out in an anhydrous CH_2Cl_2 solution (1.0 mM) containing 0.1 M tetrabutylammonium hexafluorophosphate ($TBAPF_6$) as a supporting electrolyte, while the measurement of the reduction potentials was conducted in an anhydrous THF solution (1.0 mM) containing 0.1 M tetrabutylammonium perchlorate (TBAP) as a supporting electrolyte, purged with argon prior to conduct the experiments. A glassy carbon electrode and a platinum wire was used as the working electrode and counter electrode, respectively. All potentials were recorded versus Ag/AgCl (saturated) as a reference electrode and calibrated with the ferrocene/ferrocenium (Fc/Fc$^+$) redox couple. All measurements were performed at a scan rate of 100 mV s^{-1}.

Quantum Mechanical Calculations. The electronic and optical properties of **DTDCTB** were estimated by density functional theory (DFT) and time-dependent DFT (TDDFT) calculations in CH_2Cl_2 solutions using hybrid B3LYP function with the 6-31G(d) basis set, as implemented in the Gaussian 09 (G09) program package.[45]

Solar Cell Fabrication and Testing. Fullerenes C_{60} and C_{70} as well as 2,9-dimethyl-4,7-diphenyl-1,10-phenanthroline (BCP) were subjected to purification at least once by temperature-gradient sublimation before use in this study. The organic and metal oxide thin films as well as metal electrodes were deposited onto indium tin oxide (ITO)-coated glass substrates by thermal evaporation in a high-vacuum chamber with base pressure of ~1×10^{-6} Torr. The sheet resistance of ITO was ~15 Ω/sq. The deposition was performed with the substrate held at room temperature. Thicknesses were monitored using a crystal oscillator during deposition and were verified later with spectroscopic ellipsometry. The active area of the cells had an average size of 2.5−5 mm^2 (intersection area between Ag cathode and ITO anode) and were carefully measured device-by-device using a calibrated optical microscope. Devices were encapsulated using a UV-cured sealant (Epowide EX, Everwide Chemical Co.) and a cover glass under an anhydrous nitrogen atmosphere after fabrication and were measured without a mask in air. Current density−voltage characteristics were measured with a SourceMeter Keithley 2636A under illumination of AM 1.5G solar light from a xenon lamp solar simulator (Abet Technologies). The incident light intensity was calibrated as 100 mW/cm^2. The external quantum efficiency (EQE) spectra were taken by illuminating chopped monochromatic light with a continuous-wave bias white light (from a halogen lamp) on the solar cells. The photocurrent signals were extracted with a lock-in technique using a current preamplifier (Stanford Research Systems) followed by a lock-in amplifier (AMETEK). The EQE measurement was fully computer-controlled, and the intensity of the monochromatic light was calibrated with an NIST-traceable optical power meter (Ophir Optronics).

Ultraviolet Photoelectron Spectroscopy Measurement. Organic films for photoelectron spectroscopy measurements were vacuum deposited onto fused-silica substrates. The thin-film HOMO levels of molecules were acquired with a photoelectron spectrometer (Riken Keiki Co. Ltd.).

Ellipsometry Measurement. Organic films for ellipsometry measurements were vacuum deposited onto fused-silica substrates. The measurements were carried out with a J. A. Woollam Inc. V-VASE variable-angle spectroscopic ellipsometer. The anisotropic optical constants of a sample were determined by the combination of reflection and transmission ellipsometry, which in principle is simpler and eliminates the risk of sample-to-sample variation.

Mobility Measurement. The electron and hole mobilities for the **DTDCTP/DTDCPB**:C_{70} blended films were determined using the space-charge limited current (SCLC) method.[46] The mobility values were calculated from the current density–voltage characteristics of SCLC devices that were measured with a SourceMeter Keithley 2636A and fitted by applying the modified Mott–Gurney equation:

$$J = \frac{9}{8}\varepsilon\varepsilon_0\mu_0\frac{V^2}{L^3}\exp\left(\frac{0.89\beta}{\sqrt{L}}\sqrt{V}\right)$$

Where J is the current density, V is the bias voltage, L is the thickness of the active layer, μ_0 is the zero-field mobility, ε is the dielectric constant, which was assumed to be 3, a typical value for organic materials, in the calculation, ε_0 is the permittivity of the free space (8.85×10^{-12} F/m), and β is the field-activation factor.

3-9 References

---

[1] Krebs, F. C. *Sol. Energy Mater. Sol. Cells* **2009,** *93,* 394.

[2] Tang, C. W. *Appl. Phys. Lett.* **1986,** *48,* 183.

[3] (a) Rand, B. P.; Genoe, J.; Heremans, P.; Poortmans, J. *Prog. Photovolt: Res. Appl.* **2007,** *15,* 659. (b) Walker, B.; Kim, C.; Nguyen, T.-Q. *Chem. Mater.* **2011,** *23,* 470. (c) Mishra, A.; Bäuerle, P. *Angew. Chem., Int. Ed.* **2012,** *51,* 2020. (d) Lin, Y.; Li, Y.; Zhan, X. *Chem. Soc. Rev.* **2012,** *41,* 4245.

[4] Hiramoto, M.; Fujiwara, H.; Yokoyama, M. *Appl. Phys. Lett.* **1991,** *58,* 1062.

[5] (a) Scharber, M. C.; Mühlbacher, D.; Koppe, M.; Denk, P.; Waldauf, C.; Heeger, A. J.; Brabec, C. J. *Adv. Mater.* **2006,** *18,* 789. (b) Dennler, G.; Scharber, M. C.; Ameri, T.; Denk, P.; Forberich, K.; Waldauf, C.; Brabec, C. J. *Adv. Mater.* **2008,** *20,* 579.

[6] Heliatek GmbH, press release of January 16, 2013 (http://www.heliatek.com).

[7] (a) Takacs, C. J.; Sun, Y.; Welch, G. C.; Perez, L. A.; Liu, X.; Wen, W.; Bazan, G. C.; Heeger, A. J. *J. Am. Chem. Soc.* **2012,** *134,* 16597. (b) Sun, Y.; Welch, G. C.; Leong, W. L.; Takacs, C. J.; Bazan, G. C.; Heeger, A. J. *Nat. Mater.* **2012,** *11,* 44.

[8] van der Poll, T. S.; Love, J. A.; Nguyen, T.-Q.; Bazan, G. C. *Adv. Mater.* **2012,** *24,* 3646.

[9] Kyaw, A. K. K.; Wang, D. H.; Gupta, V.; Zhang, J.; Chand, S.; Bazan, G. C.; Heeger, A. J. *Adv. Mater.* **2013,** *25,* 2397.

[10] Zhou, J.; Wan, X.; Liu, Y.; Zuo, Y.; Li, Z.; He, G.; Long, G.; Ni, W.; Li, C.; Su, X.; Chen, Y. *J. Am. Chem. Soc.* **2012,** *134,* 16345.

[11] Matsuo, Y.; Sato, Y.; Niinomi, T.; Soga, I.; Tanaka, H.; Nakamura, E. *J. Am. Chem. Soc.* **2009,** *131,* 16048.

[12] (a) Wei, G.; Wang, S.; Sun, K.; Thompson, M. E.; Forrest, S. R. *Adv. Energy Mater.*

2011, *1,* 184. (b) Wei, G.; Wang, S.; Renshaw, K.; Thompson, M. E.; Forrest, S. R. *ACS Nano* **2010,** *4,* 1927.

[13] Huang, J.; Zhan, C.; Zhang, X.; Zhao, Y.; Lu, Z.; Jia, H.; Jiang, B.; Ye, J.; Zhang, S.; Tang, A.; Liu, Y.; Pei, Q.; Yao, J. *ACS Appl. Mater. Interfaces* **2013,** *5,* 2033.

[14] Bottari, G.; de la Torre, G.; Guldi, D. M.; Torres, T. *Chem. Rev.* **2010,** *110,* 6768.

[15] Terao, Y.; Sasabe, H.; Adachi, C. *Appl. Phys. Lett.* **2007,** *90,* 103515.

[16] Xue, J.; Rand, B. P.; Uchida, S.; Forrest, S. R. *Adv. Mater.* **2005,** *17,* 66.

[17] (a) Wang, S.; Mayo, E. I.; Perez, M. D.; Griffe, L.; Wei, G.; Djurovich, P. I.; Forrest, S. R.; Thompson, M. E. *Appl. Phys. Lett.* **2009,** *94,* 233304. (b) Wei, G.; Lunt, R. R.; Sun, K.; Wang, S.; Thompson, M. E.; Forrest, S. R. *Nano Lett.* **2010,** *10,* 3555. (c) Wei, G.; Xiao, X.; Wang, S.; Zimmerman, J. D.; Sun, K.; Diev, V. V.; Thompson, M. E.; Forrest, S. R. *Nano Lett.* **2011,** *11,* 4261. (d) Wang, S.; Hall, L.; Diev, V. V.; Haiges, R.; Wei, G.; Xiao, X.; Djurovich, P. I.; Forrest, S. R.; Thompson, M. E. *Chem. Mater.* **2011,** *23,* 4789. (e) Wei, G.; Xiao, X.; Wang, S.; Sun, K.; Bergemann, K. J.; Thompson, M. E.; Forrest, S. R. *ACS Nano* **2012,** *6,* 972.

[18] Chen, G.; Sasabe, H.; Wang, Z.; Wang, X.-F.; Hong, Z.; Yang, Y.; Kido, J. *Adv. Mater.* **2012,** *24,* 2768.

[19] (a) Kronenberg, N. M.; Deppisch, M.; Würthner, F.; Lademann, H. W. A.; Deinga, K.; Meerholz, K. *Chem. Commun.* **2008,** 6489. (b) Bürckstümmer, H.; Kronenberg, N. M.; Gsänger, M.; Stolte, M.; Meerholz, K.; Würthner, F. *J. Mater. Chem.* **2010,** *20,* 240. (c) Bürckstümmer, H.; Tulyakova, E. V.; Deppisch, M.; Lenze, M. R.; Kronenberg, N. M.; Gsänger, M.; Stolte, M.; Meerholz, K.; Würthner, F. *Angew. Chem., Int. Ed.* **2011,** *123,* 11628. (d) Würthner, F.; Meerholz, K. *Chem. Eur. J.* **2010,** *16,* 9366.

[20] (a) Kronenberg, N. M.; Steinmann, V.; Bürckstümmer, H.; Hwang, J.; Hertel, D.;

Würthner, F.; Meerholz, K. *Adv. Mater.* **2010,** *22,* 4193. (b) Steinmann, V.; Kronenberg, N. M.; Lenze, M. R.; Graf, S. M.; Hertel, D.; Meerholz, K.; Bürckstümmer, H.; Tulyakova, E. V.; Würthner, F. *Adv. Energy Mater.* **2011,** *1,* 888.

[21] Fujishima, D.; Kanno, H.; Kinoshita, T.; Maruyama, E.; Tanaka, M.; Shirakawa, M.; Shibata, K. *Sol. Energy Mater. Sol. Cells* **2009,** *93,* 1029.

[22] Kageyama, H.; Ohishi, H.; Tanaka, M.; Ohmori, Y.; Shirota, Y. *Adv. Funct. Mater.* **2009,** *19,* 3948.

[23] Hirade, M.; Adachi, C. *Appl. Phys. Lett.* **2011,** *99,* 153302.

[24] Xiao, X.; Zimmerman, J. D.; Lassiter, B. E.; Bergemann, K. J.; Forrest, S. R. *Appl. Phys. Lett.* **2013,** *102,* 073302.

[25] (a) Yokoyama, D.; Wang, Z.; Pu, Y.-J.; Kobayashi, K.; Kido. J.; Hong, Z. *Sol. Energy Mater. Sol. Cells* **2012,** *98,* 472. (b) Wang, Z.; Yokoyama, D.; Wang, X.-F.; Hong, Z.; Yang, Y.; Kido, J. *Energy Environ. Sci.* **2013,** *6,* 249.

[26] (a) Schulze, K.; Uhrich, C.; Schüppel, R.; Leo, K.; Pfeiffer, M.; Brier, E.; Reinold, E.; Bäuerle, P. *Adv. Mater.* **2006,** *18,* 2872. (b) Fitzner, R.; Reinold, E.; Mishra, A.; Mena-Osteritz, E.; Ziehlke, H.; Körner, C.; Leo, K.; Riede, M.; Weil, M.; Tsaryova, O.; Weiß, A.; Uhrich, C.; Pfeiffer, M.; Bäuerle, P. *Adv. Funct. Mater.* **2011,** *21,* 897. (c) Fitzner, R.; Mena-Osteritz, E.; Mishra, A.; Schulz, G.; Reinold, E.; Weil, M.; Körner, C.; Ziehlke, H.; Elschner, C.; Leo, K.; Riede, M.; Pfeiffer, M.; Uhrich, C.; Bäuerle, P. *J. Am. Chem. Soc.* **2012,** *134,* 11064.

[27] Ohshita, J.; Nodono, M.; Kai, H.; Watanabe, T.; Kunai, A.; Komaguchi, K.; Shiotani, M.; Adachi, A.; Okita, K.; Harima, Y.; Yamashita, K.; Ishikawa, M. *Organometallics* **1999,** *18,* 1453.

[28] Coffin, R. C.; Peet, J.; Rogers, J.; Bazan, G. C. *Nat. Chem.* **2009,** *1,* 657.

---

[29] Chen, H.-Y.; Hou, J.; Hayden, A. E.; Yang, H.; Houk, K. N.; Yang, Y. *Adv. Mater.* **2010,** *22,* 371.

[30] Hou, J.; Chen, H.-Y.; Zhang, S.; Li, G.; Yang, Y. *J. Am. Chem. Soc.* **2008,** *130,* 16144.

[31] Yokoyama, D.; Setoguchi, Y.; Sakaguchi, A.; Suzuki, M.; Adachi, C. *Adv. Funct. Mater.* **2010,** *20,* 386.

[32] Ko, S.; Choi, H.; Kang, M.-S.; Hwang, H.; Ji, H.; Kim, J.; Ko, J.; Kang, Y. *J. Mater. Chem.* **2010,** *20,* 2391.

[33] Velusamy, M.; Thomas, K. R. J.; Lin, J. T.; Hsu, Y.-C.; Ho, K.-C. *Org. Lett.* **2005,** *7,* 1899.

[34] Dieckmann, A.; Bässler, H.; Borsenberger, P. M. *J. Chem. Phys.* **1993,** *99,* 8136.

[35] Ng, A. M. C.; Cheung, K. Y.; Fung, M. K.; Djurišić, A. B.; Chan, W. K. *Thin Solid Films* **2008,** *517,* 1047.

[36] Djurišić, A. B.; Fritz, T.; Leo, K. *J. Opt. A: Pure Appl. Opt.* **2000,** *2,* 458.

[37] (a) Casado, J.; Pappenfus, T. M.; Miller, L. L.; Mann, K. R.; Ortí, E.; Viruela, P. M.; Pou-AméRigo, R.; Hernández, V.; López Navarrete, J. T. *J. Am. Chem. Soc.* **2003,** *125,* 2524. (b) Pai, C.-L.; Liu, C.-L.; Chen, W.-C.; Jenekhe, S. A. *Polymer* **2006,** *47,* 699.

[38] (a) Li, G.; Shrotriya, V.; Huang, J.; Yao, Y.; Moriarty,T.; Emery, K.; Yang, Y. *Nat. Mater.* **2005,** *4,* 864. (b) Yang, L.; Zhang, T.; Zhou, H.; Price, S. C.; Wiley, B. J.; You, W. *ACS Appl. Mater. Interfaces* **2011,** *3,* 4075.

[39] Kim, M.-S.; Kim, B.-G.; Kim, J. *ACS Appl. Mater. Interfaces* **2009,** *1,* 1264.

[40] Koster, L. J. A.; Mihailetchi, V. D.; Blom, P. W. M. *Appl. Phys. Lett.* **2006,** *88,* 052104.

[41] Steinberger, S.; Mishra, A.; Reinold, E.; Levichkov, J.; Uhrich, C.; Pfeiffer, M.;

Bäuerle, P. *Chem. Commun.* **2011,** *47,* 1982.

[42] Welch, G. C.; Coffin, R.; Peet, J.; Bazan, G. C. *J. Am. Chem. Soc.* **2009,** *131,* 10802.

[43] Jørgensen, M.; Krebs, F. C. *J. Org. Chem.* **2005,** *70,* 6004.

[44] Sheldrick, G. M. SHELXL-97, Program for the Solution of Crystal Structures, University of Göttingen, Göttingen, Germany, 1997.

[45] Censo, D. D.; Fantacci, S.; Angelis, F. D.; Klein, C.; Evans, N.; Kalyanasundaram, K.; Bolink, H. J.; Grätzel, M.; Nazeeruddin, M. K. *Inorg. Chem.* **2008,** *47,* 980.

[46] Yasuda,T.; Yamaguchi, Y.; Zou, D.-C.; Tsutsui, T. *Jpn. J. Appl. Phys.* **2002,** *41* (Part 1), 5626.

Chapter 4. Development of Polymeric Donors for Bulk Heterojunction Solar Cells

4-1 Introduction

Over the past two decades, most research efforts in the organic solar cells (OSCs) community have focused on solution-processed polymer bulk heterojunction (BHJ) solar cells based on a blend of p-type conjugated polymers and n-type soluble fullerene derivatives as the active layer.[1] Significant progress on photovoltaic performance has been made in this field, primarily stemming from combined improvements in material design,[2] morphology control,[3] interface modification,[4] and device engineering.[5] Among all these various factors, the polymeric donors undoubtedly play the most critical role in determining the solar cell performance, and thereby the search for new p-type semiconducting polymers with appropriate properties such as a small bandgap, well-aligned energy levels, a sufficient solubility, a superior miscibility with fullerene acceptors, and a high hole mobility, etc. has taken center stage in the research activities.

The most widely investigated conjugated homopolymer for use in BHJ solar cells is regioregular poly(3-hexylthiophene) (**P3HT**) due to its several fascinating properties including the structural regularity, strong absorption coefficient, and high hole mobility as well as good inherent miscibility with fullerene acceptors. Reproducible PCEs of 4−5% have been realized for the **P3HT**/[6,6]-phenyl-C_{61}-butyric acid methyl ester ($PC_{61}BM$)-based cells.[3a–b, 4a] Moreover, with the indene–$C_{60(70)}$ bisadduct [$IC_{60(70)}BA$] as the acceptor,[6] a higher PCE of 6.48%[6c] and 6.68%[6d] was achieved for the **P3HT**/$IC_{60}BA$- and **P3HT**/$IC_{70}BA$-based cells, respectively. The efficiency improvements were mainly attributed to the increase in V_{oc} in that the $IC_{60}BA$ and

$IC_{70}BA$ acceptor had a higher-lying LUMO level by 0.17 and 0.19 eV than $PC_{61}BM$ and $PC_{71}BM$, respectively. However, the wide bandgap (1.9 eV) and very high-lying HOMO level (−5.1 eV) of **P3HT** severely limit further efficiency improvement.

To overcome the drawbacks of **P3HT**, materials scientists have been shifting the research focus to develop alternating conjugated copolymers of lower bandgaps, in order to harvest more photons from the solar spectrum and thus reach even higher efficiencies. Several state-of-the-art polymeric donors achieving PCEs of 7–8% in simple conventional or inverted BHJ devices with $PC_{61(71)}BM$ as the acceptor are shown in Scheme 4-1. The polymer **PTB7** developed by Yu et al. was the first to display PCEs of over 7% (see section 4-2 for a detailed description). The two-dimensional conjugated polymer **PBDTTT-C-T** with alkylthienyl groups on the benzo[1,2-*b*:4,5-*b'*]dithiophene (BDT) unit exhibited a higher PCE of 7.6% than its alkoxy-substituted counterpart, due to its smaller bandgap, lower-lying frontier energy levels, and significantly higher hole mobility.[7] With the thienopyrrole-4,6-dione as the electron-deficient unit, the three alternating D−A copolymers (**PDSTPD**,[8] **P-Ge**,[9] and **PBTTPD**[10]) all achieved PCEs of 7.3%, and high V_{oc} values of 0.85−0.92 V. Note that **P-Ge** possessed a smaller bandgap and higher-lying HOMO level than **PDSTPD** through the isoelectronic substitution of germanium for silicon as the bithiophene bridging atom. Fluorine has attracted significant attention as an electron-withdrawing substituent used in photovoltaic polymers since Yu's pioneering work, as a result of its small size that is expected to minimize the undesired steric hindrance between the adjacent monomer units. This kind of structural modification usually caused the resulting fluorinated polymers to display decreased frontier energy levels but a similar bandgap as compared to those of their non-fluorinated counterparts. By this approach, the three BDT-based D−A polymers employing various fluorinated electron-deficient units such as BT[11]

(**PBnDT-DTffBT**), [*d*][1,2,3]benzotriazole[12] (**PBnDT-FTAZ**), and quinoxaline[13] (**PBDT-TFQ**) all reached higher PCEs of over 7% than their non-fluorinated counterparts, via the simultaneous enhancement of V_{oc}, J_{sc}, and FF. It is worth mentioning that the higher hole mobility of the fluorinated polymes was responsible for the increase in J_{sc} and FF.

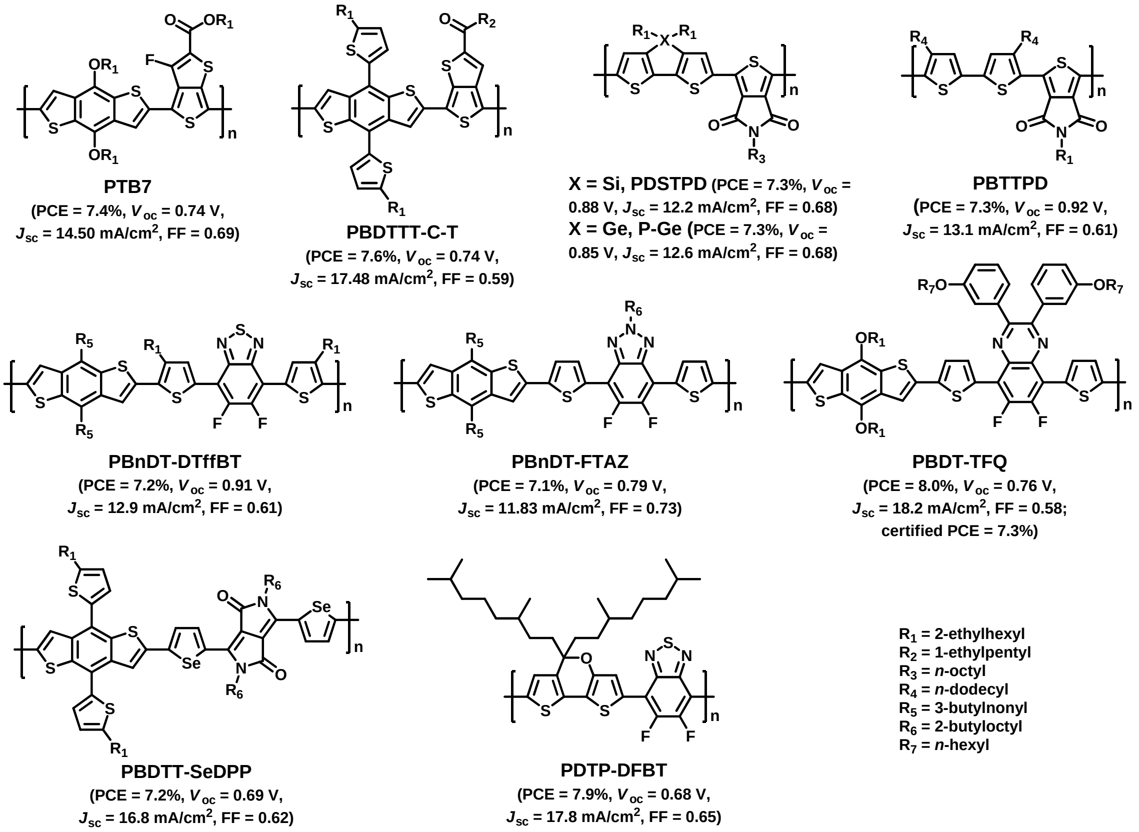

Scheme 4-1. Several state-of-the-art polymeric donors with PCEs of 7–8%.

In addition to these abovementioned medium-bandgap polymers with bandgaps of 1.8–1.6 eV (except for **PBnDT-FTAZ** that has a bandgap of 2.0 eV), two low-bandgap polymers (**PBDTT-SeDPP**[14] and **PDTP-DFBT**[15]) possessing bandgaps less than 1.5 eV also reached PCEs surpassing 7%. The selenophene-containing polymer

PBDTT-SeDPP and the dithienopyran-containing polymer **PDTP-DFBT** both exhibited a smaller bandgap, higher-lying HOMO level as well as higher hole mobility than its furan/thiophene-based analogues and cyclopentadithiophene-based analogue, respectively. These research advances in low-bandgap polymers directly contributed to the great success in tandem solar cells, whose efficiencies have been limited to below 7% for a while due to the lack of high-performance low-bandgap polymers.[16] Recently, a record-high PCE of 10.6% certified by NREL was obtained for a double-junction tandem cell consisting of two subcells and an interconnecting layer, in which the front cell contains a blend of **P3HT** and $IC_{60}BA$, while the rear cell is based on a blend of **PDTP-DFBT** and $PC_{61}BM$.[15]

In this chapter, two new p-type conjugated polymers, which were developed during my stay in the Prof. Luping Yu's lab at the Department of Chemistry, The University of Chicago, would be discussed. Their corresponding solar cell devices were fabricated and tested by Mr. Luyao Lu in the Yu research group.

4-2 A New PTB Family Polymer

Among all the p-type semiconducting polymers reported to date, the series of conjugated polymers (i.e., **PTB** series, Scheme 4-2) composed of alternating BDT and ester-substituted thieno[3,4-*b*]thiophene units represents the most successful example.[17] The BDT unit is one of the most widely employed building blocks for the construction of small-molecule and polymeric materials used in organic field-effect transistors and OSCs, due to its rigidly coplanar conformation and proper side chain patterns as well as easy functionalization.[18] The adoption of thieno[3,4-*b*]thiophene can increase the quinoid character of the ground state through stabilization of the quinoid resonance structure and thus endow the resulting polymers with small bandgaps. In addition, the electron-withdrawing ester group is introduced to stabilize the electron-rich thieno[3,4-*b*]thiophene, thus rendering the resulting polymers oxidatively stable. More importantly, the introduction of the second electron-withdrawing group, the fluorine atom, onto thieno[3,4-*b*]thiophene provides the resulting polymers with decreased frontier energy levels and similar bandgaps, leading to enhanced V_{oc} without losing J_{sc} for the BHJ devices based on the fluorinated polymers. Overall, **PTB7** exhibited the best PCEs of up to 7.40%, along with a V_{oc} of 0.74 V, a J_{sc} of 14.50 mA/cm^2, and a FF of 68.97%, in conventional devices with PC$_{71}$BM as the acceptor.[17c] Later, an exceptionally high PCE of 9.2% was achieved for the **PTB7**/PC$_{71}$BM-based device by adopting an inverted configuration in conjunction with incorporation of a thin layer of alcohol-/water-soluble conjugated polymer as a surface modifier for the ITO cathode.[19]

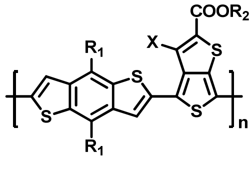

PTB1: X = H, R$_1$ = *n*-octyloxy, R$_2$ = *n*-dodecyl
PTB2: X = H, R$_1$ = *n*-octyloxy, R$_2$ = 2-ethylhexyl
PTB3: X = H, R$_1$ = *n*-octyl, R$_2$ = 2-ethylhexyl
PTB4: X = F, R$_1$ = 2-ethylhexyloxy, R$_2$ = *n*-octyl
PTB5: X = H, R$_1$ = 2-ethylhexyloxy, R$_2$ = *n*-octyl
PTB6: X = H, R$_1$ = *n*-octylloxy, R$_2$ = 2-butyloctyl
PTB7: X = F, R$_1$ = 2-ethylhexyloxy, R$_2$ = 2-ethylhexyl
PTB8: X = F, R$_1$ = 2-butyloctyloxy, R$_2$ = 2-ethylhexyl
PTB9: X = H, R$_1$ = 2-ethylhexyloxy, R$_2$ = 2-ethylhexyl

Scheme 4-2. Chemical structures of **PTB1**−**PTB9**.

The success of the **PTB** series of polymers can be attributed to their several unique features: (i) all the polymers have a small optical bandgap of about 1.6 eV and show absorption maxima around the region with the highest photon flux of the solar spectrum (about 700 nm); (ii) the lamellar packing structure with both the conjugated backbone and side chains parallel to the substrate, the rigidity induced by the BDT unit, and the planarity along the polymer backbone enhanced by the high degree of quinoidization all contribute to their high hole mobilities; (iii) the flexibility in structure modification including the incorporation of various side chains and/or an electron-withdrawing fluorine atom onto the polymer backbone makes it easy to not only fine-tune their energy levels but also control their solubilities and miscibilities with fullerene acceptors. Delicate manipulation of the latter can result in a preferred blend film morphology for efficient charge separation and charge transport.

Even though remarkable achievements have already been accomplished in the **PTB7**-based systems, further improvements in PCEs are still highly required. In this aspect, the moderate V_{oc} values suggest room for further optimization. Previous study revealed that the replacement of the alkoxy side chains on the BDT unit with less electron-donating alkyl chains lowers both the HOMO and LUMO energy levels of the resulting polymer (**PTB2** vs **PTB3**), and meanwhile keeps their optical bandgaps almost unchanged. In addition, the alkyl-grafted **PTB3** showed a higher hole mobility than the alkoxy-grafted **PTB2**. More importantly, the **PTB3**-based device exhibited a higher V_{oc} than the **PTB2**-based device without losing the J_{sc}, thus reaching a higher PCE.[17b] On the basis of the abovementioned considerations, in this work, we further synthesized a new **PTB** family polymer **PTB10** as an analogue for **PTB7** (Scheme 4-3), in which the branched 3-ethylheptyl side chains are employed in place of the 2-ethylhexyloxy chains on the BDT moiety due to their structural similarity.

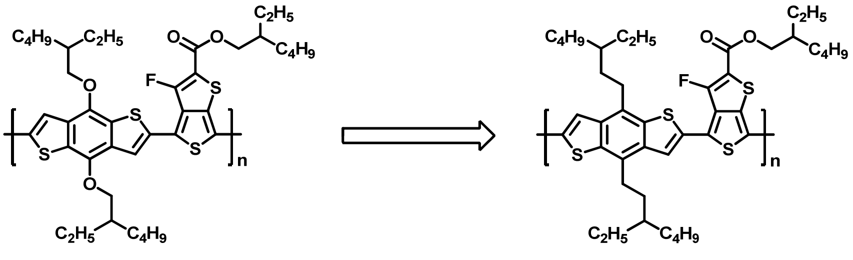

Scheme 4-3. Chemical structures of **PTB7** and **PTB10**.

4-2-1 Synthesis

The synthesis of **PTB10** is depicted in Scheme 4-4. The 3-ethylhept-1-yne **4-2** was prepared using Corey−Fuchs reaction that involved the treatment of the commercially available 2-ethylhexanal with triphenylphosphine/carbon tetrabromide to afford 1,1-dibromoalkene **4-1**, which was subsequently treated with *n*-butyl lithium followed by quenching with water. Nucleophilic addition of 3-ethylhept-1-nylmagnesium chloride, as generated *in situ* from **4-2** by reacting with isopropylmagnesium chloride, to benzo[1,2-*b*:4,5-*b′*]dithiophene-4,8-dione followed by reduction with tin(II) chloride gave **4-3**. Reduction of **4-3** using sodium borohydride and acetic acid in the presence of a catalytic amount of 10% Pd/C in isopropanol afforded **4-4**.[20] Note that the reagents used here to conduct this conversion are more easily accessible than those in the reported condition, which required an external supply of 30 atm of hydrogen gas as the reducing agent.[21] Deprotonation of **4-4** with *n*-butyl lithium followed by reaction of the resulting dianion with trimethyltin chloride yielded the distannyl monomer **4-5**. Finally, the polymer **PTB10** was synthesized via the Stille polycondensation reaction between 2'-ethylhexyl-4,6-dibromo-3-fluorothieno[3,4-*b*]thiophene-2-carboxylate and **4-5** at 120 °C in a mixture of toluene/DMF (4/1) using $Pd(PPh_3)_4$ as the catalyst. The number-average molecular weight (M_n) and polydispersity index (PDI) of **PTB10** were 15.4 kg/mol and 2.14, respectively, as determined by gel permeation chromatography using THF as the eluent and polystyrene as the standard. **PTB10** exhibited a good solubility in many common organic solvents, such as THF, chloroform, and even hexane. Nevertheless, given the low molecular weight and good solubility in hexane for this batch of **PTB10**, further optimizations in the polymerization conditions and/or purification of the monomers are necessary to obtain high-molecular-weight **PTB10**.[22] The high-molecular-weight polymers have demonstrated superior photovoltaic performance to their low-molecular-weight counterparts via promotion of hole mobility, optical property, and film morphology.[23]

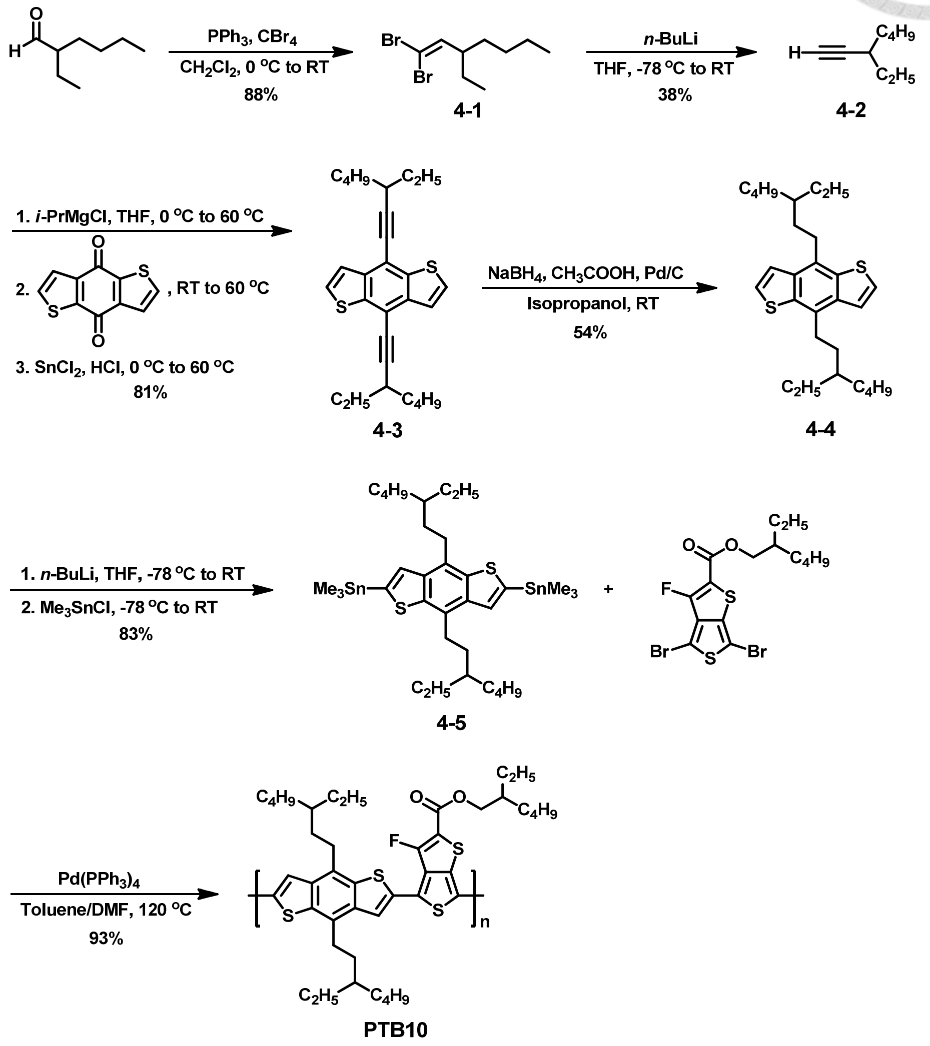

Scheme 4-4. Synthetic route to the polymer **PTB10**.

4-2-2 Optical Properties

Figure 4-1 shows the electronic absorption spectra of **PTB10** in a $CHCl_3$ solution and as a thin film spin-cast from chlorobenzene. The absorption spectrum of **PTB10** in $CHCl_3$ showed a band with a maximum at 609 nm. The **PTB10** thin film exhibited a slightly red-shifted absorption band at λ_{abs} = 612 nm accompanied by a pronounced absorption shoulder, indicative of a higher degree of chain aggregation in the solid state.[24] In addition, this shoulder was less distinct than those observed for other **PTB** family polymers,[17] which is attributed to the low molecular weight of **PTB10**. It was reported that there is a strong dependence of aggregation on the molecular weight of conjugated polymers.[25] The optical bandgap calculated from the onset of the thin-film absorption spectrum was determined to be 1.68 eV. This value is close to those for other **PTB** family polymers,[17] indicating that the structural variations of this series of polymers including the replacement of the alkoxy side chains on the BDT unit with less electron-donating alkyl chains and/or attachment of an electron-withdrawing fluorine atom on the thieno[3,4-*b*]thiophene moiety have little effects on their optical bandgaps.

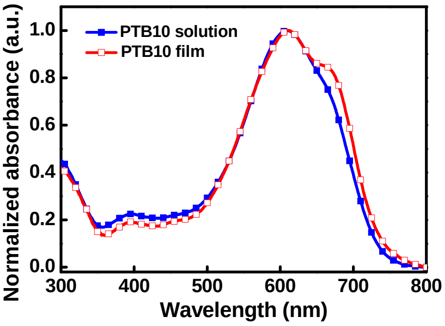

Figure 4-1. Normalized absorption spectra of **PTB10** in a $CHCl_3$ solution and as a thin film.

4-2-3 Electrochemical Properties

CV was used to study the electrochemical properties and evaluate the frontier energy levels of **PTB10**. As shown in Figure 4-2, **PTB10** showed one quasi-reversible oxidation wave and one quasi-reversible reduction wave. The HOMO and LUMO energy levels of **PTB10** were calculated to be −5.29 and −3.35 eV, respectively, on the basis of the onset redox potentials. In consistency with the previous results of **PTB2** and **PTB3**, the HOMO and LUMO levels of **PTB10** are lower than those of **PTB7**.[17c]

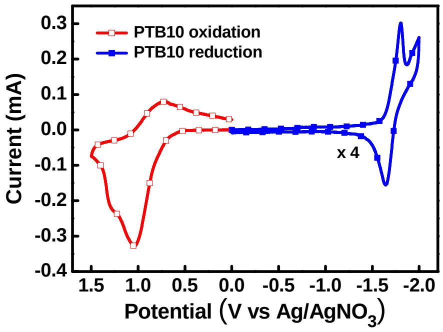

Figure 4-2. Cyclic voltammograms of **PTB10** thin film drop-cast on a glassy carbon electrode in a 0.1 M Bu_4NPF_6/CH_3CN solution.

4-2-4 Photovoltaic Characteristics

The photovoltaic performance of **PTB10** was investigated in BHJ solar cells with the device structure of ITO/PEDOT:PSS/**PTB10**:PC$_{71}$BM (1:1.5, by weight)/Ca/Al. The PC$_{71}$BM was used as the acceptor counterpart due to its stronger light absorption in the visible region relative to PC$_{61}$BM. The **PTB10**:PC$_{71}$BM composite film was prepared by spin-coating a mixed solvent of chlorobenzene/1,8-diiodoctane (97:3, v/v) solution (concentration, 25 mg mL^{-1}) at 2,000 r.p.m. for 60 sec. The 1,8-diiodoctane has been shown to be an useful additive for solvents used to cast BHJ layers.[26] Furthermore, the previous studies revealed the **PTB** series/PC$_{61(71)}$BM blend film prepared from this solvent mixture generally shows a preferred morphology for efficient charge separation and transport.[17b–c] The J–V characteristics of the **PTB10**:PC$_{71}$BM device measured under simulated AM 1.5 G illumination at an intensity of 100 mW/cm^2 is shown in Figure 4-3. The device delivered a V_{oc} of 0.77 V, a J_{sc} of 13.6 mA/cm^2, and a FF of

69.1%, leading to a PCE of 7.28%. As expected, the V_{oc} obtained here was higher than that of the **PTB7**-based device because of the lower HOMO level of **PTB10**. However, the lower J_{sc}, possibly stemming from the low molecular weight of **PTB10**, resulted in a slightly inferior PCE.[23,24]

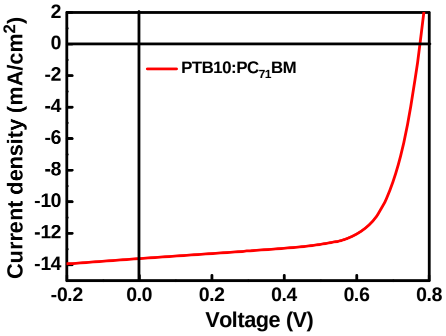

Figure 4-3. The *J*–*V* curve of the **PTB10**:PC$_{71}$BM BHJ device.

4-3 A p-Type Polymer Based on a Nine-Ringed Heteroacene

In recent few years, a popular strategy for the development of p-type alternating D–A polymers has been to utilize heteroacenes with extended π-conjugated structures as the electron-rich units. The rigid and coplanar conformation of these highly fused π-conjugated units can suppress rotational disorder around interannular single bonds and thus can allow for maximum π orbital overlap between adjacent aromatic/heteroaromatic rings, which in turn extends the effective conjugation length to facilitate π-electron delocalization. Owing to these fascinating structural features, namely coplanarity, rigidity, and extended π-conjugation, the benefits of this design concept are two-fold. First, the bandgaps of the corresponding polymers could possibly be narrowed. More importantly, an enhanced intrinsic charge carrier mobility would be realized through the reduction of reorganization energy.[27] Some of the efficient polymers in this class with PCEs in excess of 6% are shown in Scheme 4-5, the PCE being 6.4% for ***a*-PTPTBT**,[28] 7.0% for **PFDCTBT-C8**,[29] 6.6% for **PBDCPDT-TPD**,[30] 7.03% for **PIDTT-DFBT**,[31] and 7.2% for **pDTTG-TPD**.[32]

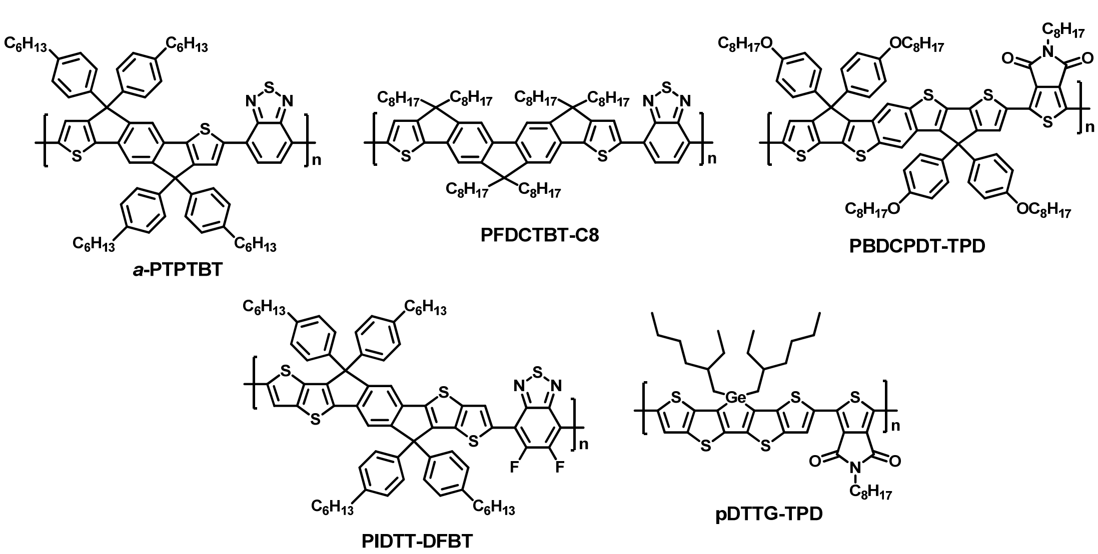

Scheme 4-5. Efficient semi-ladder polymers with PCEs of over 6%.

Compared to alternating D–A polymers, such an approach has been relatively less applied to the development of polymers based on prequinoid building blocks. Recently, Yu et al. reported a series of polymeric donors (**PTAT-x**, one of which shown in Scheme 4-6), in which the BDT block introduced in the **PTB** series of polymers is replaced with a two-dimensional extended π-conjugated unit, tetrathienoanthracene.[33] The study revealed that the **PTAT-3**:PC$_{61}$BM device exhibits a superior PCE of 5.62% to that based on **PTB8**, with similar side chains to those on **PTAT-3**. This better photovoltaic performance was mainly attributed to the more efficient charge transport that resulted from enhanced π–π staking in the polymer backbone induced by the tetrathienoanthracene unit. In addition, another series of p-type polymers **PTDBDx** based on a linearly fused conjugated unit, dithieno[2,3-*d*:2',3'-*d'*]benzo[1,2-*b*:4,5-*b'*]dithiophene, was also reported (one of which shown in Scheme 4-6).[34] The BHJ device based on the **PTDBD2**:PC$_{71}$BM blend showed the best PCE of 7.6%. Along these lines, in this work, we developed a new class of nine-ringed ladder-type heteroacene possessing three BDT units fused in a linear fashion, and utilized it as a building block to construct p-type semiconducting polymers for photovoltaic applications (Scheme 4-7 and Scheme 4-8).

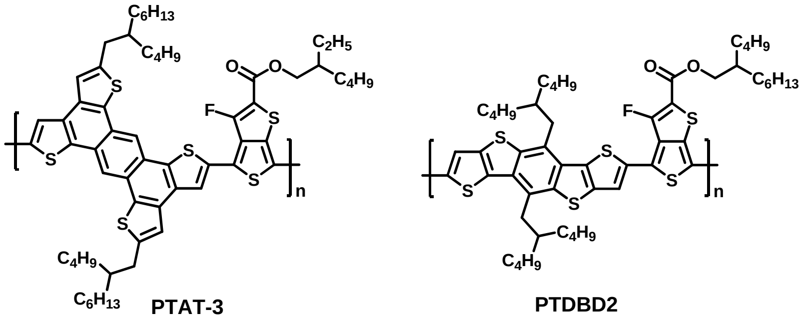

PTAT-3
(PCE = 5.62%, V_{oc} = 0.66 V,
J_{sc} = 15.0 mA/cm^2, FF = 0.58)

PTDBD2
(PCE = 7.6%, V_{oc} = 0.89 V,
J_{sc} = 13.0 mA/cm^2, FF = 0.65)

Scheme 4-6. Chemical structures of **PTAT-3** and **PTDBD2**.

4-3-1 Synthesis

Scheme 4-7 shows the synthetic pathways toward the two nine-ringed heteroacenes **4-9a** and **4-9b**, which only differ by the pendant side chains, and were independently prepared in order to examine their individual solubilities. Starting from 4,8-bis(2-ethylhexyloxy)- or 4,8-bis(3-ethylheptyl)benzo[1,2-*b*:4,5-*b*′]dithiophene, compounds **4-6** were synthesized by selective mono-deprotonation with 1.05 equiv of *n*-butyl lithium followed by reaction of the resulting monoanions with chlorotriisopropylsilane (TIPS-Cl). **4-6** were treated with *n*-butyl lithium and then quenched with tri-*n*-butyltin chloride to yield **4-7**, which were used without further purification in the next step. Stille coupling reactions of **4-7** with 1,4-dibromo-2,5-didodecyl-3,6-bis(methylsulfinyl)benzene gave **4-8**. Treatment of **4-8** with trifluoroacetic acid in the presence of phosphorus pentoxide at room temperature overnight induced double intramolecular electrophilic ring closure.[35] It is worthwhile to mention that the use of triflic acid, the most frequently used strong acid in this type of reactions,[36] failed to give the desired product in our initial attempts. Finally, demethylation of the intermediate sulfonium salts in refluxing pyridine furnished the target compounds **4-9** in moderate yields. Interestingly, the TIPS groups, which were introduced to eliminate competing intermolecular reactions at the terminal α-positions, were simultaneously removed during the acid-induced cyclization reaction.

Owing to the poor solubility of **4-9b**, only **4-9a** was converted into its corresponding distannyl derivative **4-10** (Scheme 4-8), which was then copolymerized with 2'-ethylhexyl-4,6-dibromo-3-fluorothieno[3,4-*b*]thiophene-2-carboxylate via the Stille coupling reaction to generate the polymer **PTTB**. Unfortunately, the resulting polymer still had a very poor solubility and precipitated out during polymerization. As a result, its molecular weight (M_n) only reached 9.0 kg/mol, with a PDI of 1.43.

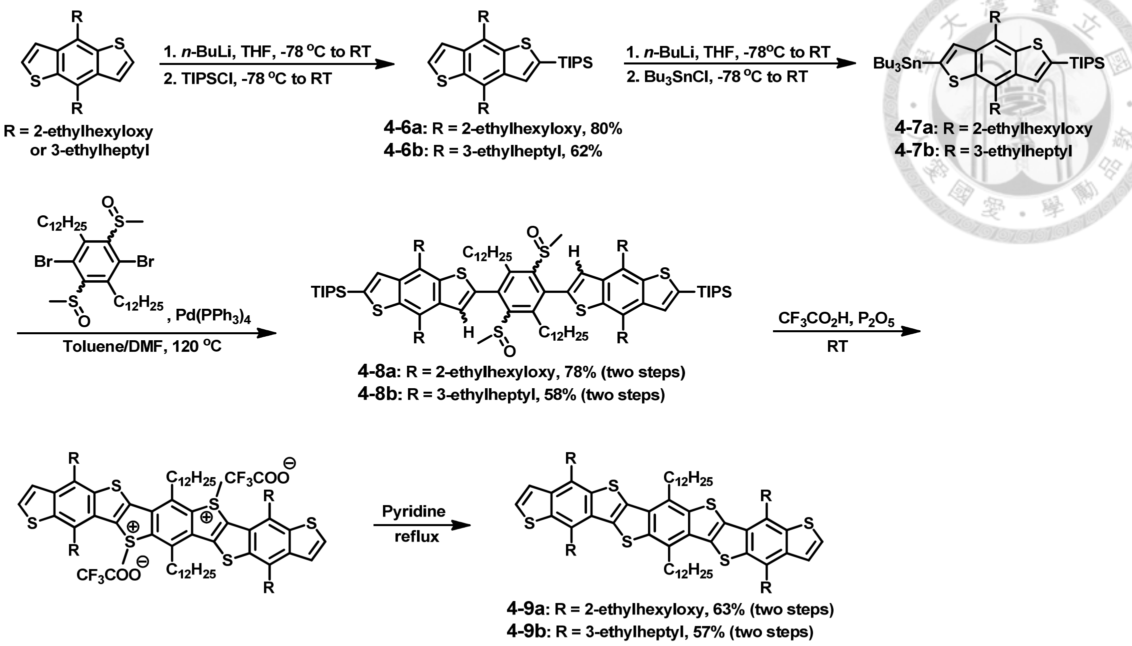

Scheme 4-7. Synthesis of the nine-ringed heteroacenes **4-9a** and **4-9b**.

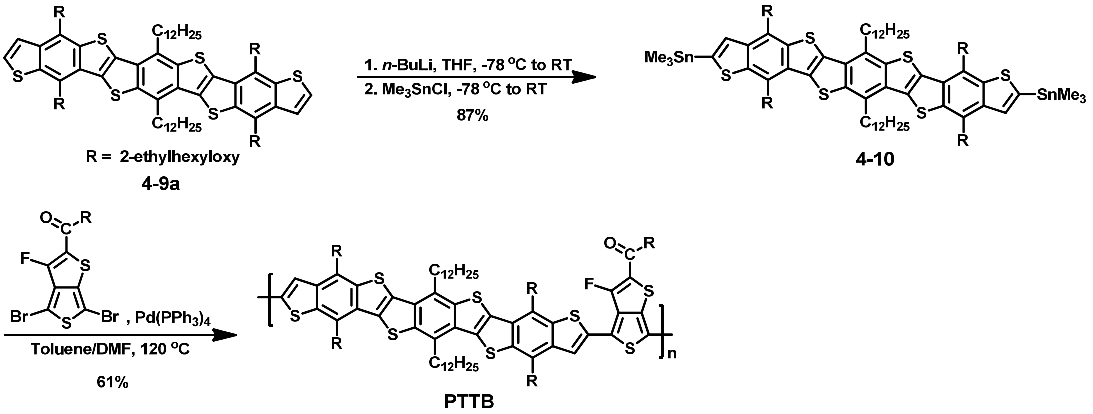

Scheme 4-8. Synthesis of the polymer **PTTB**.

4-3-2 Optical Properties

Figure 4-4 illustrates the UV−vis absorption and emission spectra of the nine-ringed heteroacenes **4-9a** and **4-9b** in $CHCl_3$ solutions, both of which showed distinct vibronic structures that are typical of rigid conjugated systems. Both molecules displayed similar absorption profiles, indicative of no pronounced perturbation on the variation of peripheral side chains, even though the longest wavelength absorption band of **4-9a** was slightly red-shifted compared to that of **4-9b** (λ_{max} = 430 nm for **4-9a** and 428 nm for **4-9b**, Figure 4-4c). The trend noted in the absorption spectra was also observed in the emission spectra with bathochromic shifts between **4-9a** and **4-9b**. The Stokes shifts were rather small and they were smaller for **4-9b** (ca. 0.03 eV) than for **4-9a** (ca. 0.09 eV). Again, the small Stokes shifts and the mirror images between the absorption and emission spectra indicate a small structural difference between the excited and ground states due to the high structural rigidity arising from a high degree of ring fusion. In addition, the larger Stokes shift of **4-9a** relative to **4-9b** suggest that **4-9a** is less rigid than **4-9b** in spite of their identical skeleton, which is in reasonable agreement with the fact that **4-9a** showed a better solubility than **4-9b**.

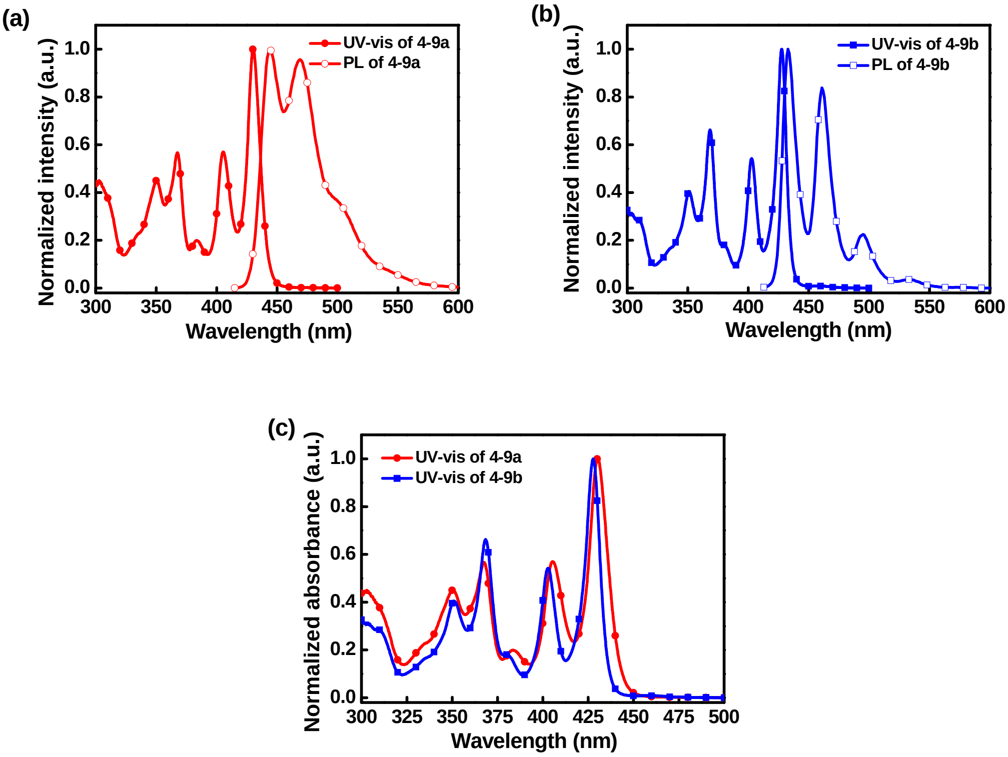

Figure 4-4. Normalized absorption and emission spectra of **4-9a** and **4-9b** in $CHCl_3$.

The absorption spectra of **PTTB** in a $CHCl_3$ solution and as a thin film are shown in Figure 4-5. In $CHCl_3$, **PTTB** displayed an intense absorption band ranging from 480−700 nm with two major peaks at 575 and 609 nm. This absorption band in the thin-film spectrum was slightly red-shifted. The nearly identical profiles of these two spectra indicate that **PTTB** shows a quite small conformational change from solution to solid state due to the high rigidity and planarity of its polymer backbone and/or the fact that **PTTB** aggregates strongly in solution.[24] Compared to the **PTB** series of polymers, **PTTB** possessed a lager optical bandgap of 1.83 eV deduced from the thin-film absorption edge. This can be rationalized by the reduced quinoid character of the **PTTB** main chain that arises from the fact that the π-electron delocalization from **4-9a** into the polymer backbone is less favorable than that from the BDT unit, due to the higher degree of aromaticity of the multifused **4-9a** over the three-ringed BDT unit.[37] In addition, it should also be noted that the relative intensity of the high-energy band next to the main absorption band, which comes from the localized π−π* transition of the linearly fused conjugated units, was higher for **PTTB** than for the **PTB** series of polymers.

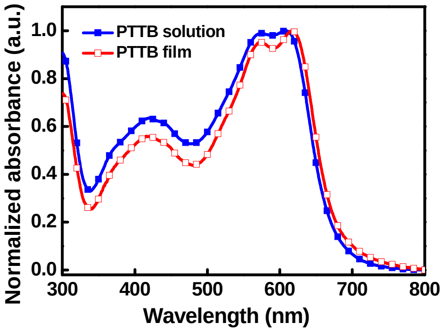

Figure 4-5. Normalized absorption spectra of **PTTB** in a $CHCl_3$ solution and as a thin film.

4-3-3 Electrochemical Properties

The electrochemical behaviors of **PTTB** were studied by CV to measure its frontier energy levels. As shown in Figure 4-6, **PTTB** presented one reversible p-doping and one irreversible n-doping process. The HOMO and LUMO energy levels of **PTTB** were estimated to be −5.36 and −3.17 eV, respectively, on the basis of the onset redox potentials.

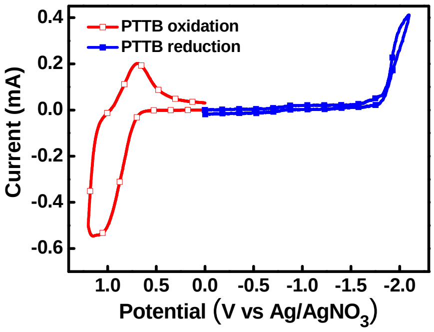

Figure 4-6. Cyclic voltammograms of **PTTB** thin film cast on a glassy carbon electrode in a 0.1 M Bu_4NPF_6/CH_3CN solution.

4-3-4 Photovoltaic Characteristics

In the preliminary investigation on the photovoltaic performance of **PTTB**, a BHJ solar cell based on the device configuration of ITO/PEDOT:PSS/**PTTB**:$PC_{71}BM$ (1:1.5 by weight)/Ca/Al was fabricated. The **PTTB**:$PC_{71}BM$ blend film was prepared by spin-coating a mixed solvent of chlorobenzene/1,8-diiodoctane (97:3, v/v) solution (concentration, 25 mg mL^{-1}) at 2,000 r.p.m. for 90 sec. Figure 4-7 shows the *J*–*V* curve of the **PTTB**:$PC_{71}BM$ device under simulated AM 1.5 G irradiation conditions (100 mW/cm^2). The device gave a V_{oc} of 0.72 V, a J_{sc} of 11.2 mA/cm^2, and a FF of 67.9%, yielding a moderate PCE of 5.47%.

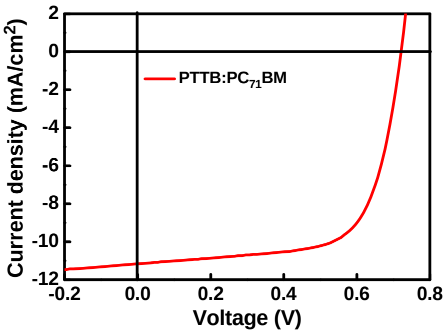

Figure 4-7. The *J–V* curve of the **PTTB**:PC$_{71}$BM BHJ device.

4-4 Conclusions

In Section 4-2, we synthesized a new **PTB** family polymer **PTB10** as an analogue for **PTB7**, in which the branched 3-ethylheptyl side chains are introduced onto the BDT unit. The most critical step in making the BDT monomer for **PTB10**, the conversion of the branched alkynyl side chains to alkyl, was carried out using easily accessible reducing agents. This structural modification to the BDT unit endowed **PTB10** with a lower-lying HOMO energy level than **PTB7**. Accordingly, an enhanced V_{oc} of 0.77 V was realized in the **PTB10**-based device. Unfortunately, the overall PCE of 7.28% obtained here was still slightly lower than that of the **PTB7**-based device due to the inferior J_{sc}. However, given the close PCEs between these two devices as well as the low molecular weight and good solubility in hexane of **PTB10**, we expect that a substantial improvement in PCEs would be highly achievable if the device is fabricated based on the high-molecular-weight **PTB10**.

In section 4-3, two novel linearly fused nine-ringed ladder-type heteroacenes **4-9a** and **4-9b**, which only differ by the pendant side chains, were synthesized through a facile synthetic route. The use of the relatively mild trifluoroacetic acid proved critical for the success in the electrophilic ring closure reaction. With a decent solubility allowing for further derivatization, **4-9a** was applied as a building block to construct a new p-type conjugated polymer **PTTB**. Optical measurements revealed that **PTTB** exhibits a hypsochromic shift in absorption as compared to the **PTB** series of polymers, due to the reduced quinoid character of the **PTTB** backbone. The BHJ device based on the **PTTB**/$PC_{71}BM$ blend delivered a moderate PCE of 5.47%. The preliminary results suggest that this new type of heteroacene is a promising building block for the development of new semiconducting polymers for photovoltaic applications.

4-5 Experimental Details

Synthesis and Materials. Unless otherwise stated, all chemicals and reagents were used as received from commercial sources without purification. Solvents for chemical synthesis were purified by distillation. All chemical reactions were carried out under an argon or nitrogen atmosphere. The benzo[1,2-*b*:4,5-*b'*]dithiophene-4,8-dione[38] and 4,8-bis(2-ethylhexyloxy)benzo[1,2-*b*:4,5-*b'*]dithiophene[17b] were synthesized according to the reported procedures. The intermediates 2'-ethylhexyl-4,6-dibromo-3-fluorothieno-[3,4-*b*]thiophene-2-carboxylate and 1,4-dibromo-2,5-didodecyl-3,6-bis(methylsulfinyl)-benzene were provided by the group members in the Yu research group, Mr. Tao Xu and Dr. Hae Jung Son, respectively.

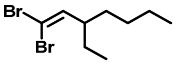

4-1

1,1-Dibromo-3-ethylhept-1-ene (4-1). To a stirring solution of triphenylphosphine (209.83 g, 800 mmol) in anhydrous dichloromethane (600 mL) was added carbon tetrabromide (132.65 g, 400 mmol) at 0 °C under an argon atmosphere. The reaction mixture was stirred for 15 min at this temperature, and then 2-ethylhexanal (31.2 mL, 200 mmol) was added to the mixture in one portion. After being stirred overnight at ambient temperature, the reaction mixture was diluted with hexane and filtered through a Celite pad. The solvent of the filtrate was removed by rotary evaporation, and the crude product was purified by column chromatography on silica gel with hexane as eluent to afford **4-1** as a colorless oil (50 g, 88%). ^{1}H NMR ($CDCl_3$, 400 MHz) δ 6.11 (d, J = 10.0 Hz, 1H), 2.31-2.27 (m, 1H), 1.50-1.24 (m, 8H), 0.89 (t, J = 7.6 Hz, 6H).

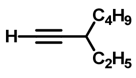

4-2

3-Ethylhept-1-yne (4-2). To a stirring solution of **4-1** (50 g, 176.04 mmol) in anhydrous THF (700 mL) was added dropwise *n*-BuLi solution (2.5 M in hexane, 154.92 mL, 387.29 mmol) at −78 °C under an argon atmosphere. The reaction mixture was warmed to room temperature over 1 hour, after which time it was poured into water and extracted with diethyl ether. The combined extracts were washed with brine, dried over anhydrous magnesium sulfate, and filtered. The solvent of the filtrate was removed by rotary evaporation, and the crude product was purified by distillation under nitrogen to afford **4-2** as a colorless oil (8.26 g, 38%). ^{1}H NMR (CDCl$_3$, 400 MHz) δ 2.29–2.21 (m, 1H), 2.04 (d, *J* = 2.4 Hz, 1H), 1.53–1.29 (m, 8H), 1.00 (t, *J* = 7.2 Hz, 3H), 0.91 (t, *J* = 7.2 Hz, 3H).

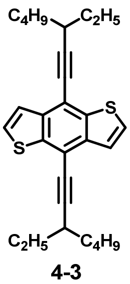

4-3

4,8-Bis(3-ethylhept-1-ynyl)benzo[1,2-*b*:4,5-*b'*]dithiophene (4-3). To a stirring solution of **4-2** (8.26 g, 66.49 mmol) in anhydrous THF (16 mL) was added dropwise isopropylmagnesium chloride solution (2M in THF, 29.93 mL, 59.85 mmol) at 0 °C under an argon atmosphere, after which the reaction mixture was stirred at 60 °C for 90 min. After the reaction mixture was cooled to room temperature, benzo[1,2-*b*:4,5-*b'*]dithiophene-4,8-dione (3.66 g, 16.63 mmol) was added to the mixture, and then it was stirred at 60 °C overnight. After the resulting slurry was cooled to 0 °C, 16.4 g of $SnCl_2$ in 42 mL of a 10% HCl solution was added dropwise to the mixture. The reaction mixture was heated at 60 °C for 60 min, cooled to room temperature, and then poured into water. It was extracted with diethyl ether. The combined extracts were washed with brine, dried over anhydrous magnesium sulfate, and filtered. The solvent of the filtrate was removed by rotary evaporation, and the crude product was purified by column chromatography on silica gel with dichloromethane/hexane (v/v, 1:10) as eluent to afford **4-3** as a light yellow solid (5.83 g, 81%). ^{1}H NMR ($CDCl_3$, 500 MHz) δ 7.57 (d, *J* = 5.5 Hz, 2H), 7.50 (d, *J* = 5.5 Hz, 2H), 2.72–2.69 (m, 2H), 1.72–1.54 (m, 12H), 1.46–1.39 (m, 4H), 1.19 (t, *J* = 7.5 Hz, 6H), 0.97 (t, *J* = 7.5 Hz, 6H); MS (*m/z*, MALDI-TOF$^+$) calcd for $C_{28}H_{34}S_2$, 434.2, found, 434.4.

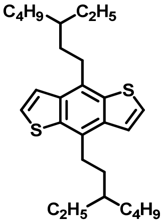

4-4

4,8-Bis(3-ethylheptyl)benzo[1,2-*b*:4,5-*b'*]dithiophene (4-4). To a stirring mixture of **4-3** (5.83 g, 13.41 mmol), acetic acid (6.14 mL, 107.28 mmol), and 10% Pd/C (1.43 g, 1.34 mmol) in isopropanol (67 mL) was added powdered sodium borohydride (8.12 g, 214.56 mmol) in one portion at room temperature in open air. After the reaction mixture was stirred for 60 min at this temperature, a 10% HCl solution was slowly added to the mixture for quenching at 0 °C. The resulting mixture was then adjusted to a pH of approximately 10 using sodium hydroxide and filtered through a Celite pad to remove the Pd/C catalyst. The filtrate was extracted with dichloromethane and water. The combined extracts were washed with brine, dried over anhydrous magnesium sulfate, and filtered. The solvent of the filtrate was removed by rotary evaporation, and the crude product was purified by column chromatography on silica gel with hexane as eluent to afford **4-4** as a sticky yellow oil (3.21 g, 54%). ^{1}H NMR ($CDCl_3$, 400 MHz) δ 7.46 (s, 4H), 3.17–3.12 (m, 4H), 1.77–1.73 (m, 4H), 1.51–1.32 (m, 18H), 0.96–0.91 (m, 12H); MS (*m/z*, MALDI-TOF$^+$) calcd for $C_{28}H_{42}S_2$, 442.3, found, 442.9.

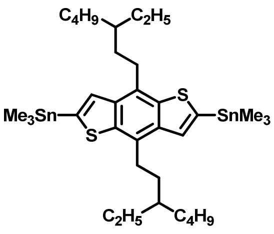

4-5

2,6-Bis(trimethyltin)-4,8-bis(3-ethylheptyl)benzo[1,2-*b*:4,5-*b′*]dithiophene (4-5). To a stirring solution of **4-4** (2.25 g, 5.08 mmol) in anhydrous THF (73 mL) was added dropwise *n*-BuLi solution (2.5 M in hexane, 5.08 mL, 12.70 mmol) at −78 °C under an argon atmosphere. The reaction mixture was stirred for 30 min at this temperature, quickly warmed to room temperature by removing the cooling bath, and then stirred for another 30 min. After the reaction mixture was recooled to −78 °C, trimethyltin chloride solution (1 M in hexane, 15.24 mL, 15.24 mmol) was added to the mixture in one portion, and then the cooling bath was removed. After being stirred overnight at room temperature, the reaction mixture was poured into water and extracted with diethyl ether. The combined extracts were washed with brine, dried over anhydrous magnesium sulfate, and filtered. The solvent of the filtrate was removed by rotary evaporation, and the crude product was recrystallized from isopropanol to afford **4-5** as white needle-like crystals (3.25 g, 83%). ^{1}H NMR ($CDCl_3$, 500 MHz) δ 7.49 (s, 2H), 3.18–3.14 (m, 4H), 1.77–1.73 (m, 4H), 1.51–1.36 (m, 18H), 0.97–0.92 (m, 12H), 0.45 (s, 18H).

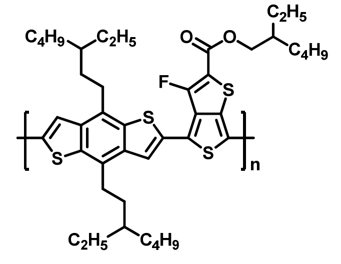

PTB10

PTB10. A mixture of **4-5** (192.1 mg, 0.25 mmol), 2'-ethylhexyl-4,6-dibromo-3-fluorothieno[3,4-*b*]thiophene-2-carboxylate (118.1 mg, 0.25 mmol), and $Pd(PPh_3)_4$ (14.4 mg, 0.0125 mmol) in a mixed solvent system of anhydrous toluene (3 mL) and anhydrous *N*,*N*-dimethylformamide (0.75 mL) was stirred and heated at 120 °C under an argon atmosphere for 1 day. After being cooled to room temperature, the reaction mixture was added dropwies into methanol. The resulting precipitate was collected by filtration through a Soxhlet thimble, and then subjected to sequential Soxhlet extraction with acetone and chloroform. The chloroform solution was filtered through a Celite pad to remove the metal catalyst. The filtrate was concentrated and then precipitated into methanol. The precipitate was collected by centrifugation and dried under vacuum overnight to afford **PTB10** as a black solid (175 mg, 93%). GPC: M_n (15.4 kg/mol), PDI (2.14).

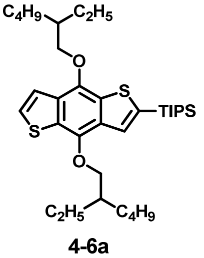

4-6a

2-[Tris(1-methylethyl)silyl]-4,8-bis(2-ethylhexyloxy)benzo[1,2-*b*:4,5-*b'*]dithiophe-

ne (4-6a). To a stirring solution of 4,8-bis(2-ethylhexyloxy)benzo[1,2-*b*:4,5-*b*′]dithiophene (4.92 g, 11.01 mmol) in anhydrous THF (110 mL) was added dropwise *n*-BuLi solution (2.5 M in hexane, 4.62 mL, 11.56 mmol) at −78 °C under an argon atmosphere. The reaction mixture was stirred for 30 min at this temperature, quickly warmed to room temperature by removing the cooling bath, and then stirred for another 30 min. After the reaction mixture was recooled to −78 °C, chlorotriisopropylsilane (2.59 mL, 12.11 mmol) was added to the mixture in one portion, and then the cooling bath was removed. After being stirred overnight at room temperature, the reaction mixture was poured into water and extracted with diethyl ether. The combined extracts were washed with brine, dried over anhydrous magnesium sulfate, and filtered. The solvent of the filtrate was removed by rotary evaporation, and the crude product was purified by column chromatography on silica gel with dichloromethane/hexane (v/v, 1:10) as eluent to afford **4-6a** as a sticky yellow oil (5.31 g, 80%). ^{1}H NMR ($CDCl_3$, 400 MHz) δ 7.64 (s, 1H), 7.47 (d, *J* = 5.6 Hz, 1H), 7.35 (d, *J* = 5.6 Hz, 1H), 4.22–4.19 (m, 4H), 1.86–1.76 (m, 2H), 1.76–1.32 (m, 19H), 1.18 (d, *J* = 7.6 Hz, 18H), 1.05–1.00 (m, 6H), 0.96–0.92 (m, 6H); MS (*m/z*, MALDI-TOF$^+$) calcd for $C_{35}H_{58}O_2S_2Si$, 602.4, found, 602.1.

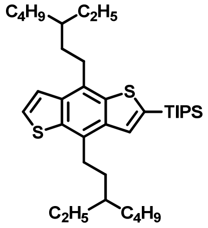

4-6b

2-[Tris(1-methylethyl)silyl]-4,8-bis(3-ethylheptyl)benzo[1,2-*b*:4,5-*b*′]dithiophene (4-6b). The synthetic procedure was similar to that described for synthesis of **4-6a**, except that the eluent for column purification was hexane. **4-6b** was isolated as a sticky yellow oil (62%). ^{1}H NMR ($CDCl_3$, 500 MHz) δ 7.62 (s, 1H), 7.45 (s, 2H), 3.18–3.15 (m, 4H), 1.76–1.75 (m, 4H), 1.49–1.30 (m, 21H), 1.18 (d, *J* = 7.5 Hz, 18H), 0.96–0.93 (m, 12H); MS (*m/z*, MALDI-TOF$^+$) calcd for $C_{37}H_{62}S_2Si$, 598.4, found, 598.3.

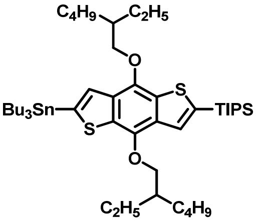

4-7a

2-Tributyltin-6-[tris(1-methylethyl)silyl]-4,8-bis(2-ethylhexyloxy)benzo[1,2-*b*:4,5-*b'*]dithiophene (4-7a). To a stirring solution of **4-6a** (2.41 g, 4 mmol) in anhydrous THF (40 mL) was added dropwise *n*-BuLi solution (2.5 M in hexane, 1.92 mL, 4.8 mmol) at －78 °C under an argon atmosphere. The reaction mixture was stirred for 30 min at this temperature, quickly warmed to room temperature by removing the cooling bath, and then stirred for another 30 min. After the reaction mixture was recooled to －78 °C, tri-*n*-butyltin chloride (1.30 mL, 4.8 mmol) was added to the mixture in one portion, and then the cooling bath was removed. After being stirred overnight at room temperature, the reaction mixture was poured into water and extracted with diethyl ether. The combined extracts were washed with brine, dried over anhydrous magnesium sulfate, and filtered. The solvent of the filtrate was removed by rotary evaporation to afford **4-7a** as a sticky yellow oil, which was used for the next step without further purification.

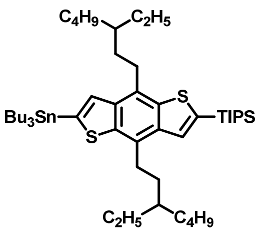

4-7b

2-Tributyltin-6-[tris(1-methylethyl)silyl]-4,8-bis(3-ethylheptyl)benzo[1,2-*b*:4,5-*b′*]dithiophene (4-7b). The synthetic procedure was similar to that described for synthesis of **4-7a**.

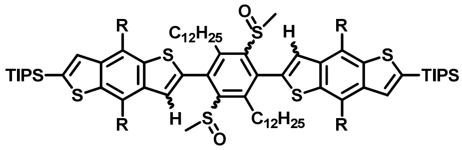

4-8a: R = 2-ethylhexyloxy

6,6’-[2,5-Didodecyl-3,6-bis(methylsulfinyl)-1,4-phenylene]bis{2-[tris(1-methylethyl)silyl]-4,8-bis(2-ethylhexyloxy)benzo[1,2-*b*:4,5-*b′*]dithiophene} (4-8a). A mixture of **4-7a** (4 mmol), 1,4-dibromo-2,5-didodecyl-3,6-bis(methylsulfinyl)benzene (1.115 g, 1.6 mmol), and $Pd(PPh_3)_4$ (185 mg, 0.16 mmol) in a mixed solvent system of anhydrous toluene (32 mL) and anhydrous *N*,*N*-dimethylformamide (8 mL) was stirred and heated at 120 °C under an argon atmosphere overnight. After the reaction mixture was cooled to room temperature, the solvent was removed by vacuum evaporation, and the crude product was purified by column chromatography on silica gel with dichloromethane/hexane (v/v, 2:1) as eluent to afford **4-8a** as a sticky yellow oil (2.17 g, 78%). The proton NMR is hard to assign because of the formation of a diastereomeric mixture; MS (*m/z*, MALDI-TOF$^+$) calcd for $C_{102}H_{170}O_6S_6Si_2$, 1739.1, found, 1739.1.

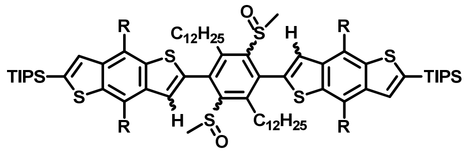

4-8b: R = 3-ethylheptyl

6,6'-[2,5-Didodecyl-3,6-bis(methylsulfinyl)-1,4-phenylene]bis{2-[tris(1-methylethyl)silyl]-4,8-bis(3-ethylheptyl)benzo[1,2-*b*:4,5-*b'*]dithiophene} (4-8b). The synthetic procedure was similar to that described for synthesis of **4-8a**, except that the eluent for column purification was dichloromethane/hexane (v/v, 3:4). **4-8b** was isolated as a sticky yellow oil (58%). The proton NMR is hard to assign because of the formation of a diastereomeric mixture; MS (*m/z*, MALDI-TOF$^+$) calcd for $C_{106}H_{178}O_2S_6Si_2$, 1731.2, found, 1731.8.

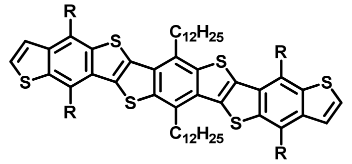

4-9a: R = 2-ethylhexyloxy

4-9a. A mixture of **4-8a** (1.78 g, 1.02 mmol), phosphorus pentoxide (1.45 g, 10.22 mmol), and trifluoroacetic acid (102 mL) was stirred at room temperature under an argon atmosphere overnight, during which time the color of the reaction mixture changed from deep red to deep yellow-green. The reaction mixture was then poured into ice-water and extracted with dichloromethane. The combined extracts were washed with brine, dried over anhydrous magnesium sulfate, and filtered. After the solvent of the filtrate was removed by rotary evaporation, the residue was dissolved in pyridine (200 mL), and the resulting solution was heated to reflux overnight. After the reaction mixture was cooled to room temperature, the solvent was removed by rotary evaporation, and the crude product was purified by column chromatography on silica gel with dichloromethane/hexane (v/v, 1:4) as eluent to afford **4-9a** as a greenish solid

(875 mg, 63%). ^{1}H NMR (CDCl$_3$, 500 MHz) δ 7.53 (d, *J* = 5.5 Hz, 2H), 7.42 (s, 2H), 4.33–4.26 (m, 8H), 3.43 (m, 4H), 2.16–1.26 (m, 76H), 1.13–1.07 (m, 12H), 1.00–0.97 (m, 12H), 0.86 (t, *J* = 6.5 Hz, 6H); MS (*m/z*, MALDI-TOF$^+$) calcd for $C_{82}H_{122}O_4S_6$, 1362.8, found, 1362.6.

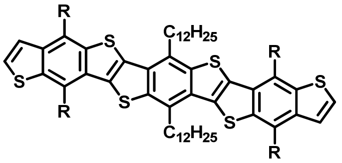

4-9b: R = 3-ethylheptyl

4-9b. A mixture of **4-8b** (1.08 g, 0.62 mmol), phosphorus pentoxide (884 mg, 6.23 mmol), and trifluoroacetic acid (62 mL) was stirred at room temperature under an argon atmosphere overnight, during which time the color of the reaction mixture changed from deep red to deep yellow-green. The reaction mixture was then poured into ice-water. The resulting precipitate was collected by filtration, and then refluxed in pyridine (120 mL) overnight. After being cooled to room temperature, the reaction mixture was poured into an ice-cold 10% HCl solution. The precipitate was collected by filtration, and then washed sequentially with water, methanol, and diethyl ether to afford **4-9b** as a yellow solid (481 mg, 57%). ^{1}H NMR (CDCl$_3$, 500 MHz) δ 7.48 (d, *J* = 5.5 Hz, 2H), 7.37 (d, *J* = 5.5 Hz, 2H), 3.27–3.18 (m, 8H), 2.93–2.90 (m, 4H), 1.92–1.03 (m, 84H), 1.00–0.95 (m, 24H), 0.86 (t, *J* = 7.0 Hz, 6H); MS (*m/z*, MALDI-TOF$^+$) calcd for $C_{86}H_{130}S_6$, 1354.8, found, 1354.4.

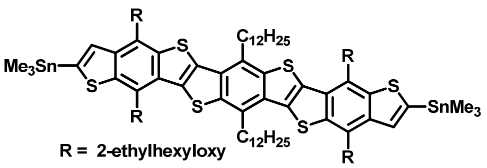

R = 2-ethylhexyloxy

4-10

4-10. To a stirring solution of **4-9a** (409 mg, 0.3 mmol) in anhydrous THF (15 mL) was added dropwise *n*-BuLi solution (2.5 M in hexane, 0.3 mL, 0.75 mmol) at −78 °C under an argon atmosphere. The reaction mixture was stirred for 30 min at this temperature, quickly warmed to room temperature by removing the cooling bath, and then stirred for another 30 min. After the reaction mixture was recooled to −78 °C, trimethyltin chloride solution (1 M in hexane, 0.9 mL, 0.9 mmol) was added to the mixture in one portion, and then the cooling bath was removed. After being stirred overnight at room temperature, the reaction mixture was poured into water and extracted with diethyl ether. The combined extracts were washed with brine, dried over anhydrous magnesium sulfate, and filtered. The solvent of the filtrate was removed by rotary evaporation, and the crude product was recrystallized from isopropanol to afford **4-10** as a yellow solid (440 mg, 87%). ^{1}H NMR ($CDCl_3$, 400 MHz) δ 7.58 (s, 2H), 4.37 (d, *J* = 5.6 Hz, 4H), 4.26 (d, *J* = 5.6 Hz, 4H), 3.41 (t, *J* = 8.4 Hz, 4H), 2.15–1.26 (m, 76H), 1.13–1.07 (m, 12H), 0.99–0.96 (m, 12H), 0.86 (t, *J* = 6.4 Hz, 6H), 0.49 (s, 18H).

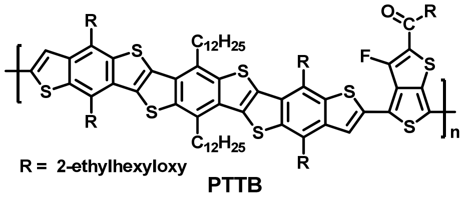

PTTB

PTTB. A mixture of **4-10** (101.4 mg, 0.06 mmol), 2'-ethylhexyl-4,6-dibromo-3-fluorothieno[3,4-*b*]thiophene-2-carboxylate (28.3 mg, 0.06 mmol), and $Pd(PPh_3)_4$ (3.5 mg, 0.003 mmol) in a mixed solvent system of anhydrous toluene (1.25 mL) and anhydrous *N*,*N*-dimethylformamide (0.25 mL) was stirred and heated at 120 °C under an argon atmosphere for 1 day. After being cooled to room temperature, the reaction mixture was added dropwies into methanol. The resulting precipitate was collected by filtration through a Soxhlet thimble, and then subjected to sequential Soxhlet extraction with hexane, heptane, and chloroform. The chloroform solution was filtered through a Celite pad to remove the metal catalyst. The filtrate was concentrated and then precipitated into methanol. The precipitate was collected by centrifugation and dried under vacuum overnight to afford **PTTB** as a black solid (61 mg, 61%). GPC: M_n (9.0 kg/mol), PDI (1.43).

Cyclic Voltammetry Measurement. The electrochemical properties of **PTB10** and **PTTB** were investigated by cyclic voltammetry (CV). The measurements were carried out in an anhydrous acetonitrile solution containing 0.1 M tetrabutylammonium hexafluorophosphate ($TBAPF_6$) as a supporting electrolyte. A glassy carbon electrode coated with a polymer thin film was used as the working electrode. All potentials were recorded versus $Ag/AgNO_3$ (saturated) as a reference electrode and calibrated with the ferrocene/ferrocenium (Fc/Fc^+) redox couple. All measurements were performed at a scan rate of 100 mV s^{-1}.

Solar Cell Fabrication and Testing. The polymer (**PTB10** or **PTTB**) and $PC_{71}BM$ (American Dye Source) were co-dissolved in a mixed solvent of chlorobenzene/1,8-diodooctane (ALDRICH) (97:3, v/v) and the resulting solution was stirred at 90 °C for 12 h under an anhydrous nitrogen atmosphere prior to use. The ITO-coated glass substrate (Thin Film Devices) with a sheet resistance of 20 ± 2 Ω/sq. was cleaned stepwise in water, acetone, and isopropyl alcohol under ultrasonication for 15 min each and exposed to ultraviolet ozone (UVO) irradiation for 60 min. A thin layer (~60 nm) of PEDOT:PSS (Clevios 4083) was spin-coated onto the ITO substrate at 4100 rpm for 1 min and dried at 90 °C under N_2 for 30 min, after which the ITO/PEDOT:PSS substrate was transferred into a nitrogen-filled glove box (< 0.1 ppm

O_2 and H_2O) for active layer coating and cathode formation. The polymer:$PC_{71}BM$ composite layer (about 150 nm) with a weight ratio of 1:1.5 was then deposited atop the PEDOT:PSS layer by spin-coating the as-prepared solution (concentration, 25 mg mL^{-1}) at 2000 r.p.m. with a duration of 60 and 90 sec for **PTB10** and **PTTB**, respectively. The film was transferred into a thermal evaporator which is located in the same glove box. Subsequently, a 20-nm-thick Ca layer and 80-nm-thick Al layer were deposited in sequence at chamber pressure of $\sim 5.0 \times 10^{-7}$ Torr. The active area of the solar cell was measured to be 3.14 mm^2. Current density–voltage characteristics of solar cells were measured in a nitrogen-filled glove box using a Keithley 2420 Source Measure Unit under AM 1.5 G, 1 sun (100 mW/cm^2) simulated solar illumination from a xenon lamp solar simulator (Oriel model 94023A). The light intensity was calibrated using a monocystalline silicon reference cell (M-91150V, with KG5 filter certificated by NREL).

4-6 References

---

[1] (a) Yu, G.; Gao, J.; Hummelen, J. C.; Wudl, F.; Heeger, A. J. *Science* **1995,** *270,* 1789. (b) Thompson, B. C.; Fréchet, J. M. J. *Angew. Chem., Int. Ed.* **2008,** *47,* 58. (c) Li, G.; Zhu, R.; Yang, Y. *Nat. Photonics* **2012,** *6,* 153.

[2] (a) Cheng, Y.-J.; Yang, S.-H.; Hsu, C.-S. *Chem. Rev.* **2009,** *109,* 5868. (b) Zhou, H.; Yang, L.; You, W. *Macromolecules* **2012,** *45,* 607. (c) Uy, R. L.; Price, S. C.; You, W. *Macromol. Rapid Commun.* **2012,** *33,* 1162.

[3] (a) Ma, W.; Yang, C.; Gong, X.; Lee, K.; Heeger, A. J. *Adv. Funct. Mater.* **2005,** *15,* 1617. (b) Li, G.; Shrotriya, V.; Huang, J.; Yao, Y.; Moriarty, T.; Emery, K.; Yang, Y. *Nat. Mater.* **2005,** *4,* 864. (c) Peet, J.; Kim, J. Y.; Coates, N. E.; Ma, W. L.; Moses, D.; Heeger, A. J.; Bazan, G. C. *Nat. Mater.* **2007,** *6,* 497.

[4] (a) Kim, J. Y.; Kim, S. H.; Lee, H.-H.; Lee, K.; Ma, W.; Gong, X.; Heeger, A. J. *Adv. Mater.* **2006,** *18,* 572. (b) Sun, Y.; Takacs, C. J.; Cowan, S. R.; Seo, J. H.; Gong, X.; Roy, A.; Heeger, A. J. *Adv. Mater.* **2011,** *23,* 2226. (c) Seo, J.-H.; Gutacker, A.; Sun, Y.; Wu, H.; Huang, F.; Cao, Y.; Scherf, U.; Heeger, A. J.; Bazan, G. C. *J. Am. Chem. Soc.* **2011,** *133,* 8416. (d) He, Z.; Zhong, C.; Huang, X.; Wong, W.-Y.; Wu, H.; Chen, L.; Su, S.; Cao, Y. *Adv. Mater.* **2011,** *23,* 4636. (e) Small, C. E.; Chen, S.; Subbiah, J.; Amb, C. M.; Tsang, S.-W.; Lai, T.-H.; Reynolds, J. R.; So, F. *Nat. Photonics* **2012,** *6,* 115. (f) Yang, T.; Wang, M.; Duan, C.; Hu, X.; Huang, L.; Peng, J.; Huang, F.; Gong, X. *Energy Environ. Sci.* **2012,** *5,* 8208.

[5] (a) Chen, L.-M.; Hong, Z.; Li, G.; Yang, Y. *Adv. Mater.* **2009,** *21,* 1434. (b) Hsieh, C.-H.; Cheng, Y.-J.; Li, P.-J.; Chen, C.-H.; Dubosc, M.; Liang, R.- M.; Hsu, C.-S. *J. Am. Chem. Soc.* **2010,** *132,* 4887. (c) Cheng, Y.-J.; Hsieh, C.-H.; He, Y.; Hsu, C.-S.; Li, Y. *J. Am. Chem. Soc.* **2010,** *132,* 17381. (d) Chang, C.-Y.; Wu, C.-E.; Chen, S.-Y.; Cui, C.;

Cheng, Y.-J.; Hsu, C.-S.; Wang, Y.-L.; Li, Y. *Angew. Chem., Int. Ed.* **2011,** *50,* 9386. (e) Yang, L.; Zhou, H.; Price, S. C.; You, W. *J. Am. Chem. Soc.* **2012,** *134,* 5432.

[6] (a) He, Y.; Chen, H.-Y.; Hou, J.; Li, Y. *J. Am. Chem. Soc.* **2010,** *132,* 1377. (b) He, Y.; Zhao, G.; Peng, B.; Li, Y. *Adv.Funct. Mater.* **2010,** *20,* 3383. (c) Zhao, G.; He, Y.; Li, Y. *Adv. Mater.* **2010,** *22,* 4355. (d) Fan, X.; Cui, C.; Fang, G.; Wang, J.; Li, S.; Cheng, F.; Long, H.; Li, Y. *Adv.Funct. Mater.* **2012,** *22,* 585.

[7] Huo, L.; Zhang, S.; Guo, X.; Xu, F.; Li, Y.; Hou, J. *Angew. Chem., Int. Ed.* **2011,** *50,* 9697.

[8] Chu, T.-Y.; Lu, J.; Beaupré, S.; Zhang, Y.; Pouliot, J.-R.; Wakim, S.; Zhou, J.; Leclerc, M.; Li, Z.; Ding, J.; Tao, Y. *J. Am. Chem. Soc.* **2011,** *133,* 4250.

[9] Amb, C. M.; Chen, S.; Graham, K. R.; Subbiah, J.; Small, C. E.; So, F.; Reynolds, J. R. *J. Am. Chem. Soc.* **2011,** *133,* 10062.

[10] Su, M.-S.; Kuo, C.-Y.; Yuan, M.-C.; Jeng, U.-S.; Su, C.-J.; Wei, K.-W. *Adv. Mater.* **2011,** *23,* 3315.

[11] Zhou, H.; Yang, L.; Stuart, A. C.; Price, S. C.; Liu, S.; You, W. *Angew. Chem., Int. Ed.* **2011,** *50,* 2995.

[12] Price, S. C.; Stuart, A. C.; Yang, L.; Zhou, H.; You, W. *J. Am. Chem. Soc.* **2011,** *133,* 4625.

[13] Chen, H.-C.; Chen, Y.-H.; Liu, C.-C.; Chien, Y.-C.; Chou, S.-W.; Chou, P.-T. *Chem. Mater.* **2012,** *24,* 4766.

[14] (a) Dou, L.; Chang, W.-H.; Gao, J.; Chen, C.-C.; You, J.; Yang, Y. *Adv. Mater.* **2013,** *25,* 825. (b) Dou, L.; Gao, J.; Richard, E.; You, J.; Chen, C.-C.; Cha, K. C.; He, Y.; Li, G.; Yang, Y. *J. Am. Chem. Soc.* **2012,** *134,* 10071. (c) Dou, L.; You, J.; Yang, J.; Chen, C.-C.; He, Y.; Murase, S.; Moriarty, T.; Emery, K.; Li, G.; Yang, Y. *Nat. Photonics*

2012, *6,* 180.

[15] You, J.; Dou, L.; Yoshimura, K.; Kato, T.; Ohya, K.; Moriarty, T.; Emery, K.; Chen, C.-C.; Gao, J.; Li, G.; Yang, Y. *Nat. Commun.* **2013,** *4,* 1446.

[16] (a) Kim, J. Y.; Lee, K.; Coates, N. E.; Moses, D.; Nguyen, T.-Q.; Dante, M.; Heeger, A. J. *Science* **2007,** *317,* 222. (b) Yang, J.; Zhu, R.; Hong, Z.; He, Y.; Kumar, A.; Li, Y.; Yang, Y. *Adv. Mater.* **2011,** *23,* 3465.

[17] (a) Liang, Y.; Wu, Y.; Feng, D.; Tsai, S.-T.; Son, H. J.; Li, G.; Yu, L. *J. Am. Chem. Soc.* **2009,** *131,* 56. (b) Liang, Y.; Feng, D.; Wu, Y.; Tsai, S.-T.; Li, G.; Ray, C.; Yu, L. *J. Am. Chem. Soc.* **2009,** *131,* 7792. (c) Liang, Y.; Xu, Z.; Xia, J.; Tsai, S.-T.; Wu, Y.; Li, G.; Ray, C.; Yu, L. *Adv. Mater.* **2010**, *22*, E135. (d) Liang, Y.; Yu, L. *Acc. Chem. Res.* **2010**, *43*, 1227. (e) Saadeh, H. A.; Lu, L.; He, F.; Bullock, J. E.; Wang, W.; Carsten, B.; Yu, L. *ACS Macro Lett.* **2012,** *1,* 361.

[18] Sista, P.; Biewer, M. C.; Stefan, M. C. *Macromol. Rapid Commun.* **2012,** *33,* 9.

[19] He, Z.; Zhong, C.; Su, S.; Xu, M.; Wu, H.; Cao, Y. *Nat. Photonics* **2012,** *6,* 591.

[20] Tran, A. T.; Huynh, V. A.; Friz, E. M.; Whitney, S. K.; Cordes, D. B. *Tetrahedron Lett.* **2009,** *50,* 1817.

[21] Braunecker, W. A.; Owczarczyk, Z. R.; Garcia, A.; Kopidakis, N.; Larsen, R. E.; Hammond, S. R.; Ginley, D. S.; Olson, D. C. *Chem. Mater.* **2012,** *24,* 1346.

[22] Carsten, B.; He, F.; Son, H.-J.; Xu, T.; Yu, L. *Chem. Rev.* **2011,** *111,* 1493.

[23] (a) Tong, M.; Cho, S.; Rogers, J. T.; Schmidt, K.; Hsu, B. B. Y.; Moses, D.; Coffin, R. C.; Kramer, E. J.; Bazan, G. C.; Heeger, A. J. *Adv. Funct. Mater.* **2010,** *20,* 3959. (b) Chu, T.-Y.; Lu, J.; Beaupré, S.; Zhang, Y.; Pouliot, J.-R.; Zhou, J.; Najari, A.; Leclerc, M.; Tao, Y. *Adv. Funct. Mater.* **2012,** *22,* 2345.

[24] Coffin, R. C.; Peet, J.; Rogers, J.; Bazan, G. C. *Nat. Chem.* **2009,** *1,* 657.

---

[25] Peet, J.; Cho, N. S.; Lee, S. K.; Bazan, G. C. *Macromolecules* **2008,** *41,* 8655.

[26] Lee, J. K.; Ma, W. L.; Brabec, C. J.; Yuen, J.; Moon, J. S.; Kim, J. Y.; Lee, K.; Bazan, G. C.; Heeger, A. J. *J. Am. Chem. Soc.* **2008,** *130,* 3619.

[27] Brédas, J. L.; Calbert, J. P.; da Silva Filho, D. A.; Cornil. J. *Proc. Natl. Acad. Sci. USA* **2002,** *99,* 5804.

[28] Chen, Y.-C.; Yu, C.-Y.; Fan, Y.-L.; Hung, L.-I; Chen, C.-P.; Ting, C. *Chem. Commun.* **2010,** *46,* 6503.

[29] Chang, C.-Y.; Cheng, Y.-J.; Hung, S.-H.; Wu, J.-S.; Kao, W.-S.; Lee, C.-H.; Hsu, C.-S. *Adv. Mater.* **2012,** *24,* 549.

[30] Chen, Y.-L.; Chang, C.-Y.; Cheng, Y.-J.; Hsu, C.-S. *Chem. Mater.* **2012,** *24,* 3964.

[31] Xu, Y.-X.; Chueh, C.-C.; Yip, H.-L.; Ding, F.-Z.; Li, Y.-X.; Li, C.-Z.; Li, X.; Chen, W.-C.; Jen, A. K.-Y. *Adv. Mater.* **2012,** *24,* 6356.

[32] Zhong, H.; Li, Z.; Deledalle, F.; Fregoso, E. C.; Shahid, M.; Fei, Z.; Nielsen, C. B.; Yaacobi-Gross, N.; Rossbauer, S.; Anthopoulos, T. D.; Durrant, J. R.; Heeney, M. *Am. Chem. Soc.* **2013,** *135,* 2040.

[33] He, F.; Wang, W.; Chen, W.; Xu, T.; Darling, S. B.; Strzalka, J.; Liu, Y.; Yu, L. *J. Am. Chem. Soc.* **2011,** *133,* 3284.

[34] Son, H. J.; Lu, L.; Chen, W.; Xu, T.; Zheng, T.; Carsten, B.; Strzalka, J.; Darling, S. B.; Chen, L. X.; Yu, L. *Adv. Mater.* **2013,** *25,* 838.

[35] Leuninger, J.; Wang, C.; Soczka-Guth, T.; Enkelmann, V.; Pakula, T.; Müllen, K. *Macromolecules* **1998,** *31,* 1720.

[36] Gao, P.; Cho, D.; Yang, X.; Enkelmann, V.; Baumgarten, M.; Müllen, K. *Chem. Eur. J.* **2010,** *16,* 5119.

[37] Mcculloch, I.; Heeney, M.; Bailey, C.; Genevicius, K.; Macdonald, I.; Shkunov, M.;

Sparrowe, D.; Tierney, S.; Wagner, R.; Zhang, W.; Chabinyc, M. L.; Kline, R. J.; McGehee, M. D.; Toney, M. F. *Nat. Mater.* **2006,** *5,* 328.

[38] (a) Beimling, P.; Kobmehl, G. *Chem. Ber.* **1986,** *119,* 3198. (b) Hou, J.; Park, M.-H.; Zhang, S.; Yao, Y.; Chen, L.-M.; Li, J.-H.; Yang, Y. *Macromolecules* **2008,** *41,* 6012.